Modelling three-phase mushy layers, with applications to air bubbles and oil droplets in sea ice

Joseph Fishlock
Brasenose College
University of Oxford

A thesis submitted for the degree of
Doctor of Philosophy

Hilary 2025

Acknowledgements

This thesis was made possible by generous funding from the Natural Environment Research Council through the Oxford Doctoral Training Programme in Environmental Research. Additional funding was provided by Brasenose College for research and travel expenses. Special thanks go to Victoria Forth and Prof. David Marshall for all their help.

I would like to thank my endlessly patient supervisors Prof. Andrew Wells and Prof. Christopher MacMinn for their unwavering support and guidance. I could not have asked for a more encouraging and knowledgeable pair of supervisors. Their positivity helped me through even the most challenging parts of my PhD and they set an excellent example of how to be a good scientist.

I am grateful to the many talented people who have studied sea ice before me and whose efforts have made this research possible. I must thank Prof. Jean-Louis Tison for providing field data for chapter 7 and for his enthusiasm. Thanks also to Dr Odile Crabeck for meeting with me to discuss bubbles in sea ice and for her contributions to the field.

I would like to thank the members of the Icy Maths, Poromechanics, and OxOceanClimate research groups for their friendship and all the amazing work that they do. Thanks also to all the friendly faces in Atmospheric, Oceanic, and Planetary Physics including Rhidian, Rosie, and Charlie and my fellow icy physicists Oscar and Debs.

Special thanks go to my wonderful housemates (and friends) Alice, Anna, Sophie, and Luke for making Ferry Road and Oxford feel like home. Thanks to all my amazing friends for doing their best to understand what a mushy layer is and to Ewan for getting me through the late stages of writing this thesis. Finally, thank you to Mum, Dad, and my brother Harry, for their unconditional love and support, and for always believing in me. I guess it's time to get a real job now.

Abstract

A *mushy layer* is a reactive porous medium that forms during the partial solidification of a multicomponent liquid. Sea ice is a naturally occurring mushy layer that forms through the freezing of seawater in the polar oceans. This multiphase mixture of solid ice crystals, liquid brine, air bubbles, and other chemical species plays a critical role in Earth's climate and ecosystems. Two-phase mushy layers, comprising a porous solid saturated with liquid, have been well studied; however, sea ice and other mushy layers in the natural environment often contain gaseous inclusions or other immiscible liquid phases, yielding a three-phase problem. This thesis formulates appropriate conservation equations for a three-phase mushy layer that accounts for the production, migration, and trapping of a third distinct phase in the pore space of sea ice. We use an idealised model of the pore geometry to derive a novel expression for the vertical flux of a buoyant third phase dispersed as bubbles/droplets in the liquid-filled pore space. The resulting model is applied to both air bubbles and oil droplets in sea ice. Two key dimensionless parameters arise: (1) the ratio of the bubble/droplet radius to the pore throat-radius and (2) the timescale of gas exsolution relative to the timescale of solidification in the mushy layer (in the case of a solid-liquid-gas system).

We explore the three-phase mushy-layer model in a variety of settings. First, we examine the three-phase mushy layer found during the steady solidification of air-saturated saltwater in a Hele-Shaw cell. We show that neglecting the volume occupied by exsolved gas yields a reduced "tracer" model for the dissolved and free-phase gas that still describes the steady-state solution well. Then, we formulate a one-dimensional transient model for sea-ice evolution that includes parameterisations for brine convection, radiative transfer, and heat exchanges with the overlying atmosphere and snowpack, and with the underlying ocean. We validate this transient model against observations of first-year landfast sea ice at Barrow, Alaska. We use ice core measurements of bulk gas concentrations from Barrow to constrain the gas dynamics in our model and predict the seasonal evolution of the gas volume fraction and ice bulk density. This has implications for biogeochemical cycles in the Arctic and the estimation of ice thickness from remote sensing measurements. Finally, we investigate the impact of low levels of weathered oil droplets on landfast sea ice, and find that the increased absorption of solar radiation by these droplets can significantly enhance ice melt rates and delay the onset of the spring under-ice algal bloom compared with year-to-year variability. The results in this thesis have important implications for the future study of sea ice as a complex multiphase reactive material.

Contents

Appendices

1

Introduction

A mushy layer is a reactive porous medium that forms during the solidification of certain multicomponent liquids in which the concentration of dissolved solute controls the freezing temperature (Worster 2000), e.g. saltwater. A two-phase mushy layer consists of a porous solid matrix filled with interstitial liquid, where segregation of the solute from the solid phase elevates the solute concentration in the interstitial liquid. Heat and solute transport within a mushy layer drive internal phase change, which changes the local porosity, and therefore the permeability to fluid transport. Therefore, mushy layers often exhibit complex feedbacks between fluid motion, and phase change (Worster 1992; Chiareli and Worster 1995; Worster 1997; Wells et al. 2019; Anderson and Guba 2020; Anderson et al. 2022). Mushy-layer theory utilises a phase-averaged approach where the porosity of a mushy layer is approximated by the volume fractions of the solid and liquid phases contained in a representative elementary volume (REV), which is larger than the individual pore scale but smaller than the macroscopic scale of the layer. In this thesis we will extend an existing two-phase mushy-layer theory to consider a three-phase mushy layer, in which an additional gas phase or second immiscible liquid phase is present in the pore space of the mushy layer.

One important geophysical example of a mushy layer is sea ice, which forms in the polar oceans during the solidification of seawater containing dissolved salts (Feltham et al. 2006; Hunke et al. 2011). Whist much of the work in this thesis applies to sea ice in general, we will focus on the Arctic when comparing model output to field data. Sea ice in the Arctic reaches a maximum extent in winter (February/March) of between 15 and 17 million square kilometers, and a minimum extent of between 4 and 8 million square kilometers in September after the summer melt season

(Perovich 2011; Stroeve et al. 2014; Serreze and Stroeve 2015; Comiso et al. 2017). Both maximum and minimum sea ice extent is declining in the Arctic due to anthropogenic climate change at a rate of around 2.5% per decade for the maximum extent, and 10.8% per decade for the minimum extent (Comiso et al. 2017).

Sea ice is an important component of the Earth's climate system because ice-covered waters reflect much more incoming solar radiation than open water (Holland and Bitz 2003; Holland et al. 2006; Hudson 2011). Sea ice also modifies exchanges of momentum, heat, water, and gases between the ocean and atmosphere, and hence plays a key role in atmospheric and oceanic circulation (Overland 1985; Andreas et al. 2002; Andreas et al. 2010; Spreen et al. 2011; Kwok et al. 2013) and global biogeochemical cycles (Loose and Schlosser 2011; Lannuzel et al. 2020). Drainage mechanisms during sea ice growth (see Notz and Worster 2009, for example) produce significant salt fluxes to the underlying ocean, which create dense water masses at the poles and contribute to the global oceanic overturning circulation (Backhaus 1997; Abernathey et al. 2016). The transmission of visible light, necessary for photosynthesis, through the ice is a strong control on primary production and biological activity under sea ice (Ehn et al. 2008; Mundy et al. 2009; Arrigo et al. 2012; Arrigo 2014). The sea ice environment is crucial to the life of many Arctic marine-based mammal species such as polar bears, seals, and walruses as well as Arctic fisheries (Huntington and Moore 2008; Johannessen and Miles 2011). Changes in the extent of Arctic sea ice also have profound implications for human uses of the Arctic Ocean, such as shipping and goods transport (Kikkas and Romashkina 2018), and the lives of indigenous people (Laidler et al. 2009).

Seawater contains dissolved sodium chloride salt (NaCl), other dissolved salts (Millero et al. 2008) and dissolved atmospheric gases (Weiss 1970; Weiss 1974; Nakayama et al. 2002). In addition, one can also find suspended sediments, phytoplankton and other biological material, microplastics, droplets of crude oil, and an array of dissolved anthropogenic pollutants (Otremba 2007; Sørensen et al. 2014; Windom 2019; Honda and Suzuki 2020). Some of these components have the potential to produce a third distinct phase in sea ice that coexists amongst the solid ice matrix and interstitial liquid brine. For example, dissolved gases present in seawater can exsolve to produce gas bubbles in the sea ice pore space (see Tison et al. 2017, for example). Oil droplets originating from crude oil spilled into the ocean can also reside in the pore space of sea ice as an additional immiscible liquid phase (see Redmond Roche 2024, for example).

Multiphase gas–liquid and liquid–liquid flows in natural porous media have been extensively studied (Blunt 2017) with applications including: the venting of methane bubbles from seafloor sediments (Skarke et al. 2014), the percolation of meltwater through snow (Meyer and Hewitt 2017; Jones et al. 2024), gas-driven volcanic eruptions (Suckale et al. 2016; Calleja and Pering 2023), the upward buoyancy-driven percolation of oil released under sea ice (Oggier et al. 2020), and the transport of argon (Moreau et al. 2014) and carbon dioxide (Moreau et al. 2015b) by bubbles in sea ice. The latter two studies treat multiphase sea ice with dynamically evolving tracers for dissolved gases and gas bubbles, although they did not systematically derive these models from mushy-layer theory. Despite the applications to gases and oil in sea ice, to the best of our knowledge, the existing two-phase mushy-layer theory used to model sea ice has not been systematically extended to deal with a third phase. A key aim of this thesis is to develop a general formulation for a three-phase mushy layer that is applicable to sea ice.

Another naturally occurring three-phase mushy layer is the multicomponent mineral melt found in magma chambers, which typically contains volatiles such as dissolved water and carbon dioxide (Huppert and Worster 2012). Gas content and transport in magmatic systems is important for the evolution of magma chambers and the intensity of volcanic eruptions (Huppert and Woods 2002; Girona et al. 2015; Parmigiani et al. 2016; Liao 2022) and has been studied using a phase-averaged approach (Keller and Suckale 2019). Unlike in sea ice, the exsolution of magmatic volatiles into gas bubbles is primarily driven by de-pressurisation and temperature variations, as opposed to concentration change due to solidification. Whilst there is definitely wider applicability of work on three-phase mushy layers in the geosciences we will focus on sea ice in much of this thesis.

It has been known since at least the 1970s that sea ice contains a significant amount of air present in gaseous inclusions (Tsurikov 1979). The presence of a gas phase in sea ice has important consequences for the remote sensing of ice thickness and the exchange of gas species between the ocean and atmosphere (which will be reviewed later in this chapter). The volume fraction of air in sea ice is often estimated from measurements of the bulk density, using the formulae given by Cox and Weeks (1983). Several studies have also examined the number and size distribution of bubbles in thin sections of sea ice using optical microscopy (Grenfell 1983; Light et al. 2003). More recently, the air fraction in sea ice cores has been estimated directly using X-ray tomography (e.g. Crabeck et al. 2016). Computational models have been developed to predict the concentrations of some gas species in sea ice (argon by Moreau et al. 2014; and carbon dioxide by Moreau et al. 2015b). However, the physics controlling gas bubble motion in the pore space of sea ice is not well understood and a model capable of predicting the air fraction in sea ice is still lacking.

In contrast to a gaseous phase, we will also consider a three-phase mushy layer with two distinct, immiscible liquid phases occupying the pore space (e.g. crude oil and water in sea ice). Crude oil often ends up in the oceans as a result of anthropogenic activities such as oil extraction, shipping and spills. Oil spilled in Arctic waters can be incorporated in growing sea ice and migrate towards the surface of sufficiently permeable ice due to the lower density of oil compared with seawater (Oggier et al. 2020). The presence of sea ice affects the fate of oil spilled in polar environments and can hinder traditional approaches to clean up spilled oil (see reviews by Fingas and Hollebone 2003; Wilkinson et al. 2017). Typically, crude oil is an effective absorber of solar radiation and is recognised to increase the melt rate of sea ice in the summer (e.g. Martin 1979; Desmond et al. 2019). It has been suggested recently that even low concentrations of dispersed weathered oil droplets in Arctic waters may have significant consequences for the absorption of solar radiation in the ice if they make their way into sea ice (Redmond Roche and King 2022b; Redmond Roche 2024). It remains an open question to what extent low concentrations of dispersed oil droplets in Arctic waters are accumulated in sea ice, and if they have a significant impact on the sea ice melt season.

Photosynthetically active radiation (PAR) is radiation in the visible part of the electromagnetic spectrum that is used by photosynthetic organisms, including phytoplankton, for photosynthesis. Studies have shown that dispersed oil droplets in the water column can reduce the amount of PAR transmitted through surface waters (Haule and Freda 2016) which could impact the primary productivity of areas of the ocean polluted with crude oil.

In this chapter, we will next review the mushy-layer theory that governs the thermodynamic growth of sea ice in §1.1. This will be followed by a review of the other geophysical processes that are important during the seasonal evolution of sea ice in the Arctic. In §1.2, we will review the existing literature concerning the exsolution and motion of gas bubbles in sea ice. In §1.3, we will review the processes by which weathered oil droplets are created and transported in the ocean, and the potential consequences of their presence in sea ice. In §1.4, we will introduce some relevant background concerning the spring algal bloom associated with algae that grow under Arctic sea ice. Finally, in §1.5 we will outline the structure and principal aims of this thesis.

1.1 The physics of sea ice

In this section, we will discuss the phase behaviour of seawater and review the thermodynamic growth of sea ice as described by mushy-layer theory. We will also discuss the impact of snow, solar radiation, and melt pond formation on the seasonal evolution of sea ice.

1.1.1 A phase diagram for sea ice

Seawater is a multicomponent solution of water and dissolved salts with complex phase behaviour (Assur 1960; Vancoppenolle et al. 2019). The Arctic Ocean is relatively fresh compared to other oceans, partly due to freshwater discharge from rivers, with the salinity of the surface mixed layer typically between $27\,\mathrm{g\,kg^{-1}}$ and

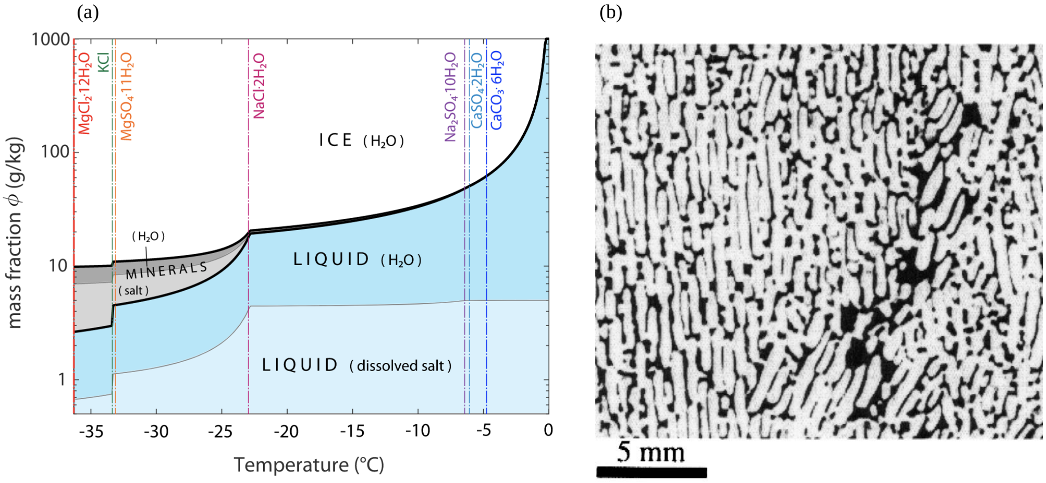

Figure 1.1: Panel (a) shows the mass fractions of liquid water, solid ice, dissolved salts, and solid salts in sea ice versus temperature, reproduced from Vancoppenolle et al. (2019). This diagram was derived for water with an absolute bulk salinity of $S_A = 5\,\mathrm{g\,kg^{-1}}$ where the relative proportion of each salt is determined by standard seawater composition (Millero et al. 2008) using the FREZCHEM computational chemistry code (Marion et al. 2010). Here, absolute salinity refers to the total mass of all dissolved salts per unit mass of solution. The coloured vertical lines indicate the temperatures below which different hydrated salt minerals precipitate from the solution. Panel (b) shows a horizontal thin-section image of the porous microstructure of mushy sea ice, adapted from figure 6 of Eicken et al. (2000). In panel (b) ice is white and interstitial liquid brine is black.

$34\,\mathrm{g\,kg^{-1}}$ (Aagaard et al. 1981; Xie et al. 2019). Figure 1.1 shows mass fractions of solid water ice, liquid water, and mineral precipitates in sea ice as a function of temperature at a bulk salinity of $S = 5\,\mathrm{g\,kg^{-1}}$. There are distinct temperatures (coloured vertical lines in figure 1.1) below which it is preferable for different dissolved salts to precipitate as hydrated minerals in the solid phase. Sodium chloride salt (NaCl) is the most abundant solute in seawater (Millero et al. 2008) and has the biggest impact on the freezing temperature and phase behaviour of sea ice (Vancoppenolle et al. 2019). Therefore, the essential physics of sea ice growth can be captured by approximating seawater as a binary solution of water and sodium chloride salt (Feltham et al. 2006). This approximation neglects the small volumes of liquid maintained in equilibrium with magnesium and potassium based salts for temperatures below $-23\,°\mathrm{C}$ (figure 1.1). Going forward “salt” will refer specifically to NaCl unless otherwise stated.

The distribution coefficient $p_c = S_s/S_l$ is the ratio of the salinity of the solid phase S_s to the salinity of the liquid phase S_l in local equilibrium. Values of $p_c \ll 1$

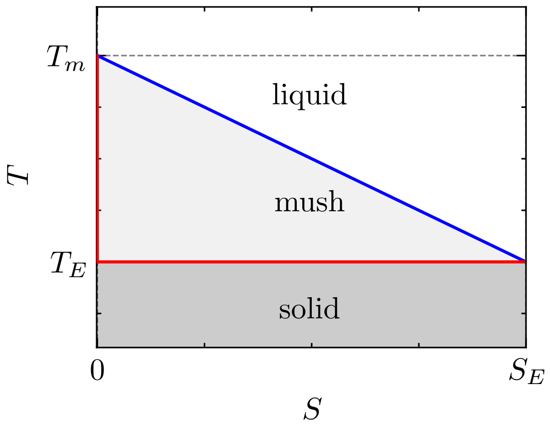

Figure 1.2: An idealised phase diagram for saltwater shown in temperature T and bulk salinity S space, with the liquid, mush, and solid phases indicated. A linearised liquidus $T = T_L(S)$ (given by equation 1.1.1) and solidus $T = T_S(S)$ are shown in blue and red, respectively. The linearised liquidus and solidus meet at the eutectic point (S_E, T_E). The super-eutectic region of the phase plane ($S > S_E$) is omitted since it is not relevant to this thesis.

do not affect the dynamics of the mushy layer (Lu and Chen 1994), although some authors have found a small, non-zero value of p_c helps to prevent numerical instabilities in computational methods (Katz and Worster 2008; Parkinson 2019). However, it is typical to assume that $p_c = 0$ for salt in sea ice so that all dissolved salt is rejected into the liquid phase during freezing (Feltham et al. 2006), which we will adopt in this thesis.

The phase behaviour of saltwater can be approximated as a binary-eutectic solution (Worster 2000) with phase diagram shown in figure 1.2. Dissolved salt, present in saltwater of bulk salinity S, depresses the freezing point of water below 0 °C according to the liquidus relation. The liquidus relation is often approximated by the linearised liquidus curve

$$T_L(S) = T_m - \gamma_L S, \tag{1.1.1}$$

where $T_m = 0\,^{\circ}\mathrm{C}$ is the freezing temperature of pure water and γ_L is the slope of the liquidus. Although a linearised liquidus is convenient for analytical work, it is a simplification of the true liquidus, which is typically non-linear and is often approximated using a cubic polynomial (Cox and Weeks 1983; Notz 2005; Vancoppenolle et al. 2019). In particular, Notz (2005) showed that using a linearised liquidus can lead to underestimate the porosity of sea ice which is important for determining the permeability of the ice. Whilst a linearised liquidus cannot accurately reproduce the freezing temperature of sea ice at all bulk salinities, we will use the linearised liquidus in this thesis for simplicity (similarly to much of the theoretical literature on mushy layers). The theoretical study in chapter 2 will use a value of the liquidus slope given by Peppin et al. (2007). However, in later chapters, where we compare model results to geophysical data, we will use a lower value for the liquidus slope in order to more accurately reproduce the freezing temperature of seawater.

When saltwater is cooled below the salinity-dependent freezing temperature, $T < T_L(S)$, it begins to solidify. Elevated salinity due to salt rejection at the freezing interface further depresses the freezing temperature, and drives a morphological instability of the interface (Mullins and Sekerka 1964). This instability promotes dendritic ice growth which forms a porous mushy layer of solid fresh ice crystals containing liquid brine inclusions. Two-phase mushy-layer theory describes the mush using phase-averaged quantities where the volume fractions of solid ϕ_s and liquid ϕ_l are controlled by the local temperature and bulk solute concentration. Recent theoretical work has investigated the effect of thermal disequilibrium on the pore scale in mushy layers (Amiri and Butler 2024). However, scaling estimates by Feltham et al. (2006) suggest that thermal disequilibrium is not important on the timescales relevant for sea ice growth. Therefore, it is typically assumed that the mushy layer is in local thermal equilibrium due to rapid thermal and solute diffusion on the pore scale (Worster 1997; Worster 2000; Notz 2005; Feltham et al. 2006; Hunke et al. 2011; Wells et al. 2019). Thermal equilibrium on the pore scale requires that the local solid and liquid fractions within the mush adjust instantaneously to ensure that the interstitial liquid is at the salinity-dependent freezing temperature $T = T_L(S_l)$. For a review of the growth of sea ice as a mushy layer see Worster (2000) and Wells et al. (2019).

The mushy phase, defined by the coexistence of both solid and liquid in thermal equilibrium, is bounded by the liquidus (blue) and solidus (red) curves in the phase diagram (figure 1.2). For a binary-eutectic solution with $p_c = 0$ the solidus curve is approximated as a vertical line segment at $S = 0$ and a horizontal line segment at the eutectic temperature T_E. At the eutectic temperature the liquid inclusions in a mushy layer reach a maximum salinity called the eutectic salinity S_E where $T_E = T_L(S_E)$. Below the eutectic temperature all remaining liquid freezes and the system exists as a solid ($\phi_s = 1$) comprising of solid water ice and precipitated hydrohalite crystals ($\mathrm{NaCl} \cdot 2\,\mathrm{H_2O}$). This is an idealisation of the true phase behaviour of sea ice shown in figure 1.1.

1.1.2 The formation & growth of sea ice

Typically, when heat loss to the atmosphere is sufficient, ice first forms in the ocean as small crystals called frazil. This frazil can accumulate at the ocean surface and consolidate into a thin initial ice cover (Svensson and Omstedt 1994). Frazil ice has a granular microstructural texture, which is characterised by randomly oriented crystals with liquid inclusions at crystal boundaries (Oggier and Eicken 2022). Subsequently, ice grows downwards by solidification of the ocean at the ice base, so-called “congelation” growth (Petrich and Eicken 2017). Ice grown by congelation is called columnar ice and has a different microstructure. In columnar ice, crystals and water-filled pores are vertically aligned due to the preferential growth direction of ice crystals (Eicken et al. 2000; Oggier and Eicken 2022). Typically, in the Arctic, columnar ice is the dominant sea ice type, while granular ice makes up only a small top layer (Petrich and Eicken 2017). However, in the Antarctic, granular ice can make up a more significant fraction of the ice cover due to differences in growth conditions (e.g. Jeffries et al. 1994). The base of sea ice is highly porous and is referred to as the skeletal layer.

Sea ice in the Arctic ocean, or pack ice, fractures into distinct floes and drifts under the stresses of surface winds and ocean currents (Thorndike and Colony 1982). As a result, the ice thickness is not just determined by thermodynamic growth and melt in response to atmospheric and oceanic conditions along its drift trajectory, but also by mechanical deformation processes and fracturing where ice motion is convergent or divergent (see Haas 2017, for a review). In contrast, landfast sea

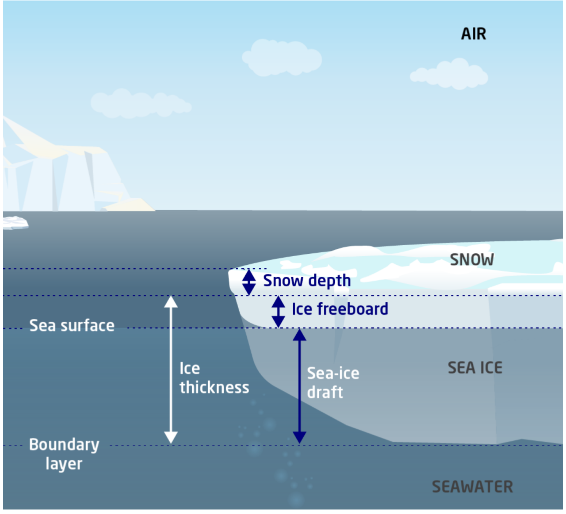

Figure 1.3: Schematic of a free-floating ice floe showing the ice freeboard, draft, and the snow thickness. Adapted from the Sea Ice Portal (`https://www.meereisportal.de/en`) under a Creative Commons license (CC-BY 4.0).

ice is attached to the coast, and does not drift. Landfast sea ice provides a useful case study of ice growth dominated by thermodynamic processes, as opposed to mechanical deformation (e.g. Druckenmiller et al. 2009), and so we focus on landfast sea ice in this thesis when comparing model results to field observations.

Figure 1.3 is a schematic diagram of an ice floe and the overlying snow pack. The ice freeboard is the height of the surface of the ice above sea level and the draft is the thickness of the submerged portion of the ice. Together the ice freeboard and draft sum to the total ice thickness. The freeboard of a free-floating ice floe is determined by the hydrostatic balance between the weight of the ice and snow and the buoyancy of the displaced seawater (e.g. Kwok 2010). This is not necessarily true for landfast sea ice or parts of the ice pack which are experiencing mechanical stress. Note that the ice freeboard can become negative, for example for thin sea ice with a deep snow cover, which can lead to seawater infiltration of the snow layer and the formation of snow ice (Provost et al. 2017).

The thermodynamic growth of columnar ice can be modelled by the balance of heat conduction through the ice, heat fluxes to the atmosphere, heat fluxes from the ocean at the ice base, and the release of latent heat (e.g. Petrich and Eicken 2017). This yields a type of free-boundary problem for the position of the ice–ocean interface called a Stefan problem. If atmospheric cooling generates a fixed surface temperature, a simple one-dimensional Stefan problem can be solved to show that sea ice grows with a characteristic square root time scaling for diffusive growth at early times (Stefan 1891; Leppäranta 1993). Idealised mushy-layer calculations of ice growth with a linearised surface energy balance (Hitchen and Wells 2025) have been able to reproduce measurements made by Notz and Worster (2008) of the early ice thickness for growing sea ice in the absence of snow. However, typical environmental growth conditions involve a more complex interplay of radiative, sensible, and latent heat fluxes, and are modified by the presence of an insulating snow cover (e.g. Taylor and Feltham 2004). Ice growth rates are typically on the order of 1 $\mathrm{cm\,day^{-1}}$, during the winter growth phase (see §1.5.3 of Petrich and Eicken 2017). Thermodynamic growth of the ice ceases when atmospheric cooling is balanced by the heat flux to the ice base from the ocean. The ocean heat flux is very important for the mass balance of Arctic sea ice, but is highly variable both spatially and temporally and depends on a variety of factors including the ocean circulation, stratification, and the input of solar energy to the ocean (McPhee 1992; Krishfield and Perovich 2005; Zhong et al. 2022).

1.1.3 Solar radiation in the Arctic

Solar radiation reaching Earth's surface primarily has wavelengths $300\,\mathrm{nm} \leq \lambda \leq 3000\,\mathrm{nm}$, covering the ultraviolet, visible, and near-infrared part of the electromagnetic spectrum (Chen et al. 2012). Solar radiation is also called shortwave radiation to distinguish it from longwave (thermal) radiation emitted by the Earth's surface and atmosphere. Latitudes above the Arctic Circle (66.5° N) experience periods of continuous daylight in summer and darkness in winter: so-called polar days and polar nights, respectively. To illustrate the seasonal cycle, Figure 1.4 shows the mean downwelling spectrally-integrated surface shortwave radiation flux F_{SW} at Barrow, Alaska in 2009. The daily mean shortwave radiation flux reaches a maximum of around $300\,\mathrm{W\,m^{-2}}$ in June, and is zero during the polar night (roughly December

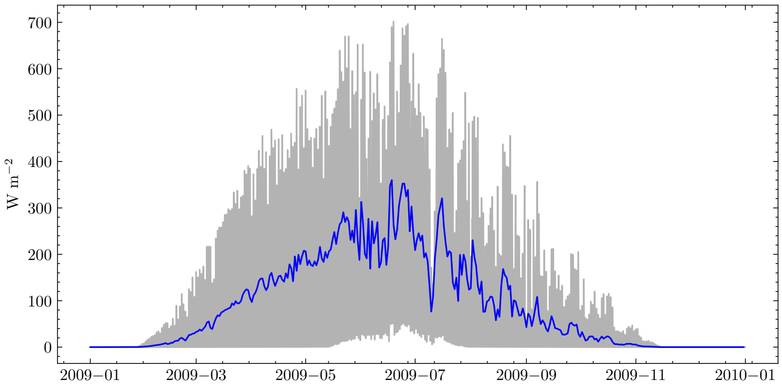

Figure 1.4: Hourly (grey) and daily (blue) mean downwelling shortwave radiation flux at Barrow, Alaska (71.37°N, 156.5°W) in 2009 obtained from ERA5 reanalysis data (C3S 2018). Major tick marks indicate the first day of every other month.

to February). The maximum mean downwelling shortwave radiation flux decreases with increasing latitude and the length of the polar night increases with latitude.

Incoming solar radiation at the top of the atmosphere is well approximated by a black body spectrum with an emission temperature of around 5700 K (Malone 1951). However, the spectral shortwave radiation flux reaching the Earth's surface is strongly modified by absorption and scattering in the atmosphere. Some typical downwelling surface shortwave spectra are shown in figure 1.5. Shortwave radiation spectra at the Earth's surface show a series of characteristic absorption bands due to absorption by different atmospheric chemical species (see Grenfell and Perovich 2008, for example). Practically no shortwave radiation of wavelength less than 300 nm is observed at the Earth's surface due to absorption by ozone in the atmosphere (Perovich 2017). The most important controls on the spectrally-integrated shortwave radiative power observed at the surface are the solar zenith angle and cloud cover (Chen et al. 2012). Low stratus cloud cover is ubiquitous during the summer in the Arctic (Herman 1986), which is more transmissive of shortwave radiation at lower wavelengths and reduces the total incident shortwave radiative power at the surface compared with the clear-sky case (figure 1.5c).

1.1.4 The melt season

The melt season in the Arctic typically begins in May or June depending on the latitude and lasts until September (Stroeve et al. 2014). During the melt season,

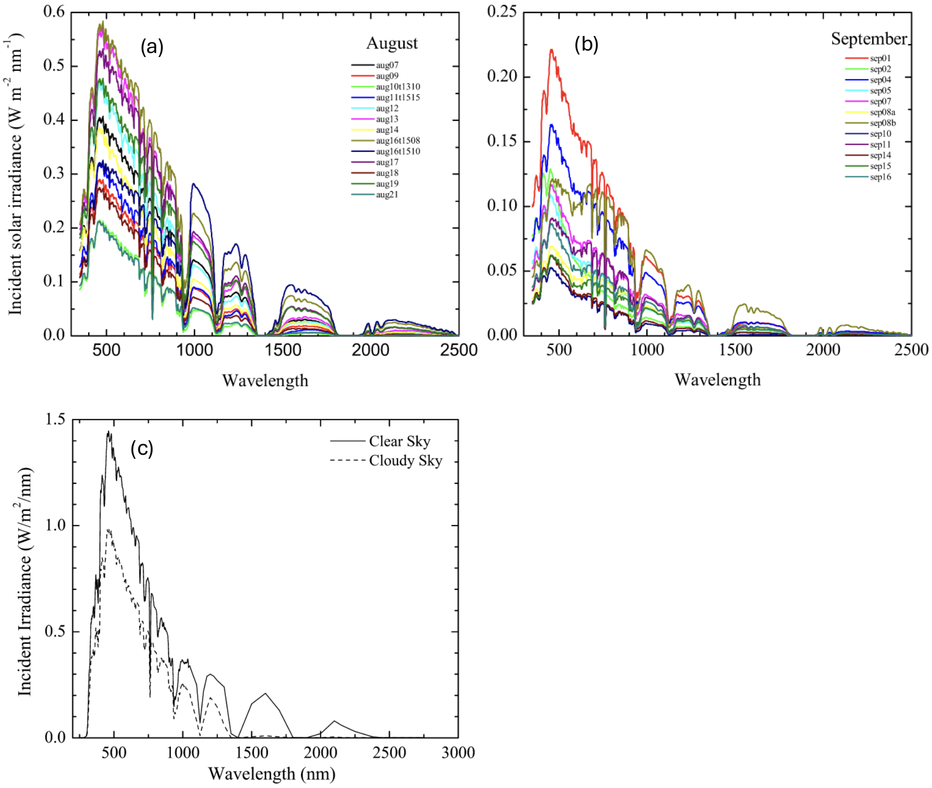

Figure 1.5: Downwelling surface spectral irradiance measurements from between 75°N and 90°N during the Healy Oden Transarctic Experiment in August 2005 (a) and September 2005 (b), reproduced from Grenfell and Perovich (2008). The legend entries refer to distinct measurements by the day of the month they were taken. Downwelling surface spectral irradiance measurements (c) for typical clear (solid) and cloudy (dashed) sky conditions at Barrow, Alaska, reproduced from Grenfell and Perovich (2004). The unit of wavelength is nanometres (nm) in all three panels.

the incoming shortwave radiation flux and air temperature increases. This first melts any snow cover on the ice which leads to the formation of ponds of melt water on the ice (Eicken et al. 2002).

The evolution of melt ponds on sea ice typically follows four stages (Eicken et al. 2002). Firstly, as the snow cover melts, ponds form in minima of the ice topography well above sea level. This first stage is characterised by the rapid increase in the area fraction covered by ponds, from 0 to around 50%, and can last for one to two weeks (Eicken et al. 2002; Polashenski et al. 2012). During this stage the ice below ponds is relatively impermeable and so melt water is primarily lost to macroscopic flaws in the ice by lateral transport. Stage two is characterised by a drop in pond area fraction, due to pond drainage, and the loss of the majority of the snow cover. During this stage, most pond surfaces are only slightly above sea level and melt water can drain downwards through the more permeable ice or laterally through macroscopic flaws (Eicken et al. 2002). Stage two again lasts for typically one to two weeks (Eicken et al. 2002; Polashenski et al. 2012). During stage three ponds deepen and the area fraction covered by ponds increases again due to lateral melt and decreasing ice freeboard (Eicken et al. 2002; Polashenski et al. 2012). Some ponds can melt all the way through the ice during this stage which can last several weeks until the end of the melt season (Polashenski et al. 2012). Stage four is refreezing of the surface of melt ponds which can occur at any point during the melt season if atmospheric forcing changes.

Once the snow cover has melted, the bare ice surface and the ice under ponds can begin to melt. The absorption of solar radiation in the ocean through leads or after transmission directly through the ice greatly enhances the ocean heat flux at the base of the ice during summer. This can drive significant melting at the ice base (Perovich et al. 2008). In large areas of the Arctic ocean the ice cover melts away completely by the end of the melt season in September, leaving areas of open water.

1.1.5 The age of sea ice

A distinction is typically made between first-year ice (FYI) and multi-year ice (MYI). FYI grows and melts completely over one seasonal cycle, whereas MYI persists beyond at least one summer melt season. Over the course of a season gravity drainage reduces the bulk salinity of sea ice (Notz and Worster 2009). Gravity drainage is driven by a convective instability within the ice that causes denser more saline brine to drain downwards to the underlying ocean, drawing comparatively less dense, less saline seawater upward into the ice. The downward drainage of melt water through the ice during the melt season, also known as flushing, can further reduce the bulk salinity of the ice. As a result, FYI is typically more saline and thus more porous than MYI at the same temperature (Malmgren 1927; Cox and Weeks 1983; Notz and Worster 2009; Petrich and Eicken 2017). In the Arctic, future climate change is expected to increase the proportion of FYI (Maslanik et al. 2011).

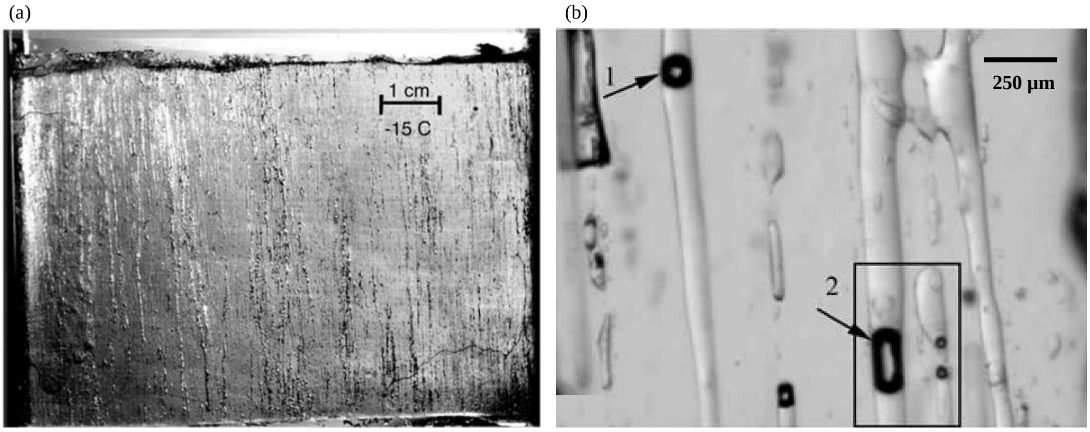

Figure 1.6: Panel (a) shows a vertical slice (roughly 5 mm thick) from the interior of first-year sea ice at −15 °C. Panel (b) shows a close-up view of bubbles (indicated by arrows 1 & 2) within brine inclusions in first-year sea ice at −15 °C. Adapted from figures 1 and 13 of Light et al. (2003).

1.2 Gases in sea ice

In this section we will review the existing literature concerning gas bubbles in sea ice and the wider importance of the air content of sea ice.

1.2.1 The bulk gas content of sea ice

Seawater contains dissolved atmospheric gas species such as argon Ar, oxygen O_2, and nitrogen N_2 (Nakayama et al. 2002). Gas molecules are not incorporated into the solid ice phase at the temperatures and pressures found in sea ice (Hobbs 1974), and so concentrations of dissolved gases in the interstitial liquid in the pore space of sea ice are elevated by freezing. If the concentration of any dissolved gases exceeds saturation, exsolution of gas bubbles can produce a free gas phase in the sea ice pore space (Tison et al. 2017). Therefore, gases exist in sea ice in two phases: dissolved in the liquid brine, or as free-phase gas bubbles within the sea ice pore space. We refer to the combined mass of dissolved and free phase gas per unit volume as the bulk gas content or bulk gas concentration in the ice. Vertical profiles of the bulk concentrations of Ar, O_2, and N_2 in sea ice cores have been measured using the dry crushing technique (Zhou et al. 2013; Zhou et al. 2014a; Crabeck et al. 2014b). See Tison et al. (2017) for a detailed review of measurements of different gases in sea ice.

The solubility of gases in water typically increases as temperature decreases, but decreases as salinity increases (Weiss 1970; Hamme and Emerson 2004). Within sea ice, local thermodynamic equilibrium couples the temperature and salinity of the interstitial liquid. As a result, the salinity of the liquid brine increases as the temperature decreases, which leads to a net decrease in the solubility of gases in the interstitial liquid (Moreau et al. 2014). However, this variation in solubility is likely small compared with the concentration/dilution effect as the ice freezes/melts (Zhou et al. 2013).

The volume occupied by the free-gas phase is quantified by the gas volume fraction ϕ_g, which is the ratio of the volume of free-phase gas to the total volume of some REV of sea ice. The in-situ gas volume fraction cannot be inferred from measurements of bulk gas concentrations directly. It is often assumed that little supersaturation of dissolved gases is tolerated in sea ice and so the volume of free-phase gas can be estimated from the degree of supersaturation compared to local solubility (Tison et al. 2017). Gas volume fractions of around a few percent have been observed in the interior of first-year sea-ice cores, using optical microscopy of thin sections of ice and X-ray tomography (Light et al. 2003; Crabeck et al. 2016). The observed gas volumes were found to be mostly distributed as spherical bubbles residing in the liquid filled pore space (figure 1.6). Gas bubbles were also seen to appear in laboratory experiments during the directional freezing of saltwater in a Hele-Shaw cell (see figure 4 of Peppin et al. 2007).

Tsurikov (1979) proposed the following nine processes that determine the evolution of the gas content of sea ice.

1. The entrapment of gas during frazil ice formation. This includes gases dissolved in surface waters and any bubbles generated by wave action that are trapped in the initial frazil ice cover.

2. The incorporation of dissolved gases in seawater during the growth of columnar ice by congelation.

3. Degassing from sediments beneath the ice (typically this is relevant as a source of CH_4 for Arctic sea ice above shallow continental shelves).

4. The entrapment of gas during the refreezing of snow melt water, or when the base of the snow layer on sea ice is flooded with seawater when the sea ice freeboard decreases. Again, this includes gases dissolved in the melt water as well as trapped air within the snow layer.

5. The voids produced by volume change during internal melting, because ice is less dense than liquid water.

6. Air infiltration from above as brine drains due to gravity if the ice freeboard increases.

7. Internal gas bubble exsolution/dissolution due to gas super-saturation/sub-saturation in the liquid brine.

8. Bubble migration along temperature gradients. This is a slow process which is not relevant on the timescales of interest for sea ice growth and is analogous to the migration of brine pockets (discussed in Notz and Worster 2009).

9. Biological activity.

In addition to these nine processes, I would add the upward migration of gas bubbles through connected portions of the sea ice pore space due to their buoyancy and the removal of interstitial liquid that is supersaturated with dissolved gas by brine convection. Buoyant migration of gas bubbles within sea ice has been proposed to explain observed seasonal changes in the vertical distribution of bulk gas concentrations in sea-ice cores (Zhou et al. 2013; Moreau et al. 2014). Existing work concerning the migration of gas bubbles in sea ice is reviewed in §1.2.3. Moreau et al. (2014) found that the removal of dissolved argon by brine convection was important to accurately reproduce the bulk concentrations of argon observed by Zhou et al. (2013) in sea ice cores from Barrow, Alaska. In chapter 2, we present a novel model for the motion of gas bubbles in sea ice using an idealised geometry to approximate the pore space of sea ice. In chapter 3, we extend an existing parameterisation of brine convection in sea ice to include the advection of dissolved gases and their removal from the ice via brine channels. In chapter 7, the results of this model applied to a transient simulation of first-year sea ice will be compared to measurements of the bulk concentrations of atmospheric gases in sea ice cores.

1.2.2 The wider importance of the gas phase in sea ice

Biogeochemical cycles

Sea ice has traditionally been assumed to act as a barrier that prevents gas exchange between the ocean and atmosphere, but field observations have measured significant ice-atmosphere gas fluxes (Nomura et al. 2010; Nomura et al. 2018; Watts et al. 2022). The gas phase within sea ice provides an additional transport pathway between the ocean and atmosphere for a variety of gas species (CO_2, Nomura et al. 2010; Miller et al. 2011; Crabeck et al. 2014a; Kotovitch et al. 2016; Nomura et al. 2018; CH_4, Kort et al. 2012; He et al. 2013; Crabeck et al. 2014a; Zhou et al. 2014b; O_2 and N_2, Zhou et al. 2014a; and Ar Zhou et al. 2013; Zhou et al. 2014a).

Because sea ice has been shown to permit gas fluxes between the ocean and atmosphere, there have been efforts to quantify the extent to which ocean covered with sea ice is a net source or sink of atmospheric carbon (Tison et al. 2017). The current understanding can be summarised as follows. Melting in the spring and summer dilutes dissolved carbon in the surface brines in the pore space. Hence, atmospheric carbon dioxide dissolves into these diluted brines, and so the ice acts as a sink for atmospheric carbon. A simple box model found Arctic sea ice acts as a sink of 0.014 Pg C in the spring/summer (Rysgaard et al. 2011), compared with an assessment of the ice-free Arctic ocean as a sink of 0.154 Pg C (Takahashi et al. 2009). However, while the sea ice is freezing up in the autumn/winter, oceanic dissolved inorganic carbon is concentrated in brines and either stored in gas bubbles or released to the atmosphere, depending on the permeability of the ice. In addition, concentrated brine drains from the ice expelling dissolved inorganic carbon (Moreau et al. 2015b). The highly saline plumes generated by brine drainage can penetrate to the deep ocean contributing to bottom water formation in the Arctic (Rudels and Quadfasel 1991) and potentially sequestering carbon there. Sea ice is currently thought to be a net source of carbon dioxide to the atmosphere in these cold months. The degree to which this carbon source in winter/autumn offsets the spring/summer sink is unknown (Tison et al. 2017). There is also the potential for a transient release of carbon dioxide to the atmosphere when the sea ice warms and first becomes permeable in the spring, as trapped gas bubbles are released, but before significant melting dilutes the sea ice brine. Such a transient flux of carbon dioxide from the ice to the atmosphere has been observed during rapid ice melt triggered by a rain event (Nomura et al. 2010). It has also been proposed that the formation of frost flowers (Fransso et al. 2015) can enhance fluxes of carbon dioxide to the atmosphere during autumn/winter to completely offset the nature of sea ice as a sink of atmospheric carbon in the spring/summer. The extent to which sea-ice cover contributes to the global carbon budget, and how this contribution will respond to future climate change, remains an open question.

Measurements of ice-atmosphere fluxes of carbon dioxide have been performed using both the chamber method and the eddy covariance method. These measurement types are usually in reasonable agreement over terrestrial ecosystems, but so far show a large discrepancy over sea ice. The chamber method has recorded fluxes of carbon dioxide from -5.2 to $9.9\ \mathrm{mmol\,m^{-2}\,day^{-1}}$ using an enclosed chamber placed on the surface of the ice, whereas eddy covariance methods have predicted fluxes one or two orders of magnitude higher (Tison et al. 2017) based on concentrations and turbulent velocity fluctuations measured several meters above the ice. It is still to be determined if the eddy covariance method is detecting additional water-atmosphere fluxes from nearby fractures and leads in the ice pack.

The production of halogens from sea ice or the snowpack in the Arctic causes local ozone depletion events (Barrie et al. 1988). The exact mechanisms for halogen production are still being investigated (Kaleschke et al. 2004; Wang and Pratt 2017; Custard et al. 2017), but ozone depletion events have been linked to the formation of young sea ice (Jones et al. 2006). Tropospheric ozone makes a significant contribution to radiative forcing (Lacis et al. 1990), and so ozone depletion events can impact local radiative feedbacks in the Arctic.

Measured profiles of nitrogen and oxygen concentrations in sea ice show broadly similar features to measurements of argon, which is a biologically inert gas. This similarity may suggest that physical controls dominate gas transport in sea ice, rather than biological processes (Tison et al. 2017). However, elevated O_2 / N_2 ratios in the base of sea ice during summer have been attributed to primary production by sea-ice algae (Zhou et al. 2014a; Arrigo 2017). In general, measurements of O_2, N_2, and Ar in sea ice are of interest for understanding the biological activity of algae, microbes, and micrograzers in sea ice (Gleitz et al. 1995; Kaartokallio 2001; Kaartokallio 2004; Rysgaard and Glud 2004; Rysgaard et al. 2008). Specific measured profiles of Ar, O_2, and N_2 concentrations in sea ice cores from Barrow, Alaska are discussed further in chapter 7.

Optical properties

Because of the large contrast between the refractive index of air (≈ 1.00) and ice (≈ 1.31) or brine (≈ 1.33), gas bubbles in sea ice are effective scatterers of shortwave radiation (Perovich 2017). The amount of scattering of light in sea ice affects the albedo of the ice (e.g. Perovich 1990), which in turn affects the energy balance of the ice and the ocean-atmosphere system (Perovich 2005). Structural-optical models of sea ice have been developed to predict the optical properties controlling scattering in sea ice at different temperatures based on the size, shape and distribution of brine inclusions, mineral precipitates, and gas bubbles (Grenfell 1983; Light et al. 2003; Light et al. 2004). Despite the strong scattering of light at air-ice and air-water interfaces in sea ice, there are typically much fewer gas bubbles (at least large enough to be observed) than brine inclusions in sea ice, and so gas bubbles are not thought to be the dominant source of scattering in sea ice (Light et al. 2003).

Bulk density

Sea-ice thickness h_{ice} is important for determining the sea-ice mass balance and the surface energy budget for the polar oceans, and so is desirable to determine at the regional scale from satellite observations. However, owing to the highly scattering nature of snow and ice, current spaceborne sensors are only able to detect the top ice/snow surface. The freeboard of the ice h_f can be measured by satellite-based laser altimeters by measuring a reference height for the ocean surface in nearby leads or areas of open water (Spreen and Kern 2017). The sea-ice thickness can be calculated from the measured freeboard assuming hydrostatic balance

$$\overline{\rho} h_{\text{ice}} + \rho_{\text{snow}} h_{\text{snow}} = \rho_l (h_{\text{ice}} - h_f), \tag{1.2.1}$$

if the depth of snow atop the ice h_{snow}, snow density ρ_{snow}, seawater density ρ_l and the mean bulk density of sea ice $\overline{\rho}$ are known (Kwok 2010). Air has a much lower density (around $1\,\text{kg}\,\text{m}^{-3}$) compared with seawater ($1024\,\text{kg}\,\text{m}^{-3}$) or ice ($917\,\text{kg}\,\text{m}^{-3}$), so the presence of even a small volume fraction of air in sea ice can significantly reduce the bulk density of the ice (Salganik et al. 2024). Therefore, uncertainty in the bulk density of sea ice due uncertainty in the air fraction impacts the accuracy of sea-ice thickness estimates from remote sensing observations (Alexandrov et al. 2010; Kwok 2010; Pustogvar and Kulyakhtin 2016; Jutila et al. 2022; Fons et al. 2023). Uncertainty in the bulk density of first-year sea ice was found to be the largest source of error in thickness estimates for Arctic first-year sea ice thicker than $0.8\,\text{m}$ (Alexandrov et al. 2010).

When discussing the bulk density of sea ice, it is important to distinguish between ice above the waterline, where drainage of brine under gravity can leave large air filled voids, and below the waterline where ice is filled with seawater. Reported values of the bulk density of sea ice below the waterline lie in the range 900–940 $\text{kg}\,\text{m}^{-3}$ and above the waterline in the range 840–910 $\text{kg}\,\text{m}^{-3}$ with the variation primarily thought to be due to the air fraction of the ice (Timco and Frederking 1996). A more recent study (Pustogvar and Kulyakhtin 2016) proposed that the hydrostatic weighing method provides more accurate measurements of sea ice bulk density than traditionally used mass-volume method and found a narrower range for the bulk density of first-year sea ice below the waterline of 894–921 $\text{kg}\,\text{m}^{-3}$. Cores for first-year ice density measurements were taken from the Van Mijen Fjord, Spitsbergen (Svalbard) in February and March 2015 and were found to have mean bulk density values in the range 906–916 $\mathrm{kg\,m^{-3}}$. Crabeck et al. (2016) found for ice cores grown artificially outdoors in January the ice bulk density varied between 840–920 $\mathrm{kg\,m^{-3}}$. However, values lower than 900 $\mathrm{kg\,m^{-3}}$ occured only in surface frazil and snow ice. The air fraction was also estimated directly using CT scanning and found to be less than 3% throughout the columnar portion of the ice. First year ice cores taken from melting ice off the coast of Barrow in the summer of 2015 were found to have a mean bulk density of 910 $\mathrm{kg\,m^{-3}}$ for a core taken in May, and 870 $\mathrm{kg\,m^{-3}}$ for a core taken in June, with even lower values of density seen for cores taken in July (Frantz et al. 2019). It seems that the bulk density of sea ice below the waterline is consistently lower than the density of ice (917 $\mathrm{kg\,m^{-3}}$) and seawater (1024 $\mathrm{kg\,m^{-3}}$) which suggests the presence of air in the ice. The lowest bulk densities are consistently found in ice above the waterline, which suggests a significant amount of brine has drained from the ice and been replaced by air.

Recent work has provided measurements of the bulk density of first year ice cores taken during the MOSAIC expedition over the 2019–2020 season (Salganik et al. 2024). The authors found a rapid increase in the bulk density of the ice early in the growth season from 893 ± 10 $\mathrm{kg\,m^{-3}}$ (4th November 2019) to 908 ± 8 $\mathrm{kg\,m^{-3}}$ (18th November 2019) (Salganik et al. 2024). The authors estimate this is due to a reduction in the mean air fraction in the ice from 3.9% to 1.8% between the dates of these two cores. The bulk density of the ice then remains relatively constant around 910 $\mathrm{kg\,m^{-3}}$, until there is a reduction in the bulk density of the ice during the melt season from around 910 $\mathrm{kg\,m^{-3}}$ in June to around 880 $\mathrm{kg\,m^{-3}}$ in July (Salganik et al. 2024). The authors also pointed out that measurements of the bulk density of the ice below the waterline were low enough to require significant air fractions in the ice. The authors proposed that air bubbles accumulated in the ice during growth, but then the pressurisation of brine inclusions due to internal freezing drives bubbles back into solution when the ice became cold and impermeable. Conversely, as the ice warms and melts internally the authors suggest that the contraction of the ice upon melting creates voids in the ice which promotes the exsolution of dissolved gases and water vapour from the interstitial brine.

Bubble shrinkage and dissolution upon cooling and bubble nucleation and enlargement upon warming, have both been observed for closed brine inclusions in samples of sea ice in the laboratory (Crabeck et al. 2019). However, such a mechanism occurs at a fixed mass and volume (constant bulk density) and so I do not believe it is sufficient to explain the density reductions observed for melting sea ice by Frantz et al. (2019) and Salganik et al. (2024). It is also likely that the pore network of melting sea ice is connected to the underlying ocean since it is much more porous than cold winter ice. Therefore, the voids created in the ice by volume change during melting could simply be filled by seawater from below.

Another possible explanation for the low ice densities measured at the start of the growth season and end of the melt season could be the drainage of ice above the freeboard. These are both times of the year when the ice has little snow cover and a large positive freeboard, and so ice above the waterline makes up a larger fraction of the total ice thickness. Brine drainage and subsequent air infiltration from above makes this ice much less dense. The low values of ice bulk density measured below the waterline during the melt season by Frantz et al. (2019) and Salganik et al. (2024) could alternatively be explained by the loss of brine during the sampling of highly porous melting sea ice. The implications of models developed in this thesis for the bulk density of sea ice and the measurements of Salganik et al. (2024) are discussed in chapter 7.

1.2.3 Previous models of gas bubbles in sea ice

Computational models for argon in sea ice have been developed (Moreau et al. 2014) to explain the observed seasonal changes in the vertical distribution of argon in sea-ice cores at Barrow, Alaska (Zhou et al. 2013). It was assumed that the bulk argon content is controlled by incorporation from seawater, gravity drainage of sea ice brine, bubble nucleation, and bubble migration. The same modelling approach was later applied to model the transport of carbon dioxide (Moreau et al. 2015b) and oxygen

(Moreau et al. 2015a) in sea ice. This work was a significant advance in modelling the concentrations of species that can exist in both the dissolved and free-phase gas in sea ice. We will now discuss the specific approach taken by Moreau et al. (2014) to model the gas phase in sea ice and ways we aim to improve upon it in this thesis.

Based on an open-ocean formulation for bubble rise velocities, the authors of Moreau et al. (2014) concluded that gas bubbles would rapidly escape from the ice. This reasoning neglects the impact of the porous structure of sea ice on the motion of gas bubbles. To reconcile this with the evidence for trapped argon bubbles from the field data, an ad-hoc porosity threshold for gas transport was added to the model. For ice below this threshold bubbles are assumed to be immobile, but above this threshold bubbles are assumed to move instantaneously to the atmosphere or the next impermeable layer. The authors find a value for this threshold of 10% best reproduces the field data. The authors of the field study at Barrow suggested a threshold of 7.5% based on the observed argon content of the ice (Zhou et al. 2013). Both of these porosity thresholds for gas transport are significantly higher than the porosity threshold for brine transport in sea ice of 5% proposed by Golden et al. (1998), or 2–3% proposed by Maus et al. (2021).

The authors of Moreau et al. (2014) used an ad-hoc linear-relaxation model for the kinetics of bubble nucleation, tuning the relaxation rate to best reproduce the observed argon content. However, they found that a single value of the relaxation rate was unable to qualitatively reproduce all of the field observations.

A structural-optical model for sea ice found that bubbles larger than a critical radius of 0.16 mm had to leave ice warmer than −8 °C in order to explain measurements of light scattering above this temperature (Light et al. 2004). This also hints at a porosity threshold for gas transport in sea ice, but the authors did not consider the mechanisms controlling bubble trapping and migration directly. In this thesis, we will extend existing models for gas bubbles in sea by developing a microstructural model of bubble motion that can relate the porosity threshold for gas transport to the characteristic lengthscales of bubbles and the geometry of the pore space. We will also systematically explore the impact of gas exsolution rates on the accumulation of gas bubbles in sea ice.

1.3 Oil pollution in oceanic and polar environments

Crude oil enters the ocean via accidental spills, burst pipelines, tanker accidents, shipping (Rogowska and Namieśnik 2010; Berenshtein et al. 2020; Khozanah et al. 2021), and in waste products from offshore oil and gas extraction (Bakke et al. 2013). Oil production has been established off the coast of Alaska in the Beaufort Sea since the 1990s and estimates place around 13% of the world's undiscovered oil reserves north of the Arctic Circle, mostly offshore at depths less than 500 m (Gautier et al. 2009). As climate change reduces sea-ice extent, shipping and industrial activities in the Arctic Ocean are expected to increase (Kikkas and Romashkina 2018; Müller et al. 2023; Mahmoud et al. 2024), which will increase the risk of oil spills in the region.

1.3.1 The weathering of crude oil in the ocean

Once crude oil is released into the ocean it can pool as a surface slick or be broken up into submerged dispersed droplets by wave action, which is sometimes aided by the application of chemical dispersants (Johansen et al. 2015). Oil in the ocean undergoes a number of weathering processes including dissolution, evaporation of volatile compounds, photodegradation, sedimentation, and biodegradation (Gong et al. 2014). Crude oil is a complex mixture of hydrocarbons the majority of which are not very soluble in water (Shiu et al. 1990). However, crude oil does contain a small fraction by mass of polycyclic aromatic hydrocarbons (PAHs), which are fairly soluble in water and can be toxic to marine life (Wang et al. 2017; Desmond et al. 2019; Honda and Suzuki 2020; Ben Othman et al. 2023).

Wave action typically produces a log-normal distribution of oil droplet sizes which depends on the balance of viscous and interfacial tension forces (Johansen et al. 2015; Li et al. 2017). Johansen et al. (2015) suggest that oil droplets with radii less than 50 µm are likely to be permanently suspended by turbulence in the water column. Laboratory measurements simulating the weathering of oil droplets in the ocean have found a log-normal distribution of oil droplet radii with a peak radius between 0.05 µm and 0.25 µm (Otremba 2007). This is similar to the oil droplet size distribution of weathered oil droplets used to dope artificially grown sea ice in the laboratory by Redmond Roche (2024). Previous theoretical work investigating the effect of oil droplets on sea ice optical properties (Redmond Roche and King 2022b) used a log-normal distribution of oil droplet radii with a median radius of $0.05\,\mu\mathrm{m} \leq R_{\mathrm{med}} \leq 5\,\mu\mathrm{m}$ and geometric standard deviation of e.

In this thesis, we will be considering the effect of low background concentrations (up to about 10 ppm) of weathered oil droplets on sea ice that may soon be present in the Arctic Ocean. For context, oil concentrations of between 0.1 ppm and 1 ppm were reported over 1000 km from the Deepwater Horizon spill (Berenshtein et al. 2020). Concentrations of oil up to 15 ppm are allowed to be discharged from ships under the MARPOL convention adopted by the International Maritime Organisation. The OSPAR Commission, which operates in the North-East Atlantic, allows for the discharge of waste products from offshore oil and gas operations with concentrations of oil up to 30 ppm. Oil concentrations of between 50 ppm and 500 ppm have been reported in seawater samples from Jakarta Bay and surrounding areas, which is a heavily industrialised and shipped region (Khozanah et al. 2021). It would be valuable if oil concentrations were measured in the Arctic Ocean to provide an estimate of typical background concentrations of oil to be considered by future studies.

1.3.2 The motion of oil in sea ice

There have been several studies on the fate of a large release of oil under sea ice. We briefly summarise the key results of these studies, as reviewed by Wilkinson et al. (2017). Oil released under sea ice will accumulate as an oil lens in a local minimum of the bottom ice topography due to the buoyancy of the oil. For cold ice, oil may enter a few centimetres into the skeletal layer or be encapsulated by new ice growth around the oil lens. As the ice warms and becomes more permeable, oil

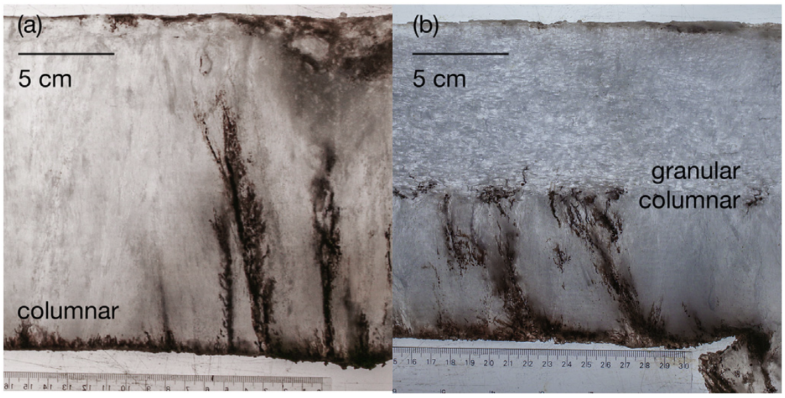

Figure 1.7: Vertical slices of sea ice grown at an ice tank facility where oil was released after 20 cm of initial growth, reproduced from Oggier et al. (2020). The ice texture is labelled as either columnar or granular.

is able to percolate upwards through the ice and may reach the surface (figure 1.7). However, a recent laboratory study has shown that the transition to granular ice near the surface can hinder the migration of oil through ice (Oggier et al. 2020). Micro CT imaging of ice cores grown in a tank in which oil was released under the ice during growth found oil throughout the pore space of the ice. The oil resided in a separate phase from the brine and was mostly found at the transition between columnar and granular ice (Desmond et al. 2021).

There has been substantially less attention paid to the motion of dispersed droplets of oil in sea ice. Redmond Roche (2024) prepared a solution containing sub-micron sized weathered oil droplets, and used this to dope artificially grown sea ice to investigate the effect of oil droplets on the ice albedo. However, the oil droplets were released on the surface of the ice as opposed to under the ice or growing the ice from initially oil-contaminated water. Dilliplaine et al. (2021) conducted experiments where both dispersed oil droplets and an oil lens were released under growing sea ice in a laboratory. The authors did not take any quantitative measurements of the distribution of the oil within the ice although images from the experiment seem to show that oil was able to migrate upwards in the ice in the case of an oil lens, whereas no visible oil is seen to have migrated upwards in the case of dispersed oil droplets. This may suggest that the buoyancy of small dispersed oil droplets is not sufficient to drive their migration through the ice, although cores were sampled

10 days after the release of oil and so vertical migration may be more significant on longer seasonal timescales. The results of our three-phase model for oil droplet migration in sea ice will be discussed in chapter 8 of this thesis.

1.3.3 The effects of crude oil pollution on sea ice

Crude oil is a much stronger absorber of shortwave radiation in the visible and ultraviolet range than ice or seawater. It has been appreciated for several decades that large quantities of oil on the surface of sea ice can drastically reduce the albedo and increase the absorption of shortwave radiation. For example, field experiments found that oil on the surface of sea ice can reduce the albedo of the ice by around 50% and accelerate the melting of the ice by 1–3 weeks (NORCOR 1975). Another study that released oil under sea ice found that melt ponds formed preferentially above oil lenses in the ice and found that oil slicks developed on the surfaces of the ponds (Martin 1979). A more recent study released oil under sea ice growing in artificial conditions, and found that ice polluted with oil warmed faster than unpolluted ice, due to the absorption of shortwave radiation by the oil (Desmond et al. 2019).

It is clear that large quantities of oil spilled under sea ice can significantly accelerate the melting of the ice. However, the extent to which the melting of the ice is affected by low concentrations of dispersed weathered oil droplets is less well understood. Redmond Roche and King (2022b) used a radiative transfer model to show that low mass fractions of oil droplets (up to 1000 ng of oil per g of ice) distributed homogeneously within sea ice will significantly reduce the shortwave albedo of the ice at visible wavelengths. It is not understood how significant this reduction in albedo will be during the sea ice melt season. The study of Redmond Roche and King (2022b) provides a framework to investigate the optical effect of oil droplets in sea ice but does not consider the effect of the surface scattering layer present on bare sea ice, or the motion of oil droplets. The largest albedo reductions were seen in first year ice which is less scattering and is becoming more common in the Arctic due to climate change (Maslanik et al. 2011). The effect of oil droplets on the albedo of sea ice may also be less significant

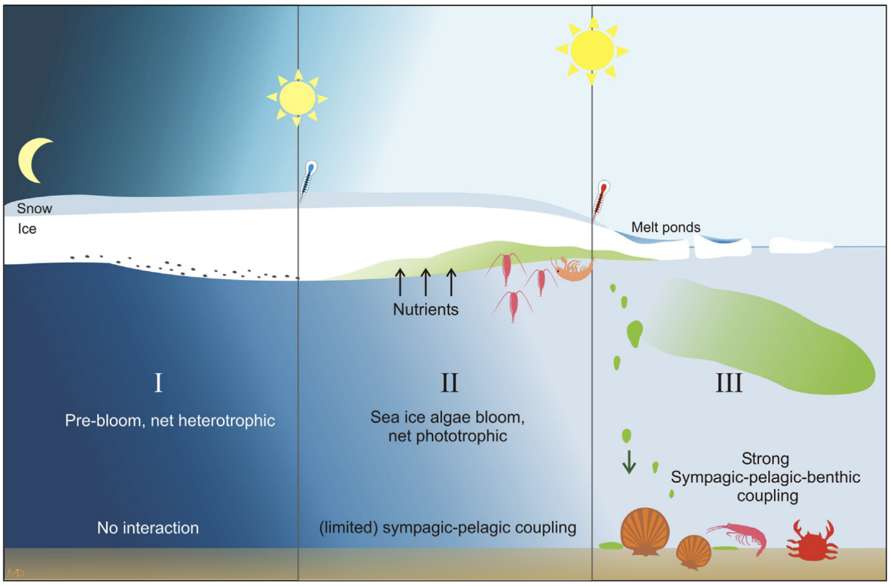

Figure 1.8: Schematic diagram showing the three stages (I, II and III), and accompanying environmental conditions, for the growth of ice-algae in sea ice reproduced from Leu et al. (2015). Stage I is the pre-bloom period characterised by a lack of light available for photosynthesis, which leads to net-heterotrophic conditions (respiration exceeds photosynthesis). Stage II is the spring ice-algal bloom characterised by a rapid increase in ice-algal biomass at the ice-ocean interface as light levels increase, which leads to net-phototrophic conditions (photosynthesis exceeds respiration). Stage III is the end of the ice-algal bloom as the ice melts. Here, sympagic, pelagic, and benthic refer to the ice, water column, and seafloor, respectively.

than the effect of dust or black carbon deposited on the ice/snow surface (Lamare et al. 2016; Redmond Roche and King 2022b).

As well as the effect of oil droplets on the albedo of sea ice, the presence of oil droplets in sea ice may also affect the availability of light for photosynthetic algae living at the ice base, as discussed in the following section.

1.4 Sea ice ecology and the spring algal bloom

As well as the pelagic photosynthetic algae (phytoplankton) that live in the water column, sea ice provides a unique habitat in the polar environment for specially adapted ice-algae (see Arrigo 2017, for example). This means that both pelagic and ice algae contribute to primary production (photosynthesis) in the Arctic Ocean. Ice-algae require photosynthetically active radiation (PAR), radiation in the wavelength range 400–700 nm, for photosynthesis. The extreme seasonal change in the availability of PAR in the Arctic (see §1.1.3), combined with the attenuation of light by sea ice and snow cover is the dominant control on Arctic ecosystems (Leu et al. 2015). This results in a short productive period that provides the base of the Arctic food web (Sakshaug 2004).

The growth and productivity of pelagic and ice-algae in the Arctic can be categorised into the three stages shown in figure 1.8 and summarised by Leu et al. (2015). The first stage, pre-bloom, is characterised by low light levels and low temperatures. At this stage there are low abundances of ice-algae present mostly at the ice-ocean interface where interstitial brine salinities are less extreme. The second stage, the spring ice-algae bloom, is initiated by an increase in the PAR reaching the ice base and occurs between March and May depending on the latitude. The spring ice-algal bloom is characterised by a rapid increase in the ice-algal biomass at the bottom of the ice where the ice is sufficiently porous to allow nutrient exchange with the ocean. The final stage, post-bloom, is characterised by a decline in the ice-algae at the ice base as the melt season progresses and the ice becomes warmer and more permeable. Depletion of available nutrients, removal of algae and nutrients by full depth convection, and potentially harmful levels of solar radiation in the ice are all thought to contribute to the end of the ice-algal bloom. The pelagic phytoplankton bloom can begin as the ice continues to thin, or melt completely and more light reaches the ocean surface (Arrigo et al. 2012; Mundy et al. 2014).

The timing of the spring algal bloom is significant as it provides a food source for higher trophic levels in the Arctic food web (Johannessen and Miles 2011). Estimates of primary productivity in the Arctic Ocean have suggested that ice-algae contribute less overall than pelagic phytoplankton. However, due to the earlier onset of the ice-algal bloom, it is estimated to provide around 10–20% of the total primary production in ice-covered parts of the Arctic Ocean in March, April and May (see figure 14.3 in Arrigo 2017).

Many modelling studies have investigated the effect of snow and ice thickness on the transmitted PAR at the ice-ocean interface (e.g. Lavoie et al. 2005; Castellani et al. 2017; Stroeve et al. 2021; Lebrun et al. 2023; Redmond Roche and King 2024). Recently a model of PAR transmission through snow and ice has been used to estimate the onset time of the spring algal bloom throughout the Arctic from remote sensing data (Stroeve et al. 2024). Gradinger and Bluhm (2005) found that sediment in ice completely suppressed the spring ice-algal bloom by blocking light transmission. The suppression of the bloom was also associated with a drop in species abundance and biological activity under the sediment-laden ice. It has been suggested that the presence of dispersed oil droplets within the water column can significantly reduce the transmission of PAR (Haule and Freda 2016). Laboratory experiments have also shown that releasing crude oil under growing sea ice, both as an oil lens or as dispersed droplets, greatly hinders the growth of ice-algae (Dilliplaine et al. 2021). The authors suggested this is due to the absorption of PAR by the oil, reducing the available light for photosynthesis as well as the potential toxicity to ice algae of some compounds in crude oil. In chapter 8, we will build on this work by using a computational model to investigate the impact of dispersed oil droplets on the potential timing of the spring ice-algal bloom.

1.5 Thesis structure & aims

In this thesis I will develop a new framework to model a three-phase mushy layer. Existing two-phase mushy-layer theory has found much success in modelling the growth and desalination of sea ice. However, the three-phase model developed in this thesis will allow us to explore the physics of both gas bubbles and oil droplets in sea ice. We have seen in this chapter that these topics are collectively significant for quantifying biogeochemical processes, the bulk density of sea ice used in remote sensing, the partitioning of shortwave radiation and resulting energy absorption in the sea-ice system, and sea-ice ecology.

In chapter 2, we will present general conservation equations for a three-phase mushy layer with a solid, liquid and gaseous phase. We will account for the exsolution of gas bubbles and use an idealised model of the pore space geometry of columnar sea ice to estimate the vertical flux of gas bubbles in the ice. From this model will emerge a porosity threshold below which gas bubbles are trapped in the ice which depends on the characteristic lengthscales of the bubbles and the geometry of the pore space. We will derive an approximate model appropriate for low gas volume fractions that yields a reduced three-phase mushy-layer model where the gas phase is treated as a reactive tracer. This model is particularly useful because the conservation equations for heat and solute return to the standard two-phase mushy-layer case for which there are many existing numerical approaches (see e.g. Parkinson 2019). We will show that the reduced model captures the essential physics of the full three-phase model for directional freezing of saltwater saturated with air. Directional freezing is a standard benchmark problem for mushy-layer theory.

In chapters 3–5, we develop a model of three-phase transport during transient mushy-layer evolution to model sea ice in geophysical applications. In chapter 3, we adapt the equations of the reduced "tracer" three-phase mushy layer to model the transient evolution of a horizontally uniform layer of sea ice. This requires the parameterisation of extra geophysically relevant processes in the snow pack above the ice and the ocean below the ice. In chapter 4, special attention is given to developing a computationally efficient spectral radiative transfer scheme for shortwave radiation in snow, sea ice, and the ocean. This is needed to be able to model the effect of oil droplets on the absorption of light in sea ice later in this thesis, because the absorption of light by oil droplets is strongly dependent on the wavelength. In chapter 5, we describe the numerical methods implemented to solve the transient three-phase sea ice model of chapter 3 coupled to the radiation scheme of chapter 4. We demonstrate the convergence of the numerical scheme to a similarity solution for mushy-layer growth from a fixed temperature boundary.

In chapter 6, we validate the performance of the model in the two-phase case against measurements of ice temperature, thickness and bulk salinity at Barrow, Alaska. This allows us to constrain parameter values and demonstrate the ability of the model to accurately reproduce first-year ice conditions. Using this validated configuration of the model, in chapter 7 we explore the impact of different bubble sizes and nucleation rates on the bulk air content of first-year sea ice. We constrain plausible parameter values for the gas dynamics using field measurements of the bulk concentrations of argon, nitrogen and oxygen collected from first-year ice at Barrow. Having chosen parameter values that best reproduce the field data, we use the modelled air fraction to estimate the bulk density of first-year sea ice over a seasonal cycle. The estimated bulk density is compared with previous observations to evaluate the model and suggest physical mechanisms that may be important to account for in future studies.

In chapter 8, we adapt the three-phase sea ice model to describe the motion of oil droplets in sea ice rather than gas bubbles. We also couple the oil concentration to the spectral radiative transfer scheme developed in chapter 4 to investigate the impact of oil droplets on the absorption of light in sea ice. We investigate if low levels of dispersed oil droplets in Arctic waters could significantly affect the melting of first-year sea ice, as well as the impact on the timing of the spring ice-algal bloom.

Finally, in chapter 9 we summarise the most significant results of the thesis and their consequences for the field at large, before suggesting directions for future work.

2

Gas exsolution and migration in a mushy layer

2.1 Introduction

In this chapter, we develop a mathematical model for a three-phase mushy layer that includes the exsolution and migration of buoyant gas bubbles. We formulate a simple pore-scale model for the motion of gas bubbles within a mushy layer that provides physical insight and yields a mechanistically-based porosity threshold for bubble transport that depends on bubble radius. In §2.2, we extend a standard two-phase mushy-layer model to include gas as an additional dissolved component in the liquid and as an additional free phase. In §2.3, we introduce a simplified model for bubble motion in an idealised pore geometry and then use it to derive an expression for the vertical flux of gas due to buoyancy. In §2.4, we solve the model for a steadily solidifying mushy layer in a Hele-Shaw cell. Finally, in §2.5, we explore the consequences of some simplifying approximations and investigate how the key dimensionless parameters control the gas content of a steadily solidifying mushy layer.

2.2 Model for a three-phase mushy layer

We consider a binary eutectic solution, comprising a solvent and a dissolved solute, where the freezing temperature of the solution decreases with increasing solute concentration. A well studied morphological instability occurs during the solidification of such a solution (Mullins and Sekerka 1964), resulting in the formation of a mushy layer (Worster 2000). Here, we allow the binary eutectic solution to contain an additional solute: dissolved gas. If the concentration of dissolved gas exceeds the saturation concentration, gas exsolution will produce a free gas phase.

Following previous theoretical work on mushy layers (Worster 2000), we work with quantities that are averaged over a representative elementary volume (REV) defined at a scale that is much larger than the pore size but still much smaller than the macroscopic scale of interest. The solid fraction ϕ_s, liquid fraction ϕ_l, and gas fraction ϕ_g are the ratio of the volume of the respective phase within the REV to the volume of the REV. These volume fractions evolve in time and space while satisfying

$$\phi_s(\boldsymbol{x},\, t) + \phi_l(\boldsymbol{x},\, t) + \phi_g(\boldsymbol{x},\, t) = 1, \tag{2.2.1}$$

where $\boldsymbol{x}$ is the spatial coordinate and t is time.

The governing equations formulated here apply generally to three-phase, three-component mushy-layer systems. However, to provide physical context we refer below to the components of the water-salt-air system relevant to sea ice: $\mathrm{H_2O}$, either as liquid water or solid ice; salt (NaCl), either dissolved in the liquid or as a solid precipitate of hydrohalite ($\mathrm{NaCl \cdot 2\,H_2O_{(s)}}$) below the eutectic temperature; and air, either dissolved in the liquid or present as free-phase gas bubbles. Air is a mixture of atmospheric gases, but for simplicity we consider air as a single component with fixed composition and a single solubility value.

The composition of each phase in the REV is determined by the mass fraction of each of its constituents. The mass fraction of a component in a phase is the ratio of the mass of that component in the phase to the total mass of the phase in the REV. The mass fractions of ice $\mathcal{W}_s$ and salt precipitate S_s in the solid phase satisfy

$$\mathcal{W}_s + S_s = 1, \tag{2.2.2}$$

since we assume no gas molecules are incorporated into the solid phase. The mass fractions of water $\mathcal{W}_l$, dissolved salt S_l, and dissolved air ξ_l in the liquid phase satisfy

$$\mathcal{W}_l + S_l + \xi_l = 1. \tag{2.2.3}$$

The gas phase consists solely of free-phase air of fixed composition. The densities ρ_s, ρ_l, and ρ_g of the solid, liquid, and gas phases, respectively, depend on the temperature, pressure, and composition of the phase.

2.2.1 Conservation of water

We derive conservation equations for a three-phase mushy-layer system with a rigid solid phase, working in a frame of reference in which the solid phase is stationary. The liquid phase may flow through the pore space of the mushy layer, with volumetric flow rate per unit area (i.e., Darcy flux) $\boldsymbol{u}_l$ relative to the solid. In a saturated porous medium, $\boldsymbol{u}_l$ is calculated using Darcy's Law,

$$\boldsymbol{u}_l = -\frac{\Pi}{\mu_l}\left(\boldsymbol{\nabla} p_l + \rho_l g \boldsymbol{e}_z\right), \tag{2.2.4}$$

where $\Pi(\phi_s)$ is the permeability as a function of solid fraction, μ_l is the dynamic viscosity of the liquid phase, p_l is the liquid (pore) pressure, g is the body force per unit mass due to gravity, and $\boldsymbol{e}_z$ is the vertical unit vector with coordinate z increasing upwards. Several studies of mushy layers have utilised the Darcy–Brinkman equation which reduces to Darcy's Law or the Navier–Stokes equations in the limits $\phi_s \to 1$ and $\phi_s \to 0$, respectively (Le Bars and Worster 2006; Parkinson 2019). For simplicity, we determine $\boldsymbol{u}_l$ using Darcy's Law in the mushy layer and the Navier–Stokes equations in the liquid where $\phi_s = 0$.

The presence of a gas phase in the pore space is known to modify the liquid flux, as commonly modelled via relative-permeability and capillary-pressure effects (Blunt 2017). In the present setting, however, only a relatively small volume of gas is dissolved in the liquid phase at saturation. Therefore, we assume that $\phi_g \ll 1 - \phi_s$ and neglect the impact of the free gas phase on the liquid flux and thus retain equation (2.2.4).

Conservation of water for this system can be expressed as

$$\frac{\partial}{\partial t}\left(\rho_s \phi_s \mathcal{W}_s + \rho_l \phi_l \mathcal{W}_l\right) + \boldsymbol{\nabla} \cdot \left(\rho_l \mathcal{W}_l \boldsymbol{u}_l\right) = 0. \tag{2.2.5}$$

For sea ice, the mass concentrations of salt and air are typically small and so $\mathcal{W}_l \approx \mathcal{W}_s \approx 1$ from equations (2.2.2) and (2.2.3). Note that here we have assumed that $p_c = 0$ and so $\mathcal{W}_s = 1$ in the mushy phase, however some mass of solid salt may be present in the solid phase below the eutectic temperature.

Equation (2.2.5) predicts that volume changes occurring due to density changes upon the freezing of water and the exsolution of gas will drive a divergent liquid flux. In the steady problem investigated in §2.4, volume changes due to freezing and gas exsolution are of similar magnitudes in principle. However, the effects of the flow driven by density change during freezing are small compared with buoyancy driven flows, well understood, and often neglected when modelling sea ice (Notz and Worster 2009). For the remainder of this chapter, we focus on the flow driven by gas exsolution. We neglect volume change upon freezing and melting by taking the liquid and solid phase densities to be constant and equal (i.e., $\rho_s = \rho_l$). Under these assumptions and using equation (2.2.1), equation (2.2.5) simplifies to

$$\frac{\partial \phi_g}{\partial t} = \boldsymbol{\nabla} \cdot \boldsymbol{u}_l. \tag{2.2.6}$$

2.2.2 Conservation of salt

Salt can be present as an aqueous solute or a solid precipitate (below the eutectic temperature). Solid salt is assumed to be stationary relative to the ice, whereas dissolved salt is advected with the liquid and diffuses down salinity gradients with molecular diffusivity κ_S. Conservation of salt is expressed as

$$\frac{\partial}{\partial t}\left(\rho_s \phi_s S_s + \rho_l \phi_l S_l\right) + \boldsymbol{\nabla} \cdot \left(\rho_l S_l \boldsymbol{u}_l\right) = \boldsymbol{\nabla} \cdot \left(\rho_l \phi_l \kappa_S \boldsymbol{\nabla} S_l\right). \tag{2.2.7}$$

2.2.3 Conservation of air

Air is present as a solute in the liquid (i.e., dissolved air) or as a free gas phase in the form of bubbles. Similar to dissolved salt, dissolved air is transported by advection with the liquid and by diffusion with molecular diffusivity κ_ξ. Conservation of dissolved air can be written as

$$\frac{\partial}{\partial t}\left(\rho_l \phi_l \xi_l\right) + \boldsymbol{\nabla} \cdot \left(\rho_l \xi_l \boldsymbol{u}_l\right) = \boldsymbol{\nabla} \cdot \left(\rho_l \phi_l \kappa_\xi \boldsymbol{\nabla} \xi_l\right) - N, \tag{2.2.8}$$

where N is the mass of gas exsolved per unit volume per unit time.

Air bubbles move through the pore space with volumetric flux $\boldsymbol{u}_g$ and conservation of the free-phase gas is therefore given by

$$\frac{\partial}{\partial t}\left(\rho_g \phi_g\right) + \boldsymbol{\nabla} \cdot \left(\rho_g \boldsymbol{u}_g\right) = N, \tag{2.2.9}$$

where a novel expression for $\boldsymbol{u}_g$ is derived in §2.3. Equations (2.2.8) and (2.2.9) can be summed to yield a conservation statement for air that does not involve N.

The kinetics of gas bubble nucleation in this setting are poorly understood. To avoid the complexities of individual bubble nucleation and growth, and for consistency with previous work, we follow Moreau et al. (2014) and take N to be proportional to the mass of dissolved gas above saturation,

$$N = \frac{\rho_l \phi_l}{\tau_{\text{nuc}}} \left(\xi_l - \xi_{\text{sat}}\right) I\left(\xi_l,\, \phi_g\right), \tag{2.2.10}$$

so that the concentration of dissolved gas in supersaturated liquid will relax toward the saturation concentration ξ_{sat} as gas exsolves. The rate of gas exsolution is controlled by an exsolution timescale τ_{nuc}, the value of which is poorly constrained. For simplicity we take both ξ_{sat} and τ_{nuc} to be constant and independent of temperature, pressure and composition. The indicator function

$$I\left(\xi_l,\, \phi_g\right) = \begin{cases} 0, & \xi_l < \xi_{\text{sat}} \quad \text{and} \quad \phi_g = 0 \\ 1, & \text{otherwise} \end{cases} \tag{2.2.11}$$

prevents unphysical dissolution when no free-phase gas is present.

For simplicity, we assume that the free-phase gas exists as a homogeneous population of identical spherical bubbles of prescribed radius R_B. It is appropriate to assume that bubbles smaller than the pore size are spherical since the capillary number $Ca = \mu_l V_g/\gamma$ is small in this setting, where $\gamma = 77\,\mathrm{mN\,m^{-1}}$ is the air-liquid interfacial tension, μ_l is the dynamic viscosity of the liquid, and V_g is the vertical interstitial velocity of a bubble within the pore space. Once the radius of a bubble approaches or exceeds the pore radius it will deform to an elongated shape (Bretherton 1961) with equivalent spherical radius R_B.

The gas density is related to the surrounding liquid pressure through the ideal gas law and the Laplace pressure jump for a spherical bubble,

$$\rho_g \mathcal{R} T_K - p_l = \frac{2\gamma}{R_B}, \tag{2.2.12}$$

where $\mathcal{R}$ is the specific gas constant, γ is the air-water interfacial tension, and T_K is the absolute temperature.

2.2.4 Conservation of energy

We assume local thermal equilibrium, meaning that all three phases are at the same bulk temperature T, and write conservation of energy as

$$\overline{\rho c_p}\frac{\partial T}{\partial t} + \rho_l c_{p,l}\boldsymbol{u}_l \cdot \boldsymbol{\nabla} T + \rho_g c_{p,g}\boldsymbol{u}_g \cdot \boldsymbol{\nabla} T = \rho_s L \frac{\partial \phi_s}{\partial t} + \boldsymbol{\nabla} \cdot \left(\overline{k}\boldsymbol{\nabla} T\right), \tag{2.2.13}$$

where L is the latent heat of fusion for water,

$$\overline{\rho c_p} = \phi_s \rho_s c_{p,s} + \phi_l \rho_l c_{p,l} + \phi_g \rho_g c_{p,g} \tag{2.2.14}$$

is the phase averaged heat capacity, and

$$\overline{k} = \phi_s k_s + \phi_l k_l + \phi_g k_g \tag{2.2.15}$$

is the phase averaged thermal conductivity. Subscripts denote values of the specific heat capacity c_p or thermal conductivity k in the solid (s), liquid (l) or gas phase (g). The second and third terms on the left-hand side arise due to the advection of heat by fluid flow. The two terms on the right-hand side reflect the rate of latent-heat release during freezing and the rate of conductive heat transfer, respectively. Since water and ice constitute the majority of the system by mass, we have neglected energy changes associated with salt precipitation and gas exsolution (see appendix A for details).

2.3 A model for vertical bubble motion in a mushy layer

We now present a novel model for the vertical volumetric flux of gas due to buoyant bubble motion in the pore space of a mushy layer. We take $\boldsymbol{u}_g = w_g \boldsymbol{e}_z$ and develop a phenomenological model for w_g by assuming a population of identical bubbles rising in cyindrical pores (figure 2.1) and drawing on theoretical results for the steady motion of a single bubble in a cylindrical tube. For the case of sea ice, we use pore-geometry parameters derived from X-ray CT images of sea-ice microstructure.

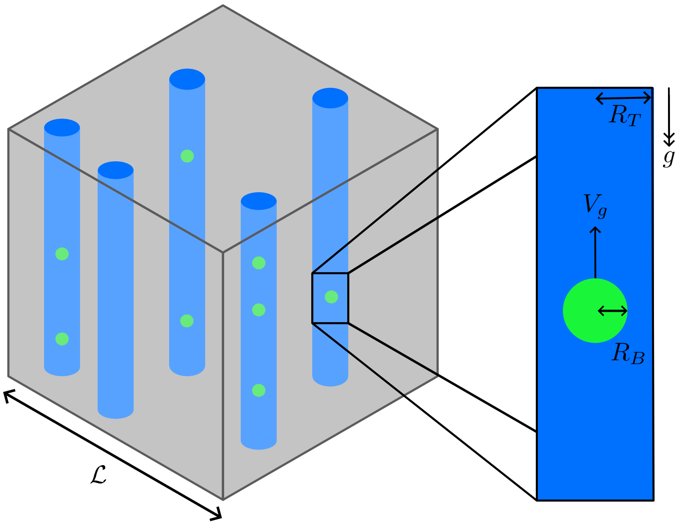

Figure 2.1: Diagram showing a cuboidal REV of idealised columnar sea ice with side length $\mathcal{L}$. The pore space of the ice is approximated by vertically oriented cylinders of radius R_T, filled with liquid (blue) and spherical gas bubbles of radius R_B (green). Also shown is a closer view of a bubble moving along the centreline of a cylindrical pore with velocity V_g.

2.3.1 Idealised pore geometry

The microstructure of columnar sea ice typically consists primarily of highly anisotropic, vertically elongated pores (Maus et al. 2021; Oggier and Eicken 2022). Motivated by these observations, we approximate the microscale elements of the pore geometry of a mushy layer that control vertical gas flow as a set of identical cylindrical pores with evolving radius. We consider a cuboidal REV of the mushy layer, with side length $\mathcal{L}$, that contains n liquid-filled cylindrical pores of radius R_T (figure 2.1). For a given porosity $1 - \phi_s$, the number of cylindrical pores n in the REV is then

$$n = \frac{(1-\phi_s)\mathcal{L}^2}{\pi R_T^2}. \tag{2.3.1}$$

Flow in cylindrical pores is a common toy model for flow in porous media (Olbricht 1996) that has been used to investigate gas transport in a geophysical setting (Mahabadi et al. 2018) and thermal disequilibrium in the pore space of a mushy layer (Amiri and Butler 2024). In a mushy layer, the pore geometry changes due to the transport of heat and salt. We capture these variations here by allowing the pore radius R_T to evolve in space and time.

X-ray CT measurements of the pore space of sea ice show that the median pore-throat radius scales as a power law of the porosity $1-\phi_s$ (Maus et al. 2021), so we take

$$R_T = R_0(1-\phi_s)^q, \tag{2.3.2}$$

where R_0 and q are empirical fitting parameters (table 2.1; Maus et al. 2021). Note that equation (2.3.2) is fitted to data in the porosity range $0.031 < 1-\phi_s < 0.3$, but we use it for all values of ϕ_s in the absence of other data.

Observational and theoretical work suggests that the pore network becomes disconnected at low porosity values in some mushy layers, including sea ice, thus preventing further fluid transport (Golden et al. 1998). Maus et al. (2021) calculate a threshold value $\phi_c = 0.024$, which we adopt here, such that sea ice is impermeable for $1-\phi_s < \phi_c$. The values R_0, q, and ϕ_c may change for other materials. The porosity threshold ϕ_c at which the pore network becomes disconnected provides a lower bound on the porosity needed for the mushy layer to be permeable to fluid transport. However, in §2.3.2, we calculate an additional evolving porosity threshold for gas transport that depends on the bubble radius and the pore-geometry scale.

In the remainder of this thesis, we assume for simplicity that the bubble radius R_B is uniform in space and constant in time. Hence, the number of bubbles m within the REV is determined by the local gas fraction,

$$m = \frac{3\phi_g \mathcal{L}^3}{4\pi R_B^3}. \tag{2.3.3}$$

2.3.2 Interstitial bubble motion

The vertical gas flux $w_g = \phi_g V_g$ is the volume flux of bubbles per unit area within the REV passing through the top surface. We assume that every bubble is independent, meaning that they do not interact. We determine V_g by balancing the forces acting on a bubble moving along the centreline of an infinite liquid-filled cylinder at low Reynolds number *Re* (i.e., for Stokes flow), which is a classical problem in fluid mechanics. The parameter $\delta = R_B/R_T$ is the ratio of the equivalent spherical bubble radius to the pore radius. We assume no-penetration and free slip boundary conditions at the bubble surface and an undisturbed parabolic liquid velocity profile in the far field above and below the bubble, with maximum value U_0 along the centreline (e.g., Higdon and Muldowney 1995). The maximum liquid velocity U_0 is related to the macroscopic liquid flux $\boldsymbol{u}_l = w_l \boldsymbol{e}_z$ by $U_0 = 2w_l/(1-\phi_s)$.

This problem has been widely studied using analytical and numerical methods (Haberman and Sayre 1958; Hartholt et al. 1994; Higdon and Muldowney 1995; Al Quddus et al. 2008). The linearity of Stokes flow allows the drag on the bubble $\boldsymbol{F}_d = F_d \boldsymbol{e}_z$ to be decomposed as a sum of two terms,

$$F_d = 4\pi\mu_l R_B \left(V_g K_1 - U_0 K_2\right), \tag{2.3.4}$$

where $K_1(\delta)$ and $K_2(\delta)$ are dimensionless functions that give the drag on a bubble moving through an otherwise stagnant fluid in a cylindrical tube, and the drag on a stationary bubble in a cylindrical tube that carries a steady liquid flow, respectively. We balance F_d against the buoyancy force $4\pi\Delta\rho g R_B^3/3$ to arrive at

$$V_g = \begin{cases} \dfrac{\Delta\rho g R_B^2}{3\mu_l K_1(\delta)} + U_0 G(\delta), & (1-\phi_s) > \phi_c \\ 0, & (1-\phi_s) \leq \phi_c \end{cases}, \tag{2.3.5}$$

where $G = K_2/K_1$ and the density difference is $\Delta\rho \approx \rho_l$ because $\rho_g \ll \rho_l$. In the steady problem considered in §2.4, the only liquid flow through the mushy layer is the weak flow driven by gas exsolution. For simplicity, going forward, we neglect the impact of this flow on bubble motion by setting $U_0 = 0$ in equation (2.3.5). Note that the above is based on a free-slip condition at the bubble surface, but impurities in the liquid can modify the surface so that a no-slip condition is more appropriate (Thorpe 1982), which changes the prefactor in equation (2.3.5) from 1/3 to 2/9.

Approximate expressions for $K_1(\delta)$ have been determined via asymptotic and numerical methods (Haberman and Sayre 1958; Hartholt et al. 1994; Higdon and Muldowney 1995; Al Quddus et al. 2008). For computational ease, we use the empirical expression proposed by Hartholt et al. (1994) for the free-slip case,

$$K_1(\delta) = \begin{cases} \dfrac{1 + c\delta^5}{1 - c\delta + c\delta^5 - \delta^6}, & 0 \leq \delta < 1 \\ +\infty, & \delta \geq 1 \end{cases}, \tag{2.3.6}$$

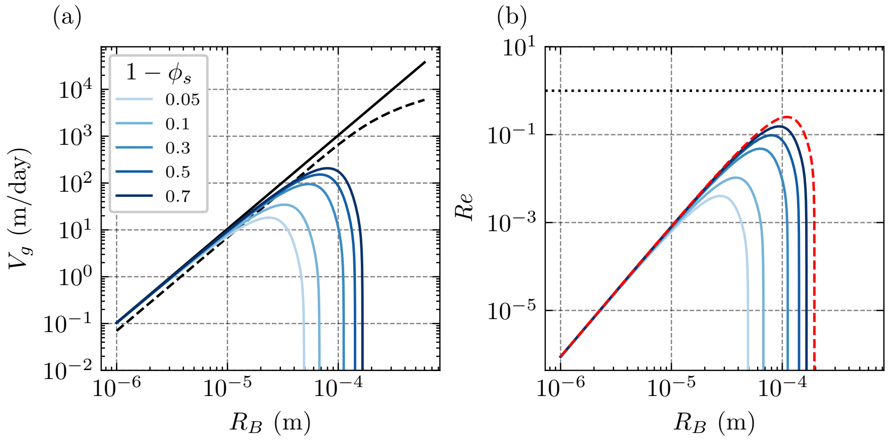

Figure 2.2: Plot of (a) the terminal rise velocity V_g and (b) the resulting Reynolds number Re, both calculated via equation (2.3.5), versus bubble radius R_B, for different porosities (blue curves). In panel (a), we show for comparison the rise velocity of a free-slip bubble in an unbounded Stokes flow (solid black) and the open-ocean bubble rise velocity with a high Re correction (dashed black; Thorpe 1982). In panel (b), we indicate $Re = 1$ (dotted black) and Re as calculated from equation (2.3.5) at $\phi_s = 0$ (dashed red).

where $c = 1.4567$, which was determined to match the results of finite element simulations for $0 \leq \delta \lessapprox 0.8$. The most important properties of K_1 for our purposes are that $K_1 \to 1$ as $\delta \to 0$, recovering the terminal Stokes rise velocity for a bubble in an unbounded fluid, and that $K_1 \to \infty$ as $\delta \to 1$, so that bubbles larger than the pore radius do not move under their own buoyancy.

Equation (2.3.5) is an expression for the terminal rise velocity of a free-slip bubble in a mushy layer with cylindrical pores in the Stokes regime. We plot the resulting rise velocity for different porosities in figure 2.2a using parameter values for the sea-ice system (table 2.1). The steady vertical rise velocity V_g follows the Stokes terminal velocity for a free-slip bubble in an unbounded fluid until the bubble radius approaches the porosity-dependent pore radius, at which point the rise velocity vanishes (i.e., $V_g \to 0$ as $R_B \to R_T(\phi_s)$). The associated Reynolds number $Re = 2\rho_l R_B V_g/\mu_l$ is plotted against R_B for different values of $1 - \phi_s$ in figure 2.2b, confirming $Re < 1$ for $0 \leq \phi_s \leq 1$.

For $\delta \gg 1$, we enter the regime of a long, deformed gas "slug" in the tube, as investigated theoretically by Bretherton (1961) and experimentally by Borhan and Pallinti (1995). Both studies report that long bubbles are unable to move under their own buoyancy for Bond number $Bo \lessapprox 0.8$. Using parameter values

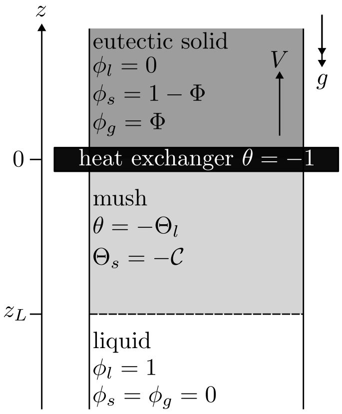

Figure 2.3: Schematic diagram of a steadily solidifying mushy layer in a Hele-Shaw cell that is translated upward at a constant speed V through a cold heat exchanger at $z = 0$. The dimensionless variables θ, Θ_l, Θ_s, Φ and $\mathcal{C}$ are defined in §2.4.1.

from table 2.1, we find that $Bo = \Delta\rho g R_0^2/\gamma \approx 5.3 \times 10^{-3}$, suggesting that long bubbles should be immobile in the present context; equation (2.3.5) is consistent with this limit. Therefore, bubbles of radius R_B can only migrate vertically under their own buoyancy when $\delta < 1$, which yields

$$1 - \phi_s > \delta_0^{1/q}, \tag{2.3.7}$$

where $\delta_0 = R_B/R_0$ is the dimensionless bubble radius. Hence, in contrast to previous work (Moreau et al. 2014), the porosity theshold for vertical bubble transport is here determined as a function of bubble radius and pore-geometry characteristics.

2.4 A one-dimensional steady-state mushy layer

We next build physical insight by considering a standard model problem: steady directional solidification (figure 2.3). The system comprises a saltwater-filled Hele-Shaw cell of gap width b with perfectly insulating walls, that is translated upward with a constant pulling speed V through a heat exchanger that imposes a constant temperature $T = T_E$ at the fixed position $z = 0$.

The conservation equations derived in §2.2 are valid in the frame of the Hele-Shaw cell ($\boldsymbol{x}$, t), where the solid phase is stationary. This frame moves with velocity $\boldsymbol{V} = V\boldsymbol{e}_z$ relative to the heat exchanger. The laboratory frame ($\tilde{\boldsymbol{x}}$, $\tilde{t}$), in which the

Parameter	Symbol	Value
(a)		
fresh melting temperature	T_m	$0\,°\mathrm{C}$
saltwater eutectic temperature (Peppin et al. 2007)	T_E	$-21.2\,°\mathrm{C}$
liquidus slope (Peppin et al. 2007)	γ_L	$0.07\,°\mathrm{C}/(\mathrm{g\,kg^{-1}})$
thermal conductivity of water	k_l	$0.52\,\mathrm{W\,m^{-1}\,K^{-1}}$
thermal conductivity of ice	k_s	$2.22\,\mathrm{W\,m^{-1}\,K^{-1}}$
specific heat capacity of water	$c_{p,l}$	$4209\,\mathrm{J\,kg^{-1}\,K^{-1}}$
specific heat capacity of ice	$c_{p,s}$	$2009\,\mathrm{J\,kg^{-1}\,K^{-1}}$
latent heat of fusion of ice	L	$333 \times 10^3\,\mathrm{J\,kg^{-1}}$
density of seawater	ρ_l	$1028\,\mathrm{kg\,m^{-3}}$
gravitational acceleration	g	$9.81\,\mathrm{m\,s^{-2}}$
dynamic viscosity of water	μ_l	$2.78 \times 10^{-3}\,\mathrm{kg\,m^{-1}\,s^{-1}}$
atmospheric pressure	p_{atm}	$1.01 \times 10^5\,\mathrm{Pa}$
reference permeability	K	$1 \times 10^{-8}\,\mathrm{m^2}$
Hele-Shaw gap width (Peppin et al. 2007)	b	$0.5\,\mathrm{cm}$
reference density of air	ρ_g^0	$1.31\,\mathrm{kg\,m^{-3}}$
specific gas constant	$\mathcal{R}$	$286\,\mathrm{J\,m^{-1}\,K^{-1}}$
air-water interfacial tension	γ	$77 \times 10^{-3}\,\mathrm{N\,m^{-1}}$
gas exsolution timescale	τ_{nuc}	$1000\,\mathrm{s}$
solubility of air in seawater	ξ_{sat}	$3.71 \times 10^{-5}\,\mathrm{kg\,kg^{-1}}$
bubble radius	R_B	$1 \times 10^{-3}\,\mathrm{m}$
reference pore throat radius (Maus et al. 2021)	R_0	$195\,\mathrm{\mu m}$
pore-throat-radius exponent (Maus et al. 2021)	q	0.46
impermeable transition porosity (Maus et al. 2021)	ϕ_c	0.024
pulling speed (Peppin et al. 2007)	V	$1\,\mathrm{\mu m\,s^{-1}}$
far-field temperature	T_∞	$0.1\,°\mathrm{C}$
far-field salinity	S_∞	$35\,\mathrm{g\,kg^{-1}}$
far-field dissolved-air concentration	ξ_∞	$3.71 \times 10^{-5}\,\mathrm{kg\,kg^{-1}}$
(b)		
Stefan number	St	4.2
concentration ratio	$\mathcal{C}$	0.13
Damköhler number	Da	120
expansion coefficient	χ	0.029
dimensionless bubble velocity scale	$\mathcal{B}$	4.6×10^4
dimensionless pore throat radius	δ_0	5.1
dimensionless Hele-Shaw permeability	$\mathcal{K}^{\dagger}$	210
dimensionless atmospheric pressure	$p_0{}^{\dagger}$	3×10^6
dimensionless hydrostatic pressure scale	$\mathcal{H}^{\dagger}$	0.012
dimensionless Laplace pressure jump	$La^{\dagger}$	1.5×10^{-3}
dimensionless absolute reference temperature	$\theta_K{}^{\dagger}$	14
dimensionless far-field temperature	θ_∞	0.14
dimensionless far-field dissolved air concentration	ω_∞	1

Table 2.1: Parameters for the freezing of air-saturated seawater. The dimensionless parameters (b) are calculated from the dimensional values (a) using the definitions in §2.4.1. The dimensionless parameters marked with a † are not required under the approximations of the reduced model given in §2.4.7. The value of R_B given here inhibits the motion of gas bubbles since $\delta_0 > 1$; however smaller values of R_B for which $\delta_0 < 1$ are considered in §2.5.3.

heat exchanger is stationary, is therefore related to the frame of the Hele-Shaw cell by the Galilean transformations $\tilde{\boldsymbol{x}} = \boldsymbol{x} + \boldsymbol{V}t$ and $\tilde{t} = t$. Spatial and temporal derivatives in the frame of the Hele-Shaw cell are related to those in the laboratory frame by

$$\boldsymbol{\nabla} = \tilde{\boldsymbol{\nabla}}, \quad \text{and} \quad \frac{\partial}{\partial t} = \frac{\partial}{\partial \tilde{t}} + \boldsymbol{V} \cdot \tilde{\boldsymbol{\nabla}}.$$

Going forward, we drop the tilde notation and refer only to coordinates in the laboratory frame. We seek steady solutions ($\partial/\partial t = 0$) to equations (2.2.6)–(2.2.9),(2.2.13), and (2.3.5) with variation only in the vertical direction.

In the far field ($z \to -\infty$), the Hele-Shaw cell contains liquid water at temperature $T_\infty > T_L(S_\infty)$ with salinity S_∞ and dissolved-air concentration $\xi_\infty \le \xi_{\text{sat}}$. A steady mushy layer forms in the region $z_L < z < 0$, where z_L is to be determined, and a eutectic solid forms in the region $z > 0$.

2.4.1 Dimensionless model

We next make the model above dimensionless, indicating dimensionless versions of the dimensional quantities above with a superscript *. The vertical liquid and gas fluxes $w_{l,g} = V w_{l,g}^*$ are scaled by the pulling speed V. Lengths are scaled by κ/V, where $\kappa = k_l/(\rho c_{p,l})$ is the thermal diffusivity of the liquid, so that $z = \kappa z^*/V$. Dimensionless temperature $\theta = [T - T_L(S_\infty)]/[T_L(S_\infty) - T_E]$ and salinities $\Theta_l = (S_l - S_\infty)/(S_E - S_\infty)$ and $\Theta_s = (S_s - S_\infty)/(S_E - S_\infty)$ are scaled by changes over the mushy layer. We introduce the dimensionless concentration of dissolved air $\omega = \xi_l/\xi_{\text{sat}}$ and the dimensionless gas density $\psi = \rho_g/\rho_g^0$, where the reference gas density ρ_g^0 is the density of an ideal gas at temperature $T_L(S_\infty)$ and atmospheric pressure. Finally, we scale the pressures as $p_g = P p_g^*$ and $p_l = P p_l^*$, where $P = \kappa\mu_l/K$ and K is a reference permeability, so that $\Pi = K\Pi^*$.

The dimensionless conservation equations are then

$$\frac{\mathrm{d}\phi_g}{\mathrm{d}z^*} - \frac{\mathrm{d}w_l^*}{\mathrm{d}z^*} = 0, \tag{2.4.1}$$

$$\frac{\mathrm{d}}{\mathrm{d}z^*}\left[\phi_s\left(\Theta_s + \mathcal{C}\right) + \phi_l\left(\Theta_l + \mathcal{C}\right)\right] + \frac{\mathrm{d}}{\mathrm{d}z^*}\left[w_l^*\left(\Theta_l + \mathcal{C}\right)\right] = 0, \tag{2.4.2}$$

$$\frac{\mathrm{d}}{\mathrm{d}z^*}\left[\omega\phi_l\right] + \frac{\mathrm{d}}{\mathrm{d}z^*}\left[\omega w_l^*\right] = -Da\,\mathcal{N}, \tag{2.4.3}$$

$$\frac{\mathrm{d}}{\mathrm{d}z^*}\left[\psi\phi_g\right]+\frac{\mathrm{d}}{\mathrm{d}z^*}\left[\psi w_g^*\right]=\chi Da\mathcal{N}, \tag{2.4.4}$$

where $\mathcal{N} = I(\omega,\, \phi_g)\phi_l\,(\omega-1)$, and

$$\left(\zeta_s\phi_s+\phi_l+\varepsilon\psi\zeta_g\phi_g\right)\frac{\mathrm{d}\theta}{\mathrm{d}z^*}+\left(w_l^*+\varepsilon\psi\zeta_g w_g^*\right)\frac{\mathrm{d}\theta}{\mathrm{d}z^*}=St\frac{\mathrm{d}\phi_s}{\mathrm{d}z^*}+\frac{\mathrm{d}}{\mathrm{d}z^*}\left[\left(\nu_s\phi_s+\phi_l+\nu_g\phi_g\right)\frac{\mathrm{d}\theta}{\mathrm{d}z^*}\right], \tag{2.4.5}$$

where the resulting dimensionless parameters are defined below. The dimensionless Stefan number $St = L/\{c_{p,l}[T_L(S_\infty)-T_E]\}$ and concentration ratio $\mathcal{C} = S_\infty/(S_E - S_\infty)$ control the thickness and porosity structure of the mushy layer. We neglect the diffusive transport of dissolved salt and gas in equations (2.4.2) and (2.4.3) since $\kappa_S/\kappa \ll 1$ and $\kappa_\xi/\kappa \ll 1$. Ratios of the specific heat capacities ($\zeta_s = c_{p,s}/c_{p,l}$ and $\zeta_g = c_{p,g}/c_{p,l}$), and thermal conductivities ($\nu_s = k_s/k_l$ and $\nu_g = k_g/k_l$) appear in equation (2.4.5). To focus on building understanding of the role of the gas phase, we focus on the so-called “thermally ideal” mushy layer by taking $\zeta_s = \nu_s = 1$.

The gas phase introduces perturbations of $O(\varepsilon)$ to the heat-capacity and advection terms in equation (2.4.5), where $\varepsilon = \rho_g^0/\rho_l$. Since $\varepsilon \approx 10^{-3}$ for air and water, we neglect these perturbations going forward (i.e., we take $\varepsilon = 0$). We also neglect the term $\nu_g\phi_g$ in equation (2.4.5) since both ν_g and ϕ_g are expected to be small ($\nu_g = 0.038$ for air and water).

The dimensionless Damköhler number $Da = \kappa/(V^2\tau_{\mathrm{nuc}})$ is the ratio of the timescale for solidification to the timescale for gas exsolution. The expansion coefficient $\chi = \rho_l\xi_{\mathrm{sat}}/\rho_g^0$ quantifies the increase in volume upon complete exsolution of the gas dissolved within a unit volume of saturated liquid (see appendix B).

The dimensionless form of Darcy's Law for the vertical liquid flux is

$$w_l^* = -\Pi^*(\phi_l)\frac{\mathrm{d}p_H^*}{\mathrm{d}z^*}, \tag{2.4.6}$$

where $p_H^* = p_l^* - p_0 + p_0\mathcal{H}z^*$ is the pressure deviation from hydrostatic in the liquid, shifted so that $p_H^* = 0$ when $p_l^* = p_0$ and $z^* = 0$. Here, $p_0 = p_{\mathrm{atm}}/P$ is the dimensionless atmospheric pressure, and $\mathcal{H} = \rho_l g\kappa/(p_{\mathrm{atm}}V)$ is the ratio of the hydrostatic pressure variation over the characteristic distance κ/V, to the atmospheric pressure. As the system is contained in a Hele-Shaw cell, equation (2.4.6) holds throughout the liquid and mushy regions ($z^* < 0$) with total permeability given by (Katz and Worster 2008)

$$\Pi^*(\phi_l) = \left(\frac{1}{\mathcal{K}} + \frac{1}{\Pi^*_{\mathrm{CK}}(\phi_l)} \right)^{-1}, \tag{2.4.7}$$

where $\mathcal{K} = b^2/(12K)$ is the dimensionless permeability of the empty Hele-Shaw cell and Π^*_{CK} is the dimensionless permeability of the mushy layer. We parameterise the latter using the Carmen-Kozeny relation (e.g., Blunt 2017):

$$\Pi^*_{\mathrm{CK}}(\phi_l) = \frac{\phi_l^3}{(1-\phi_l)^2}. \tag{2.4.8}$$

From §2.3, the dimensionless vertical volumetric gas flux due to bubble motion is

$$w_g^* = \phi_g V_g^*, \tag{2.4.9}$$

where

$$V_g^* = \begin{cases} \dfrac{\mathcal{B}\delta_0^2}{K_1(\delta)}, & (1-\phi_s) > \phi_c \\ 0, & (1-\phi_s) \leq \phi_c \end{cases}, \tag{2.4.10}$$

and $\mathcal{B} = \rho_l g R_0^2/(3\mu_l V)$ is the ratio of the bubble rise velocity scale to the pulling speed.

Finally, the dimensionless gas density is determined by

$$\psi = \left(1 + \frac{\theta}{\theta_K}\right)^{-1} \left(1 + \frac{p_H^*}{p_0} + La - \mathcal{H} z^*\right), \tag{2.4.11}$$

where $La = 2\gamma/(R_B p_{\mathrm{atm}})$ is the ratio of the Laplace pressure jump for a bubble of radius R_B to the atmospheric pressure and $\theta_K = T_L(S_\infty)/[T_L(S_\infty) - T_E]$ is the dimensionless absolute reference temperature, evaluated using the thermodynamic absolute temperature. Going forward, we drop the superscript * and refer only to dimensionless quantities.

2.4.2 Conserved quantities

We next identify three conserved quantities for this system. Firstly, we integrate equation (2.4.1) (representing conservation of water mass) and determine the constant of integration by considering the eutectic solid ($z > 0$), where $w_l = 0$ and $\phi_g = \Phi$, with Φ yet to be determined. This yields the conserved quantity

$$w_l - \phi_g = -\Phi, \tag{2.4.12}$$

which determines w_l in terms of ϕ_g throughout domain. Although w_l and ϕ_g are going to be discontinuous at $z = 0$, $w_l - \phi_g$ must remain continuous to conserve mass. Volume change due to gas exsolution drives a liquid flow out of the mushy layer, which is similar to the liquid flow found by Chiareli and Worster (1995) for a steadily solidifying two-phase mushy layer with $\rho_s \neq \rho_l$.

Next, we integrate equation (2.4.2) using the far-field boundary condition $\Theta_l(z \to -\infty) = 0$. When $z < z_L$, $\phi_l = 1$, $\phi_s = \phi_g = 0$, and equation (2.4.12) implies that $w_l = -\Phi$. Hence, the second conserved quantity is

$$\phi_s(\Theta_s + \mathcal{C}) + (\phi_l + w_l)(\Theta_l + \mathcal{C}) = (1 - \Phi)\mathcal{C}. \tag{2.4.13}$$

Finally, we integrate the sum of equation (2.4.3) and $1/\chi$ times equation (2.4.4), which represents conservation of total air mass. We evaluate the integration constant as $z \to -\infty$, for which $\phi_l \to 1$, $w_l \to -\Phi$, $w_g \to 0$, $\phi_g \to 0$, and $\omega \to \omega_\infty$, yielding

$$\frac{\psi}{\chi}(w_g + \phi_g) + \omega(w_l + \phi_l) = (1 - \Phi)\omega_\infty. \tag{2.4.14}$$

2.4.3 Solution in the solid region ($z > 0$)

After passing through the cold heat exchanger at the eutectic temperature $\theta(z = 0) = -1$, any remaining liquid freezes and the liquid fraction jumps discontinuously to $\phi_l(z = 0^+) = 0$. The region $z > 0$ is a mixture of ice, salt precipitate and air bubbles, such that $\phi_s = 1 - \Phi$, $\phi_l = 0$, and $\phi_g = \Phi$. Applying equation (2.4.14) in $z > 0$, where $w_g = w_l = 0$, yields

$$\Phi = \left[1 + \frac{\psi(z = 0)}{\chi\omega_\infty}\right]^{-1}, \tag{2.4.15}$$

where we have assumed that the free-phase dimensionless gas density $\psi(z)$ remains continuous at $z = 0$ despite the discontinuous jump in $\phi_g(z)$.

2.4.4 Solution in the liquid region ($z < z_L$)

In the liquid region, $\phi_l = 1$ and equations (2.4.12)–(2.4.14) and the far-field boundary conditions yield $\Theta_l = 0$, $w_l = -\Phi$, and $\omega = \omega_\infty$. Hence, equation (2.4.5) becomes

$$\frac{\mathrm{d}\theta}{\mathrm{d}z} - \Phi\frac{\mathrm{d}\theta}{\mathrm{d}z} = \frac{\mathrm{d}^2\theta}{\mathrm{d}z^2}. \tag{2.4.16}$$

The temperature at the mush-liquid interface is the salinity-dependent freezing temperature $\theta(z_L) = 0$ and the temperature in the far field satisfies $\theta(z \to -\infty) = \theta_\infty$. Subject to these two boundary conditions, we integrate equation (2.4.16) to find

$$\theta(z) = \theta_\infty \left\{1 - \exp\left[(1-\Phi)(z - z_L)\right]\right\} \tag{2.4.17}$$

for $-\infty < z < z_L$.

2.4.5 Solution in the mushy layer ($z_L < z < 0$)

All three phases can coexist within the mushy layer. The total segregation of salt into the interstitial liquid and the liquidus constraint (equation 1.1.1) together imply that $\Theta_s = -\mathcal{C}$ and $\Theta_l = -\theta$. Using equations (2.4.12), (2.4.13), and (2.2.1), we find

$$\phi_s(\theta) = -\frac{(1-\Phi)\theta}{\mathcal{C} - \theta} \quad \text{and} \quad \phi_l(\phi_g, \theta) = 1 - \phi_s(\theta) - \phi_g. \tag{2.4.18a, b}$$

Equations (2.4.9), (2.4.12), (2.4.14) and (2.4.18) yield

$$\phi_g = \frac{\chi(1-\Phi)}{\psi\,(1 + V_g)}\left[\omega_\infty - \frac{\omega\mathcal{C}}{\mathcal{C} - \theta}\right], \tag{2.4.19}$$

where ψ is evaluated using equation (2.4.11). Using the relations (2.4.9), (2.4.12), (2.4.18), and (2.4.19), we solve equations (2.4.3), (2.4.5), and (2.4.6) numerically in the mush for ω, θ, and p_H subject to the boundary conditions $\omega(z_L) = \omega_\infty$, $\theta(z_L) = 0$, $\theta(0) = -1$, and $p_H(0) = 0$ (see appendix C).

Following Chiareli and Worster (1995), the appropriate boundary condition to determine the position z_L of the mush-liquid interface is continuity of the temperature derivative, which yields

$$\frac{\mathrm{d}}{\mathrm{d}z}\theta(z = z_L^+) = -\theta_\infty(1 - \Phi), \tag{2.4.20}$$

where Φ is given by equation (2.4.15). The continuity of the temperature and temperature gradient at the mush-liquid interface during steady solidification is a consequence of the liquidus relation and the condition of marginal equilibrium (Worster 1986). See Schulze and Worster (2005) for a more general discussion of the boundary conditions at the mush-liquid interface.

We also consider the limit $Da \to \infty$, where no supersaturation of dissolved gas can be tolerated. Hence, instead of solving equation (2.4.3), we have

$$\omega = \min\left[1, \frac{(1-\Phi)\omega_\infty}{\phi_l - \Phi}\right], \tag{2.4.21}$$

where the concentration of dissolved gas in a subsaturated region is determined by applying equation (2.4.14) with $\phi_g = w_g = 0$, and $w_l = -\Phi$ from equation (2.4.12).

2.4.6 Subsaturated region of the mushy layer

If the incoming far-field liquid is saturated or supersaturated with dissolved gas ($\omega_\infty \geq 1$), then freezing will drive gas exsolution throughout the mushy layer. However, if the incoming liquid is subsaturated ($\omega_\infty < 1$), then there will exist a subsaturated region of the mush, $z_L \leq z < z_G$, in which no gas exsolution occurs. Using equations (2.4.18), (2.4.14), (2.4.12), and (2.2.1) with $\phi_g = 0$ and $\omega(z_G) = 1$, we find a condition for z_G:

$$\theta(z_G) = \theta_G = -\frac{\mathcal{C}(1-\omega_\infty)}{\omega_\infty}, \quad \text{for} \quad \frac{\mathcal{C}}{\mathcal{C}+1} < \omega_\infty < 1, \tag{2.4.22}$$

where the latter constraint on ω_∞ ensures that $-1 < \theta_G < 0$ lies within the range of temperatures in the mushy region. If $\omega_\infty < \mathcal{C}/(\mathcal{C}+1)$, the entire mushy layer will remain subsaturated and no gas exsolution will occur. Integrating equation (2.4.5) twice and using the boundary conditions $\theta(z_L) = 0$ and equation (2.4.20), the thickness of the subsaturated region is

$$z_G - z_L = \frac{1}{\theta_\infty(1-\Phi)} \int_{\theta_G}^{0} \frac{1}{1 - \frac{\theta}{\theta_\infty}\left(1 + \frac{St}{\mathcal{C}-\theta}\right)} \, \mathrm{d}\theta. \tag{2.4.23}$$

2.4.7 Reduced model for $\phi_g \ll 1$

We now introduce two approximations that greatly simplify the model above to yield a reduced "tracer" model that is likely to be valid for many systems of interest. This reduced model consists of the standard conservation equations for a two-phase mushy layer that are decoupled from the gas phase with an extra conservation equation for the gas. Firstly, we assume that the gas phase is essentially incompressible by setting $\psi = 1$. To justify this assumption, we re-write equation (2.4.11) to leading order in θ/θ_K as

$$\psi \approx \left(1 - \frac{\theta}{\theta_K}\right)\left(1 + \frac{p_l - p_0}{p_0} + La\right). \tag{2.4.24}$$

Neglecting variations in the pore pressure compared with the atmospheric pressure, i.e., $(p_l - p_0)/p_0 \approx 0$, we find that ψ is determined by thermal contraction and the Laplace pressure jump, which combined lead to less than a 10% variation in ψ in the mushy layer for the parameter values in table 2.1 (figure 2.4f). Note that the impact of the Laplace pressure on the gas density can become significant for smaller bubbles since $La \propto R_B^{-1}$. For sea ice, the size distribution of bubbles has been measured by Light et al. (2003) and Crabeck et al. (2016), in which the smallest scales resolved were 10 µm and 97 µm, respectively. Bubbles were observed with radii between these resolution limits and approximately 1 mm. Motivated by these observations, we focus on bubbles with radii in the micron to millimetre range, such that $La \ll 1$ for all but the smallest bubbles.

Secondly, we assume that the gas phase occupies only a small volume fraction, i.e., $\phi_g \ll 1$. This assumption is reasonable when the gas dissolved in the incoming liquid occupies only a small volume fraction upon exsolution, $\chi\omega_\infty \ll 1$ (with the parameters in table 2.1 yielding $\chi\omega_\infty = 0.029$). In this case, equation (2.4.15) yields $\Phi \approx \chi\omega_\infty \ll 1$ at leading order. Since Φ is the maximum gas fraction achieved in the system, we conclude that $\phi_g \leq \Phi \ll 1$ when $\chi\omega_\infty \ll 1$. Using equation (2.4.12), we then find that $w_l = O(\chi\omega_\infty)$ and thus neglect the liquid flow driven by gas exsolution by setting $w_l = 0$. Since $\phi_g \ll 1$, we also take $\phi_s + \phi_l = 1$, neglecting the small volume occupied by the gas phase.

Approximating equation (2.4.18) for $\Phi \approx \chi\omega_\infty \ll 1$ yields

$$\phi_s = -\frac{\theta}{\mathcal{C} - \theta}. \tag{2.4.25}$$

The ϕ_g and w_g terms are retained in equation (2.4.14) since they are divided by the small parameter χ, which with equations (2.4.9) and (2.4.25) yields

$$\phi_g = \frac{\chi}{(1 + V_g)} \left[\omega_\infty - \frac{\omega \mathcal{C}}{\mathcal{C} - \theta} \right]. \tag{2.4.26}$$

We take $w_l = 0$ in equation (2.4.3) to obtain

$$\frac{\mathrm{d}}{\mathrm{d}z}(\omega \phi_l) = -Da\,\mathcal{N}. \tag{2.4.27}$$

In the limit $Da \to \infty$, we instead approximate equation (2.4.21) for $\Phi \ll 1$ as

$$\omega = \min\left(1,\, \omega_\infty / \phi_l\right). \tag{2.4.28}$$

We note that in the infinite Damköhler number case, no additional differential equation is required since ϕ_g and ω can be determined from equations (2.4.26) and (2.4.21), respectively. Finally, setting $\zeta_s = \nu_s = 1$ and $\varepsilon = w_l = \nu_g = 0$ in equation (2.4.5) yields

$$\frac{\mathrm{d}\theta}{\mathrm{d}z} = St \frac{\mathrm{d}\phi_s}{\mathrm{d}z} + \frac{\mathrm{d}^2\theta}{\mathrm{d}z^2}. \tag{2.4.29}$$

To solve this reduced model, we solve equations (2.4.27) and (2.4.29) numerically in the mushy layer, using equations (2.4.25) and (2.4.26) (see appendix C) subject to $\theta(0) = -1$, $\theta(z_L) = 0$ and $\omega(z_L) = \omega_\infty$, where z_L is determined by

$$\frac{\mathrm{d}}{\mathrm{d}z}\theta(z = z_L^+) = -\theta_\infty, \tag{2.4.30}$$

which is equation (2.4.20) under the approximation $\Phi \ll 1$.

In this reduced model, the equations for conservation of heat and salt reduce to standard relations for the solid fraction (equation 2.4.25) and temperature (equation 2.4.29) of a two-phase mushy layer with $\phi_s + \phi_l = 1$ (Worster 1992). However, we retain the ability to evolve the small gas volume fraction ϕ_g as a tracer. This is valuable because extra equations describing the gas phase can be added to existing two-phase mushy-layer models without modification of the original equations and numerical methods.

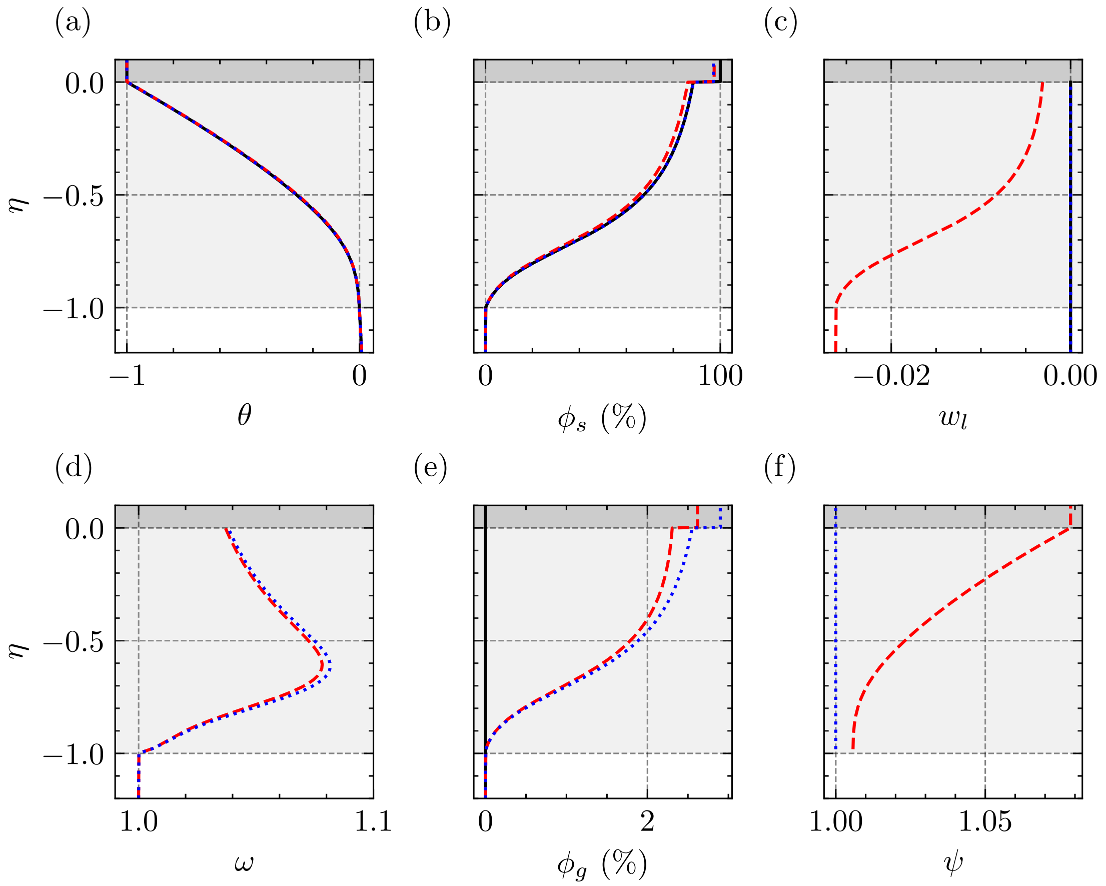

Figure 2.4: Solution profiles as a function of scaled height $\eta = z/(-z_L)$ for a steady mushy layer, as described in §2.4. We compare results for the freezing of saltwater with no dissolved gas ($\omega_\infty = 0$; solid black curves in panels a, b, c and e) and the freezing of saltwater saturated with dissolved gas ($\omega_\infty = 1$) from the full model (dashed red curves) and the reduced model (dotted blue curves; see §2.4.7). Parameter values are otherwise as reported in table 2.1.

2.5 Results

Figure 2.4 illustrates the solution of the system described in §2.4 in the scaled domain $\eta = z/(-z_L)$, so that the steady mushy layer occupies $-1 < \eta < 0$. We contrast the steady solutions for the freezing of saltwater with no dissolved gas ($\omega_\infty = 0$; solid black curve) and saltwater saturated with dissolved gas ($\omega_\infty = 1$; dashed red curve). In the saturated case, we compare the full model (dashed red curve) with the reduced model derived in §2.4.7 (dotted blue curve). When $\omega_\infty = 0$, the steady problem is equivalent to the directional solidification of a two-phase mushy layer as analysed by Worster (1992). Heat removal at the cold heat exchanger ($\eta = 0$) is balanced by upward advection of warm fluid from the far field and by the latent heat of freezing in the mushy layer. This balance yields a steady temperature profile in the mushy layer that decreases monotonically from $\theta = 0$ at $\eta = -1$ to $\theta = -1$ at $\eta = 0$ (figure 2.4a). Because $\rho_s = \rho_l$, there is no liquid flow through the mushy layer in the absence of gas, $w_l = 0$ (figure 2.4c). When the incoming liquid is saturated with dissolved gas, $\omega_\infty = 1$, gas exsolution reduces the effective heat capacity and thermal conductivity of the mush and induces a liquid flow that advects colder liquid downward (see equation 2.4.5). Comparison with the reduced model, in which all of these effects are neglected, suggests that none of them have a significant impact on the temperature profile (figure 2.4a).

Within the mushy layer, the solid fraction increases upwards, reaching a maximum value of $\phi_s(0^-) = 0.88$ when $\omega_\infty = 0$ (figure 2.4b; equation 2.4.18). At the boundary with the eutectic region ($\eta = 0$), any remaining liquid in the mushy layer freezes, the solid fraction jumps discontinuously to $\phi_s = 1$, and the dissolved salt precipitates as solid crystals of hydrohalite. The solid fraction toward the top of the mushy layer is slightly smaller when $\omega_\infty = 1$ than in the case without gas ($\omega_\infty = 0$) due to the volume occupied by exsolved gas bubbles in the full model (dashed red curve in figure 2.4b). This effect is neglected in the reduced model (dotted blue curve in figure 2.4b). The solid-fraction profile adjusts to maintain local thermal equilibrium via salt rejection during freezing, modifying the liquid salinity in order to satisfy the liquidus relation for a given temperature. The solid fraction is controlled by the dimensionless concentration ratio $\mathcal{C}$. In figure 2.4, we use a value of $\mathcal{C}$ appropriate for freezing seawater (table 2.1). This value lies between the extreme low-salinity ($\mathcal{C} \to 0$) and high-salinity ($\mathcal{C} \to \infty$) cases, which are investigated further in §2.5.1.

When $\omega_\infty = 1$, the concentration of dissolved air in the mushy layer is driven above the saturation concentration by freezing, and bubbles of free gas exsolve within the mushy layer (figure 2.4e). The concentration of dissolved gas reaches a maximum supersaturation before decreasing upward in the mushy layer as dissolved gas is converted to bubbles (figure 2.4d). The reduced model slightly overestimates the peak supersaturation achieved in the liquid (dotted blue curve in figure 2.4d) because this model neglects the downward liquid flow driven by gas exsolution, which would otherwise advect some dissolved gas out of the mushy layer. The bubble radius is larger than the pore radius in figure 2.4 ($\delta_0 > 1$), so there is no buoyant motion of gas bubbles.

At $\eta = 0$, all remaining liquid freezes and all remaining dissolved gas exsolves, such that the liquid fraction jumps discontinuously to $\phi_l = 0$ and the gas fraction jumps discontinuously to $\phi_g = \Phi$, as determined by equation (2.4.15). The reduced model slightly overestimates the gas fraction in the upper, colder portion of the mushy layer and in the solid region, because thermal contraction of the gas phase and advection of some dissolved gas out of the mushy layer are both neglected.

Figure 2.4 shows that the reduced model reproduces the temperature, solid fraction, dissolved gas concentration and gas fraction profiles of the full model reasonably well, despite neglecting variations in gas density and the liquid flow driven by gas exsolution. This liquid flow is around two orders of magnitude smaller than the pulling speed ($V = 1\,\mu\mathrm{m\,s^{-1}}$), or about $0.02\,\mu\mathrm{m\,s^{-1}}$ in dimensional terms, which is unlikely to be consequential in sea ice where other processes drive larger liquid flows. For example, laboratory experiments have shown that unstable salinity gradients in growing sea ice can drive upwelling convective velocities of around $10\,\mathrm{cm\,day^{-1}}$, or $1.16\,\mu\mathrm{m\,s^{-1}}$ (Eide and Martin 1975). The same convection mechanism has been found to drive downwelling brine plumes at the base of Arctic sea ice with velocities of around $2\,\mathrm{cm\,s^{-1}}$ (Peterson 2018).

It is possible to produce around a 10% error in the solid fraction obtained from the reduced model compared with the full model by increasing χ to $\chi = 0.1$, which corresponds to increasing the solubility of gas in the liquid. In this case, a larger volume of gas is exsolved that drives a larger liquid flow out of the mushy layer, which has a stronger advective feedback on salt and dissolved gas within the mushy layer. However, in this case the volume fraction of exsolved gas becomes comparable to the porosity of the mushy layer just below $\eta = 0$ and so our assumption that free-phase gas resides in disconnected bubbles may no longer hold. Therefore, in the remainder of this chapter, we investigate the distribution of gas bubbles in a

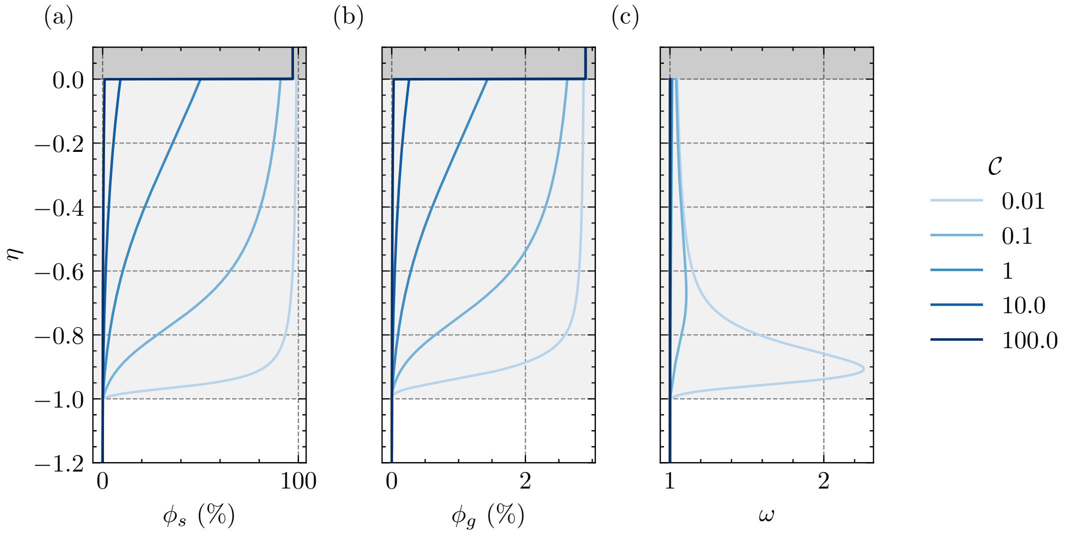

Figure 2.5: Vertical profiles of (a) solid fraction ϕ_s, (b) gas fraction ϕ_g, and (c) dissolved air concentration ω for a steady three-phase mushy layer from the reduced model (§2.4.7) for several values of C in the range $0.01 \leq \mathcal{C} \leq 100$ (increasing from light to dark blue line colours). Parameter values are otherwise as reported in table 2.1.

steadily solidifying mushy layer using the reduced model. The reduced model is computationally simpler, does not require modifying the governing equations for a two-phase mushy layer, and is likely to be valid for values of χ corresponding to the typical solubility of air in seawater.

2.5.1 Impact of the concentration ratio on the three-phase mushy layer

We next use the reduced model to explore how the concentration ratio $\mathcal{C}$ impacts the solid-fraction structure and resulting gas distribution within a three-phase mushy layer (figure 2.5). For a low-salinity mushy layer ($\mathcal{C} \ll 1$), freezing is focused primarily in a thin region near the mush-liquid interface, $\eta = -1$ (figure 2.5a). This focusing drives a rapid increase in dissolved gas concentration near $\eta = -1$. Since $Da \gg 1$, the supersaturation here is rapidly converted to gas bubbles (figure 2.5b). The result is a mushy layer with several percent volume fraction of bubbles present over most of the depth after this initial boundary region.

In contrast, a high-salinity mushy layer ($\mathcal{C} \gg 1$) has low solid fraction throughout (figure 2.5a), with freezing focused almost entirely at the eutectic boundary ($\eta = 0$). Therefore, there is little internal solidification to substantially elevate the

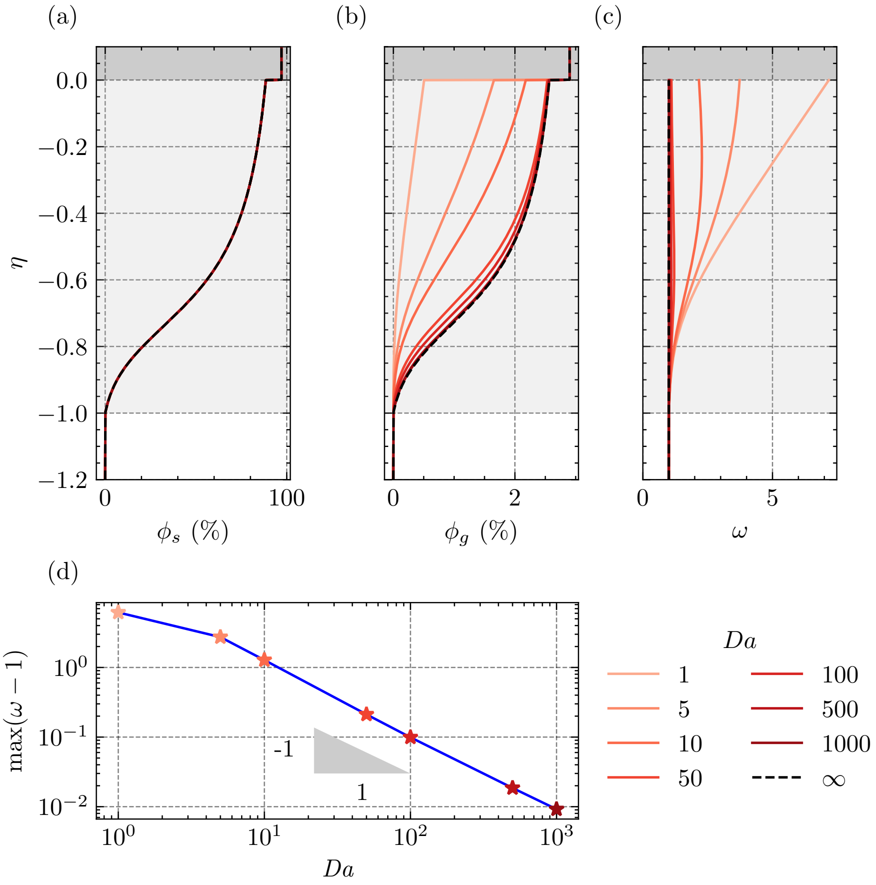

Figure 2.6: Vertical profiles of (a) solid fraction ϕ_s, (b) gas fraction ϕ_g, and (c) dissolved air concentration ω for a steady three-phase mushy layer from the reduced model (§2.4.7). Results are shown for several values of Da in the range $1 \leq Da \leq 1000$ (increasing light to dark red line colours). Parameter values are otherwise as stated in table 2.1. The case $Da = \infty$ is computed separately using equation (2.4.28) (dashed black). (d) The maximum supersaturation in the mushy layer $\max_{-1<\eta<0} [\omega(\eta) - 1]$ versus Da.

concentration of dissolved gas. The resulting mushy layer mostly has a very low volume fraction of gas bubbles until reaching the eutectic temperature.

2.5.2 Impact of gas exsolution rate

The rate of gas exsolution is controlled by the Damköhler number Da. The value of this parameter is poorly constrained for geophysical settings, such as the air-water-ice system, so we use the reduced model to investigate the steady three-phase mushy layer for a wide range of Da values (figure 2.6).

For low $Da \lessapprox 10$, the gas volume fraction initially grows slowly with distance from the mush-liquid interface as supersaturation increases, before increasing roughly linearly from $\eta = -0.8$ to $\eta = 0$ (figure 2.6b). In this case, the timescale for gas exsolution is comparable with the timescale over which the mushy layer is freezing. The interstitial liquid is increasingly supersaturated with dissolved air (figure 2.6c) and the increase in gas fraction over the mushy layer is limited by the kinetics of gas exsolution.

For high $Da \gtrapprox 50$, the gas fraction profiles mirror the solid fraction profiles and collapse toward the solution for $Da \to \infty$ (figure 2.6a). In this case, gas exsolution is fast compared with the generation of supersaturation by freezing and so the increase in gas fraction is limited by the increase in solid fraction. The resulting mushy layer has a concentration of dissolved gas close to saturation throughout (figure 2.6c).

Figure 2.6d shows that the maximum degree of supersaturation in the mushy layer is inversely proportional to Da when $Da \geq 10$. For $Da < 10$, the concentration of dissolved gas in the mushy layer increases monotonically with η and does not reach a local maximum. A least-squares fit to the points with $Da \geq 10$ yields

$$\max_{-1<\eta<0} [\omega(\eta) - 1] = m_0 Da^{m_1} \quad \text{for} \quad Da \geq 10, \tag{2.5.1}$$

where $m_0 = 14.34$ and $m_1 = -1.070$. Physically, this maximum supersaturation is achieved at the point where the production of supersaturation by freezing is balanced by the exsolution of dissolved gas. In appendix D, we use equation (2.4.27) with $Da \gg 1$ to justify $m_1 = -1$ on theoretical grounds.

2.5.3 Conditions for gas-bubble mobility

We next use the reduced model to investigate the impact of the dimensionless bubble size $\delta_0 = R_B/R_0$ on the gas-fraction distribution in a steadily growing three-phase mushy layer. Figure 2.7 shows the solid fraction ϕ_s, gas fraction ϕ_g, and vertical gas flux w_g for $0.005 \leq \delta_0 \leq 1$. We include results for $Da = 500$ (figures 2.7a–c) and $Da = 5$ (figures 2.7d–f) as representative of high-Da and low-Da behaviour, respectively. For $\delta_0 \geq 1$, the exsolved bubbles are always larger than the pore-throat radius within the mush and are therefore immobile throughout the entire mushy

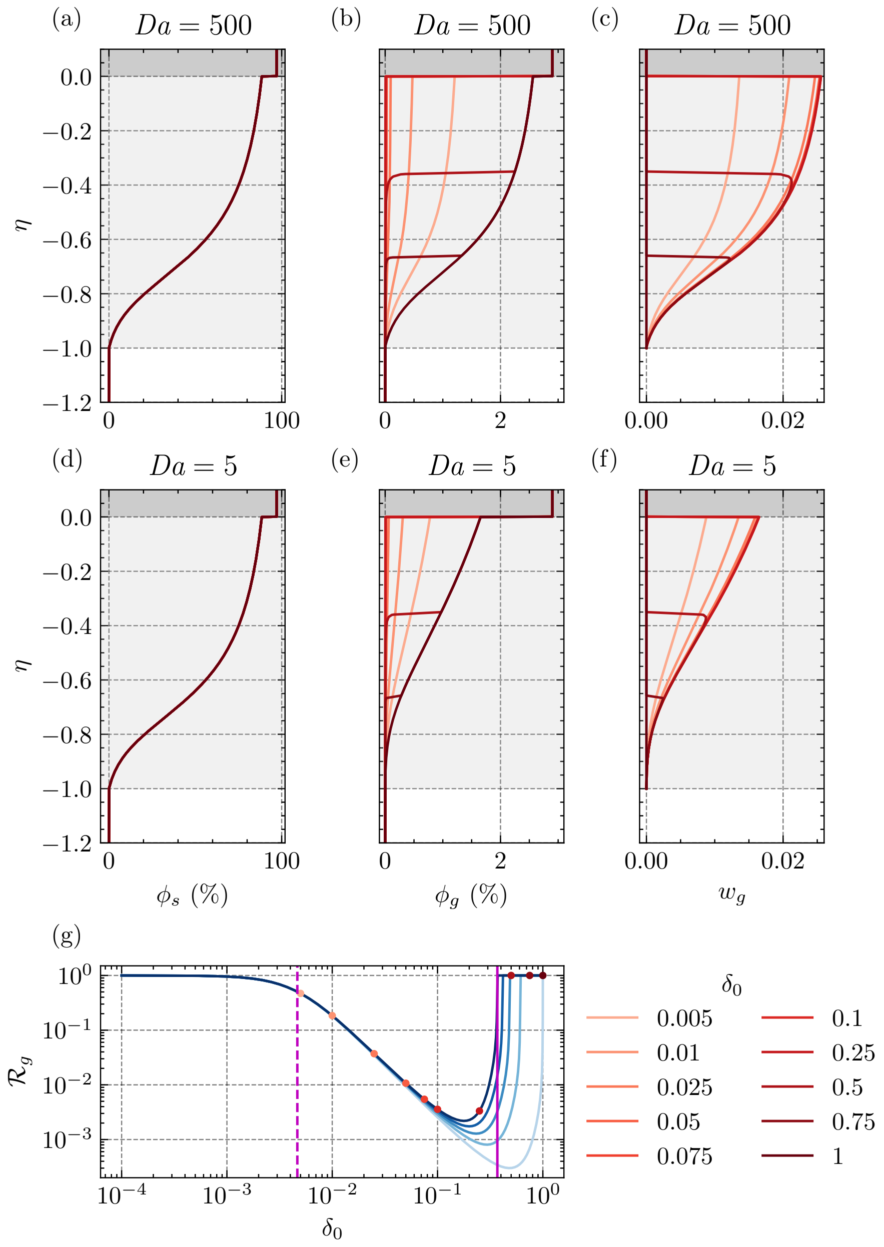

Figure 2.7: Vertical profiles of (a,d) solid fraction ϕ_s, (b,e) gas fraction ϕ_g, and (c,f) vertical gas flux w_g in a steady three-phase mushy layer from the reduced model (§2.4.7). We show curves for several values of δ_0 in the range $5 \times 10^{-3} \leq \delta_0 \leq 1$ (increasing light to dark red coloured lines) for representative high $Da = 500$ (a)–(c), and low $Da = 5$ (d)–(f) cases. Parameter values are otherwise as stated in table 2.1. Panel (g) shows the ratio $\mathcal{R}_g$ (see equation 2.5.3) as a function of $\delta_0 = 1$ at $\eta = -1, -0.75, -0.5, -0.25, 0$ (increasing light to dark blue line colours). The coloured circles indicate the values of $\mathcal{R}_g$ at $\eta = 0$ for each simulated δ_0 ($Da = 5$ and $Da = 500$ are indistinguishable). The solid vertical purple line at $\delta_0 = \phi_l(\eta = 0^-)^q = 0.37$ shows the largest value of δ_0 that allows bubbles to migrate vertically over the entire mushy layer. The dashed vertical purple line at $\delta_0 = 1/\sqrt{\mathcal{B}}$ shows the value of δ_0 around which the vertical rise velocity of bubbles in the mushy layer is comparable to the freezing rate.

layer ($w_g = 0$). As a result, the gas-fraction profile for $\delta_0 = 1$ provides an upper bound on ϕ_g at each position at a particular value of *Da*.

For $\delta_0 < [\mathcal{C}/(\mathcal{C}+1)]^{1/q} = 0.37$, bubbles are sufficiently small to be able to migrate vertically throughout the mushy layer. This threshold is calculated from equation (2.3.7) using the minimum porosity at the mush-eutectic interface, $\phi_l(\eta = 0^-) = \mathcal{C}/[\mathcal{C}+1]$, determined from equation (2.4.25) with $\theta(\eta = 0^-) = -1$.

For $0.37 < \delta_0 < 1$, the exsolved bubbles are initially small enough to migrate vertically until they reach a colder part of the mushy layer where the pore throats are small enough that the bubbles become trapped (i.e., $\delta = 1$). The intermediate bubble sizes shown in figure 2.7, $\delta_0 = 0.75$ and $\delta_0 = 0.5$, exhibit a region of low ϕ_g in the lower portion of the mushy layer, from which bubbles have migrated upward, and a region of high ϕ_g in the upper portion of the mushy layer, where migrating bubbles become trapped by smaller pore throats. This natural segregation of the mushy layer into a relatively gas-poor lower portion and a relatively bubbly (i.e., gas-rich) upper portion was observed experimentally during steady freezing of saltwater in a Hele-Shaw cell (Peppin et al. 2007). However, we note that an experiment with water that is subsaturated with dissolved air would also produce a similar segregation of gas within the mushy layer (see §2.4.6).

We quantify the impact of δ_0 on ϕ_g within the mushy layer via the ratio $\mathcal{R}_g$ of the gas fraction for that value of δ_0 to the gas fraction when $\delta_0 = 1$ with other parameters held fixed,

$$\mathcal{R}_g(\eta,\, \delta_0) \equiv \frac{\phi_g(\eta;\, \delta_0)}{\phi_g(\eta;\, \delta_0 = 1)}. \tag{2.5.2}$$

In the reduced model (§2.4.7), the profiles of ω and θ do not depend on δ_0 and equation (2.4.26) yields

$$\mathcal{R}_g(\eta,\, \delta_0) = \begin{cases} \left[1 + \dfrac{\mathcal{B}\delta_0^2}{K_1(\delta)}\right]^{-1}, & (1-\phi_s) > \phi_c \\ 1, & (1-\phi_s) \le \phi_c \end{cases}, \quad \text{where} \quad \delta = \frac{\delta_0}{[1-\phi_s(\eta)]^q}. \tag{2.5.3}$$

Note that $\delta_0 \geq 1$ implies $\delta \geq 1$, in which case $1/K_1(\delta) = 0$ from equation (2.3.6). The dependence on ϕ_c is shown in equation (2.5.3) for completeness but is not relevant for the results shown in figure 2.7 since $1 - \phi_s > \phi_c$ throughout the mush.

Figure 2.7g shows that $\mathcal{R}_g$ decreases from 1 to a minimum value as δ_0 becomes smaller than the threshold value for bubble motion determined by equation (2.3.7). Gas bubbles with radii in the range $0.01 < \delta_0 < 0.37$ are able to efficiently transport gas from the mushy layer to the eutectic region, resulting in substantially lower gas fractions within the mushy layer compared to the case of trapped bubbles (with $\delta_0 = 1$). This observation is supported by the results for $0.025 \leq \delta_0 \leq 0.25$, which all exhibit significantly lower gas fractions compared with the case when $\delta_0 = 1$ (figures 2.7b and 2.7e). As δ_0 decreases further, $\mathcal{R}_g$ increases back toward unity as bubble motion becomes slower compared to the pulling speed V. Results with $\delta_0 \leq 0.01$ show larger gas volume fractions within the mush (figures 2.7b and 2.7e). The dimensionless bubble radius $\delta_0 = 1/\sqrt{\mathcal{B}} \approx 0.005$ (dashed purple line in figure 2.7g) yields $\mathcal{R}_g \approx \frac{1}{2}$ since $K_1 \approx 1$ for $\delta_0 \ll 1$.

In summary, large gas fractions are observed throughout the mush when bubbles are large and trapped ($\delta_0 \geq 1$), or when bubbles are so small that they rise slowly compared to the freezing rate ($\delta_0 \ll 1/\sqrt{\mathcal{B}}$). Bubbles of intermediate size are able to rapidly rise, leaving lower portions of the mush relatively depleted of free-phase gas until they encounter a region of higher solid fraction or the eutectic boundary.

2.6 Discussion & conclusions

We have extended the continuum theory for a solid–liquid mushy layer to include an additional dissolved gas component and a free gas phase. Using a simplified model of mushy-layer pore-geometry, we derived a novel expression for the vertical gas flux due to buoyant bubble motion. This model predicts a porosity threshold (equation 2.3.7) for vertical bubble motion in terms of the ratio $\delta_0 = R_B/R_0$ of the bubble radius to the pore-throat radius in contrast to past models that relied on ad-hoc empirical thresholds (Moreau et al. 2014; Moreau et al. 2015b; Moreau et al. 2015a). We applied the model to the geophysically relevant sea-ice system using empirical expressions for the pore-throat radius in sea ice derived from X-ray CT measurements.

We analysed the model in the context of steady mushy-layer growth in a Hele-Shaw cell, which is a standard model problem for mushy-layer theories (Peppin et al. 2007; Chiareli and Worster 1995; Worster 1992). Internal solidification in the mushy layer elevates the concentration of dissolved gas in the liquid, which drives exsolution of gas bubbles. The resulting volume change drives a small liquid flow out of the mushy layer, which we have shown has a negligible impact on heat and solute transport for the steady freezing of seawater. We derived a significantly simpler reduced model that neglects this volume change, as well as variations in the gas density and the impact of the gas phase on the effective thermal and hydraulic properties. These simplifications are reasonable for systems with low gas solubility and where gas density does not vary significantly, and thus may prove useful for describing gas exsolution and transport in geophysically relevant three-phase mushy layers such as sea ice. Because the reduced model regains the same equations for the conservation of heat and salt within the mushy layer, existing two-phase mushy-layer models can be extended to include gas exsolution without major modification.

We have identified two dimensionless parameters that control the distribution of gas bubbles within the mushy layer, the Damköhler number Da and the dimensionless bubble radius δ_0. The Damköhler number quantifies the timescale of bubble exsolution relative to the timescale for thermal diffusion and controls the amount of gas exsolution. Gas exsolution is slow for $Da \ll 1$, resulting in a highly supersaturated mushy layer with low gas fraction. In contrast, available supersaturation is rapidly converted to gas bubbles for $Da \gg 1$, resulting in a mushy layer with low supersaturation and high gas fraction. The ratio of the bubble radius to the characteristic pore throat radius δ_0 determines whether and where bubbles are able to migrate vertically, which is of key concern for the transport of gas species in natural mushy-layer systems. We have identified three distinct regimes in this regard, when bubbles are either: (1) immobile throughout the mush, (2) mobile in regions of the mush above a critical porosity, or (3) mobile throughout the mush. The intermediate case produces a distribution of bubbles within the mushy layer that is qualitatively consistent with observations of directional freezing of saltwater in laboratory experiments (Peppin et al. 2007).

The model presented here can be used to investigate the impact of gas bubbles on bulk properties and chemical transport in mushy systems. The model is well-suited to describe the sea-ice system (Feltham et al. 2006), but could be adapted to investigate magmatic systems (Huppert and Worster 2012) or other three-phase mushy layers. Future work could investigate gas exsolution and transport during the transient growth and melt of a mushy layer, more akin to the seasonal growth and melt of first-year sea ice.

In natural settings, it is likely that the gas phase would be composed of multiple chemical species with differing solubilities, which may take part in chemical reactions within the mushy layer (Tison et al. 2017). Furthermore, the solubility of dissolved gases in the liquid phase around a bubble is proportional to the partial pressure of the gas at the gas–liquid interface (see §18.1.3 of Tison et al. 2017, for example). This pressure dependence is neglected in our model, but it may be important for small bubbles with $La > 1$, which may tend to redissolve into the liquid phase, or for bubbles trapped in disconnected liquid inclusions that are not considered here (Crabeck et al. 2019).

In reality, the geometry of the pore-space microstructure and the sizes and shapes of the gas bubbles are complex and both spatially and temporally non-uniform (Light et al. 2003). For simplicity, the polydispersity of gas bubble sizes in sea ice was neglected in our model. The tortuosity of the pore space as well as the growth, merging, and breakup of gas bubbles may all play a role in the transport of gas species within the mushy layer. Gas bubbles can accumulate below low porosity regions of the mushy layer where ϕ_g can become comparable to $1 - \phi_s$, violating the assumptions of the reduced model. For mushy layers with larger gas volume fractions, the gas phase may become connected and would need to be described using multiphase theories for gas–liquid flow in a porous medium (see Blunt 2017, for example). The assumption that ϕ_g smoothly varies across an REV may also become less accurate for larger gas bubbles. However, we believe that the simplifications in this chapter provide physical insight on the importance of the sizes of gas bubbles in a mushy layer compared with the pore-geometry scale for mushy layers where the free gas phase resides in isolated bubbles. Finally, we have revealed the importance of the Damköhler number, which is poorly constrained in geophysical settings, and may depend on the timescales associated with other processes known to occur in mushy layers but not modelled here, such as convection driven by unstable density profiles produced during freezing (Anderson and Guba 2020).

3

A one-dimensional transient three-phase mushy-layer model for sea ice

3.1 Introduction

In this chapter, we use the conservation equations for a three-phase mushy layer derived in chapter 2 to model the transient evolution of three-phase sea ice. In what follows, we refer to a gaseous additional phase that is relevant to the solidification of a saltwater ocean containing dissolved atmospheric gases. In chapter 8, we modify this model to instead describe oil droplets in sea ice.

Here, we consider the solidification of a horizontally uniform ocean containing dissolved salt and atmospheric gases with an overlying atmosphere, snow cover (if present), and surface melt pond (if present) and an underlying ocean (see figure 3.1). In §3.2, using the reduced "tracer" model of a three-phase mushy layer described in chapter 2 as a starting point, we additionally account for turbulent mixing in the ocean (and melt pond) using an eddy diffusivity parameterisation, the absorption of shortwave radiation, brine convection within the ice, heat transport through any snow cover, and the atmospheric heat flux, which are necessary to accurately model sea ice in a geophysical setting. We introduce characteristic scales to obtain a system of dimensionless partial differential equations (PDEs) that determine the evolution of the system. In the limit of instantaneous exsolution and dissolution of gas (i.e., $Da \to \infty$), we combine the conservation equations for dissolved and free-phase gas to obtain a single equation for the bulk gas content. In §3.3, we introduce the so-called enthalpy method to determine expressions for the temperature, liquid salinity, liquid fraction, and solid fraction in terms of the bulk enthalpy and salinity. This approach has been used previously to simulate first-year sea ice (Parkinson

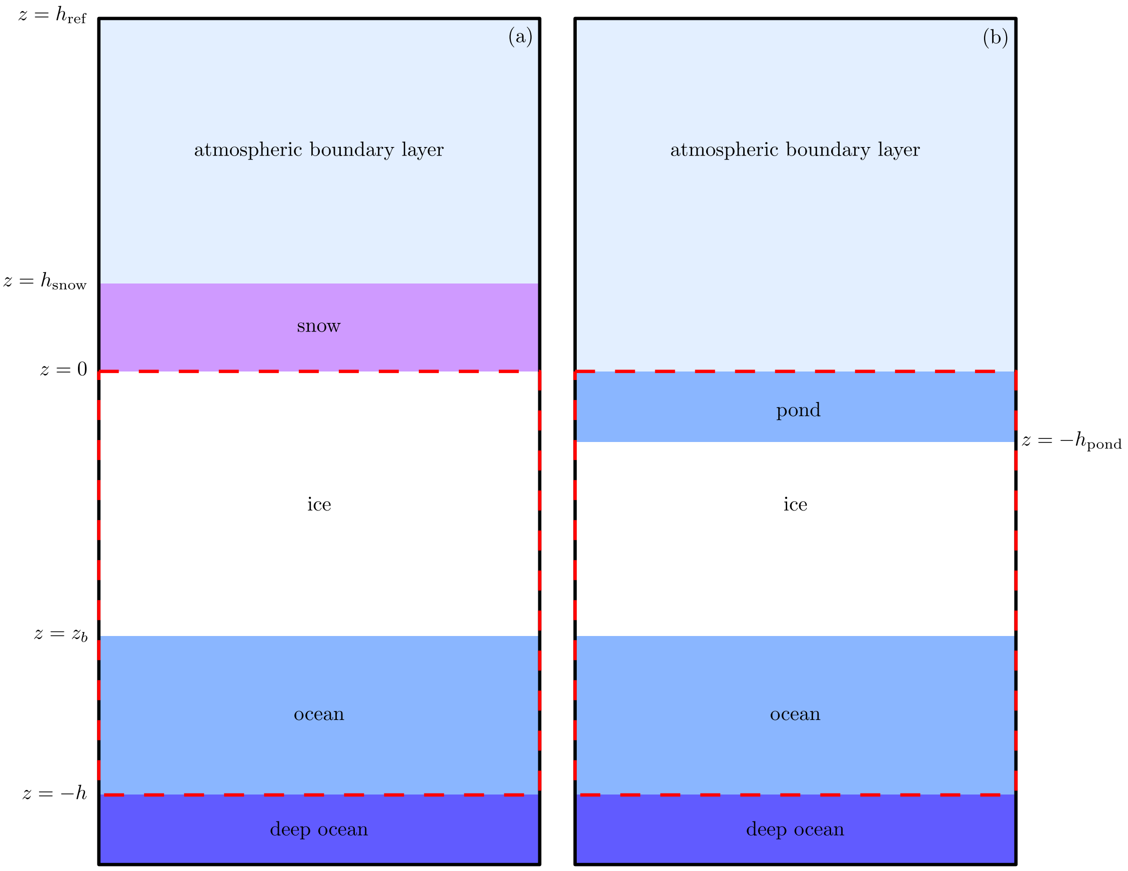

Figure 3.1: Schematic diagram of the one-dimensional domain for the transient model for (a) snow-covered ice and (b) ponded ice. Conservation equations for heat, salt, and gas are solved in the region $-h < z < 0$ (dashed red box), which contains an ocean (pure liquid), a layer of porous sea ice, and potentially an overlying liquid melt pond $-h_{\text{pond}} < z < 0$ if the ice surface melts. Heat flux to the domain from the atmospheric boundary layer (through a snow layer, if present) is used to provide a heat-flux boundary condition at $z = 0$. The heat flux, salinity and dissolved gas concentration in the deep ocean are used to provide boundary conditions at $z = -h$.

2019) and allows the associated conservation equations to be solved numerically without explicitly tracking the positions of the interfaces between the solid, liquid, and mushy phases. In §3.4, we describe appropriate boundary conditions at the lower boundary (with the deep ocean) and upper boundary (with the snowpack or atmosphere). The chapter is summarised in §3.5.

3.2 Model

In chapter 2, we derived a reduced “tracer” model appropriate for a mushy layer that contains a small volume fraction of incompressible gas. The reduced model involves three key approximations:

1. The volume fraction of free-phase gas is small $\phi_g \ll 1$, such that $\phi_s + \phi_l \approx 1$ and the gas phase can be treated as a passive tracer.

2. Variations in the density of the gas phase are small, such that the free-gas phase can be treated as approximately incompressible with constant density ρ_g.

3. The solid and liquid phase are of equal and constant density, $\rho_s = \rho_l$. Note that density variations in the liquid phase due to thermal and salinity gradients are here retained where they drive a convective flow (i.e., the Boussinesq approximation as in Worster 1997).

3.2.1 Conservation equations

Under the approximations of the reduced model, the five conservation equations (2.2.6)–(2.2.9) and (2.2.13) for water, salt, dissolved gas, free-phase gas, and energy, respectively, become

$$\nabla \cdot \boldsymbol{u}_l = 0, \tag{3.2.1}$$

$$\frac{\partial}{\partial t}\left(\phi_s S_s + \phi_l S_l\right) + \nabla \cdot \left(S_l \boldsymbol{u}_l\right) = \nabla \cdot \left(\phi_l D_S \nabla S_l\right), \tag{3.2.2}$$

$$\frac{\partial}{\partial t}\left(\rho_l \phi_l \xi_l\right) + \nabla \cdot \left(\rho_l \xi_l \boldsymbol{u}_l\right) = \nabla \cdot \left(\rho_l \phi_l D_\xi \nabla \xi_l\right) - N, \tag{3.2.3}$$

$$\frac{\partial}{\partial t}\left(\rho_g \phi_g\right) + \nabla \cdot \left(\rho_g \boldsymbol{u}_g\right) = N, \tag{3.2.4}$$

and

$$\frac{\partial H}{\partial t} + \nabla \cdot \left(H_l \boldsymbol{u}_l\right) = \nabla \cdot \left(\rho_l c_{p,l} D_H \nabla T\right) + Q_{\mathrm{SW}}, \tag{3.2.5}$$

where we have made three modifications to model sea ice in a geophysical setting.

Firstly, we have stated conservation of energy in terms of the bulk enthalpy

$$H = \phi_s H_s + \phi_l H_l, \tag{3.2.6}$$

where $H_l = \rho_l c_{p,l}(T - T_i)$, $H_s = \rho_s c_{p,s}(T - T_i) - \rho_s L$, T_i is the freezing temperature of seawater, and the specific heat capacities $c_{p,l}$, $c_{p,s}$ and latent heat of fusion L are assumed to be constant. See appendix A for more details. Writing the conservation of energy in terms of the bulk enthalpy allows us to leverage the enthalpy method to solve the conservation equations computationally without explicitly tracking the boundaries between different phases in the system (see §3.3).

Secondly, the diffusive terms in equations (3.2.2), (3.2.3), and (3.2.5) now involve the effective diffusivities D_S, D_ξ, and D_H respectively, which parameterise the effect of turbulent mixing in purely liquid regions as well as molecular diffusion. In chapter 2, we considered the growth of a mushy layer into a quiescent liquid in a Hele-Shaw cell where turbulent mixing was not important. However, the turbulent mixing of heat and solutes in the ocean and any melt ponds is an important extra consideration for sea ice in the natural environment. We adopt a common approach to model turbulent mixing and introduce an extra eddy diffusivity term to the effective diffusivities

$$D_S = \phi_l \kappa_S + \kappa_\varepsilon \mathsf{H}(\phi_l - 1), \tag{3.2.7}$$

$$D_\xi = \phi_l \kappa_\xi + \kappa_\varepsilon \mathsf{H}(\phi_l - 1), \tag{3.2.8}$$

and

$$D_H = \frac{\overline{k}}{\rho_l c_{p,l}} + \kappa_\varepsilon \mathsf{H}(\phi_l - 1), \tag{3.2.9}$$

where κ_ε is the eddy diffusivity, and $\overline{k} = \phi_s k_s + \phi_l k_l$ is the phase-averaged thermal conductivity. See appendix E for further explanation of the eddy diffusivity parameterisation. The unit step function

$$\mathsf{H} = \begin{cases} 1 & x \geq 0 \\ 0 & x < 0 \end{cases}, \tag{3.2.10}$$

ensures eddy diffusion occurs only in purely liquid parts of the domain where $\phi_l = 1$.

Finally, we have added the absorption of shortwave radiation Q_{SW} as a source term in equation (3.2.5). We neglected this term in chapter 2 because we focussed on the solidification of a mushy layer in a laboratory setting. However, the absorption of shortwave radiation is a significant source of surface and internal melting during summer for sea ice in the natural environment. Shortwave radiation has wavelengths in the range 300–3000 nm, originates from the sun, and is refelected, transmitted, and absorbed by the ice, snow, and ocean. A two-stream model for the propagation and absorption of shortwave radiation in the snow-ice-ocean system is introduced in chapter 4.

Bubble motion

In chapter 2, we derived a novel expression for the vertical component of the volumetric gas flux $\boldsymbol{u}_g \cdot \boldsymbol{e_z}$ in sea ice as a function of porosity and bubble radius using an idealised model of the pore-geometry (see §2.3). For the steady problem considered in chapter 2, no bubbles were present in the liquid region and the effect of liquid flow through the pore space on the motion of gas bubbles was neglected. However, for the transient problem we make two ad-hoc extensions to the bubble transport term given by equation (2.3.5).

Firstly, we set $K_1 = 1$ for $\phi_l = 1$ so that bubbles in completely liquid regions of the domain rise with the Stokes terminal velocity for a bubble in an unbounded fluid. Secondly, we include the most general effect of liquid flow on gas bubble motion using a coupling tensor $\boldsymbol{G}$. This coupling tensor is an extension of the function $G(\delta)$, introduced in §2.3.2, that quantifies the drag due to the liquid flow in the vertical direction on a bubble in a tube. When $\phi_l = 1$, we assume that $\boldsymbol{G}$ is isotropic with diagonal components of magnitude $\mathcal{I}$. These extensions of equation (2.3.5) yield

$$\boldsymbol{u}_g = \begin{cases} 0 & \phi_l \leq \phi_c \\ \phi_g \left[\dfrac{\Delta \rho g R_0^2 \delta_0^2}{3\mu_l} \dfrac{\boldsymbol{e_z}}{K_1(\delta)} + \boldsymbol{G} \cdot \dfrac{2\boldsymbol{u}_l}{\phi_l} \right] & \phi_c < \phi_l < 1 \\ \phi_g \left[\dfrac{\Delta \rho g R_0^2 \delta_0^2}{3\mu_l} \boldsymbol{e_z} + 2\mathcal{I}\boldsymbol{u}_l \right] & \phi_l = 1 \end{cases}. \tag{3.2.11}$$

For gas bubbles, it is likely that buoyancy effects will dominate over viscous drag from the interstitial fluid. Therefore, going forward, we consider only the buoyant motion of gas bubbles in the ice and liquid by setting $\boldsymbol{G} = \boldsymbol{0}$ and $\mathcal{I} = 0$. Oil droplets in sea ice are much less buoyant than gas bubbles and so their advection by the liquid flow is more significant. Therefore, we will utilise a different $\boldsymbol{G}$ appropriate for oil droplets in chapter 8.

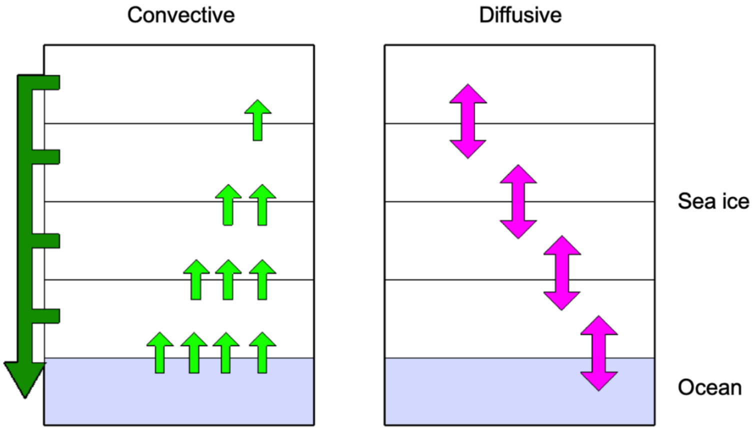

Figure 3.2: Schematic diagram illustrating the difference between diffusive (right) and convective (left) parameterisations of brine drainage in sea ice (reproduced from Thomas et al. 2020). In the diffusive parameterisation, the magenta arrows represent diffusive exchange of salt between adjacent layers of a computational sea ice model. In the convective parameterisation, in contrast, salt is advected upwards by an upwelling flow (light green arrows) and expelled from each layer of the ice downward to the ocean through brine channels (dark green arrow).

3.2.2 Brine convection

The dominant process that controls the transport of salt (and other dissolved species) during sea-ice growth is brine convection, also referred to as gravity drainage (Notz and Worster 2009). As temperatures decrease towards the ice surface ($z = 0$), the salinity of the interstitial brine increases due to the rejection of salt during freezing. This salinity gradient generates an unstable density profile in the pore fluid that, for sufficiently permeable ice, can drive an internal convective flow. The convective instability results in the formation of narrow brine channels through which cold, highly-saline brine is expelled downward to the underlying ocean. This focussed downwelling flow is balanced by a broad region of upwelling flow of seawater into the ice (Eide and Martin 1975; Worster 1997; Worster and Rees Jones 2015; Parkinson 2019; Wells et al. 2019). This process desalinates growing sea ice (Vancoppenolle et al. 2007; Notz and Worster 2009) and is also important for the exchange of dissolved gases (Zhou et al. 2013; Moreau et al. 2014) and other dissolved tracers (Vancoppenolle et al. 2010) between the ice and ocean.

Brine convection is a two/three-dimensional process, but a number of parameterisations have been developed to account for the impact of brine convection on sea-ice bulk salinity in one-dimensional models (see Thomas et al. 2020, for an overview).

Fundamentally, these parameterisations fall into two categories: convective and diffusive. Diffusive parameterisations (e.g., Vancoppenolle et al. 2010; Jeffery et al. 2011) exchange salt between adjacent portions of the ice and ocean via an enhanced diffusivity, akin to turbulent mixing in some ocean models. In contrast, convective parameterisations (e.g., Turner et al. 2013; Griewank and Notz 2013; Rees Jones and Worster 2014) model the transport of salt with a divergent upwelling liquid velocity within the mush and a sink term that captures the loss of interstitial fluid through brine channels (figure 3.2). Convective parameterisations better represent the physical mechanism of brine convection and performed best when parameterised bulk salinity profiles were compared with measured bulk salinity profiles of sea ice grown in laboratory experiments (Thomas et al. 2020). Although designed to parameterise the impact of brine convection on the bulk salinity of sea ice, these schemes can also be applied to other dissolved tracers in the ice (Thomas et al. 2020) — including, for our purposes, dissolved gases. Therefore, we choose to adopt the convective parameterisation of Rees Jones and Worster (2014), referred to going forward as the RJW14 scheme, to parameterise the impact of brine convection in our sea-ice model. The RJW14 scheme is described in the remainder of this section.

Consider a two-dimensional layer of sea ice occupying $z_b \leq z \leq 0$ and $-l \leq x \leq l$, with a vertical brine channel located at $x = 0$ (figure 3.3). Under the channel-active-passive (CAP) model (described fully in Rees Jones and Worster 2013b), the convecting portion of the ice ($z_b \leq z \leq z_c$) can be divided into three regions: (1) a passive region far from the brine channel where properties do not vary in the x direction, (2) an active adjustment region near the brine channel, and (3) the brine channel itself.

The onset of convection is determined using the mushy-layer Rayleigh number

$$Ra(z) = \frac{\rho_l g \beta}{\kappa \mu_l} \left[S_l(z) - S_i \right] (z - z_b) \Pi_H(z), \tag{3.2.12}$$

where β is the haline contraction coefficient, $\kappa = k_l/(\rho_l c_{p,l})$ is the thermal diffusivity, S_i is the salinity of the seawater, and $\Pi_H(z)$ is the harmonic mean permeability

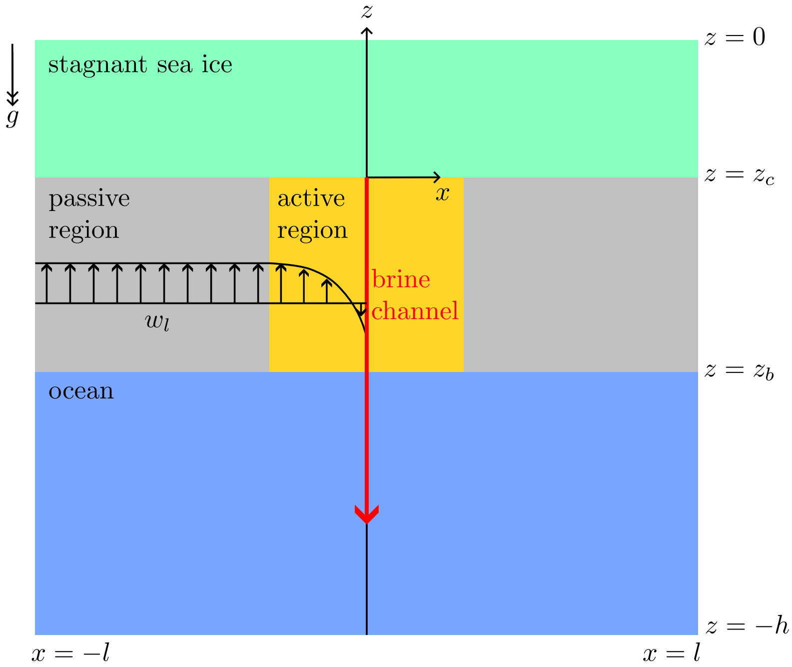

Figure 3.3: Schematic diagram of the CAP model (Rees Jones and Worster 2013a) for sea ice in a two-dimensional domain where the ice occupies $z_b < z < 0$ with periodic boundary conditions at $x = \pm l$. Convecting ice is shown in the diagram in $z_b < z < z_c$ divided into the brine channel (red), active region (orange) and passive region (grey). The upwelling velocity profile w_l is shown in the convecting region. The stagnant region (green), where $\boldsymbol{u_l} = \boldsymbol{0}$, occupies $z_c < z < 0$. The remainder of the domain ($-h < z < z_b$) is occupied by a liquid ocean (blue).

between z and the base of the ice

$$\Pi_H(z) = \Pi_0 \left[\frac{1}{z - z_b} \int_{z_b}^{z} \frac{1}{\pi_l(\phi_s(z'))} \, \mathrm{d}z' \right]^{-1}, \tag{3.2.13}$$

where $\pi_l(\phi_s) = (1 - \phi_s)^3$. The mushy-layer Rayleigh number is the ratio of the potential energy of the unstable stratification within the ice to the viscous and thermal dissipation. The height of the convecting region,

$$z_c = \max\left(\{\, z \in [z_b, 0] : Ra(z) \geq Ra_c \,\}\right), \tag{3.2.14}$$

is the largest value of z at which $Ra(z)$ exceeds a critical value Ra_c. If $Ra(z) < Ra_c$ $\forall z \in [z_b, 0]$, then there is no convecting region.

In the passive region, the temperature and solute fields are horizontally uniform and are assumed to represent the bulk properties of the ice, neglecting deviations in the narrow active and brine channel regions. The convective flow $\boldsymbol{u_l} = u_l \boldsymbol{e_x} + w_l \boldsymbol{e_z}$ in the passive region is found to be a simple corner flow, $u_l \propto x \pm l$ and $w_l \propto z_c - z$

satisfying $\boldsymbol{\nabla} \cdot \boldsymbol{u}_l = \mathbf{0}$, and driven by the baroclinic torque exerted by the brine channel in the active region (Rees Jones and Worster 2013b). Therefore, we can write the advection of a quantity $f(z)$ in the passive region as

$$\boldsymbol{\nabla} \cdot [\boldsymbol{u}_l f(z)] = \frac{\partial}{\partial z} [w_l f(z)] - \frac{\partial w_l}{\partial z} f(z), \tag{3.2.15}$$

using

$$\frac{\partial u_l}{\partial x} = -\frac{\partial w_l}{\partial z}.$$

Following Rees Jones and Worster (2014), the upwelling flow in the passive region is given by

$$w_l = \begin{cases} \alpha_{\mathrm{RJW14}} \kappa Ra_e \dfrac{1}{z_c - z_b} & z < z_b \\ \alpha_{\mathrm{RJW14}} \kappa Ra_e \dfrac{z_c - z}{(z_c - z_b)^2} & z \leq z_b \leq z_c \\ 0 & z > z_c \end{cases}, \tag{3.2.16}$$

where α_{RJW14} is the dimensionless convection strength and the effective Rayleigh number is given by

$$Ra_e = \max_{z_b \leq z \leq z_c} [Ra(z) - Ra_c]. \tag{3.2.17}$$

Equation (3.2.16) yields a convergent upwelling flow, with the second term on the right hand side of equation (3.2.15) acting as a sink term in the conservation equations for heat, salt and dissolved gas. This sink term represents the flux from the ice to the ocean through brine channels and desalinates convecting sea ice.

The velocity profile (equation 3.2.16) in $z > z_b$ is the same as in the original RJW14 scheme (Rees Jones and Worster 2014). Flow in the underlying ocean was not modelled by Rees Jones and Worster (2014) but here we impose a uniform upward flow in the underlying ocean to conserve mass. However, in a turbulent well-mixed ocean we expect heat to efficiently mix between the cold downwelling plumes emitted by brine channels and warmer upwelling ocean water. Therefore, to avoid introducing an unrealistic advective heat flux deeper in the ocean we use the modified velocity profile

$$w_l^T = [1 - \mathsf{H}(\phi_l - 1)]\, w_l \tag{3.2.18}$$

in equation (3.2.5). This is important for correctly predicting the ice thickness.

3.2.3 Snow

Snow typically covers Arctic sea ice from within a few days of its initial formation until the beginning of the melt season (Sturm and Massom 2017). The snow layer is a complex multiphase material in its own right, consisting of a matrix of ice crystals containing air and potentially meltwater (see Sturm and Massom 2017, for an overview). Snow has two major impacts on the freezing and melting of sea ice that cannot be ignored. Firstly, snow has a high shortwave albedo, reflecting a substantial amount of incoming shortwave radiation and thus preventing it from reaching the ice (see chapter 4). Secondly, snow thermally insulates the ice surface, modulating heat transport between the ice and atmosphere.

Our aim here is to capture the two key impacts above without modelling the complex evolution of snow thickness, density, and water content in detail. Rather, we consider a snow layer with homogeneous density ρ_{snow}, specific heat capacity $c_{p,\,\text{snow}}$, and thermal conductivity k_{snow}, with the snow depth $h_{\text{snow}}(t)$ prescribed as a forcing to the model (figure 3.1). We neglect the latent heat associated with the melting (or refreezing) of snow as well as the additional water produced by snow melt. Under these assumptions, heat transport in the snow layer is governed by

$$\rho_{\text{snow}} c_{p,\,\text{snow}} \frac{\partial T}{\partial t} = \frac{\partial}{\partial z}\left(k_{\text{snow}} \frac{\partial T}{\partial z}\right), \quad \text{for} \quad 0 < z < h_{\text{snow}}. \tag{3.2.19}$$

On scaling equation (3.2.19), we find that the time derivative is negligible for timescales larger than $h_{\text{snow}}^2 \rho_{\text{snow}} c_{p,\,\text{snow}}/k_{\text{snow}}$, or around 0.4–10 days for $10\,\text{cm} \leq h_{\text{snow}} \leq 50\,\text{cm}$ and typical snow thermal properties (Sturm and Massom 2017). This timescale is relatively short compared with the seasonal evolution of sea ice. Going forward, we assume for simplicity that the snow layer is in a quasi-steady state,

$$\frac{\partial^2 T}{\partial z^2} = 0. \tag{3.2.20}$$

Solving equation (3.2.20) subject to both continuity of heat flux,

$$k_{\text{snow}} \frac{\partial T}{\partial z}(z = 0^+) = \overline{k} \frac{\partial T}{\partial z}(z = 0^-), \tag{3.2.21}$$

and temperature

$$T(z = 0^+) = T(z = 0^-), \tag{3.2.22}$$

at the ice–snow interface ($z = 0$) allows us to relate both the temperature

$$T_{\text{surf}}(t) \equiv T(z = h_{\text{snow}},\, t) = T(z = 0^-,\, t) + h_{\text{snow}} \frac{\overline{k}}{k_{\text{snow}}} \frac{\partial}{\partial z} T(z = 0^-,\, t), \tag{3.2.23}$$

and the heat flux

$$k_{\text{snow}} \frac{\partial T}{\partial z}(z = h_{\text{snow}},\, t) = \overline{k} \frac{\partial}{\partial z} T(z = 0^-,\, t), \tag{3.2.24}$$

at the snow–atmosphere interface ($z = h_{\text{snow}}$) to those at the ice–snow interface ($z = 0$).

3.2.4 Surface energy balance

The atmospheric heat flux F_{atm} to the snow/ice surface at $z = h_{\text{snow}}$ is a function of the surface temperature T_{surf} (measured in units of absolute temperature) given by equation (3.2.23). Following Taylor and Feltham (2004), the atmospheric heat flux

$$F_{\text{atm}}(t) = F_{\text{LW}} - F_{\text{OLW}} + F_{\text{sens}} + F_{\text{lat}}, \tag{3.2.25}$$

can be decomposed as the sum of four terms: the incoming longwave radiative flux F_{LW}, the outgoing longwave radiative flux F_{OLW}, the turbulent sensible heat flux F_{sens}, and the turbulent latent heat flux F_{lat}.

Longwave radiation, also called thermal radiation, generally spans the wavelength range 4–100 µm and is distinct from the shortwave radiation originating from the sun because it is emitted by the Earth's atmosphere and surface at lower temperatures than the sun. The incoming longwave radiative flux is emitted from the atmosphere and clouds and absorbed by the snow/ice surface. The outgoing longwave radiative flux is emitted from the snow/ice surface and is determined from the surface temperature by the Stefan-Boltzmann law,

$$F_{\text{OLW}} = \Upsilon \sigma_{\text{SB}} T_{\text{surf}}^4, \tag{3.2.26}$$

where σ_{SB} is the Stefan-Boltzmann constant and the emissivity of the surface is

$$\Upsilon = \begin{cases} \Upsilon_{\mathrm{ice}} & \text{for a snow or ice surface} \\ \Upsilon_{\mathrm{water}} & \text{for a surface melt pond} \end{cases} . \tag{3.2.27}$$

We have assumed that the emissivity of ice and snow are equal, the emissivity of water is different in the case of a surface melt pond or open ocean. The surface type (snow, ice or water) is determined from the snow depth and the bulk enthalpy using the phase relations in §3.3. The formulation of equation (3.2.25) by Taylor and Feltham (2004) also includes a portion of the shortwave radiation absorbed at the ice surface, which avoids the need to resolve the absorption of shortwave radiation at fine scales in the uppermost portion of the ice at the cost of introducing another parameter. This simplification is not necessary here since we solve a two-stream model for the propagation of shortwave radiation (see chapter 4) with higher spatial resolution (see chapter 5) and account for all absorbed shortwave radiation in the source term in equation (3.2.5).

The turbulent sensible and latent heat fluxes, F_{sens} and F_{lat}, respectively, depend on the atmospheric boundary layer above the snow/ice surface. The former flux is associated with convective heat transport between the surface and atmosphere, whereas the latter flux is associated with latent heat exchange due to evaporation and condensation of water vapour at the surface. Following Taylor and Feltham (2004), we use parameterisations of these turbulent heat fluxes introduced by Ebert and Curry (1993)

$$F_{\mathrm{sens}} = \rho_{\mathrm{air}} c_{p,\,\mathrm{air}} C_T u_{\mathrm{wind}} (T_{\mathrm{air}} - T_{\mathrm{surf}}), \tag{3.2.28}$$

$$F_{\mathrm{lat}} = \rho_{\mathrm{air}} L_{\mathrm{vap}} C_T u_{\mathrm{wind}} (q_{\mathrm{air}} - q_{\mathrm{surf}}). \tag{3.2.29}$$

Here, $\rho_{\mathrm{air}} = 1.275\,\mathrm{kg\,m^{-3}}$ is the density of dry air; $c_{p,\mathrm{air}} = 1005\,\mathrm{J\,kg^{-1}\,K^{-1}}$ is the specific heat capacity of dry air; $L_{\mathrm{vap}} = 2.501 \times 10^6\,\mathrm{J\,K^{-1}}$ is the latent heat of vaporisation; C_T is the bulk transfer coefficient; u_{wind}, T_{air}, and q_{air} are the wind speed, air temperature, and specific humidity, respectively, at the reference height h_{ref}; and T_{surf} and q_{surf} are the air temperature and specific humidity, respectively, at the snow/ice surface. Following Taylor and Feltham (2004), we assume that the air at the snow/ice surface is saturated with water vapour such that

$$q_{\mathrm{surf}} = \frac{0.622 p_{\mathrm{vap}}}{p_{\mathrm{atm}} - 0.378 p_{\mathrm{vap}}}, \tag{3.2.30}$$

where the partial pressure of water vapour at the surface p_{vap} is related to the absolute temperature T_{surf} by $p_{\mathrm{vap}} = 2.53 \times 10^8 \exp(-5420/T_{\mathrm{surf}})$ (Rogers and Yau 1996).

The bulk transfer coefficient is calculated using the formula proposed by Ebert and Curry (1993),

$$C_T = \begin{cases} C_{\mathrm{EC}} \left(1 - \dfrac{2 b_{\mathrm{EC}} Ri}{1 + c_{\mathrm{EC}} |Ri|^{1/2}}\right) & Ri < 0 \\ C_{\mathrm{EC}} \left(1 + b_{\mathrm{EC}} Ri\right)^{-2} & Ri \geq 0 \end{cases}, \tag{3.2.31}$$

which depends on the stability of the atmospheric boundary layer through the Richardson number

$$Ri = \frac{g(T_{\mathrm{air}} - T_{\mathrm{surf}}) h_{\mathrm{ref}}}{T_{\mathrm{air}} u_{\mathrm{wind}}^2}. \tag{3.2.32}$$

Here

$$C_{\mathrm{EC}} = \begin{cases} 1.3 \times 10^{-3} & \text{for snow or ice surface} \\ 1.0 \times 10^{-3} & \text{for a surface melt pond} \end{cases}, \tag{3.2.33}$$

with $b_{\mathrm{EC}} = 20$ and $c_{\mathrm{EC}} = 1961 b_{\mathrm{EC}} C_{\mathrm{EC}}$. The value $C_{\mathrm{EC}} = 1.0 \times 10^{-3}$ for the case of a surface melt pond was used by Ebert and Curry (1993) to describe turbulent fluxes over leads (exposed areas of ocean between ice floes). However, this same value was used by Taylor and Feltham (2004) to describe turbulent fluxes over melt ponds.

3.2.5 Non-dimensionalisation

We now state a dimensionless set of equations for the evolution of a horizontally uniform domain containing saltwater, ice and a gaseous phase (figure 3.1). We consider only variations in the vertical direction and parameterise the effect of brine convection using the liquid velocity profile w_l and sink term $\mathcal{S}_{\mathrm{RJW14}} = -\frac{\partial w_l}{\partial z}$ derived in §3.2.2. We introduce scales for length $z \sim h$, time $t \sim h^2/\kappa$, and velocities $w_l \sim \kappa/h$ and $w_g \sim \kappa/h$, where h is the depth of the domain and κ is the thermal diffusivity of the liquid. We define the dimensionless temperature θ, salinities Θ, Θ_l,

Θ_s, and dissolved gas concentration ω as in chapter 2, where $S_\infty = S_i = S(z=-h)$ is taken to be the salinity of the deep ocean. The Rayleigh number for the onset of brine convection (see §3.2.2) becomes $Ra(z) = Ra_S \Theta_l(z-z_b)\pi_H(z)$, where $Ra_S = \rho_l g \beta \Delta S \Pi_0 h/\kappa\mu_l$, $\Delta S = S_E - S_i$, and $\pi_H(z) = \Pi_H(z)/\Pi_0$.

Equations (3.2.5), (3.2.9), (3.2.15) and (3.2.18) can be combined to yield

$$\frac{\partial \mathcal{H}}{\partial t} + \frac{\partial}{\partial z}\left(\theta w_l^T\right) = \frac{\partial}{\partial z}\left[\left(\overline{\nu} + \frac{\mathsf{H}(\phi_l - 1)}{Le_\varepsilon}\right)\frac{\partial \theta}{\partial z}\right] - \mathcal{S}_{\mathrm{RJW14}}\theta + \frac{\partial \widetilde{\mathcal{F}}_{\mathrm{net}}}{\partial z}, \tag{3.2.34}$$

where $\mathcal{H} = \zeta_s\phi_s\theta + \phi_l\theta - St\phi_s$ is the dimensionless bulk enthalpy, $\zeta_s = c_{p,s}/c_{p,l}$ is the ratio of the specific heat capacity of the solid to that of the liquid, $St = L/(c_{p,l}\Delta T)$ is the Stefan number, $\Delta T = T_i - T_E$, $\overline{\nu} = \phi_s\nu_s + \phi_l$, $\nu_s = k_s/k_l$ is the ratio of thermal conductivity of the solid to that of the liquid, and $Le_\varepsilon = \kappa/\kappa_\varepsilon$ is the Lewis number for eddy diffusivity. The dimensionless spectrally-integrated net shortwave radiation is given by

$$\widetilde{\mathcal{F}}_{\mathrm{net}}(z) = \frac{h\widetilde{F}_{\mathrm{net}}(z)}{k_l \Delta T}, \tag{3.2.35}$$

where $\widetilde{F}_{\mathrm{net}}(z)$ is the dimensional broadband net shortwave irradiance, as determined using a two-stream radiative transfer model (see chapter 4).

Equations (3.2.2), (3.2.7), (3.2.15) and (3.2.16) can be combined to yield

$$\frac{\partial \Theta}{\partial t} + \frac{\partial}{\partial z}\left[w_l\left(\Theta_l + \mathcal{C}\right)\right] = \frac{\partial}{\partial z}\left[\left(\frac{\phi_l}{Le_S} + \frac{1}{Le_\varepsilon}\mathsf{H}(\phi_l - 1)\right)\frac{\partial \Theta_l}{\partial z}\right] - \mathcal{S}_{\mathrm{RJW14}}(\Theta_l + \mathcal{C}), \tag{3.2.36}$$

where $\Theta = \phi_s\Theta_s + \phi_l\Theta_l$ is the dimensionless bulk salinity, $\mathcal{C} = S_i/\Delta S$ is the concentration ratio, and $Le_S = \kappa/\kappa_S$ is the Lewis number for the diffusion of salt.

Equations (3.2.3), (3.2.8), (3.2.15) and (3.2.16) can be combined to yield

$$\frac{\partial \Gamma_d}{\partial t} + \frac{\partial}{\partial z}\left[\chi w_l \omega\right] = \chi\frac{\partial}{\partial z}\left[\left(\frac{\phi_l}{Le_\xi} + \frac{1}{Le_\varepsilon}\mathsf{H}(\phi_l - 1)\right)\frac{\partial \omega}{\partial z}\right] - \chi Da \mathcal{N} - \chi\mathcal{S}_{\mathrm{RJW14}}\omega, \tag{3.2.37}$$

where $\Gamma_d = \chi\phi_l\omega$ is the dimensionless dissolved bulk gas content, $\chi = \rho_l\xi_{\mathrm{sat}}/\rho_g$ is the dimensionless expansion coefficient, $Da = h^2/(\kappa\tau_{\mathrm{nuc}})$ is the Damköhler number for gas exsolution with timescale τ_{nuc}, $Le_\xi = \kappa/\kappa_\xi$ is the Lewis number for the diffusion of dissolved gas, and $\mathcal{N}$ is the dimensionless gas exsolution rate, as defined in chapter 2.

Finally, equations (2.2.9) and (3.2.11) can be combined to yield

$$\frac{\partial \phi_g}{\partial t} + \mathcal{B}\delta_0^2 \frac{\partial}{\partial z}\left[d(\delta)\phi_g\right] = \chi Da \mathcal{N}, \tag{3.2.38}$$

where $\mathcal{B} = \Delta\rho g R_0^2 h/(3\mu_l \kappa)$ is the dimensionless bubble rise velocity, $\delta_0 = R_B/R_0$ is the constant dimensionless bubble radius, and

$$d(\delta) = \begin{cases} 0 & \phi_l \leq \phi_c \\ \dfrac{1}{K_1(\delta)} & \phi_c < \phi_l < 1 \\ 1 & \phi_l = 1 \end{cases} \tag{3.2.39}$$

gives the effect of viscous drag on the vertical migration of bubbles within the ice.

Equations (3.2.34)–(3.2.38) determine the evolution of the four dimensionless bulk variables $\mathcal{H}$, Θ, Γ_d and ϕ_g. Immediately, by definition,

$$\omega = \frac{\Gamma - \phi_g}{\chi \phi_l}, \tag{3.2.40}$$

where $\Gamma = \Gamma_d + \phi_g$ is the dimensionless bulk gas content. We derive expressions for θ, Θ_l, Θ_s, ϕ_s and ϕ_l in terms of the four bulk variables using the enthalpy method in §3.3.

Rapid gas exsolution $Da \to \infty$

Equations (3.2.37) and (3.2.38) can be summed to find a single conservation equation for the total dimensionless bulk gas content:

$$\frac{\partial \Gamma}{\partial t} + \mathcal{B}\delta_0^2 \frac{\partial}{\partial z}\left[d(\delta)\phi_g\right] + \frac{\partial}{\partial z}\left[\chi w_l \omega\right] = \frac{\chi}{Le_\xi}\frac{\partial}{\partial z}\left[\left(\phi_l + \frac{Le_\xi}{Le_\varepsilon}\mathsf{H}(\phi_l - 1)\right)\frac{\partial \omega}{\partial z}\right] - \chi \mathcal{S}_{\text{RJW14}}\omega. \tag{3.2.41}$$

In the case of instantaneous gas exsolution (i.e., $Da \to \infty$), ϕ_g and ω are determined at equilibrium by

$$\phi_g = \begin{cases} 0 & \Gamma \leq \Gamma_{\text{sat}} \\ \Gamma - \Gamma_{\text{sat}} & \Gamma > \Gamma_{\text{sat}} \end{cases}, \tag{3.2.42}$$

and

$$\omega = \begin{cases} \dfrac{\Gamma}{\Gamma_{\text{sat}}} & \Gamma \leq \Gamma_{\text{sat}} \\ 1 & \Gamma > \Gamma_{\text{sat}} \end{cases}, \tag{3.2.43}$$

where $\Gamma_{\text{sat}} = \chi \phi_l$ is the dimensionless bulk gas content at saturation.

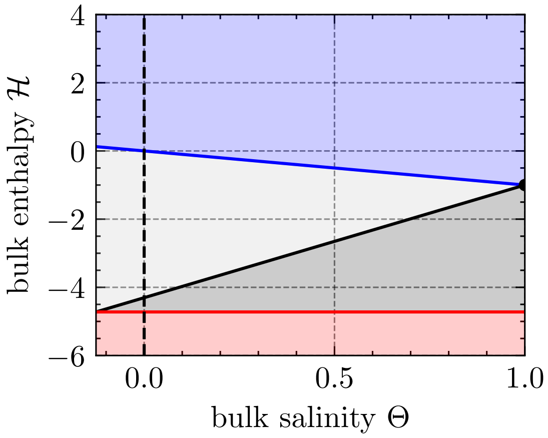

Figure 3.4: Saltwater phase diagram in bulk enthalpy $\mathcal{H}$, bulk salinity Θ space. The liquidus $\mathcal{H}_L$, eutectic $\mathcal{H}_E$, and solidus $\mathcal{H}_S$ phase boundaries, given by equations (3.3.4)–(3.3.6), are shown as blue, black and, red lines, respectively. Above the liquidus boundary (shaded blue), the system is completely liquid (i.e., $\phi_l = 1$). Between the liquidus and eutectic boundaries (shaded light grey), the system is a partially solid mushy layer. Between the eutectic and solidus boundaries (shaded darker grey), the system is at the eutectic temperature and salt precipitates as a solid hydrated mineral (hydrohalite). Below the solidus boundary (shaded red), the system is completely solid (i.e., $\phi_s = 1$). The liquidus meets the eutectic boundary at the eutectic point (filled black half circle). Note that Θ is the dimensionless bulk salinity relative to the initial salinity of the ocean S_i, and so $\Theta = -\mathcal{C}$ corresponds to a completely fresh system.

3.3 Enthalpy method

Formulating this problem in terms of the dependent variables θ, Θ_l, Θ_s, ϕ_s, and ϕ_l, as done in chapter 2, requires the explicit tracking of boundaries between phases. It is useful to instead formulate the system in terms of the bulk enthalpy $\mathcal{H}$ and bulk salinity Θ, which are continuous across phase boundaries. We can then use $\mathcal{H}$ and Θ to determine piecewise expressions for θ, Θ_l, Θ_s, ϕ_s, and ϕ_l from the saltwater phase diagram (figure 3.4). This so-called "enthalpy method" has been used to successfully simulate the formation of brine channels in sea ice (Parkinson 2019) and similar convective instabilities in other mushy layers (Katz and Worster 2008).

In dimensionless terms, the linear liquidus and solidus boundaries (defined in chapter 2) are given by $\theta_L = -\Theta$, and $\theta_S = -1$, respectively, where θ_S is simply the dimensionless eutectic temperature. The system is completely liquid when $\theta > \theta_L$, a porous mushy layer when $\theta_S \leq \theta \leq \theta_L$, and completely solid when $\theta < \theta_S$. At the eutectic temperature $\theta = -1$, all remaining liquid in the system freezes, requiring a finite change in enthalpy given by the latent heat. Therefore, in bulk enthalpy and salinity space (Θ, $\mathcal{H}$) the system passes through an extra eutectic phase, at a fixed temperature $\theta = -1$, between the mushy and solid phases $\mathcal{H}_S \leq \mathcal{H} < \mathcal{H}_E$, where $\mathcal{H}_E$ is the upper boundary of this extra eutectic phase in (Θ, $\mathcal{H}$) space.

Regardless of the phase, the system must satisfy the following three constraints for the bulk enthalpy, bulk salinity, and total volume:

$$\mathcal{H} = \zeta_s \phi_s \theta + \phi_l \theta - St \phi_s, \tag{3.3.1}$$

$$\Theta = \phi_s \Theta_s + \phi_l \Theta_l, \tag{3.3.2}$$

and

$$\phi_s + \phi_l = 1. \tag{3.3.3}$$

Additionally, we derive two extra constraints for each phase from the phase diagram:

- when $\mathcal{H} > \mathcal{H}_L$, there is only liquid $\phi_l = 1$ and the solid phase salinity Θ_s is arbitrary;
- when $\mathcal{H}_E < \mathcal{H} \leq \mathcal{H}_L$, the temperature satisfies the liquidus constraint $\theta = -\Theta_l$ in the mush and we assume all of the salt is rejected into the interstitial liquid $\Theta_s = -\mathcal{C}$;
- when $\mathcal{H}_S < \mathcal{H} \leq \mathcal{H}_E$, the system is at the eutectic temperature $\theta = -1$ and the interstitial liquid is at the eutectic salinity $\Theta_l = 1$; and
- when $\mathcal{H} \leq \mathcal{H}_S$, there is only solid $\phi_s = 1$ and the liquid phase salinity Θ_l is arbitrary.

Using the above constraints, we determine the following expressions for the phase boundaries of the system:

$$\mathcal{H}_L(\Theta) = -\Theta, \tag{3.3.4}$$

$$\mathcal{H}_E(\Theta) = (St + \zeta_s - 1)\frac{\Theta - 1}{1 + \mathcal{C}} - 1, \tag{3.3.5}$$

and

$$\mathcal{H}_S(\Theta) = -\zeta_s - St. \tag{3.3.6}$$

Additionally, we find piecewise expressions for ϕ_s, θ, and Θ_l :

$$\phi_s = \begin{cases} 0 & \mathcal{H} > \mathcal{H}_L \\ \dfrac{1}{2\mathsf{A}}\left(-\mathsf{B} - \sqrt{\mathsf{B}^2 - 4\mathsf{AC}}\right) & \mathcal{H}_E < \mathcal{H} \leq \mathcal{H}_L \\ -\dfrac{1+\mathcal{H}}{St + \zeta_s - 1} & \mathcal{H}_S < \mathcal{H} \leq \mathcal{H}_E \\ 1 & \mathcal{H} < \mathcal{H}_S \end{cases}, \tag{3.3.7}$$

where $\mathsf{A} = St + \mathcal{C}(1-\zeta_s)$, $\mathsf{B} = \mathcal{H} - St - \mathcal{C} + \Theta(1-\zeta_s)$, and $\mathsf{C} = -(\Theta + \mathcal{H})$,

$$\theta = \begin{cases} \mathcal{H} & \mathcal{H} > \mathcal{H}_L \\ \dfrac{\mathcal{H} + St\phi_s}{1 + (\zeta_s - 1)\phi_s} & \mathcal{H}_E < \mathcal{H} \leq \mathcal{H}_L \\ -1 & \mathcal{H}_S < \mathcal{H} \leq \mathcal{H}_E \\ \dfrac{\mathcal{H} + St}{\zeta_s} & \mathcal{H} < \mathcal{H}_S \end{cases}, \tag{3.3.8}$$

and

$$\Theta_l = \begin{cases} \Theta & \mathcal{H} > \mathcal{H}_L \\ -\theta & \mathcal{H}_E < \mathcal{H} \leq \mathcal{H}_L \\ 1 & \mathcal{H}_S < \mathcal{H} \leq \mathcal{H}_E \\ 1 & \mathcal{H} < \mathcal{H}_S \end{cases}. \tag{3.3.9}$$

3.4 Boundary conditions

We now specify boundary conditions for the system of conservation equations (3.2.34)–(3.2.38). In all cases, advective fluxes are never downward and we need only specify an inflow condition at the bottom boundary. When diffusive terms are present, we must specify boundary conditions at both the top and bottom of the domain.

Beginning with equation (3.2.36), we impose a fixed ocean salinity at the bottom of the domain,

$$\Theta(z = -1,\, t) = 0, \tag{3.4.1}$$

and a no-salt-flux boundary condition at the top of the domain,

$$\frac{\partial \Theta_l}{\partial z}(z = 0,\, t) = 0. \tag{3.4.2}$$

Note that equation (3.4.2) is only required when $\phi_l > 0$ at $z = 0$.

Because salinity gradients are coupled to thermal gradients in a mushy layer through the liquidus relation, $\theta = -\Theta$, strictly a cooling heat flux at the top boundary must imply a corresponding diffusive salt flux. If there is no source of salt above the top boundary, the ice surface desalinates, forming a solid impermeable crust (Wells et al. 2019). This is not thought to occur at the surface of sea ice, where there is a more complicated, poorly understood, surface condition featuring ice, brine, air, and snow (Wells et al. 2019).

For equation (3.2.37), we impose a fixed concentration of dissolved gas in the ocean, $\omega_\infty \leq 1$, such that

$$\Gamma_d(z = -1,\, t) = \chi\omega_\infty, \tag{3.4.3}$$

and we impose that the surface is saturated with dissolved gas from the atmosphere,

$$\Gamma_d(z = 0,\, t) = \chi, \tag{3.4.4}$$

when $\phi_l > 0$ at $z = 0$. For equation (3.2.38), we impose that there is no gas phase in the ocean,

$$\phi_g(z = -1,\, t) = 0. \tag{3.4.5}$$

No condition is needed at the top of the domain as there is no diffusive flux in this case. In the limit of rapid bubble exsolution ($Da \to \infty$), the boundary conditions on Γ are the same as those on Γ_d (i.e., equations 3.4.3 and 3.4.4).

Finally, for equation (3.2.34), we can impose fixed-temperature boundary conditions,

$$\theta(z = -1,\, t) = \theta_{\text{ocean}}(t), \tag{3.4.6}$$

and

$$\theta(z = 0,\, t) = \theta_{\text{atm}}(t), \tag{3.4.7}$$

or heat-flux boundary conditions

$$\left[1 + \frac{1}{Le_\varepsilon}\right] \frac{\partial \theta}{\partial z}(z = -1,\, t) = \mathcal{F}_{\text{ocean}}(t), \tag{3.4.8}$$

and

$$\left[\overline{\nu} + \frac{1}{Le_{\varepsilon}}\mathsf{H}(\phi_l^0 - 1)\right]\frac{\partial \theta}{\partial z}(z = 0,\, t) = \mathcal{F}_{\mathrm{atm}}(t), \tag{3.4.9}$$

where $\mathcal{F}_{\mathrm{atm}}(t) = F_{\mathrm{atm}}(t)h/(k_l \Delta T)$ and $\phi_l^0 = \phi_l(z = 0,\, t)$. In principle we may also impose Robin boundary conditions (see e.g. Hitchen and Wells 2025), but this case is not investigated in this thesis.

3.5 Summary

In this chapter, we used the reduced model for a three-phase mushy layer developed in chapter 2 to derive a set of one-dimensional transient equations for the evolution of sea ice containing dissolved gas and an additional gaseous phase. As discussed in chapter 2, the assumptions underlying this reduced model — that the gas phase is incompressible, that it occupies only a small fraction of the total volume, and that it is dispersed among spherical bubbles — are likely to be reasonable for sea ice except potentially in regions of sustained gas accumulation below low porosity ice. We introduced parameterisations for geophysical processes relevant to the evolution of sea ice: turbulent mixing in the ocean, absorption of shortwave radiation, brine convection, heat transport through the snow layer, and the atmospheric heat flux. In chapter 4, we will derive a two-stream radiative transfer model to determine $\widetilde{\mathcal{F}}_{\mathrm{net}}$, which is required to determine the energy source due to the absorption of shortwave radiation in equation (3.2.34).

Under the approximations of the reduced model, the equations for heat and salt conservation reduce to those appropriate for a two-phase mushy layer. As a result, we were able to use the enthalpy method to determine piecewise expressions for the temperature, salinities, and solid and liquid volume fractions in terms of the bulk enthalpy and salinity. In chapter 5, we develop and validate a finite-volume scheme to solve the resulting system of equations (3.2.34), (3.2.36), (3.2.37), and (3.2.38) numerically. In chapters 6–8, we use this model to simulate the evolution of sea ice for comparison with field observations and to investigate gas bubbles and oil droplets in the sea-ice system.

4

A spectral two-stream model for shortwave radiative transfer in the sea-ice system

4.1 Introduction

Shortwave radiation reaching Earth's surface originates from the sun with wavelengths 300 nm $\leq \lambda \leq$ 3000 nm, covering the ultraviolet, visible, and near-infrared parts of the electromagnetic spectrum (Chen et al. 2012). The fate of shortwave radiation in the sea-ice system (see figure 4.1) is controlled by absorption and scattering in the different media present, i.e., ice, snow, and water (Perovich 2017). The absorption of shortwave radiation is not a large part of the energy budget of Arctic sea ice from September to May during which the Arctic receives little or no solar radiation and/or the ice is covered by a highly reflecting, optically thick layer of snow (Sturm and Massom 2017). However, as the melt season progresses and the snow cover melts, the absorption of shortwave radiation contributes substantially to both surface and internal melting of the ice and heating of the upper ocean (Perovich 2005). Therefore, to accurately simulate sea ice in the melt season, it is important to model the propagation of shortwave radiation within the ice. Additionally, the transmission of light in the visible range (400–700 nm) determines the availability of photosynthetically active radiation (PAR) for algae found at the ice–ocean interface (Gradinger 2009).

In this chapter, we summarise the relevant aspects of radiative-transfer theory and introduce a spectral two-stream model for the vertical propagation of shortwave radiation through snow, sea ice, and water, which closely follows existing schemes used in sea-ice models. In §4.2, we introduce simple exponential decay laws to model the transmission of shortwave radiation through a surface snow cover and a surface scattering layer (SSL) atop sea ice. In §4.3, we state the equation for radiative transfer in a plane-parallel medium, which governs the propagation of shortwave radiation in the sea-ice system. In §4.4, we introduce the so-called "two-stream" approximation, which yields a pair of coupled ordinary differential equations (ODEs) for the hemispherically averaged upwelling and downwelling spectral irradiances. In §4.5, we relate the intrinsic optical properties governing the absorption and scattering of shortwave radiation in sea ice used in previous studies to the absorption and scattering coefficients used in the two-stream model. In §4.6, we define some optical parameters of interest for the sea-ice system using the upwelling and downwelling irradiances obtained from the two-stream model. In §4.7, we discretise the spectral two-stream model into six spectral bands that provide sufficient spectral resolution to capture the wavelength dependence of optical properties, whilst maintaining computational efficiency. Finally in §4.8, we validate our approach by comparing some optical parameters computed using the derived two-stream model to literature values.

Spectral resolution and computational efficiency is essential since, later in this thesis (chapter 8), we use the transient model to investigate the impact of oil droplets in sea ice on the absorption of shortwave radiation (at low wavelengths) over a season. We modify the spectral absorption coefficient to account for oil droplets in the ice in due course.

4.2 Transmission of shortwave radiation through a snow layer and a SSL

For large parts of the year, Arctic sea ice is covered by snow. Snow is highly scattering and has one of the highest shortwave albedos of any natural material (Sturm and Massom 2017). To build understanding of ice processes, we consider the snow layer as a boundary condition to the sea ice model where the snow thickness h_{snow} is prescribed (see chapter 3 for more details). This avoids the need to accurately model the deposition, compaction, melting and re-freezing of the snow cover.

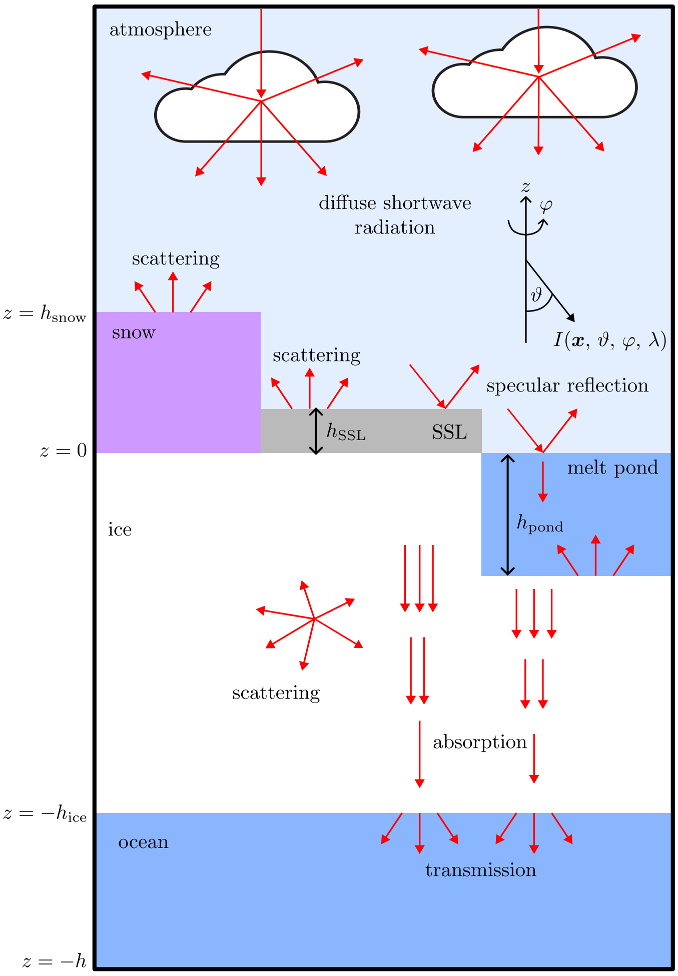

Figure 4.1: A schematic diagram showing the processes controlling the vertical propagation of shortwave radiation in the sea-ice system. The spherical polar angles (ϑ, φ) used to describe the shortwave spectral radiance $I(\boldsymbol{x},\,\vartheta,\,\varphi,\,\lambda)$ are indicated relative to the vertical direction z. Three possible surface conditions are illustrated: snow-covered ice, bare ice, and a surface melt pond. Also shown (with an exaggerated thickness) is the surface scattering layer (SSL), which is a thin ($h_{\text{SSL}} \ll h_{\text{ice}}$) and highly scattering layer present at the surface of bare ice during the melt season. The case of diffuse incident shortwave radiation from the atmosphere (under cloudy sky conditions) is shown. Both snow cover and the SSL scatter and absorb incoming shortwave radiation, hence reducing the incident shortwave radiation reaching the ice surface $z = 0$. Absorption and scattering in the ice interior control the fractions of the incident radiation that are transmitted to the ocean, scattered back out of the ice, and absorbed within the ice. For ice with an overlying melt pond, incident radiation is first transmitted through the pond, where a fraction is absorbed, before entering the ice interior. Specular reflection at the ice–air or water–air interfaces is also shown, although we neglect it in this chapter.

The reflection and transmission of shortwave radiation by the snow pack is important as it determines the amount of shortwave radiation reaching the underlying ice. To prescribe the shortwave radiation flux reaching the ice surface, we define the spectral transmittance of the snow layer $\mathcal{T}_{\text{snow}}(\lambda)$ as the fraction of the incident shortwave radiation exiting the base of the snow layer at each wavelength. We parameterise the spectral transmittance through a uniform snow layer of thickness h_{snow} using an exponential decay, also called Beer's law,

$$\mathcal{T}_{\text{snow}}(\lambda) = [1 - \alpha_{\text{surf}}(h_{\text{snow}},\, \lambda)] \exp\left[-\kappa_{\text{snow}}(\lambda) h_{\text{snow}}\right], \tag{4.2.1}$$

as is commonly done in other modelling studies (Fukami et al. 1985; Lavoie et al. 2005; Castellani et al. 2017; Lebrun et al. 2023; Stroeve et al. 2024). Here, $\kappa_{\text{snow}}(\lambda)$ is the spectral extinction coefficient for the snow and

$$\alpha_{\text{surf}}(h_{\text{snow}},\, \lambda) = \alpha_{\text{snow}}(\lambda)\left[1 - \exp\left(-h_{\text{snow}}/l_{\alpha}\right)\right] + \alpha_{\text{SSL}}(\lambda) \exp\left(-h_{\text{snow}}/l_{\alpha}\right) \tag{4.2.2}$$

is the spectral surface albedo, where $\alpha_{\text{snow}}(\lambda)$ is the spectral albedo for an optically thick snow cover, $\alpha_{\text{SSL}}(\lambda)$ is the bare ice spectral albedo, and l_{α} is a characteristic length scale. Going forward, we take $l_{\alpha} = 2\,\text{cm}$, which was found to provide a good fit to measured albedo over snow (see figure 12 of Grenfell and Perovich 2004).

Under suitable conditions in summer, the snow cover atop Arctic sea ice melts away; however, the albedo of bare ($h_{\text{snow}} = 0$) first-year sea ice remains consistently high — in the range 0.6–0.7 (Perovich and Polashenski 2012; Light et al. 2022) — until the formation of melt ponds. This high albedo is due to the formation of a thin, coarse-grained drained SSL on the ice surface, with thickness h_{SSL} typically between 1 and 10 cm, that is one to two orders of magnitude more scattering than the interior of the ice (Smith et al. 2022; Light et al. 2008). Going forward, we take $h_{\text{SSL}} = 4\,\text{cm}$, which was a typical value observed by Smith et al. (2022). We model the spectral transmittance of shortwave radiation through the SSL $\mathcal{T}_{\text{SSL}}(\lambda)$ using Beer's law,

$$\mathcal{T}_{\text{SSL}} = [1 - \alpha_{\text{SSL}}(\lambda)] \exp\left[-\kappa_{\text{SSL}}(\lambda) h_{\text{SSL}}\right], \tag{4.2.3}$$

where $\kappa_{\text{SSL}}(\lambda)$ is the spectral extinction coefficient in the SSL.

To ensure continuity of the transmitted shortwave radiation as $h_{\text{snow}} \to 0$, we calculate the fraction of incident shortwave radiation transmitted to the ice as

$$\mathcal{T}_{\text{surf}}(\lambda) = \min\left[\mathcal{T}_{\text{snow}}(\lambda), \mathcal{T}_{\text{SSL}}(\lambda)\right]. \tag{4.2.4}$$

The transmission of shortwave radiation through the snow cover and SSL yields the following boundary condition for the downwelling radiation flux at the ice surface, $z = 0$:

$$F_{\text{inc}}(\lambda) = F_{\text{SW}}(\lambda)\mathcal{T}_{\text{surf}}(\lambda), \tag{4.2.5}$$

where $F_{\text{SW}}(\lambda)$ is the spectral downwelling shortwave radiation flux from the atmosphere.

We consider three possible surface configurations:

1. snow covered ice: $h_{\text{snow}} > 0$, $h_{\text{SSL}} = 4\,\text{cm}$;
2. bare ice: $h_{\text{snow}} = 0$, $h_{\text{SSL}} = 4\,\text{cm}$; and
3. ponded ice: $h_{\text{snow}} = 0$, $h_{\text{SSL}} = 0$.

Beer's Law is suitable for optically thick media such as snow and the SSL, which are both highly scattering. However, Beer's law has been shown to overestimate the transmission of shortwave radiation by up to 200% through thin sea ice ($h_{\text{ice}} < 0.8\,\text{m}$) (Grenfell 1979). Therefore, as described below, we adopt a more sophisticated approach to model the transmission of shortwave radiation through the ice interior.

4.3 Radiative transfer theory

The shortwave radiation field at a position $\boldsymbol{x}$ is characterised by the spectral radiance $I(\boldsymbol{x}, \vartheta, \varphi, \lambda)$ in units of radiative power per unit area per unit solid angle per unit wavelength, where ϑ is the angle the radiation makes to the downward vertical direction, φ is the azimuthal angle, and λ is the wavelength (see figure 4.1). In general, the incident shortwave radiation field from the atmosphere has a diffuse (isotropic) component and a direct beam component. For simplicity, we assume all incident shortwave radiation is diffuse, which is a good approximation for the Arctic due to the presence of low stratus clouds over sea ice in summer (Perovich 1990). Due to substantial changes in the index of refraction, a component of the incident radiation undergoes specular reflection at the air–ice or air–water interface. Here, we neglect specular reflection because it is typically only around 5% of the incident radiation under diffuse sky conditions (Perovich and Grenfell 1982).

For shortwave radiation propagating through a horizontally uniform plane-parallel medium with no internal sources, the spectral radiance field is governed by the radiative transfer equation (Chandrasekhar 2016),

$$\cos\vartheta \frac{\mathrm{d}I}{\mathrm{d}\tau} = -I + \frac{\varpi_0}{4\pi}\int_0^{2\pi}\int_0^{\pi} \mathscr{P}(\vartheta,\, \vartheta',\, \varphi,\, \varphi') I(\tau,\, \vartheta',\, \varphi',\, \lambda) \sin\vartheta' \,\mathrm{d}\vartheta' \,\mathrm{d}\varphi', \quad (4.3.1)$$

where τ is the optical depth, ϖ_0 is the single scattering albedo, and $\mathscr{P}(\vartheta,\, \vartheta',\, \varphi,\, \varphi')$ is the phase function, which gives the fraction of radiation scattered from the $(\vartheta',\, \varphi')$ direction into the $(\vartheta,\, \varphi)$ direction. The optical depth and single scattering albedo are defined by

$$\mathrm{d}\tau = [k(z,\, \lambda) + r(z,\, \lambda)]\,\mathrm{d}z \quad (4.3.2)$$

and

$$\varpi_0 = \frac{r(z,\, \lambda)}{k(z,\, \lambda) + r(z,\, \lambda)}, \quad (4.3.3)$$

respectively, where $k(z,\, \lambda)$ is the spectral absorption coefficient and $r(z,\, \lambda)$ is the spectral scattering coefficient. Sea ice is a highly scattering medium ($\varpi_0 \approx 1$), and we assume here that water (in the ocean or melt pond) is not scattering ($\varpi_0 = 0$). See Perovich (2017) for a detailed review of absorption and scattering in sea ice.

The full radiative transfer equation is a complex integro-differential equation with no general solution. Many different models have been developed to describe radiative transfer in sea ice, which are distinguished by the number of streams (angular directions) in which the radiance field is calculated. Beer's Law, as used previously in this section, is essentially a one-stream radiative transfer model that does not capture scattering and requires the albedo to be specified. Two-stream models are common because they are the simplest models that can capture the essential physics of absorption and scattering, and are computationally inexpensive (Perovich 1990; Taylor and Feltham 2004). The dEdd-AD two-stream model for snow and ice (Briegleb and Light 2007) is used in the Icepack, CICE and MPAS-Seaice models (Dang et al. 2019). The major limitation of two-stream models is the isotropic treatment of scattering, which can be improved upon by using more streams (Grenfell 1983; Grenfell 1991). For example, TUV-snow is an eight-stream model originally developed to describe radiative transfer in snow (Lee-Taylor and Madronich 2002) and later adapted to be used in sea ice (Redmond Roche and King 2022b).

4.4 The two-stream model

We define the downwelling and upwelling spectral irradiances as the spectral power per unit area incident on the horizontal plane from the lower hemisphere

$$F_\lambda^-(\tau) = \int_0^{2\pi}\int_0^{\pi/2} I(\tau,\, \vartheta,\, \varphi,\, \lambda)\cos\vartheta\sin\vartheta\,\mathrm{d}\vartheta\,\mathrm{d}\varphi, \tag{4.4.1}$$

and upper hemisphere

$$F_\lambda^+(\tau) = \int_0^{2\pi}\int_{\pi/2}^{\pi} I(\tau,\, \vartheta,\, \varphi,\, \lambda)\cos\vartheta\sin\vartheta\,\mathrm{d}\vartheta\,\mathrm{d}\varphi, \tag{4.4.2}$$

respectively. It is common (e.g. Stamnes et al. 2017) to approximate equation (4.3.1) with a pair of coupled ODEs for the upwelling and downwelling spectral irradiances (see appendix F for details), which yields a two-stream model given by

$$\frac{\mathrm{d}f_\lambda^-}{\mathrm{d}z} = (k_{2\mathrm{S}} + r_{2\mathrm{S}})f_\lambda^- - r_{2\mathrm{S}}f_\lambda^+, \tag{4.4.3}$$

and

$$\frac{\mathrm{d}f_\lambda^+}{\mathrm{d}z} = -(k_{2\mathrm{S}} + r_{2\mathrm{S}})f_\lambda^+ + r_{2\mathrm{S}}f_\lambda^-, \tag{4.4.4}$$

where we have normalised the spectral irradiances using the incident spectral downwelling radiation flux from the atmosphere $F_{\mathrm{SW}}(\lambda)$, such that $f_\lambda^+(z) = F_\lambda^+(z)/F_{\mathrm{SW}}(\lambda)$ and $f_\lambda^-(z) = F_\lambda^-(z)/F_{\mathrm{SW}}(\lambda)$. The normalised net shortwave radiation flux in the ice is given by

$$f_{\lambda,\,\mathrm{net}}(z) = f_\lambda^-(z) - f_\lambda^+(z). \tag{4.4.5}$$

The two-stream absorption coefficient $k_{2\mathrm{S}}$ and scattering coefficient $r_{2\mathrm{S}}$ are related to the absorption and scattering coefficients k and r by

$$k_{2\mathrm{S}} = \frac{k}{\overline{\mu}} \tag{4.4.6}$$

and

$$r_{2\mathrm{S}} = \frac{rb}{\overline{\mu}}, \tag{4.4.7}$$

respectively, where b is the backscatter fraction and $1/\overline{\mu}$ is the mean vertical path extension of the diffuse radiance field. These quantities are related to the ice scattering phase function and the angular distribution of the radiance field (see appendix F). The simplest approach is to assume an isotropic radiance field in each hemisphere, which yields $\overline{\mu} = 1/2$, which we use going forward.

The boundary conditions for equations (4.4.3) and (4.4.4) are

$$f_\lambda^-(z = 0) = \mathcal{T}_{\mathrm{surf}}(\lambda), \tag{4.4.8}$$

which arises from equation (4.2.4) with fixed incident downwelling flux, and

$$f_\lambda^+(z = -h) = 0, \tag{4.4.9}$$

which arises from the assumption that there is no upwelling irradiance at the bottom of the domain. The latter is reasonable for ice atop a sufficiently deep ocean that does not contain any significant light-scattering impurities.

4.5 Ice optical properties

The optical properties, $k_{2\mathrm{S}}$ and $r_{2\mathrm{S}}$, depend on space, time and wavelength as the sea ice thickness changes. Previous two-stream models have split the domain into discrete layers with uniform optical properties, such as the snow, SSL, melt pond, ice interior and ocean (Perovich 1990; Taylor and Feltham 2004). We parameterise the transmission of shortwave radiation through any snow cover and SSL as a boundary condition at $z = 0$ (§4.2) and determine $k_{2\mathrm{S}}$ and $r_{2\mathrm{S}}$ as functions of ϕ_s in $-h < z < 0$ to avoid explicitly tracking the ice–ocean and ice-melt-pond interfaces.

4.5.1 Scattering

In snow, ice, and water, the scattering coefficient does not vary significantly with wavelength (Grenfell 1983). A previous two-stream model for the propagation of shortwave radiation in the sea-ice system used values of $r_{2\mathrm{S}}$ in the range 1.2–2.5 m^{-1} for interior sea ice and $r_{2\mathrm{S}} = 0\,\mathrm{m}^{-1}$ for clear seawater (Perovich 1990). We calculate the $r_{2\mathrm{S}}$ value for interior sea ice using equation (4.4.7), where $r = \rho'_{\mathrm{ice}}\sigma_{\mathrm{sca}}$, $\sigma_{\mathrm{sca}} = 0.15\,\mathrm{m}^2\,\mathrm{kg}^{-1}$ is the mass sacttering cross section of first-year sea ice, and $\rho'_{\mathrm{ice}} = 800\,\mathrm{kg}\,\mathrm{m}^{-3}$ is the bulk density of first-year sea ice. The latter value was used by Redmond Roche and King (2022b) and may seem unrealistically low compared with the range of values reported in the literature (Timco and Frederking 1996). However, we use this value to calculate the value of $r_{2\mathrm{S}}$ for consistency with Redmond Roche and King (2022b).

It is known that the scattering phase function in sea ice is highly anisotropic and strongly peaked in the forward direction, both from measurements (Grenfell and Hedrick 1983) and from calculations using a Mie scattering model (Grenfell 1983). Therefore, it is common practice in sea-ice radiative transfer models to use a Henyey-Greenstein (HG) phase function (Henyey and Greenstein 1941) with an asymmetry parameter close to 1. Indeed, Redmond Roche and King (2022b) used a HG phase function with an asymmetry parameter of 0.98, which yields a backscatter fraction $b = 0.00423$ for a single scattering event (see appendix F).

It is notoriously difficult to accurately resolve highly anisotropic scattering with a two-stream model (see Stamnes et al. 2017, for an overview), which has led to the development of approximations such as the delta-Eddington approximation (Joseph et al. 1976; Briegleb and Light 2007). We find that using $b = 0.00423$ with $\overline{\mu} = 1/2$ in our two-stream model results in values for the spectral albedo ($350\,\mathrm{nm} \leq \lambda \leq 800\,\mathrm{nm}$) of 0.8 m thick first-year sea ice that are too low compared with the results found by Redmond Roche and King (2022b) using the eight-stream TUV-snow model for the same optical properties. To resolve this discrepancy, we calculate the value b that minimises the mean squared difference between the spectral albedo of 0.8 m thick first-year ice calculated using our model and the values reported by Redmond Roche and King (2022b). This procedure yields $b = 0.00715$ as the most appropriate value for the backscatter fraction in our two-stream model, and we use this value going forward. Since we neglect scattering in the ocean and melt ponds, we set $r_{2\mathrm{S}} = 0$ where no ice is present ($\phi_s = 0$) and we use equation (4.4.7) when $\phi_s > 0$, which yields

$$r_{2\mathrm{S}}(\phi_s) = \begin{cases} 1.716\,\mathrm{m}^{-1} & \phi_s > 0, \\ 0\,\mathrm{m}^{-1} & \phi_s = 0, \end{cases}. \tag{4.5.1}$$

Here we have used $b = 0.00715$ and optical parameters from Redmond Roche and King (2022b), yielding an $r_{2\mathrm{S}}$ value consistent with the range of values reported by Perovich (1990).

4.5.2 Absorption

Unlike scattering, absorption in sea ice is strongly wavelength dependent. The spectral absorption coefficient $k(\lambda)$ in sea ice increases rapidly by several orders of magnitude with increasing wavelength in the shortwave range, making sea ice fairly transparent to visible light but optically thick to near infrared wavelengths. Therefore, following Redmond Roche and King (2022b), we use equation (4.4.6) to calculate $k_{2\mathrm{S}}(\lambda)$ by using experimentally determined values of $k(\lambda)$ for pure ice (Warren and Brandt 2008). The spectral absorption coefficient for water is very similar to that of pure ice, suggesting that it is reasonable to use the same values of $k_{2\mathrm{S}}(\lambda)$ throughout liquid and ice filled portions of the domain (Perovich 2017). This treatment of absorption is sufficient for sea ice and ocean water, however it is known that the presence of impurities can significantly alter the absorption of shortwave radiation in the sea-ice system (Grenfell et al. 2002; Marks and King 2013a; Marks and King 2013b; Lamare et al. 2016; Redmond Roche and King 2022b). In chapter 8, we extend this treatment of absorption to investigate the impact of oil droplets on radiative heating and light transmission in sea ice.

4.6 Optical parameters of interest for the sea-ice system

In this section, we define some optical parameters of interest that quantify the partitioning of the incident shortwave radiation into reflected, transmitted, and absorbed components. We also define the metrics used to quantify the transmission of PAR at the ice–ocean interface. We define quantities using the spectral irradiances obtained from the two-stream model and also the broadband counterpart obtained by averaging over the incident shortwave radiation spectrum (indicated with a tilde). For example the incident broadband shortwave radiation flux is given by

$$\widetilde{F}_{\mathrm{SW}} = \int_{\lambda_{\min}}^{\lambda_{\max}} F_{\mathrm{SW}}(\lambda)\,\mathrm{d}\lambda. \tag{4.6.1}$$

4.6.1 Surface albedo

In the absence of snow cover or a SSL, the spectral albedo of the ice is the fraction of the incident shortwave radiation that is reflected back to the atmosphere at each wavelength,

$$\alpha_{\mathrm{ice}}(\lambda) = f_{\lambda}^{+}(0). \tag{4.6.2}$$

Accounting for the fraction of the incident radiation scattered back to the atmosphere by any snow layer or SSL yields the total spectral albedo,

$$\alpha(\lambda) = \alpha_{\mathrm{surf}}(\lambda) + \alpha_{\mathrm{ice}}(\lambda). \tag{4.6.3}$$

Equation (4.6.3) can be integrated over the spectrum of the incident shortwave radiation to yield the total albedo,

$$\widetilde{\alpha} = \frac{\int_{\lambda_{\min}}^{\lambda_{\max}} F_{\mathrm{SW}}(\lambda)\alpha(\lambda)\,\mathrm{d}\lambda}{\int_{\lambda_{\min}}^{\lambda_{\max}} F_{\mathrm{SW}}(\lambda)\,\mathrm{d}\lambda}. \tag{4.6.4}$$

4.6.2 Transmittance

Similarly, we define the spectral transmittance through the ice to the ocean as the fraction of the incident shortwave radiation that is transmitted through the ice to the ocean at each wavelength,

$$\mathcal{T}(\lambda) = f_\lambda^-(-h_{\text{ice}}). \tag{4.6.5}$$

Integrating over the spectrum of the incident shortwave radiation yields the total transmittance,

$$\widetilde{\mathcal{T}} = \frac{\int_{\lambda_{\min}}^{\lambda_{\max}} F_{\text{SW}}(\lambda)\mathcal{T}(\lambda)\,\mathrm{d}\lambda}{\int_{\lambda_{\min}}^{\lambda_{\max}} F_{\text{SW}}(\lambda)\,\mathrm{d}\lambda}. \tag{4.6.6}$$

4.6.3 Radiative heating

The spectrally-integrated net shortwave radiation flux in the ice is

$$\widetilde{F}_{\text{net}}(z) = \int_{\lambda_{\min}}^{\lambda_{\max}} F_{\text{SW}}(\lambda) f_{\lambda,\,\text{net}}(z)\mathrm{d}\lambda, \tag{4.6.7}$$

which is used to compute the radiative heating term in equation (3.2.34) for the transient model of sea ice growth given in chapter 3.

4.6.4 Photosynthetically active radiation (PAR) at the ice–ocean interface

Radiation in the visible range (400–700 nm), so-called PAR, is used for photosynthesis by under-ice algae in Arctic waters. Since photosynthesis is a fundamentally quantum process, a more appropriate measure of light availability used to estimate photosynthesis rates in the ocean is the photon flux of PAR Q_{PAR} ($\text{mol}\,\text{m}^{-2}\,\text{s}^{-1}$). Following Morel and Smith (1974), we define the downwelling planar PAR irradiance and photon flux as

$$F_{\text{PAR}}^-(z) = \int_{400\,\text{nm}}^{700\,\text{nm}} F_\lambda^-(z)\,\mathrm{d}\lambda \tag{4.6.8}$$

and

$$Q_{\text{PAR}}^-(z) = \frac{1}{N_A}\int_{400\,\text{nm}}^{700\,\text{nm}} F_\lambda^-(z)\frac{\lambda}{2\pi\hbar c}\,\mathrm{d}\lambda, \tag{4.6.9}$$

respectively, where $N_A = 6.023 \times 10^{23}\,\mathrm{mol^{-1}}$ is Avogadro's number, $\hbar = 1.055 \times 10^{-34}\,\mathrm{J\,s}$ is the reduced Planck constant, and $c = 3.00 \times 10^{8}\,\mathrm{m\,s^{-1}}$ is the speed of light.

Equations (4.6.8) and (4.6.9) define the downwelling "flat plate" PAR irradiance and photon flux, respectively, which are measured by typical instruments in the field. However, photosynthetic tissues act as scalar collectors of light, such that rates of photosynthesis are more closely related to the scalar photon flux Q°_{PAR}, which can be 1.8–4.2 times greater than the "flat plate" value (Redmond Roche and King 2024). Assuming the radiance field is isotropic in both hemispheres (see appendix F), we find

$$Q^{\circ}_{\mathrm{PAR}}(z) = 2\left[Q^{-}_{\mathrm{PAR}}(z) + Q^{+}_{\mathrm{PAR}}(z)\right] \tag{4.6.10}$$

and, in particular, $Q^{\circ}_{\mathrm{PAR}}(-h_{\mathrm{ice}}) = 2Q^{-}_{\mathrm{PAR}}(-h_{\mathrm{ice}})$ at the ice–ocean interface, where there is no upwelling radiation stream. For comparison with previous studies, we also define the plane PAR transmittance,

$$\mathcal{T}_{\mathrm{PAR}} = \frac{F^{-}_{\mathrm{PAR}}(-h_{\mathrm{ice}})}{\int_{400\,\mathrm{nm}}^{700\,\mathrm{nm}} F_{\mathrm{SW}}(\lambda)\,\mathrm{d}\lambda}, \tag{4.6.11}$$

as the ratio of the downwelling "flat plate" irradiance in the PAR range at the ice–ocean interface to the incident irradiance in the PAR range (see Redmond Roche and King 2024, for example).

4.7 The Six-band two-stream (6B2S) model

To minimise computational cost, two-stream shortwave radiative transfer schemes in sea-ice models often use optical properties averaged over the entire shortwave wavelength band (Taylor and Feltham 2004). We choose to instead resolve some spectral variation in the optical properties, especially in the visible range, for two reasons: (1) to investigate the impact of oil pollution in sea ice, which only significantly alters the ice absorption coefficient for wavelengths less than 800 nm (see chapter 8), and (2) to investigate the transmittance of PAR at the ice–ocean interface.

We partition the incoming shortwave radiative power into six spectral bands, see $\mathcal{S}_i$ in table 4.1, where the index $i = 1, 2, \ldots, 6$ corresponds to:

1. near ultra-violet (NUV): 300–400 nm;

Parameter	**Value**
Cloudy sky spectral irradiance fraction ($\mathcal{S}_i$)	0.086 (NUV) 0.217 (VIS1) 0.196 (VIS2) 0.155 (VIS3) 0.301 (NIR) 0.045 (SWIR)
Wavelength weighted spectral power ($\mathcal{P}_i$)	– (NUV) 9.81×10^{-8} m (VIS1) 1.08×10^{-7} m (VIS2) 1.00×10^{-7} m (VIS3) – (NIR) – (SWIR)

Table 4.1: The fraction of the radiative power $\mathcal{S}_i$ in each wavelength band, as calculated from the incident shortwave spectrum under cloudy sky conditions (the dashed curve in figure 11 of Grenfell and Perovich 2004), and the wavelength weighted radiative power in each band divided by the total radiative power in the spectrum $\mathcal{P}_i$. The latter quantity is needed to calculate the PAR photon flux via equation (4.7.4).

2. visible 1 (VIS1): 400–500 nm;
3. visible 2 (VIS2): 500–600 nm;
4. visible 3 (VIS3): 600–700 nm;
5. near-infrared (NIR): 700–1200 nm; and
6. shortwave infrared (SWIR): 1200–3000 nm.

This partitioning is a compromise between computational efficiency and spectral resolution. We assume that the incoming shortwave radiation follows the spectrum given in Grenfell and Perovich (2004) for cloudy sky conditions and then calculate the fraction of the radiative power in each band via

$$\mathcal{S}_i = \frac{\int_{\lambda_{\min,\,i}}^{\lambda_{\max,\,i}} F_{\mathrm{SW}}(\lambda)\,\mathrm{d}\lambda}{\widetilde{F}_{\mathrm{SW}}}, \tag{4.7.1}$$

where $\lambda_{\min,\,i}$ and $\lambda_{\max,\,i}$ are the minimum and maximum wavelengths in the ith spectral band (see table 4.1). The three visible bands, which collectively contain over half of the incident radiation, are the same three bands available in the red-green-blue (RGB) shortwave radiative transfer scheme used in the NEMO ocean model, which was found to suitably capture spectral irradiance profiles in the ocean (Madec et al. 2024). The remaining bands do not directly correspond to any official designations, but are useful distinctions for our purposes in this thesis.

We have collected the required spectral optical properties for the radiative transfer model from published sources and then calculated the averaged values over each of the six spectral bands of interest (table 4.2). Dry snow, wet snow, and SSL albedo data is available for all spectral bands except SWIR, in which we set the albedo to the representative low value of 0.1. Since wet snow has significantly fewer ice–air interfaces than dry snow, it is therefore a much less effective scatterer of shortwave radiation. We found that both the dry and wet snow extinction coefficients given by Perovich (1990) underestimated the transmission of shortwave radiation in the visible range. Therefore, we use the values proposed by Lebrun et al. (2023) for the NUV and VIS1–3 bands, the value given by Perovich (1990) in the NIR band, and a large representative value of $1000\,\mathrm{m}^{-1}$ in the SWIR band (table 4.2). These values well reproduce observed light transmission (see §4.8.3). We use the SSL extinction coefficient values reported by Perovich (1990) and again set the value in the SWIR band to $1000\,\mathrm{m}^{-1}$ (table 4.2). More values for the albedo of dry snow and the SSL collected from the literature but not used in this work are given in table 4.2 for comparison.

We neglect the absorption of energy in the snow from shortwave radiation, but energy absorbed in the SSL is added back to the net radiation flux at $z = 0$ to ensure energy conservation in the ice. As a result, the computed radiation fluxes are discontinuous at $z = 0$ when an SSL is present. This discontinuity represents absorption in the SSL at the ice surface at the sub-grid scale.

The absorption coefficient in ice increases with wavelength such that radiation with wavelength larger than 1200 nm is completely absorbed within the first few centimetres of ice. Since our simulations will typically have a grid resolution larger than 1 cm we therefore avoid solving the two-stream equations for the SWIR band by assuming that all the radiation in this band is absorbed within the first grid cell.

Material	**Optical property**	**NUV**	**VIS1**	**VIS2**	**VIS3**	**NIR**	**SWIR**	**Source**
dry snow	albedo	0.88	0.88	0.87	0.87	0.73	–	Figure 2 of Light et al. (2022)
dry snow	albedo	0.88	0.88	0.90	0.90	0.71	0.10	Curve labelled May 21 in figure 3 of Grenfell and Perovich (1984)
dry snow	albedo	0.93	0.96	0.98	0.98	0.86	0.12	Curve labelled "cold snow" in figure 10(a) of Grenfell and Perovich (2004)
dry snow	albedo	0.97	0.97	0.97	0.96	0.84	–	Median of the box plots in figure 7(a) of Vérin et al. (2022)
dry snow	extinction coefficient (m^{-1})	15.8	15.8	19.0	30.1	127.8	–	Perovich (1990)
dry snow	extinction coefficient (m^{-1})	7	7	7	7	–	–	Lebrun et al. (2023)
wet snow	albedo	0.81	0.81	0.81	0.80	0.69	–	Figure 2 of Light et al. (2022)
wet snow	extinction coefficient (m^{-1})	8.9	8.9	10.8	17.1	88.8	–	Perovich (1990)
wet snow	extinction coefficient (m^{-1})	5	5	5	5	–	–	Lebrun et al. (2023)
SSL	albedo	0.74	0.75	0.74	0.72	0.48	–	Figure 2 of Light et al. (2022)
SSL	albedo	0.79	0.79	0.78	0.75	0.50	–	Undisturbed measurement labelled 20/07 in figure 2(a) of Smith et al. (2022)
SSL	albedo	0.80	0.82	0.82	0.79	0.56	–	Undisturbed measurement labelled 23/07 in figure 2(a) of Smith et al. (2022)
SSL	albedo	0.78	0.79	0.78	0.75	0.49	–	Undisturbed measurement labelled 24/07 in figure 2(a) of Smith et al. (2022)
SSL	albedo	0.80	0.84	0.85	0.83	0.56	–	Undisturbed measurement labelled 27/07 in figure 2(a) of Smith et al. (2022)
SSL	extinction coefficient (m^{-1})	3.0	3.1	4.3	7.8	85.6	–	Perovich (1990)
ice	absorption coefficient (m^{-1})	6.83×10^{-4}	4.18×10^{-3}	5.75×10^{-2}	0.285	14.6	9.61×10^{4}	Warren and Brandt (2008)

Table 4.2: Optical properties for dry snow, wet snow, the SSL, and ice collected from the literature and averaged over each wavelength band. In the case of the extinction coefficient for wet and dry snow values are provided from two different sources. The lower values given by Lebrun et al. (2023) in the UV and visible range are found to give better agreement with observed light transmittance under sea ice. Here, we use the values from Lebrun et al. (2023) for the extinction coefficient of dry and wet snow in the NUV, VIS1, VIS2, and VIS3 bands, but the value calculated from the data of Perovich (1990) for the NIR band.

This leaves five spectral bands in which we must solve a boundary value problem with two coupled ODEs. We do so numerically using a collocation method (see chapter 5).

To evaluate integrals over the incident radiation spectrum of a spectral quantity q_λ, we replace the integral with a sum weighted by the fraction of the incident radiation in each spectral band,

$$\int_{\lambda_{\min}}^{\lambda_{\max}} F_{\mathrm{SW}}(\lambda) q_\lambda \,\mathrm{d}\lambda \approx \widetilde{F}_{\mathrm{SW}} \sum_{i=1}^{i=6} q_i \,\mathcal{S}_i. \tag{4.7.2}$$

For example, equation (4.6.7) becomes

$$\widetilde{F}_{\mathrm{net}}(z) \approx \widetilde{F}_{\mathrm{SW}} \sum_{i=1}^{i=6} f_{i,\,\mathrm{net}}(z)\,\mathcal{S}_i. \tag{4.7.3}$$

Integrals over the PAR range are approximated by a sum over the visible bands (i.e., $i = 2,\ 3,\ 4$). The calculation of $Q^-_{\mathrm{PAR}}(z)$ requires summing over the incident spectrum weighted by wavelength,

$$Q^-_{\mathrm{PAR}}(z) \approx \frac{\widetilde{F}_{\mathrm{SW}}}{2\pi\hbar c N_A} \sum_{i=2}^{i=4} f_i^-(z)\,\mathcal{P}_i, \tag{4.7.4}$$

where average first moments of the incident spectrum in each band $\mathcal{P}_i$ are given in table 4.1.

4.8 Results

We next present some calculations using the 6B2S model developed above. First, we illustrate the typical net irradiance profiles in the ice for each spectral band for snow-covered ice, bare ice, and ponded ice (§4.8.1). We then confirm that the model is able to reproduce observed albedos for snow-covered, bare, and ponded ice (§4.8.2). These three cases are informative because each of these surface conditions can occur at some point during the evolution of first-year sea ice over one season, and the change from one case to another is accompanied by a large change in the relative fractions of incoming shortwave radiation reflected, absorbed, and transmitted by the ice. Finally, we validate the predicted transmittance of PAR at the ice–ocean interface against field data for both dry and wet snow cover (§4.8.3). We also compare the transmitted PAR predicted by our model with another model from the literature (Redmond Roche and King 2024).

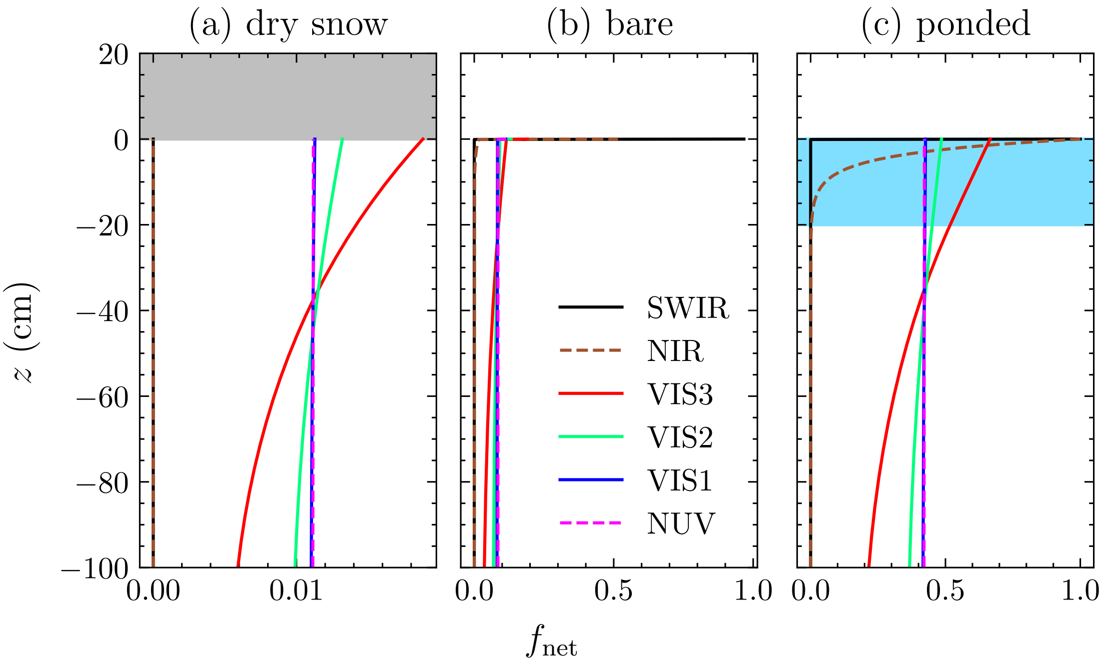

Figure 4.2: Normalised net irradiance profiles calculated using the 6B2S model for a 100 cm thick layer of sea ice for each spectral band: NUV (dashed pink), VIS1 (solid blue), VIS2 (solid green), VIS3 (solid red), NIR (dashed brown), and SWIR (solid black). Profiles for three different surface conditions are shown: (a) dry-snow covered ice with $h_{\mathrm{snow}} = 20\,\mathrm{cm}$, (b) bare ice with $h_{\mathrm{SSL}} = 4\,\mathrm{cm}$, (c) ponded ice with $h_{\mathrm{pond}} = 20\,\mathrm{cm}$. The ice surface is at $z = 0$ in panels (a) and (b), and the ice–ocean interface is at $z = -100\,\mathrm{cm}$. Snow is shaded grey in panel (a) and the melt pond is shaded light blue in panel (c). The optical parameters are those given in the text. Note that the scale on the horizontal axis is different in panels (b) and (c) compared with panel (a).

4.8.1 Irradiance profiles

Figure 4.2 shows the net irradiance profile in the ice for each wavelength band normalised by the incident irradiance in that band for three surface conditions: (a) dry-snow-covered ice, (b) bare ice, (c) and ponded ice. When dry snow covers the ice (figure 4.2a), almost all infrared radiation (NIR and SWIR bands) is reflected or absorbed by the snow layer before reaching the ice. Around 1% of the incident radiation in the NUV and visible bands is transmitted through the snow layer to the ice. There is more significant absorption of the longer visible wavelengths in the VIS3 band compared with the VIS1 and VIS2 bands in the ice. As a result, the spectrum of transmitted radiation at the ice–ocean interface is heavily shifted towards the blue and green wavelengths.

For bare ice with a SSL (figure 4.2b), there is significant absorption of all wavelengths on a sub-grid scale at the ice surface, and as a result the modelled net irradiance profiles are discontinuous at $z = 0$. Radiation in the NIR and SWIR bands, which makes up 34.6% of the incident radiation (table 4.1), is effectively completely absorbed at the surface. Between 5 and 10% of the incident radiation in the NUV and visible bands is transmitted through the ice to the ocean, which is around one order of magnitude larger than in the snow-covered case.

For ponded ice (figure 4.2a), radiation in the SWIR band is assumed to be absorbed entirely at the surface of the pond. Radiation in the NIR band is almost entirely absorbed within a pond of depth 20 cm before reaching the underlying ice. Between 20 and 50% of the incident radiation in the NUV and visible bands is transmitted to the ocean, with higher transmission of the shorter wavelengths.

In summary, snow cover permits only a small fraction of the incident radiation in the visible and UV wavelength bands to reach the ice and underlying ocean. Bare ice still reflects a significant fraction of the incoming radiation due to the SSL, but also experiences heating at the surface and internally. The formation of a melt pond leads to much more penetration of visible wavelengths through the ice to the ocean, with significant absorption of radiation in the pond itself. These results are all consistent with previous studies of shortwave radiation partitioning in the sea ice system (e.g. Perovich 2017).

4.8.2 Spectrally-integrated albedo & transmittance

Figure 4.3 shows the spectrally-integrated transmittance, PAR transmittance, and albedo of snow-covered (top row) and ponded (bottom row) sea ice. The variation in these three spectrally-integrated properties with ice depth is minor for the values considered when the ice is snow covered, which is to be expected from previous work (Perovich et al. 1986). There is greater variation with ice depth for ponded ice. The largest effect of varying ice thickness is on the transmitted PAR for ponded ice, with around a twofold increase in transmittance between the thickest and thinnest ice considered.

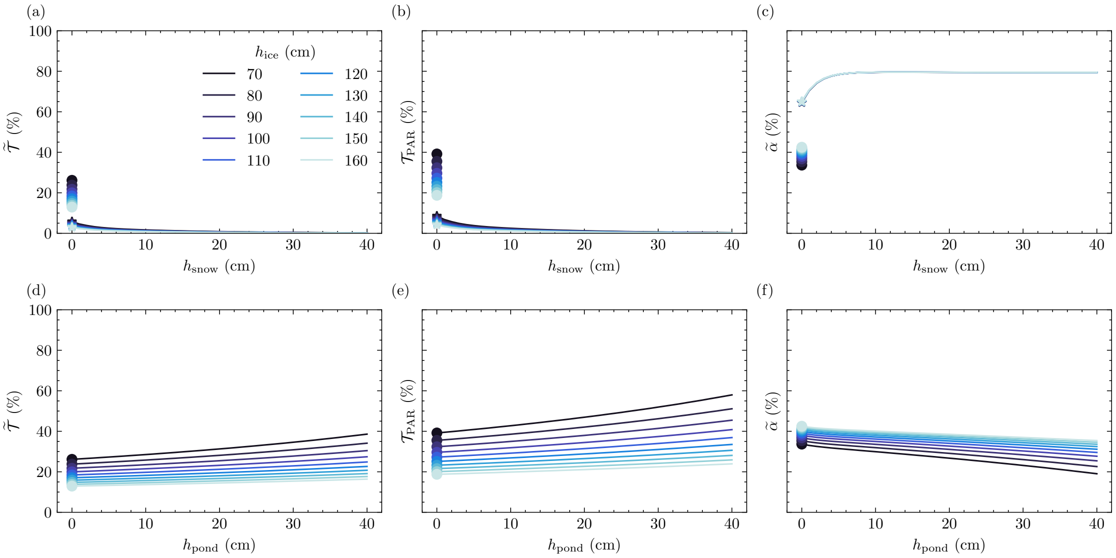

Figure 4.3: The broadband transmittance (equation 4.6.6; left column), PAR transmittance (equation 4.6.11; middle column), and broadband albedo (equation 4.6.4; right column) of sea ice with varying thickness (blue lines) calculated using the 6B2S model with the optical properties in table 4.2 (dry snow values). The top row shows how the calculated optical properties vary with snow thickness. The points marked with a star indicate values for bare ice with $h_{\text{SSL}} = 4\,\text{cm}$. The points marked with a circle indicate values for bare ice with no SSL. The bottom row shows how the calculated optical properties vary with surface melt pond depth.

Examining the surface albedo (right column of figure 4.3), we see that the albedo of ice covered with a layer of dry snow thicker than around 5 cm is around 0.8, which is consistent with the lower end of the range of values reported in the literature (Grenfell and Maykut 1977; Grenfell and Perovich 2004; Vérin et al. 2022; Light et al. 2022). As the snow thickness decreases, the albedo decreases to around 0.65 for bare ice with a SSL before decreasing to between 0.2 and 0.4 for ponded ice, again consistent with observations in the literature (Perovich et al. 2002; Light et al. 2022).

The transmittance and PAR transmittance (left column and middle column of figure 4.3) decrease rapidly from a few percent for bare ice with a SSL to very low values as snow thickness increases, as examined further in §4.8.3. The loss of the SSL and formation of a melt pond acts to dramatically increase transmittance and PAR transmittance to the ocean, which is a well documented phenomenon (e.g. Perovich 1990).

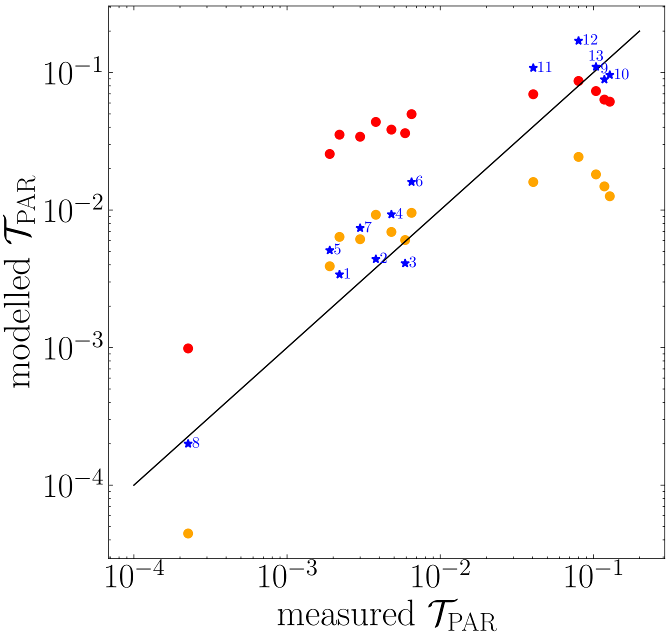

Figure 4.4: Modelled PAR transmittance (equation 4.6.11) versus measured PAR transmittance values compiled from the literature (Redmond Roche and King 2024). The numbered blue stars indicate the values predicted by the TUV-snow model used by Redmond Roche and King (2024), where the numbers refer to the entry for the observation in their table A1. The orange and red circles indicate modelled values calculated for dry and wet snow, respectively, using our 6B2S model with snow and ice thickness given by the measured values. The black line indicates perfect agreement between the modelled and measured values.

4.8.3 Transmitted PAR

Stroeve et al. (2021) observed that the transmitted PAR photon flux at the ice–ocean interface $Q^{-}_{\mathrm{PAR}}(-h_{\mathrm{ice}})$ is linearly related to the transmitted broadband shortwave irradiance $\widetilde{F}_{\mathrm{net}}(-h_{\mathrm{ice}})$ via

$$\frac{Q^{-}_{\mathrm{PAR}}(-h_{\mathrm{ice}})}{\widetilde{F}_{\mathrm{net}}(-h_{\mathrm{ice}})} = (3.5100 \pm 0.0173)\,\mu\mathrm{mol\,J^{-1}}. \tag{4.8.1}$$

This linear fit was calculated using light transmission data from the *GreenEdge* field campaign in the Arctic Ocean, sampling both landfast and pack ice, and is suggested to be appropriate for snow-covered, bare, and ponded ice. Our 6B2S model predicts values of this ratio that are in good agreement with Stroeve et al. (2021):

- 3.414–$3.825\,\mu\mathrm{mol\,J^{-1}}$ (for ice with $h_{\mathrm{snow}} = 20\,\mathrm{cm}$),
- 3.352–$3.737\,\mu\mathrm{mol\,J^{-1}}$ (for bare ice with $h_{\mathrm{SSL}} = 4\,\mathrm{cm}$),
- 3.417–$3.796\,\mu\mathrm{mol\,J^{-1}}$ (for ponded ice with $h_{\mathrm{pond}} = 20\,\mathrm{cm}$),

where the range of values is found by varying the ice thickness from 2 m to 0.5 m.

A previous study compiled values of PAR transmittance though sea ice of varying thickness and snow cover from the literature (see table A1 in Redmond Roche and King 2024), which was used to validate the performance of the TUV-Snow model for predicting PAR transmittance at the ice–ocean interface. Using the same dataset, we compare the performance of our 6B2S model with the TUV-snow model in figure 4.4. We identify two main clusters of PAR transmittance observations.

Observations numbered 1–7 are from winter/spring, have snow thickness greater than 10 cm, and exhibit PAR transmittance values around 1% or less. These observations are well reproduced by our model using optical parameters for dry snow (orange). Both our model with optical properties for dry snow and the TUV-snow model show a slight bias towards overestimating the PAR transmittance for these winter/spring observations.

Observations numbered 9–13 are from summer, have thinner snow cover, and exhibit PAR transmittance values around 10%. These observations are well reproduced by our model using optical parameters for wet snow (red).

Observation number 8 had an extremely thick snow cover (95 cm of snow on 110 cm of ice) and is not particularly well reproduced by our model. However, uncertainties are high when measuring such small transmittance values and such large snow depths do not occur at the field site investigated later in this thesis (chapters 6–8).

We conclude that our model is capable of accurately predicting the transmission of radiation in the PAR range through sea ice throughout the year for a range of snow and ice thicknesses so long as we choose optical parameters for dry snow in the Winter / Spring and optical parameters for wet snow in the summer.

4.9 Conclusions

In this chapter, we reviewed the role of shortwave radiation in the sea-ice system and the typical yearly cycle in the incident shortwave radiation in the Arctic. We introduced the fundamentals of absorption and scattering that govern the propagation of shortwave radiation in snow, ice, and water. Following existing literature, we parameterised the transmission of shortwave radiation through the snow and SSL using Beer's law with appropriate albedos and extinction coefficients to arrive at a boundary condition for the incident shortwave radiation reaching the ice interior. Within the ice, ocean, and any surface melt pond, we utilise the two-stream approximation to solve for the upwelling and downwelling spectral irradiance profiles. We introduce six spectral bands in which we solve the two-stream model, which maintains a good balance between computational efficiency and spectral resolution. We use this model to calculate the energy source due to the absorption of shortwave radiation required by the transient sea ice model developed in chapter 3.

We used the 6B2S model to perform some idealised calculations illustrating typical irradiance profiles for snow-covered, bare, and ponded ice. We also confirmed that the model is capable of accurately reproducing broadband albedos typical for snow-covered, bare, and ponded ice. Finally, we showed that, for our choice of optical parameters, the model can accurately predict the transmitted PAR through snow-covered ice reported in the literature. This suggests that the shortwave radiative transfer scheme developed in this chapter is suitable for investigating the transmission of PAR at the ice–ocean interface.

In chapter 5 we describe the implementation of a numerical method to solve the 6B2S model. The resulting implementation is used throughout chapters 6–8 as the radiative transfer scheme for the transient sea ice model described in chapter 3. In chapter 8 we modify the absorption coefficient of the model to account for the enhanced absorption of ice polluted with oil droplets. This allows us to investigate the impact of oil droplets on the partitioning of shortwave radiation in the sea-ice system.

5

Numerical methods for the transient problem

5.1 Introduction

In chapter 3, we derived a horizontally uniform, transient, three-phase mushy-layer model for sea ice growth in a saltwater ocean containing dissolved atmospheric gasses. The model comprises a system of coupled dimensionless partial differential equations (PDEs) for the bulk enthalpy $\mathcal{H}(z,\, t)$, bulk salinity $\Theta(z,\, t)$, bulk dissolved gas content $\Gamma_d(z,\, t)$, and gas fraction $\phi_g(z,\, t)$ as functions of the dimensionless time $t \in [0,\, t_f]$ and dimensionless vertical coordinate $z \in [-1,\, 0]$. From these bulk variables the dimensionless temperature, liquid and solid phase salinities, and liquid and solid volume fractions are calculated using piecewise expressions derived using the enthalpy method. We impose boundary conditions at the bottom of the domain, $z = -1$, that specify the oceanic heat flux, salinity, and saturation state of dissolved gas. We impose boundary conditions at the top of the domain, $z = 0$, that prevent the flux of dissolved salt and gas, and that specify the atmospheric heat flux using a surface energy balance that includes sensible and latent heat fluxes, the net longwave radiative flux, and conductive heat transport through a quasi-steady homogeneous snow layer (if present). In chapter 4, we introduced a spectral model for the propagation of shortwave radiation that provides the energy source due to the absorption of shortwave radiation. In this chapter, we describe a finite volume scheme used to solve the dimensionless conservation equations for heat, salt, and gas in the cases of finite Damköhler number Da and infinite Damköhler number $Da \to \infty$.

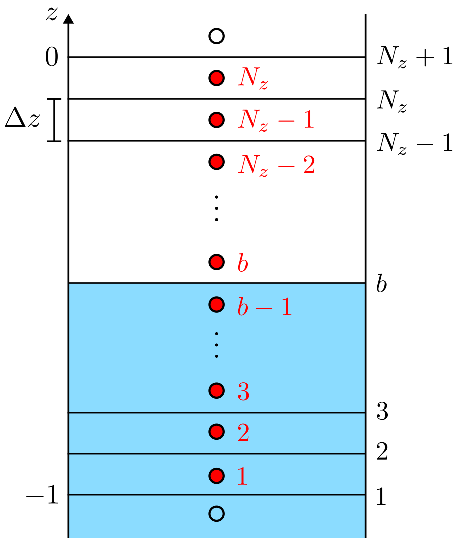

Figure 5.1: Schematic diagram showing the spatial discretisation of the non-dimensionalised domain $-1 < z < 0$, with the grid spacing Δz indicated on the z axis on the left of the diagram. The cell centre positions $\boldsymbol{z}^{\odot}$ are shown as red filled circles between the black lines showing cell edge positions $\boldsymbol{z}^{\ominus}$. The ghost grid with positions $\boldsymbol{z}^{\circledast}$ includes two extra points at the top and bottom of the domain shown as unfilled black circles. The indices of the cell edge positions are labelled in black text on the right hand side of the diagram and the indices of the cell centre positions are labelled in red text. The index of the cell edge labelled b is the position of the ice–ocean interface with the completely liquid region of the domain coloured in blue.

In §5.2, we describe the implementation of a finite volume scheme to solve the PDE system, including our implementation of the RJW14 brine convection scheme and the six-band two-stream (6B2S) model described in chapter 4. We then briefly describe the explicit algorithm used by the Python package `SciPy` to numerically integrate the spatially discretised system. In §5.3, we validate these numerical methods against two benchmark problems. We first consider, the diffusive growth of sea ice from a cooled top boundary, for which a semi-analytical solution is available for two-phase mushy layers. We then compare the spectral albedo, transmittance, and net irradiance calculated using the 6B2S model to the same model with higher spectral resolution, and to the TUV-snow model from the literature.

5.2 Finite-volume scheme

5.2.1 Spatial discretisation

To implement a finite-volume method (LeVeque 2002), the domain $(-1 < z < 0)$ is discretised using N_z cells of equal width $\Delta z = 1/N_z$ shown in figure 5.1. The dimensionless conservation equations for the transient model, derived in chapter 3, are integrated over each cell to obtain a system of ordinary differential equations (ODEs) for the mean values of each primary variable in each cell. Typical spatial resolutions for the simulations in this thesis range from $N_z = 50$ to $N_z = 100$, as discussed further in §5.3. The mean values of the bulk enthalpy $\mathcal{H}$, bulk salinity Θ, dissolved gas content Γ_d, and gas fraction ϕ_g are evaluated at the position of cell centres $\boldsymbol{z}^{\circledcirc} = [z_1^{\circledcirc}, z_2^{\circledcirc}, \ldots, z_{N_z}^{\circledcirc}]$, where

$$z_i^{\circledcirc} = -1 + (2i-1)\frac{\Delta z}{2}, \qquad i = 1, 2, \ldots, N_z. \tag{5.2.1}$$

Fluxes are evaluated at cell edges $\boldsymbol{z}^{\ominus} = [z_1^{\ominus}, z_2^{\ominus}, \ldots, z_{N_z+1}^{\ominus}]$, where

$$z_i^{\ominus} = -1 + (i-1)\Delta z, \qquad i = 1, 2, \ldots, N_z + 1. \tag{5.2.2}$$

Boundary conditions are implemented using a ghost cell at the top and bottom of the domain that extends the grid of cell centres to $\boldsymbol{z}^{\circledast} = [z_1^{\circledast}, z_2^{\circledast}, \ldots, z_{N_z+2}^{\circledast}]$, where

$$z_i^{\circledast} = -1 + (2i-3)\frac{\Delta z}{2}, \qquad i = 1, 2, \ldots, N_z + 2. \tag{5.2.3}$$

For the remainder of this chapter, quantities evaluated on each of these grids are denoted by vectors with the corresponding superscript.

We solve equations (3.2.34), and (3.2.36)–(3.2.38) from chapter 3 numerically using a finite volume scheme. To do so, we write the system in the form

$$\frac{\mathrm{d}\boldsymbol{y}^{\circledcirc}}{\mathrm{d}t} = \boldsymbol{f}^{\circledcirc}(\boldsymbol{y}^{\circledcirc}, t), \tag{5.2.4}$$

subject to the initial condition $\boldsymbol{y}^{\circledcirc}(0) = \boldsymbol{y}^{\circledcirc}{}_0$, where $\boldsymbol{y}^{\circledcirc}$ is the vector of length $4N_z$ formed by concatenating the vectors storing the four bulk variables evaluated on cell centres,

$$\boldsymbol{y}^{\circledcirc} = \left[\boldsymbol{\mathcal{H}}^{\circledcirc}, \boldsymbol{\Theta}^{\circledcirc}, \boldsymbol{\Gamma}_{\boldsymbol{d}}^{\circledcirc}, \boldsymbol{\phi}_{\boldsymbol{g}}^{\circledcirc}\right], \tag{5.2.5}$$

where $\boldsymbol{\mathcal{H}}^{\circledcirc}$, $\boldsymbol{\Theta}^{\circledcirc}$, $\boldsymbol{\Gamma}_{\boldsymbol{d}}^{\circledcirc}$, and $\boldsymbol{\phi}_{\boldsymbol{g}}^{\circledcirc}$ are the bulk enthalpy, bulk salinity, dissolved gas content, and gas fraction evaluated on cell centres, respectively. The function $\boldsymbol{f}^{\circledcirc}$ encodes the spatially discretised conservation equations (3.2.34), and (3.2.36)–(3.2.38) at each cell centre and can be written as the concatenation:

$$\boldsymbol{f}^{\circledcirc}(\boldsymbol{y}^{\circledcirc}, t) = \left[\boldsymbol{f}^{\circledcirc}_{\boldsymbol{\mathcal{H}}}(t, \boldsymbol{y}^{\circledcirc}),\, \boldsymbol{f}^{\circledcirc}_{\boldsymbol{\Theta}}(t, \boldsymbol{y}^{\circledcirc}),\, \boldsymbol{f}^{\circledcirc}_{\boldsymbol{\Gamma_d}}(t, \boldsymbol{y}^{\circledcirc}),\, \boldsymbol{f}^{\circledcirc}_{\boldsymbol{\phi_g}}(t, \boldsymbol{y}^{\circledcirc})\right], \tag{5.2.6}$$

where $\boldsymbol{f}^{\circledcirc}_{\boldsymbol{\mathcal{H}}}$, $\boldsymbol{f}^{\circledcirc}_{\boldsymbol{\Theta}}$, $\boldsymbol{f}^{\circledcirc}_{\boldsymbol{\Gamma_d}}$, and $\boldsymbol{f}^{\circledcirc}_{\boldsymbol{\phi_g}}$ are derived below.

The boundary conditions in §3.4 are used to add values in the ghost cells to the bulk variables to obtain $\boldsymbol{\mathcal{H}}^{\circledast}$, $\boldsymbol{\Theta}^{\circledast}$, $\boldsymbol{\Gamma}^{\circledast}_{\boldsymbol{d}}$, and $\boldsymbol{\phi}^{\circledast}_{\boldsymbol{g}}$. Dirichlet boundary conditions are applied directly in the ghost cells; for example,

$$\Theta^{\circledast}_{1} = 0$$

from equation (3.4.1). Neumann (flux) boundary conditions are applied by calculating the flux at the top or bottom boundary using a first-order finite-difference approximation. For example, the boundary condition given by equation (3.4.2) is discretised as

$$\frac{\Theta^{\circledast}_{N_z+2} - \Theta^{\circledast}_{N_z+1}}{\Delta z} = 0,$$

which can be rearranged to find the appropriate value for $\Theta^{\circledast}_{N_z+2}$ to be imposed in the ghost cell. For the heat-flux boundary conditions (equations 3.4.8 and 3.4.9), this procedure requires solving a non-linear equation for the ghost-cell value at each timestep and is implemented using the `scipy.optimize.fsolve` function from the `SciPy` Python library (Virtanen et al. 2020).

The dimensionless dissolved gas concentration $\boldsymbol{\omega}^{\circledast}$, dimensionless temperature $\boldsymbol{\theta}^{\circledast}$, liquid salinity $\boldsymbol{\Theta}^{\circledast}_{\boldsymbol{l}}$, solid fraction $\boldsymbol{\phi}^{\circledast}_{\boldsymbol{s}}$, and liquid fraction $\boldsymbol{\phi}^{\circledast}_{\boldsymbol{l}}$ are obtained from $\boldsymbol{y}^{\circledast}$ via equations (3.2.40), (3.3.8), (3.3.9), (3.3.7), and (3.3.3).

The differentiation matrix $\boldsymbol{D}_M$ of dimensions $(M,\, M+1)$ is

$$(\boldsymbol{D}_M)_{ij} = \begin{cases} \dfrac{1}{\Delta z}, & j = i+1, \\ -\dfrac{1}{\Delta z}, & j = i, \\ 0, & \text{otherwise}, \end{cases} \qquad i = 1, 2, \ldots, M, \quad j = 1, 2, \ldots, M+1. \tag{5.2.7}$$

Multiplication by the matrix $\boldsymbol{D}^{\ominus} = \boldsymbol{D}_{N_z}$ provides a centred finite-difference approximation at cell centres of the first z-derivative of a quantity defined on cell edges.

Multiplication by the matrix $\boldsymbol{D}^{\circledast} = \boldsymbol{D}_{N_z+1}$ provides a centred finite-difference approximation at cell edges of the first z-derivative of a quantity defined on the ghost grid.

The geometric-average-operator is

$$[\mathcal{G}(\boldsymbol{q}^{\circledast})]_i = \sqrt{q_i^{\circledast} q_{i+1}^{\circledast}}, \quad i = 1, 2, \ldots, N_z + 1, \tag{5.2.8}$$

and interpolates values on the ghost grid to the cell edges. The upwinding operator is

$$[\mathcal{U}(\boldsymbol{q}^{\circledast},\, \boldsymbol{u}^{\ominus})]_i = \begin{cases} q_i^{\circledast} u_i^{\ominus}, & u_i^{\ominus} \geq 0, \\ q_{i+1}^{\circledast} u_i^{\ominus}, & u_i^{\ominus} < 0, \end{cases}, \quad i = 1, 2, \ldots, N_z + 1, \tag{5.2.9}$$

and evaluates the flux of a quantity at the cell edges according to the sign of the velocity $\boldsymbol{u}^{\ominus}$. Using this operator, advective fluxes are discretised using the first-order upwind scheme for numerical stability (LeVeque 2002).

For use in equation (5.2.4), equation (3.2.34) is discretised as

$$\boldsymbol{f}_{\boldsymbol{\mathcal{H}}}^{\circledcirc} = -\boldsymbol{D}^{\ominus} \cdot \mathcal{U}\left(\boldsymbol{\theta}^{\circledast},\, \boldsymbol{w}^{\ominus}{}_{l}^{T}\right) + \boldsymbol{D}^{\ominus} \cdot \left[\boldsymbol{d}^{\ominus}{}_{\mathcal{H}} * \left(\boldsymbol{D}^{\circledast} \cdot \boldsymbol{\theta}^{\circledast}\right)\right] - \boldsymbol{\mathcal{S}}_{\mathrm{RJW14}}^{\circledcirc} * \boldsymbol{\theta}^{\circledcirc} + \boldsymbol{D}^{\ominus} \cdot \widetilde{\boldsymbol{\mathcal{F}}}_{\mathrm{net}}^{\ominus}, \tag{5.2.10}$$

where $\boldsymbol{w}_{\boldsymbol{l}}^{\ominus \boldsymbol{T}}$ and $\boldsymbol{\mathcal{S}}_{\mathrm{RJW14}}^{\circledcirc}$ are the convective upwelling velocity and brine-channel sink term (see §3.2.2), $\widetilde{\boldsymbol{\mathcal{F}}}_{\mathrm{net}}^{\ominus}$ is the net shortwave radiative flux (see chapter 4), $\cdot$ denotes the standard matrix product, $*$ denotes the element-wise product, and

$$\boldsymbol{d}_{\boldsymbol{\mathcal{H}}}^{\ominus} = \boldsymbol{\phi}_{\boldsymbol{s}}^{\ominus} \nu_s + \boldsymbol{\phi}_{\boldsymbol{l}}^{\ominus} + \frac{\mathsf{g}(\boldsymbol{\phi}_{\boldsymbol{l}}^{\ominus} - 1)}{Le_{\varepsilon}} \tag{5.2.11}$$

is the phase-averaged dimensionless thermal diffusivity, where $\boldsymbol{\phi}_{\boldsymbol{l}}^{\ominus} = \mathcal{G}(\boldsymbol{\phi}_{\boldsymbol{l}}^{\circledast})$ and $\boldsymbol{\phi}_{\boldsymbol{s}}^{\ominus} = 1 - \boldsymbol{\phi}_{\boldsymbol{l}}^{\ominus}$. We evaluate $\phi_l^{\ominus}$ using the geometric average to ensure that there can be no liquid flux across the edge of a cell that is completely solid. For numerical stability, we have replaced the unit step function H with a smooth alternative,

$$\mathsf{g}(x) = \begin{cases} e^{x/d_{\phi}}, & x < 0, \\ 1, & x \geq 0, \end{cases}, \tag{5.2.12}$$

where $d_{\phi} \ll 1$ is a smoothing parameter, the precise value of which should not have a meaningful qualitative or quantitative impact on our results. We use $d_{\phi} = 0.01$ throughout this thesis, which ensures that the last term in equation (5.2.11) is less than 1×10^{-3} for $\phi_l < 0.9$ and the value of $Le_\varepsilon = 0.126$ considered in this thesis. To ensure that eddy diffusivity only plays a significant role in liquid regions of the domain, the value of d_ϕ should be decreased if the eddy diffusivity is increased. Note that $\mathsf{g}(x)$ is evaluated element-wise when x is vector valued.

For use in equation (5.2.4), equation (3.2.36) is discretised as

$$\boldsymbol{f}^{\circledcirc}_{\boldsymbol{\Theta}} = -\boldsymbol{D}^{\ominus} \cdot \mathcal{U}\left(\boldsymbol{\Theta}^{\circledast}_{\boldsymbol{l}} + \mathcal{C},\, \boldsymbol{w}^{\ominus}_{\boldsymbol{l}}\right) + \frac{1}{Le_S}\boldsymbol{D}^{\ominus} \cdot \left[\boldsymbol{d}^{\ominus}_{\boldsymbol{S}} * \left(\boldsymbol{D}^{\circledast} \cdot \boldsymbol{\Theta}^{\circledast}_{\boldsymbol{l}}\right)\right] - \boldsymbol{\mathcal{S}}^{\circledcirc}_{\mathrm{RJW14}} * (\boldsymbol{\Theta}^{\circledcirc}_{\boldsymbol{l}} + \mathcal{C}), \tag{5.2.13}$$

where

$$\boldsymbol{d}^{\ominus}_{\boldsymbol{S}} = \boldsymbol{\phi}^{\ominus}_{\boldsymbol{l}} + \frac{Le_S}{Le_\varepsilon}\mathsf{g}(\boldsymbol{\phi}^{\ominus}_{\boldsymbol{l}} - 1). \tag{5.2.14}$$

For us in equation (5.2.4), equation (3.2.37) is discretised as

$$\boldsymbol{f}^{\circledcirc}_{\boldsymbol{\Gamma_d}} = -\chi\boldsymbol{D}^{\ominus} \cdot \mathcal{U}\left(\boldsymbol{\omega}^{\circledast},\, \boldsymbol{w}^{\ominus}_{\boldsymbol{l}}\right) + \frac{\chi}{Le_\xi}\boldsymbol{D}^{\ominus} \cdot \left[\boldsymbol{d}^{\ominus}_{\boldsymbol{\xi}} * (\boldsymbol{D}^{\circledast} \cdot \omega^{\circledast})\right] - \chi\boldsymbol{\mathcal{S}}^{\circledcirc}_{\mathrm{RJW14}} * \boldsymbol{\omega}^{\circledcirc} - \chi Da\boldsymbol{\mathcal{N}}^{\circledcirc}, \tag{5.2.15}$$

where $\boldsymbol{\mathcal{N}}^{\circledcirc}$ is the dimensionless gas exsolution rate (defined in chapter 2) evaluated at cell centers and

$$\boldsymbol{d}^{\ominus}_{\boldsymbol{\xi}} = \boldsymbol{\phi}^{\ominus}_{\boldsymbol{l}} + \frac{Le_\xi}{Le_\varepsilon}\mathsf{g}(\boldsymbol{\phi}^{\ominus}_{\boldsymbol{l}} - 1). \tag{5.2.16}$$

Finally, for use in equation (5.2.4), equation (3.2.38) is discretised as

$$\boldsymbol{f}^{\circledcirc}_{\boldsymbol{\phi_g}} = -\mathcal{B}\delta_0^2\boldsymbol{D}^{\ominus} \cdot \mathcal{U}\left(d(\boldsymbol{\delta}^{\circledast}) * \boldsymbol{\phi}^{\circledast}_{\boldsymbol{g}},\, \mathbf{1}^{\ominus}\right) + \chi Da\boldsymbol{\mathcal{N}}^{\circledcirc}, \tag{5.2.17}$$

where $\mathbf{1}^{\ominus}$ is a vector of ones of length $N_z + 1$ and $d(\boldsymbol{\delta}^{\circledast})$ is the dimensionless bubble drag function, as given by equation (3.2.39), where

$$\boldsymbol{\delta}^{\circledast} = \frac{\delta_0}{\boldsymbol{\phi}^{\circledast q}_{\boldsymbol{l}} + \varepsilon_{\mathrm{re}}} \tag{5.2.18}$$

with the division performed element-wise and $\varepsilon_{\mathrm{re}} = 1 \times 10^{-6}$ is a numerical regularisation to prevent floating-point errors as $\phi_l \to 0$. Equation (5.2.18) recovers the definition of δ given in chapter 2 when $\varepsilon_{\mathrm{re}} = 0$.

In the case of rapid gas exsolution ($Da \to \infty$), we need only calculate the bulk gas content $\Gamma = \Gamma_d + \phi_g$ and the evolution of the system is determined by equation (5.2.4) with

$$\boldsymbol{y}^{\circledcirc} = [\boldsymbol{\mathcal{H}}^{\circledcirc},\, \boldsymbol{\Theta}^{\circledcirc},\, \boldsymbol{\Gamma}^{\circledcirc}], \quad \text{and} \quad \boldsymbol{f}^{\circledcirc}(\boldsymbol{y}^{\circledcirc}, t) = \left[\boldsymbol{f}^{\circledcirc}_{\boldsymbol{\mathcal{H}}},\, \boldsymbol{f}^{\circledcirc}_{\boldsymbol{\Theta}},\, \boldsymbol{f}^{\circledcirc}_{\boldsymbol{\Gamma_d}} + \boldsymbol{f}^{\circledcirc}_{\boldsymbol{\phi_g}}\right], \tag{5.2.19}$$

and the appropriate boundary conditions described in §3.4. In this case, $\boldsymbol{\phi}_{\boldsymbol{g}}^{\circledast}$ and $\boldsymbol{\omega}^{\circledast}$ are determined via the equilibrium constraints given by equations (3.2.42) and (3.2.43).

Implementation of the RJW14 brine convection scheme

The position of the base of the ice z_b is taken to lie at $z_{i_b}^{\ominus}$ on the edge grid where the index i_b is given by

$$i_b = \min\Big\{i : \phi_{s,\,i}^{\circledcirc} > 0, \quad \text{for} \quad i = 1, \ldots, N_z\Big\}. \tag{5.2.20}$$

The Rayleigh number for the onset of convection is found at cell centres using

$$Ra^{\circledcirc} = Ra_S \boldsymbol{\Theta}_{\boldsymbol{l}}^{\circledcirc} * (\boldsymbol{z}^{\circledcirc} - z_{i_b}^{\ominus}) * \boldsymbol{\pi}_{\boldsymbol{H}}^{\circledcirc}, \tag{5.2.21}$$

where the dimensionless harmonic mean permeability evaluated at cell centres is

$$\pi_{H\,i}^{\circledcirc} = \begin{cases} \dfrac{i+1-i_b}{\sum_{k=i_b}^{k=i} \frac{1}{\pi_k^{\circledcirc}}}, & i \geq i_b \\ 0, & i < i_b \end{cases}, \quad \text{for} \quad i = 1, 2, \ldots, N_z, \tag{5.2.22}$$

with

$$\pi_k^{\circledcirc} = (1 - \phi_{s,\,k}^{\circledcirc})^3 \quad \text{for} \quad k = 1, 2, \ldots, N_z. \tag{5.2.23}$$

The porosity-permeability relationship given by equation (5.2.23) is not strictly compatible with the porosity threshold ϕ_c for gas and liquid flow introduced in chapter 2 motivated by the measurements of Maus et al. (2021). However, in practice at low porosities the permeability given by equation (5.2.23) is very small and so the Rayleigh number is also very small which prevents convection from occurring. It has also been suggested that a porosity-permeability relationship with an exponent of 2 is more appropriate for the onset of convection in sea ice (Rees Jones 2014). However, in this thesis we use an exponent of 3 in equation (5.2.23) for consistency with Rees Jones and Worster (2014).

If $Ra_i^{\circledcirc} < Ra_c$ for $i = 1, \ldots, N_z$, then no convection occurs and $\boldsymbol{w}_{\boldsymbol{l}}^{\ominus} = \boldsymbol{\mathcal{S}}_{\text{RJW14}}^{\circledcirc} = \boldsymbol{0}$. If Ra exceeds the critical value Ra_c in the domain, then convection occurs for $z_{i_b}^{\ominus} < z < z_{i_c}^{\ominus}$ where

$$i_c = \max\Big\{i + 1 : Ra_i^{\circledcirc} \geq Ra_c \quad \text{for} \quad i = 1, \ldots, N_z\Big\}. \tag{5.2.24}$$

The convective upwelling velocity at cell edges is given by

$$w_{l\,i}^{\ominus} = \begin{cases} \dfrac{\alpha_{\mathrm{RJW14}} Ra_e}{z_{i_c}^{\ominus} - z_{i_b}^{\ominus}}, & i \leq i_b, \\ \dfrac{\alpha_{\mathrm{RJW14}} Ra_e (z_{i_c}^{\ominus} - z_{i}^{\ominus})}{(z_{i_c}^{\ominus} - z_{i_b}^{\ominus})^2}, & i_b < i < i_c, \\ 0, & i \geq i_c, \end{cases} \quad \text{for} \quad i = 1, 2, \ldots, N_z + 1, \tag{5.2.25}$$

where

$$Ra_e = \max_{i_b \leq i \leq i_c - 1} \Big(Ra_i^{\circledcirc} - Ra_c \Big). \tag{5.2.26}$$

The brine channel sink term at cell centres is given by

$$\mathcal{S}_{\mathrm{RJW14}\ \ \mathrm{i}}^{\circledcirc} \equiv -\frac{\partial w_l}{\partial z} = \begin{cases} 0, & i < i_b, \\ \dfrac{\alpha_{\mathrm{RJW14}} Ra_e}{(z_{i_c}^{\ominus} - z_{i_b}^{\ominus})^2}, & i_b \leq i \leq i_c - 1, \\ 0, & i \geq i_c, \end{cases} \quad \text{for} \quad i = 1, 2, \ldots, N_z. \tag{5.2.27}$$

Implementation of the 6B2S radiative transfer scheme

The net shortwave radiative flux $\widetilde{\boldsymbol{\mathcal{F}}}_{\mathrm{net}}^{\ominus}$ at cell edges (required by equation 5.2.10) is calculated using the 6B2S radiative transfer model described in §4. Given the integrated broadband incident shortwave radiation flux $\widetilde{F}_{\mathrm{SW}}$, the upwelling f_i^+ and downwelling f_i^- irradiances are calculated in each of the six wavelength bands enumerated in chapter 4 ($i = 1,\ 2,\ \ldots,\ 6$). From the upwelling and downwelling irradiances, the spectrally integrated net shortwave irradiance is calculated via equation (4.7.3).

The absorption coefficient of ice in the SWIR band ($i = 6$) is $k_6 = 9.61 \times 10^4\,\mathrm{m}^{-1}$ (table 4.2), such that numerical calculation of the normalised irradiances in this band would require resolving length scales $1/k_6 = 10.4\,\mu\mathrm{m}$, or smaller which is computationally infeasible, given that we take $\Delta z \geq 1\,\mathrm{cm}$ in this thesis We make the approximation that all incoming radiation in the SWIR band is absorbed within the first grid cell:

$$f_6^-(z) = \begin{cases} 1, & z = 0, \\ 0, & z < 0, \end{cases} \quad \text{and} \quad f_6^+(z) = 0. \tag{5.2.28}$$

We solve the coupled ODEs (4.4.3) and (4.4.4) numerically subject to the boundary conditions given by equations (4.4.8) and (4.4.9) for each of the wavelength bands $i = 1, 2, \ldots 5$. The optical properties required for the ODEs and boundary conditions in each wavelength band are given in table 4.2. We do this using a 4th order collocation method (Kierzenka and Shampine 2001) implemented by the function `scipy.integrate.solve_bvp` from the `SciPy` Python library (Virtanen et al. 2020). This collocation method (as implemented by `SciPy`) is an established, accurate, and efficient method for solving boundary value problems. Separating the solution of the two-stream model at each timestep from the rest of the alogrithm discussed above allows for the use of a higher spatial resolution (determined by the collocation method) to accurately resolve the shortwave irradiances (in bands $i = 1, 2, \ldots, 5$) without slowing down the rest of the simulation. We then evaluate the numerical solutions for the normalised irradiances at the cell edges $\boldsymbol{z}^{\ominus}$ using cubic-spline interpolation.

Equation (4.5.1) is discontinuous as $\phi_s \to 0$. For numerical stability, we replace it with the smooth alternative

$$r_{2\mathrm{S}}(\phi_s) = (1.716\,\mathrm{m}^{-1}) \tanh(100\phi_s), \quad \text{for} \quad 0 \leq \phi_s \leq 1. \tag{5.2.29}$$

We have developed the Python package `oilrad v2.0.2` available at `https://github.com/JoeFishlock/oilrad`, to solve the 6B2S model introduced in chapter 4 using the numerical method described above. The package `oilrad` is written in Python v3.12.3 and built on top of the `SciPy v1.15.1` (Virtanen et al. 2020) and `NumPy v2.2.1` (Harris et al. 2020) Python libraries.

5.2.2 Temporal discretisation

The spatial discretisation of the PDE system above yields a coupled system of $4N_z$ ODEs specified by equations (5.2.4),(5.2.5), and (5.2.6) for finite Da, or $3N_z$ coupled ODEs specified by equation (5.2.19) for $Da \to \infty$. At $t = 0$, we provide the initial conditions $\boldsymbol{\mathcal{H}}_{\mathbf{0}}^{\circledcirc}$, $\boldsymbol{\Theta}_{\mathbf{0}}^{\circledcirc}$, $\boldsymbol{\Gamma}_{\boldsymbol{d0}}^{\circledcirc}$, and $\boldsymbol{\phi}_{\boldsymbol{g0}}^{\circledcirc}$ and integrate the system numerically until $t = t_f$. The initial configuration and forcing data used for the results shown in chapters 6–8 are discussed in §6.3. Time integration is performed by the function `scipy.integrate.solve_ivp` provided by the `SciPy` Python library (Virtanen et al. 2020) using an explicit Runge-Kutta 5(4)[1] ("RK45") method, which utilises adaptive timestepping (Dormand and Prince 1980), with a relative error tolerance of 10^{-3} and an absolute error tolerance of 10^{-6}.

Here, for convenience, we have used an out-of-the-box explicit method provided by `SciPy` to integrate the ODE system. This has proved sufficient for our purposes but may not be the best approach. For example, the RJW14 brine convection scheme is a stiff system that is more efficiently solved using a semi-implicit predictor-corrector method (Rees Jones and Worster 2014). In chapter 6, we show that our implementation of the RJW14 brine convection scheme still yields good results for the bulk salinity profile in the ice compared with field observations. However, the explicit nature of our numerical scheme means that often the timestep is heavily restricted by the brine convection and scheme and eddy diffusion terms and so considerable computational resources were required to run a substantial number of simulations with $N_z = 100$.

We have developed the Python package `seaice3p v1.0.0` (`https://github.com/JoeFishlock/seaice3p`) to implement the numerical method described above. The package `seaice3p` depends on the following Python libraries: `SciPy v1.15.2` (Virtanen et al. 2020), `NumPy v2.2.3` (Harris et al. 2020), `pyserde v0.22.3`, `Xarray v2024.11.0` (Hoyer and Hamman 2017), `netCDF4 v1.7.2`, and `MetPy v1.6.3` (May et al. 2022).

5.3 Benchmark problems

5.3.1 Diffusive growth from a cooled boundary

To assess the accuracy of the numerical method described above for heat transport we consider the well-studied benchmark problem of the diffusive growth of a two-phase mushy layer from a cooled boundary (Huppert and Worster 1985; Hitchen

---

[1] The notation 5(4) indicates that the method uses a 5th order accurate Runge-Kutta method to take a step, and a 4th order accurate Runge-Kutta method to estimate the error.

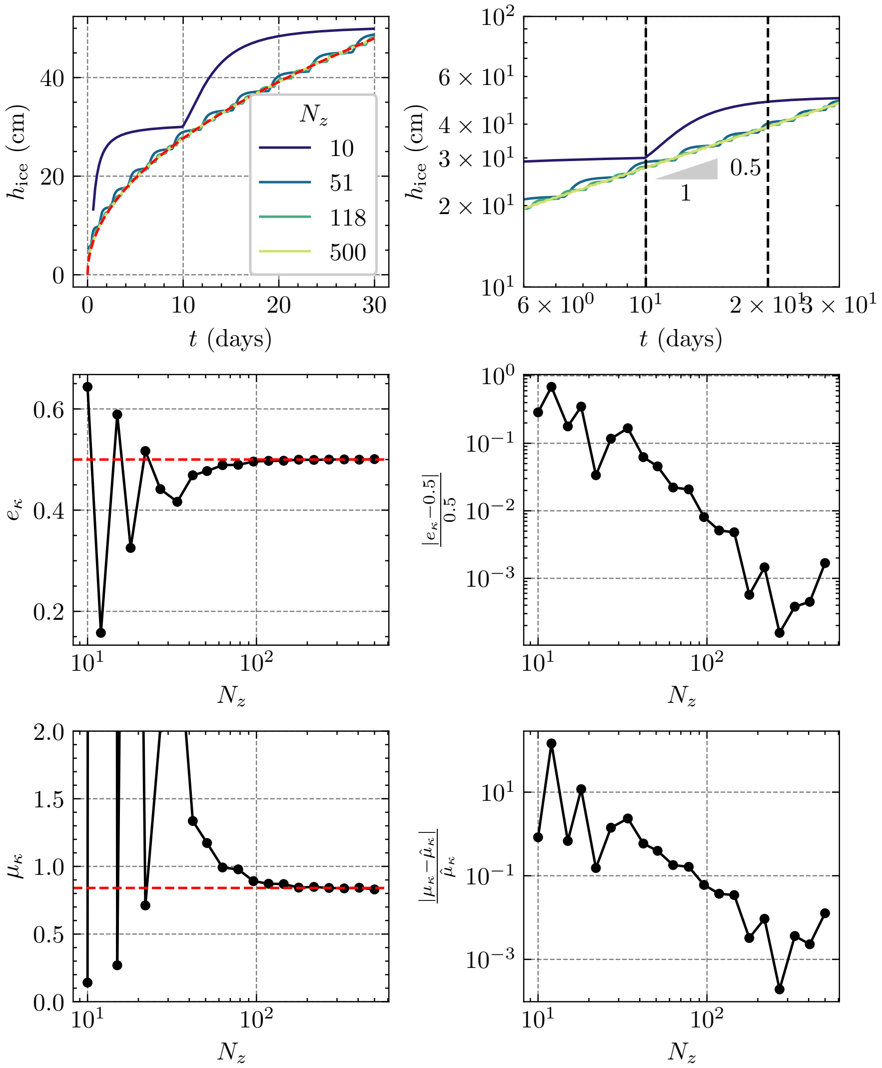

Figure 5.2: The top two panels show the ice thickness of the ice versus time for an initially liquid domain with $T_B = -15\,°\mathrm{C}$, $T_\infty = -1\,°\mathrm{C}$, and $S_\infty = 34\,\mathrm{g\,kg^{-1}}$. The thermal conductivities, specific heat capacities, and densities are assumed to be constant and equal in the solid and liquid phases, with values $k = 0.54\,\mathrm{W\,m^{-1}\,K^{-1}}$, $c_p = 4184\,\mathrm{J\,kg^{-1}\,K^{-1}}$, and $\rho = 1028\,\mathrm{kg\,m^{-3}}$, respectively. The salinity-dependent freezing temperature is calculated from the liquidus relation (1.1.1) with $\gamma_L = 0.078\,148\,°\mathrm{C}/(\mathrm{g\,kg^{-1}})$. The coloured lines correspond to different spatial resolutions N_z (see legend) and the dashed red line in the top left panel is the semi-analytical solution given by equation (5.3.1), where the dimensionless growth rate $\hat{\mu}_\kappa = 0.8405889$ and exponent $\hat{e}_\kappa = 1/2$ are calculated using the MATLAB code provided by Hitchen and Wells (2025) for these parameter values. The top right panel shows the same quantities on a logarithmic scale, where values between the dashed black lines are fitted with a line to determine estimates of μ_κ and e_κ. The middle and bottom rows show the convergence of μ_κ and e_κ as N_z increases. The values found by Hitchen and Wells (2025) are indicated with dashed red lines.

2017; Hitchen and Wells 2025). For comparison with existing work, we neglect the gas phase ($\Gamma = 0$) and brine convection, in which case our model reduces to only a single non-trivial conservation equation for the bulk enthalpy. Consider a domain of depth $h = 2\,\mathrm{m}$ filled initially with water at temperature T_∞ and salinity S_∞. We impose fixed temperature boundary conditions $T(z = 0,\, t) = T_B$ and $T(z = -1,\, t) = T_\infty$ with $T_B < T_L(S_\infty)$ and $T_\infty > T_L(S_\infty)$. We neglect salt diffusion (i.e., $Le_S = \infty$) and assume that the thermal conductivities, specific heat capacities, and densities are constant and equal in the solid and liquid phases.

In this setting, a mushy layer grows downwards with a lengthscale $\sqrt{\kappa t}$ that is controlled by the thermal diffusivity $\kappa = k/(\rho c_p)$. For early times $t \ll h^2/\kappa \approx 369\,\mathrm{days}$, the bottom boundary has no significant effect on the solution and the domain can be regarded as semi-infinite. In this case, the position of the ice-liquid interface $z = z_b(t) = -h_{\mathrm{ice}}(t)$ is determined from a semi-analytical similarity solution that yields

$$h_{\mathrm{ice}}(t) = \hat{\mu}_\kappa \sqrt{\kappa t}, \tag{5.3.1}$$

where the dimensionless growth rate $\hat{\mu}_\kappa$ depends on the temperature difference, the liquidus relation, and the Stefan number (Hitchen and Wells 2025). Here, we calculate $\hat{\mu}_\kappa$ using the MATLAB code provided by Hitchen and Wells (2025).

As noted above, the ice–ocean interface position is approximated by $z_b \approx z^{\ominus}_{i_b}$, where $z^{\ominus}_{i_b}$ is the bottom edge of the lowermost cell for which $\phi_s > 0$. The discrete ice–ocean edge position therefore moves downward in a series of steps of size Δz as the ice grows. We calculate a continuous approximation to the ice–ocean interface as follows. We construct a linear approximation for the enthalpy $\mathcal{H}_{\mathrm{linear}}(z)$ for $z_{i_b-1} \leq z \leq z_{i_b}$ between the cell centers above and below the discrete ice–ocean interface position. We then solve the equation $\mathcal{H}_{\mathrm{linear}}(z_b) = 0$ to find the continuous ice–ocean interface position z_b^{cts},

$$z_b^{\mathrm{cts}} = z_{i_b} - \mathcal{H}_{i_b} \frac{z_{i_b} - z_{i_b-1}}{\mathcal{H}_{i_b} - \mathcal{H}_{i_b-1}}, \tag{5.3.2}$$

where $\mathcal{H}_{i_b}$ is the enthalpy evaluated on the center grid at position $z = z_{i_b}$, and $\mathcal{H}_{i_b-1}$ is the enthalpy evaluated on the center grid at position $z = z_{i_b-1}$. Due to the first-order accuracy of our spatial discretisation we expect the error in the estimate of the ice–ocean interface position to be first order in the grid spacing.

To validate our numerical scheme, we assume that the simulated ice–ocean interface position satisfies $z_b^{\text{cts}} = -\mu_\kappa \sqrt{\kappa}\, t^{e_\kappa}$. We run a range of simulations with $10 \leq N_z \leq 500$ using `seaice3p v1.0.0` and use a least-squares algorithm implemented by `NumPy` to fit a line to $\log\left(z_b^{\text{cts}}\right)$ versus $\log\left(t\right)$ over the time window $10 \leq t \leq 20$ days. Estimates of e_κ and μ_κ for each N_z are given from the slope and intercept of this linear fit. We choose the time window of $10 \leq t \leq 20$ days to ensure that the ice has grown larger than the grid size but is still far enough from the bottom boundary to be in the self-similar diffusive growth regime.

Simulated positions of the ice–ocean interface are shown in the top panel of figure 5.2 for some illustrative values of N_z in the range $10 \leq N_z \leq 500$. The middle and bottom panels illustrate convergence of the numerical estimates $e_\kappa \to 1/2$ and $\mu_\kappa \to \hat{\mu}_\kappa$, respectively, as N_z increases. We find that $N_z \geq 50$ and $N_z \geq 100$ are sufficient to obtain e_κ to within 10% and 1% accuracy, respectively, for these parameter values. Estimates of μ_κ are less accurate, with $N_z \geq 50$ and $N_z \geq 100$ giving estimates to within a factor of 2 and to within 10% accuracy, respectively. The relative error in μ_κ and e_κ plateaus at around 10^{-3}, which is the relative error tolerance used for the time integration (see §5.2.2).

5.3.2 The spectral albedo, transmittance, and net irradiance for a uniform layer of ice

Next we validate our implementation of the two-stream model by comparing the spectral albedo for a 0.8 m thick layer of first-year ice with no snow cover or SSL to the values found by Redmond Roche and King (2022b) using the TUV-snow model. We also calculate the transmittance and normalised net irradiance at a depth of -2 cm to examine the impact of discretising the shortwave radiation into the six spectral bands described in chapter 4, compared with using spectral bands with 1 nm resolution. We will refer to the latter case as having high spectral resolution.

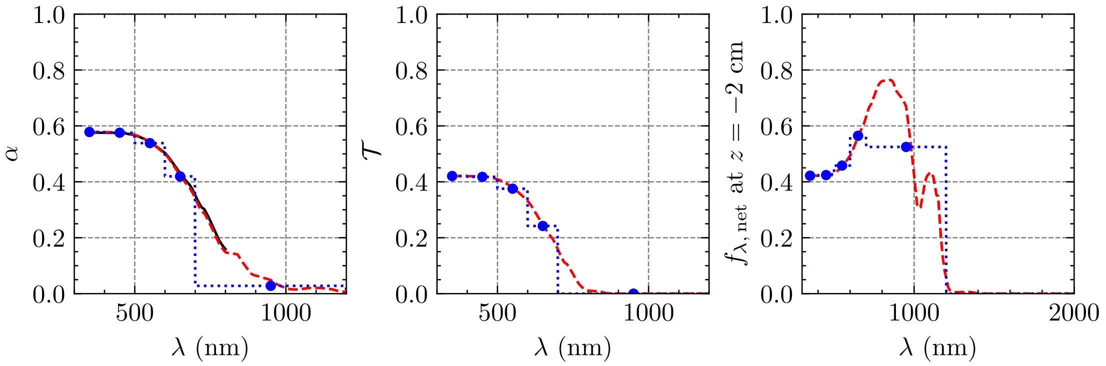

Figure 5.3: The spectral albedo α_λ (left), transmittance $\mathcal{T}_\lambda$ (middle), and normalised net irradiance $f_{\lambda,\,\mathrm{net}}(z = -2\,\mathrm{cm})$ (right) versus wavelength λ for a 0.8 m thick layer of first-year ice with no snow cover or SSL. The numerical solutions were calculated using $r_{2\mathrm{S}} = 1.717\,\mathrm{m}^{-1}$ and $k_{2\mathrm{S}}(\lambda)$, as described in chapter 4. The dashed red lines and dotted blue lines are obtained by solving the two-stream model numerically using `oilrad v2.0.2` with wavelengths discretised into bands 1 nm wide or with the six bands described in §4.7, respectively. The filled blue circles indicate the midpoints of the NUV, VIS1, VIS2, VIS3, and NIR wavelength bands. The solid black line in the left panel shows the spectral albedo calculated by Redmond Roche and King (2022b) for the same optical parameters using the TUV-snow model (data provided by Redmond Roche and King 2022a).

Quantity	**RMSE**					
	NUV	**VIS1**	**VIS2**	**VIS3**	**NIR**	**Total**
α	1.72×10^{-5}	0.002 78	0.0201	0.0451	0.108	0.0441
$\mathcal{T}$	1.96×10^{-5}	0.003 17	0.0228	0.0496	0.0381	0.0243
$f_{\lambda,\,\mathrm{net}}(z = -2\,\mathrm{cm})$	1.57×10^{-5}	0.002 54	0.0183	0.0396	0.203	0.0714
$f_{\lambda,\,\mathrm{net}}(z = -4\,\mathrm{cm})$	1.43×10^{-5}	0.002 31	0.0165	0.0344	0.27	0.0902
$f_{\lambda,\,\mathrm{net}}(z = -8\,\mathrm{cm})$	1.16×10^{-5}	0.001 87	0.0131	0.0248	0.292	0.0947
$f_{\lambda,\,\mathrm{net}}(z = -16\,\mathrm{cm})$	6.39×10^{-6}	0.001 03	0.006 72	0.008 38	0.227	0.0711

Table 5.1: Tabulated values of the root mean square error (RMSE) for each of the quantities denoted in the first column. The RMSE is computed in each of the named spectral bands between the 6B2S model and the two-stream model with wavelength bands of 1 nm width. The final column shows the sum of the RMSE values in each of the bands weighted by the fraction of the incident shortwave radiative power in each band for cloudy-sky conditions (see table 4.1).

The left panel of figure 5.3 shows the spectral albedo calculated using the 6B2S model (dotted blue line), the two-stream model with high spectral resolution (dashed red line), and the TUV-snow model (solid black line). Firstly, we note that the value of $r_{2\mathrm{S}} = 1.717\,\mathrm{m}^{-1}$ chosen in §4.5.1 yields excellent agreement in the calculated spectral albedo with high spectral resolution versus the values found by Redmond Roche and King (2022b). The root-mean-square error (RMSE) between the dashed red and solid black lines in the left panel of figure 5.3 is 0.007 54 for $350 \leq \lambda \leq 800\,\mathrm{nm}$ (the range over which the TUV-snow data is available).

It is not computationally feasible to use high spectral resolution for the entire shortwave spectrum in a transient sea ice model, so we now consider the error incurred by using only six spectral bands. The RMSE between the numerical solutions for the spectral albedo, transmittance, and normalised net irradiance (at several depths) with high wavelength resolution and with six spectral bands are tabulated in table 5.1. The SWIR band is not included in this analysis as we have assumed that all radiation in this band is absorbed at the ice surface. The RMSE remains very low for the short-wavelength bands NUV, VIS1, VIS2, and VIS3, suggesting that these wavelength bands are able to sufficiently represent spectral variations in the calculated optical parameters. The RMSE is substantially higher for the NIR band, which is much wider and therefore cannot accurately account for spectral variations in optical properties in this range. However, this inaccuracy is not a major problem for the overall accuracy of our radiation scheme because 65.4% of the incoming radiation lies in the ultra-violet and visible bands (see table 4.1). These results suggest that the 6B2S model is able to reproduce spectrally integrated quantities to within 10% accuracy compared with the high spectral resolution model.

The results presented in chapters 6 and 8 were run with $N_z = 100$ and $h = 2\,\mathrm{m}$, giving a vertical resolution of $\Delta z = 2\,\mathrm{cm}$. The right panel of figure 5.3 confirms that very little radiation with $\lambda > 1200\,\mathrm{nm}$ penetrates beyond 2 cm into the ice. This suggests that the approximation (see equation 5.2.28) that radiation in the SWIR band is absorbed entirely in the first grid cell is reasonable.

5.4 Code availability

The three Python packages developed for this thesis are available on GitHub and via their respective doi identifiers.

- `mush3p v1.0.1` `https://github.com/JoeFishlock/mush3p` `https://doi.org/10.5281/zenodo.15670329`
- `oilrad v2.0.2` `https://github.com/JoeFishlock/oilrad` `https://doi.org/10.5281/zenodo.15670481`

- `seaice3p v1.0.0` `https://github.com/JoeFishlock/seaice3p` `https://doi.org/10.5281/zenodo.15670493`

5.5 Conclusions

In this chapter, we have described our implementation of a first-order upwind finite-volume scheme to solve the coupled conservation equations for heat, salt, dissolved gas, and free-phase gas for a three-phase mushy layer derived in chapter 3. We have demonstrated the convergence of the numerical method for diffusive growth of sea ice from a cooled boundary and given estimates of numerical error for the typical grid resolutions (N_z =50–100) used in the remainder of this thesis. The implementation of the RJW14 scheme closely follows descriptions in the literature and was not tested in this chapter. We instead validate the performance of the RJW14 scheme in chapter 6 by comparing modelled ice salinity profiles with observations from first-year landfast sea ice at Barrow, Alaska.

We have also described our numerical implementation of the 6B2S model for shortwave radiation (see chapter 4), which uses a collocation algorithm to solve the boundary value problem in each spectral band. We have shown that our implementation of the 6B2S model accurately reproduces spectral albedo values found previously using the TUV-snow model for 0.8 m thick first-year sea ice. We have demonstrated, that less than 10% error is introduced for the spectral albedo, transmittance, and net irradiance by discretising the shortwave spectrum into the six bands described in §4.7, compared with using a high spectral resolution of 1 nm. This is important as it is only computationally feasible to run simulations of sea ice on a seasonal timescale with a low number of wavelength bands.

In the remainder of this thesis, we use the numerical methods described in this chapter to run simulations to validate modelled ice temperature and salinity profiles against field observations (chapter 6), to investigate the air content of first-year sea ice (chapter 7), and to investigate the impact of oil droplets on radiative transfer in first-year sea ice (chapter 8).

6

Simulating first-year sea ice at Barrow, Alaska

6.1 Introduction

In this chapter, we use the one-dimensional transient sea ice model (chapter 3) with the six-band two-stream (6B2S) shortwave radiation scheme (chapter 4) to simulate the growth of first-year Arctic sea ice over a single seasonal cycle using the numerical methods developed in chapter 5. These simulations consider a domain consisting solely of water and salt, in which two-phase sea ice forms with no additional gaseous phase. This two-phase configuration allows us to compare the simulated ice thickness, temperature, and bulk salinity with observational data. This comparison provides confidence for when we later use the model to investigate the air content (chapter 7) and the impact of oil pollution (chapter 8) in first-year sea ice.

We choose to simulate one season of ice growth at Barrow (Utqiagvik)[1] , Alaska (71.37°N, 156.5°W). Barrow is located on the northern coastline of Alaska, with the Chukchi Sea to the west and the Beaufort Sea to the north-east, and has a long history of sea-ice observations. Seasonal landfast ice (i.e., ice that is attached to the coastline) appears at Barrow in the autumn, typically in November (Druckenmiller et al. 2009). The landfast ice at Barrow forms primarily from in-situ freezing, with little ice advection or deformation. As a result, ice thickness and snow depth measurements are representative of level first-year ice (Druckenmiller et al. 2009). By mid-June, large stretches of the landfast ice break up and either melt in place or are carried out to sea (Mahoney et al. 2007). A sequence of satellite

---

[1] The name was officially changed from Barrow to Utqiagvik in 2016. However, much of the literature and data used throughout this thesis pre-dates this change and therefore uses the name Barrow; for clarity and consistency, we do the same.

images shows the seasonal growth, melt, and breakup of first-year sea ice at Barrow in 2018–2019 (figure 6.1).

We simulate the growth of first-year sea ice at Barrow from September 2008 to June 2009, for which period data is available from the Barrow mass balance site (MBS) and ice cores were collected during a field campaign. We describe the available observational data in §6.2 and the model intialisation and forcing in §6.3. Finally, in §6.4, we perform and analyse a suite of simulations to identify the set of parameter values that best reproduces the observed ice characteristics.

6.2 Field data

6.2.1 The Barrow mass balance site (MBS)

The Barrow MBS consists of a collection of automated instruments (figure 6.2) that were deployed on the landfast first-year ice just north of Barrow (Druckenmiller et al. 2009). The instruments were deployed each year from 2006 to 2015 when the ice became sufficiently stable (January) and were removed when the ice began to melt and breakup (June). The MBS is equipped with: acoustic instruments, which measure ice thickness and snow depth; air temperature and relative humidity sensors, located at an elevation of 2 m above the ice surface; and a thermistor string, which measures temperatures at 10 cm intervals through the air, snow, ice and ocean.

6.2.2 Ice core data from the 2009 Barrow Field Campaign

Within 40 m of the MBS, a field campaign (described in Zhou et al. 2013) collected ice cores over 10 sampling periods (referred to as BRW1–10) from January to June 2009. Temperature measurements were taken at 5 cm intervals for each core within 5 minutes of extraction. Each core was then sectioned into 5 cm segments that were melted to measure bulk salinity. Additional cores from each sampling period were transported to a laboratory in Belgium, where they were sectioned into 5 cm segments to measure the bulk concentrations of argon, oxygen and nitrogen. Measurements of bulk gas concentrations were made for 5 of the 10 sampling periods, spaced roughly evenly throughout the course of the field study. In this

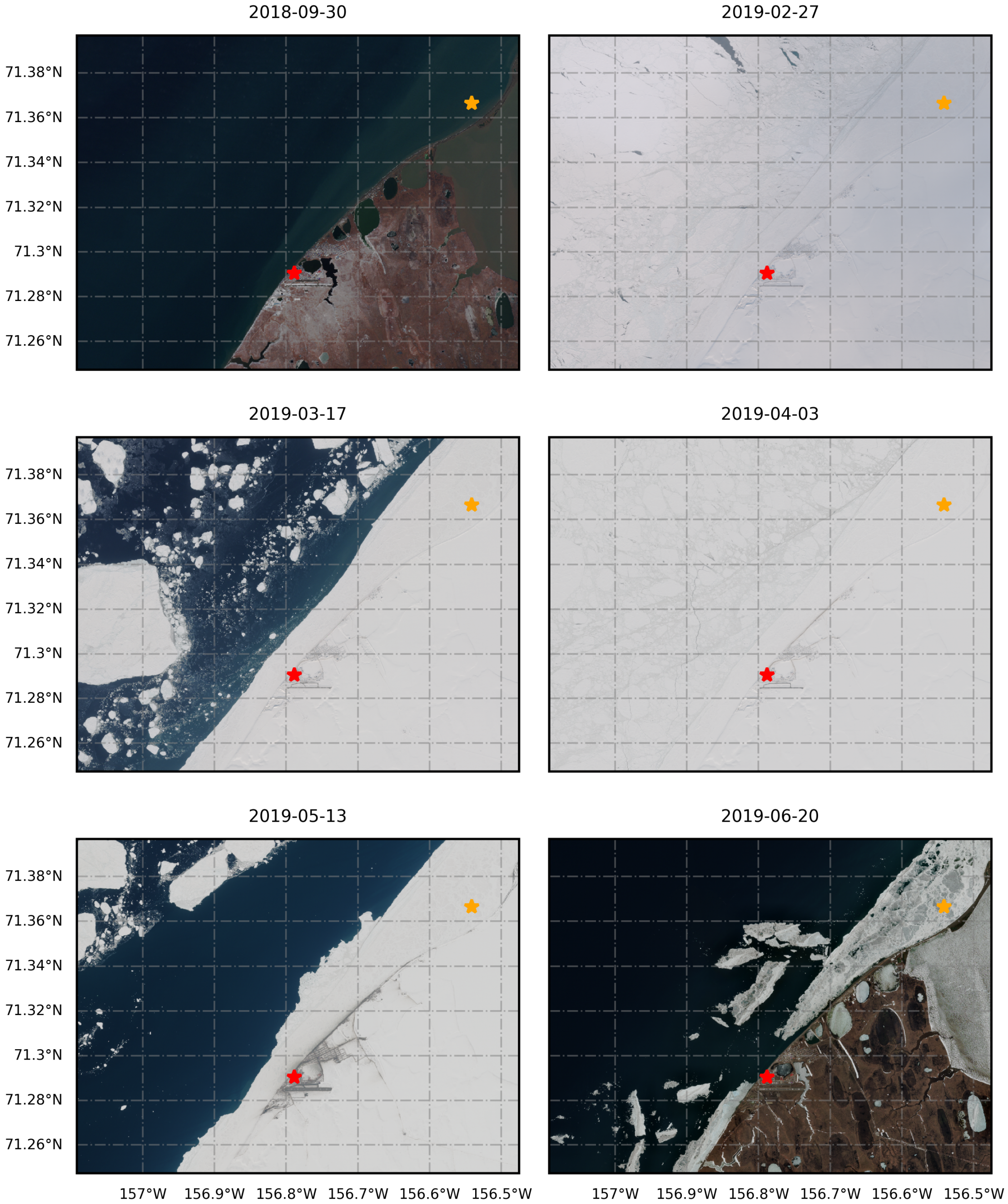

Figure 6.1: Satellite images showing the seasonal growth, melt and breakup of first-year sea ice along the Barrow coastline in 2018-2019. The position of the city of Barrow is marked with a red star and the position of the mass balance site deployed in 2009 is marked with an orange star. The images are from the Sentinel 2 L2A product for atmospherically corrected surface reflectance, retrieved from the Copernicus Browser `https://dataspace.copernicus.eu/browser/` on 14th of November 2024. These images illustrate the typical growth of landfast ice at Barrow from ice-free conditions in September until melt in June, but are not from the same year as the observational data used in this thesis (The Sentinel 2 satellite only began operation in 2015). Note that the breakout event seen between the second and third panels is a common occurrence at Barrow in the spring (Druckenmiller et al. 2009).

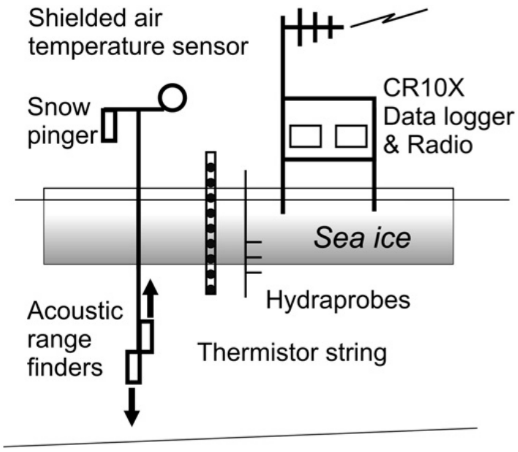

Figure 6.2: Schematic of the Barrow MBS instrumentation, reproduced from Druckenmiller et al. (2009). The thermistor string records the temperature profile through the snow, ice and ocean down to a depth of 2.4 m below the ice surface. The snow pinger above the ice records snow depth, while the acoustic range finders below the ice record ice thickness.

chapter, we compare the measured temperature and bulk salinity profiles in the ice to simulated profiles from our transient model. We then do the same for bulk gas concentrations in chapter 7.

6.3 Model

We use the Python package `seaice3p v1.0.0` described in chapter 5 to model the transient evolution of a horizontally uniform layer of sea ice. The heat source due to the absorption of shortwave radiation is calculated using the 6B2S radiation scheme described in chapter 4. In this chapter, we use `seaice3p` to run simulations of the growth of first-year sea ice at Barrow with $N_z = 100$ grid points in a domain of depth $h = 2\,\mathrm{m}$, with the parameter values given in table 6.1. The timestep for the numerical integration is chosen adaptively by the “RK45” method and data is saved at 3 hour intervals.

During freezing, the rejection of salt into the interstitial liquid creates an unstable density gradient in the ice that drives a convective flow of brine out of the ice that is replenished by seawater from the underlying ocean. This brine convection is the primary mechanism by which first-year sea ice desalinates during ice growth (Notz and Worster 2009). As discussed in §3.2.2, the RJW14 brine-convection

Parameter	**Symbol**	**Value**
(a)		
domain depth	h	$2\,\mathrm{m}$
initial temperature	T_{init}	$3.53\,°\mathrm{C}$
fresh melting temperature	T_m	$0\,°\mathrm{C}$
saltwater eutectic temperature	T_E	$-22.9\,°\mathrm{C}$
liquidus slope	γ_L	$0.056\,°\mathrm{C}/(\mathrm{g\,kg^{-1}})$
thermal conductivity of water	k_l	$0.54\,\mathrm{W\,m^{-1}\,K^{-1}}$
thermal conductivity of ice	k_s	$2.22\,\mathrm{W\,m^{-1}\,K^{-1}}$
specific heat capacity of water	$c_{p,l}$	$4184\,\mathrm{J\,kg^{-1}\,K^{-1}}$
specific heat capacity of ice	$c_{p,s}$	$2009\,\mathrm{J\,kg^{-1}\,K^{-1}}$
latent heat of fusion of ice	L	$333 \times 10^3\,\mathrm{J\,kg^{-1}}$
ocean salinity	S_∞	$29.6\,\mathrm{g\,kg^{-1}}$
haline contraction coefficient	β	$7.5 \times 10^{-4}\,\mathrm{ppt^{-1}}$
molecular diffusivity of salt	κ_S	$0\,\mathrm{m^2\,s^{-1}}$
eddy diffusivity	κ_ε	$1 \times 10^{-6}\,\mathrm{m^2\,s^{-1}}$
density of seawater	ρ_l	$1024\,\mathrm{kg\,m^{-3}}$
gravitational acceleration	g	$9.81\,\mathrm{m\,s^{-2}}$
dynamic viscosity of water	μ_l	$2.78 \times 10^{-3}\,\mathrm{kg\,m^{-1}\,s^{-1}}$
reference permeability	Π_0	$1 \times 10^{-8}\,\mathrm{m^2}$
air density	ρ_{air}	$1.275\,\mathrm{kg\,m^{-3}}$
specific heat capacity of air	$c_{p,\mathrm{air}}$	$1005\,\mathrm{J\,kg^{-1}\,K^{-1}}$
latent heat of vaporisation of water	L_{vap}	$2.501 \times 10^6\,\mathrm{J\,kg^{-1}}$
reference height	h_{ref}	$2\,\mathrm{m}$
windspeed	u_{wind}	$2\,\mathrm{m\,s^{-1}}$
longwave emissivity of ice	Υ_{ice}	0.99
longwave emissivity of water	$\Upsilon_{\mathrm{water}}$	0.97
scattering coefficient of ice	$r_{2\mathrm{S}}$	$1.716\,\mathrm{m^{-1}}$
SSL depth	h_{SSL}	$4\,\mathrm{cm}$
snow density	ρ_{snow}	$225\,\mathrm{kg\,m^{-3}}$
(b)		
Stefan number	St	3.75
ice-water thermal conducitivity ratio	ν_s	4.11
ice-water specific heat capacity ratio	ζ_s	0.48
concentration ratio	$\mathcal{C}$	0.078
salinity Rayleigh number	Ra_S	1.63×10^5
convection strength	α_{RJW14}	0.03
critical Rayleigh number	Ra_c	2.9
salt Lewis number	Le_S	∞
eddy Lewis number	Le_ε	0.126

Table 6.1: Parameter values (a) and dimensionless numbers (b) for the simulations run using `seaice3p v1.0.0` in chapter 6. The value for the liquid density is calculated using the UNESCO equation of state for seawater at temperature T_{init} and salinity S_∞. In these simulations, molecular diffusion of salt is neglected by setting $\kappa_S = 0$. The eutectic temperature for NaCl in water is taken from Vancoppenolle et al. (2019). The liquidus slope is calculated to give $T_m = 0$ at $S = 0$ and the freezing point of water at S_∞ calculated from the third-order polynomial fit given by Vancoppenolle et al. (2019). Note the values of T_E and γ_L are different from the values used in chapter 2 to obtain a more realistic freezing point of seawater.

scheme parameterises the loss of salt from the ice through brine channels and requires two dimensionless tuning parameters, Ra_c and α_{RJW14}, that determine the onset and strength of convection in the ice. A previous study compared bulk salinity profiles predicted using the RJW14 scheme with measurements of laboratory-grown sea ice and found the best agreement when $Ra_c = 2.9$ (Thomas et al. 2020), which we therefore also use here. Although Thomas et al. (2020) tuned both $Ra_c = 2.9$ and $\alpha_{\mathrm{RJW14}} = 0.13$ together, in this thesis we have chosen to use $\alpha_{\mathrm{RJW14}} = 0.03$ as suggested by the original authors of the RJW14 scheme (Rees Jones and Worster 2014). It was noted by Rees Jones and Worster (2014) that there is very little sensitivity to the value of α_{RJW14} a few hours after the onset of convection. Furthermore, sensitivity experiments have shown that the simulated bulk salinity profiles are not very sensitive to the choice of α_{RJW14}.

During the simulation, incident shortwave radiation from the sun (see §1.1.3) that is absorbed in the ice provides an additional internal heat source in the domain. The reflection, absorption, and transmission of incident shortwave radiation during the simulation are calculated using the 6B2S model described in chapter 4 with the optical parameters given in table 4.2. The fractions of the incoming shortwave radiative power in each spectral band (given in table 4.1) are assumed to follow the spectrum reported for cloudy-sky conditions by Grenfell and Perovich (2004). We showed in chapter 4 that choosing the appropriate optical parameters for dry snow during ice growth, and for wet snow during the melt season, is important to accurately determine the transmittance of radiation in the visible range at the ice–ocean interface. However, we have found that the simulated ice thickness and temperature profiles at Barrow are not sensitive to the choice of wet or dry optical parameters for snow. For simplicity, going forward, we use the optical properties appropriate for dry snow throughout the simulation.

In regions of pure liquid (i.e., $\phi_l = 1$, as in melt ponds and the underlying ocean), turbulence leads to enhanced transport of heat and salt. As discussed in §3.2, the eddy diffusivity κ_ε parameterises this enhanced mixing. For the underlying ocean, the eddy diffusivity for heat has been estimated to be around $0.1\,\mathrm{m}^2\,\mathrm{s}^{-1}$

from measurements of vertical temperature and velocity fluctuations (McPhee 1992). Melt ponds on top of the ice can form in our model during summer due to surface melt (but not snow melt). Melt ponds are turbulent due to unstable density stratifications (Taylor and Feltham 2004) and due to wind-driven surface stresses (Eicken et al. 2002). Flocco et al. (2015) use an eddy diffusivity of $0.01\,\mathrm{m}^2\,\mathrm{s}^{-1}$ to model turbulent heat and salt transport in a melt pond, although they find that their results are not sensitive to varying this value by two orders of magnitude.

Since we are using an explicit numerical method (see §5.2.2), large values of κ_ε quickly become computationally infeasible due to the restrictive timestep required for numerical stability. We use a value of $\kappa_\varepsilon = 1 \times 10^{-6}\,\mathrm{m}^2\,\mathrm{s}^{-1}$ to capture the effect of some enhancement to heat and salt transport in the ocean and melt pond, but we note that this value is likely to underestimate the true turbulent transport in these regions. During ice growth, heat transfer between the ocean and the base of the ice is ultimately constrained by the ocean heat flux F_{ocean} imposed at the bottom boundary of the domain and so using a lower value for κ_ε is not a significant issue. Later in this chapter, we find that our choice of κ_ε is sufficiently large to keep the temperature profile in the ocean relatively uniform during ice growth, in agreement with the measurements from the Barrow MBS. However, our low value of κ_ε does lead to unrealistically high temperatures in the ocean and in the interior of the melt pond in the summer, when heat produced by the absorption of shortwave radiation is less efficiently mixed compared with more realistic turbulent transport. This could have consequences for the predicted rate of surface melt during the melt season, as the pond deepens, although our current model is also missing a description of pond drainage which also occurs as ponds deepen.

6.3.1 Initialisation

We begin the simulation at $t = 0$, corresponding to 2008-09-01 00:00, with a completely liquid domain of uniform temperature and salinity that represents an ice-free, well-mixed ocean at Barrow. We use an initial temperature of 3.53 °C and salinity of $29.6\,\mathrm{g\,kg}^{-1}$, taken from the monthly mean surface values for September

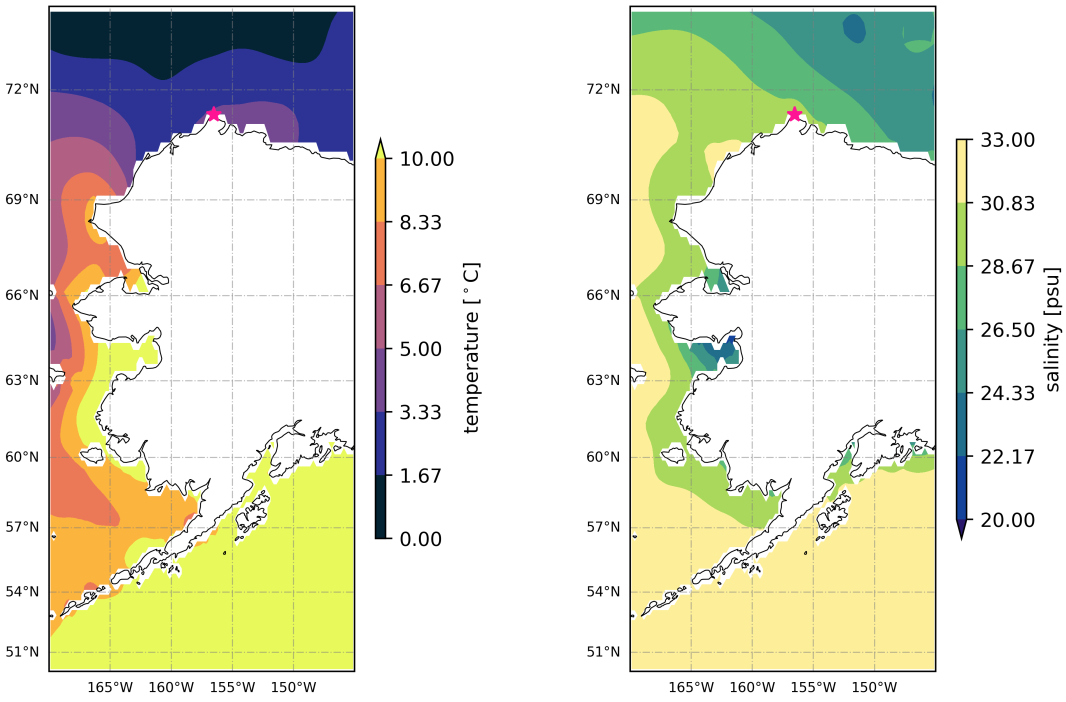

(a) (b)

Figure 6.3: Monthly mean ocean surface temperature (a) and surface salinity (b) for September (1991-2020) around the coast of Alaska extracted from the World Ocean Atlas dataset at quarter-degree resolution (Reagan et al. 2023). The location of Barrow (71.38°N, 156.5°W) is marked with a pink star.

extracted from World Ocean Atlas data (figure 6.3). To focus on reproducing realistic ice growth and bulk salinities, we set the concentration of dissolved air in the ocean to zero so no gas phase is present. The gas content of the ice is investigated in chapter 7.

6.3.2 Forcing

After initialisation, we simulate the evolution of the ice over a period of 365 days. Boundary conditions on the bulk enthalpy and salinity are imposed at the top of the domain using equations (3.4.9) and (3.4.2). The atmospheric variables required to calculate the surface heat flux in equation (3.4.9) are calculated by linearly interpolating daily averaged quantities extracted from ERA5 hourly reanalysis data (C3S 2018) for (71.37°N, 156.5°W). Some quantities, such as the incoming shortwave and longwave radiation fluxes, exhibit a strong diurnal cycle. By averaging out the diurnal cycle, the model receives the same total daily energy flux but avoids the need to resolve rapid changes in the forcing, which can result in rapid freeze/melt cycles at the onset of the melt season that reduce the accuracy of the simulation (Taylor and Feltham 2004).

We take $h_{\mathrm{ref}} = 2\,\mathrm{m}$ and obtain the air temperature $T_{\mathrm{air}}(t)$ at $2\,\mathrm{m}$, mean surface downward long-wave radiation flux $F_{\mathrm{LW}}(t)$, mean surface downward short-wave radiation flux $F_{\mathrm{SW}}(t)$, and surface pressure $p_{\mathrm{atm}}(t)$ from daily averages of the reanalysis data. The specific humidity $q_{\mathrm{air}}(t)$ at $2\,\mathrm{m}$ is calculated from the dew-point temperature and surface pressure at $2\,\mathrm{m}$ from the reanalysis using standard meteorological formulae implemented by the Python library `MetPy v1.6.3` (May et al. 2022). We estimate the wind speed at $h_{\mathrm{ref}} = 2\,\mathrm{m}$, u_{wind}, from the ERA5 zonal and meridional daily average wind speeds at $10\,\mathrm{m}$, $u_{\mathrm{wind\ 10m}}$, and $v_{\mathrm{wind\ 10m}}$, respectively. We do so by assuming a logarithmic profile for the surface winds,

$$u_{\mathrm{wind}} = \frac{\log\left(h_{\mathrm{ref}}/l_{\mathrm{rough}}\right)}{\log\left(h_{\mathrm{ERA5}}/l_{\mathrm{rough}}\right)} \sqrt{u^2_{\mathrm{wind\ 10m}} + v^2_{\mathrm{wind\ 10m}}}, \tag{6.3.1}$$

where $h_{\mathrm{ERA5}} = 10\,\mathrm{m}$ and the roughness length for sea ice is taken to be $l_{\mathrm{rough}} = 1 \times 10^{-4}\,\mathrm{m}$ (Untersteiner and Badgley 1965). The assumption of a logarithmic wind profile is not always appropriate over sea ice and there are order-of-magnitude variations in measurements of the roughness length. We note that equation (6.3.1) only depends on l_{rough} logarithmically, and so increasing or decreasing l_{rough} by an order of magnitude changes u_{wind} by less than 5%. Furthermore, sensitivity experiments show that the simulated ice thickness is not sensitive to the value of u_{wind}.

In our model, the snow layer impacts the surface energy balance by changing the effective surface temperature T_{surf} through equation (3.2.23), which depends on the snow thermal conductivity k_{snow} and the snow thickness h_{snow}. The ERA5 reanalysis dataset does not provide estimates of the snow depth on sea ice. Instead, we use daily average snow depth calculated using an existing Lagrangian model of snow on sea ice that was forced using ERA5 reanalysis data (SnowModel-LG Liston et al. 2021). These snow depths reproduce the observed snow depth at the Barrow MBS reasonably well (see figure 6.4a), although the modelled snow depth in January–March is significantly larger than the observations. However, the snowpack on sea ice is typically highly heterogeneous (Sturm and Massom 2017) and even the two different instruments measuring the snow depth at the Barrow MBS in 2009 do not always agree (figure 6.4a). We determine an appropriate value of k_{snow} that best reproduces the observed ice thickness at Barrow in §6.4.

Determining the ocean heat flux is a challenging problem of significant importance to understanding the mass balance of sea ice in the Arctic. The ocean heat flux varies strongly over a season and is highly heterogeneous in space due patterns of ocean circulation in the Arctic Ocean. Ice growth during the winter is not very sensitive to the value of F_{ocean}, when the atmospheric heat fluxes dominate. However, F_{ocean} is important to obtain the correct maximum ice depth and basal melting of the ice in summer. Theoretical estimates of the ocean heat flux have shown that an annual average value of around $2\,\mathrm{W\,m^{-2}}$ is required to reproduce observed ice thicknesses (Maykut and Untersteiner 1971). However, there is a strong seasonal cycle in F_{ocean} with maximum values of 40–60 $\mathrm{W\,m^{-2}}$ in summer, when the ocean absorbs a significant amount of solar radiation (Maykut and McPhee 1995), and minimum values of less than $2\,\mathrm{W\,m^{-2}}$ in winter (Krishfield and Perovich 2005). There is also significant year-to-year variability in the ocean heat flux; for example Zhong et al. (2022) reported annual average estimates of the ocean heat flux for the Beaufort Gyre region of the Arctic Ocean of 0.76 ± 0.05 $\mathrm{W\,m^{-2}}$ and 1.63 ± 0.08 $\mathrm{W\,m^{-2}}$ for the periods 2006–2012 and 2013–2018, respectively. We note that the landfast ice at Barrow is in a coastal region and so the ocean heat flux is likely to be controlled by different factors than the open ocean.

We impose the ocean heat flux in equation (3.4.8) by interpolating monthly average values of the ocean heat flux with a winter value of $1\,\mathrm{W\,m^{-2}}$ and a maximum summer value of $20\,\mathrm{W\,m^{-2}}$ in July and August (see figure 6.4c). These are similar to monthly average values measured in the Arctic Ocean (Krishfield and Perovich 2005). At the bottom boundary of the domain, we impose a fixed salinity of $S = 29.6\,\mathrm{g\,kg^{-1}}$ via equation (3.4.1).

6.4 Results & Discussion

In this section, we validate the performance of our sea ice model by comparing the modelled ice depth, temperature profiles and bulk salinity profiles with measurements from the Barrow MBS (ice depth and temperature) and the 2009 field campaign (temperature and bulk salinity profiles from ice cores).

It is well known that modelled sea-ice thickness is highly sensitive to the thermal conductivity of snow k_{snow}, the value of which is poorly constrained. In §6.4.1, we discuss the physical processes that control heat transport in the snowpack and the range of values of k_{snow} that have been reported in the literature. The thermal conductivity of the snow pack is treated as the only tuning parameter for our model. This is a reasonable approach, since the snowpack is highly heterogeneous and we have already neglected much of the complexity of the snowpack in our model by treating it as a single layer with a prescribed thickness. Note that this approach is vulnerable to errors in the snow depth (see appendix G) and so simulations should be validated against observations of ice thickness where available. As discussed in detail in §6.4.2, our approach here is to run a suite of simulations to determine the value of k_{snow} that best reproduces the observed ice thickness at Barrow.

6.4.1 Snow thermal conductivity

Snow that falls on Arctic sea ice undergoes various complex metamorphosis pathways that depend on environmental conditions such as temperature and wind speed. The result is a complex snowpack composed of a variety of snow types with very different microstructures, densities, and thermal conductivities (see Sturm and Massom 2017, for a review). In our model, a single value of k_{snow} must account for effective thermal transport across the snowpack as a whole. Measurements of the thermal conductivity of snow can be as low as around $0.07\,\mathrm{W\,m^{-1}\,K^{-1}}$ in new snow and depth hoar, and as high as around $0.45\,\mathrm{W\,m^{-1}\,K^{-1}}$ in very hard wind slab (Sturm et al. 1997). Based on recent measurements, Macfarlane et al. (2023) propose a value of $0.25\,\mathrm{W\,m^{-1}\,K^{-1}}$ to best represent the thermal conductivity of the Arctic snowpack on sea ice. This is significantly lower than the value of $0.42\,\mathrm{W\,m^{-1}\,K^{-1}}$ chosen in

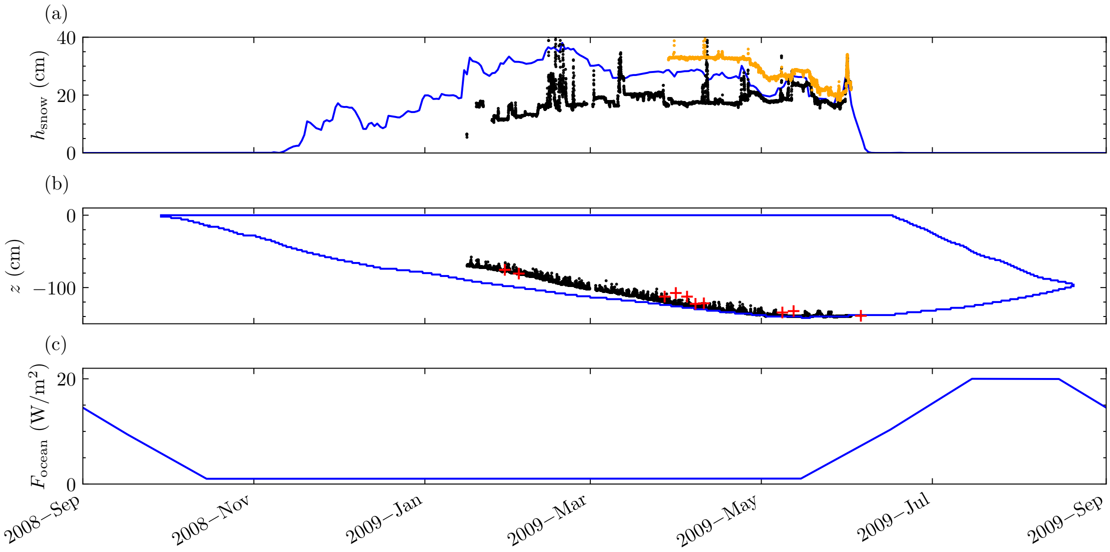

Figure 6.4: Panel (a) shows the snow depth at the MBS from SnowModel-LG (blue curve) and from two different acoustic instruments installed at the Barrow MBS (black and orange dots). Panel (b) shows the simulated ice depth with $k_{\text{snow}} = 0.42\,\mathrm{W\,m^{-1}\,K^{-1}}$ and the other parameters as reported in table 6.1 (blue curve), the ice depth recorded by the MBS from 2009-01-15 to 2009-06-02 (black dots), and the depth of ice cores retrieved during the sampling periods BRW1-10 (red crosses). Panel (c) shows the ocean heat flux used in the simulation.

this thesis. It is also lower than the value of $0.31\,\mathrm{W\,m^{-1}\,K^{-1}}$ that is widely used in sea ice models (Lecomte et al. 2013), and has also been used in simulations of the sea ice at Barrow in the 1999–2000 and 2000–2001 seasons (Vancoppenolle et al. 2007).

It is a well known unresolved problem that the thermal conductivity of snow required for thermodynamic models of sea ice growth to accurately predict ice thickness is higher than measured values of snow thermal conductivity. Three plausible explanations for enhanced thermal conductivity of the snowpack on sea ice were summarised by Sturm and Massom (2017): (1) buoyancy-driven convection of the air in a porous snow cover by strong temperature gradients (Powers et al. 1985), (2) wind pumping in the snow cover driven by wind blowing over the snow surface (Albert and Mcgilvary 1992), and (3) uneven distribution of snow on the ice (drifts) (Sturm et al. 2002).

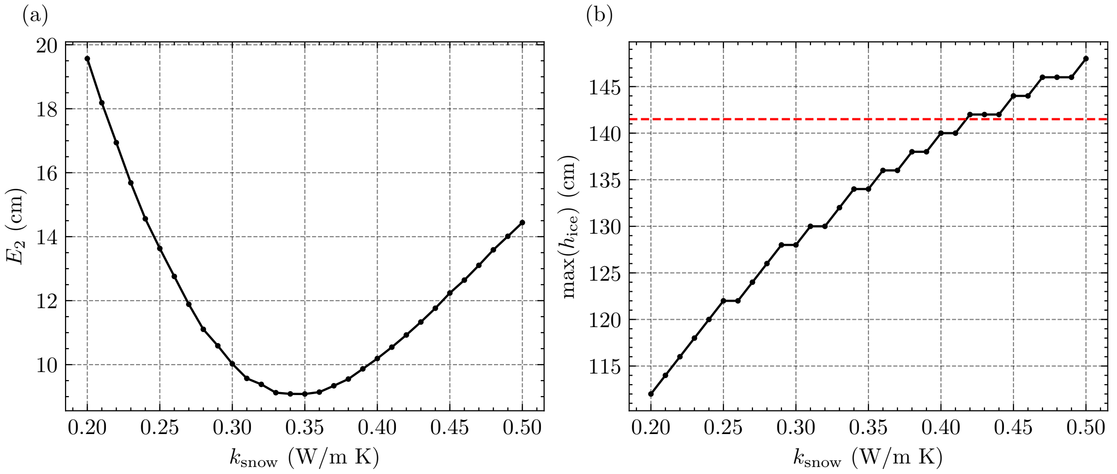

Figure 6.5: The RMSE E_2 versus k_{snow} (a) and the maximum simulated ice depth versus k_{snow} (b). The remaining parameters for the simulations are as reported in table 6.1. The dashed red horizontal line on the right panel indicates the maximum ice core depth of 141.50 cm recorded during the field campaign (BRW10).

6.4.2 Ice thickness and choosing the thermal conductivity of the snow

First, we compare the simulated ice depth $h_{\text{ice}}(t)$ to the measurements of ice depth from the Barrow MBS $\hat{h}_{\text{ice},\,i}$. Figure 6.4b shows the observed ice depth from the MBS and ice core measurements at Barrow compared with the simulated ice depth for $k_{\text{snow}} = 0.42\,\text{W}\,\text{m}^{-1}\,\text{K}^{-1}$, which is determined below to provide the best fit to the observations in the remainder of this section. The ice grows downward from January–May, reaching a maximum depth of 141.50 cm measured from ice cores taken during BRW10 (2009-06-05). The ice thickness record ends in June, prior to the breakup of the ice.

We define the root mean square error (RMSE) between the modelled ice depth $h_{\text{ice},\,i} = h_{\text{ice}}(t_i)$ at measurement time t_i and the measured ice depth from the Barrow MBS $\hat{h}_{\text{ice},\,i}$ as

$$E_2 = \sqrt{\frac{1}{N}\sum_i (h_{\text{ice},\,i} - \hat{h}_{\text{ice},\,i})^2}, \tag{6.4.1}$$

where N is the number of measurements.

Figure 6.5 shows the RMSE (panel a) and the maximum ice depth (panel b) for $0.2\,\text{W}\,\text{m}^{-1}\,\text{K}^{-1} < k_{\text{snow}} < 0.5\,\text{W}\,\text{m}^{-1}\,\text{K}^{-1}$. We select a best-fit value for k_{snow}

by minimising E_2 subject to the condition that the simulated maximum ice depth exceeds the maximum ice core depth of 141.50 cm recorded during the field campaign (BRW10). We impose this additional constraint because ice-core measurements are known to underestimate the true ice thickness due to loss of highly porous, fragile ice at the base of the core during extraction (see §6.4.5 for more discussion). Therefore, ensuring simulated ice depth at least exceeds the observed ice depth will aid comparison with field data in the remainder of this chapter and in chapter 7. Although the global minimum RMSE of 9.08 cm occurs for $k_{\text{snow}} = 0.35\,\text{W}\,\text{m}^{-1}\,\text{K}^{-1}$, the minimum RMSE subject to this additional constraint on maximum ice depth occurs for a somewhat higher value of $k_{\text{snow}} = 0.42\,\text{W}\,\text{m}^{-1}\,\text{K}^{-1}$ (RMSE of 10.93 cm); we use the latter value in simulations going forward. Simulation results for this value of k_{snow} are shown in figure 6.4. This value of k_{snow} overestimates the ice thickness in January–March, but we find excellent agreement with the observations from the MBS for the rest of the season. A comparison of the simulated ice depth to the full MBS record (2006–2015) for this value of k_{snow} is given in appendix G.

6.4.3 Seasonal ice evolution and melt pond formation

Figure 6.6a shows contours of the solid fraction (with the ice–ocean boundary as a red curve and snow cover shown in purple) for $k_{\text{snow}} = 0.42\,\text{W}\,\text{m}^{-1}\,\text{K}^{-1}$. From initial ice formation (September/October) until the onset of the melt season (May/June), snow cover insulates the ice surface and reflects the majority of incoming shortwave radiation. Once the snow cover melts in early June, surface melting of the ice leads to the formation of a melt pond (figure 6.6a). The onset of ponding in June is comparable to the observed time of pond formation atop the landfast ice at Barrow (Polashenski et al. 2012; Polashenski et al. 2017), which can be seen in the last satellite image in figure 6.1. As the melt season continues, the ice melts from above and below, and disappears completely in August (figure 6.6a).

Note that in reality, the position of the waterline for free-floating ice (the freeboard) is determined by the hydrostatic balance of the ice and snow cover, as discussed further in chapter 1. This is further complicated at Barrow, where

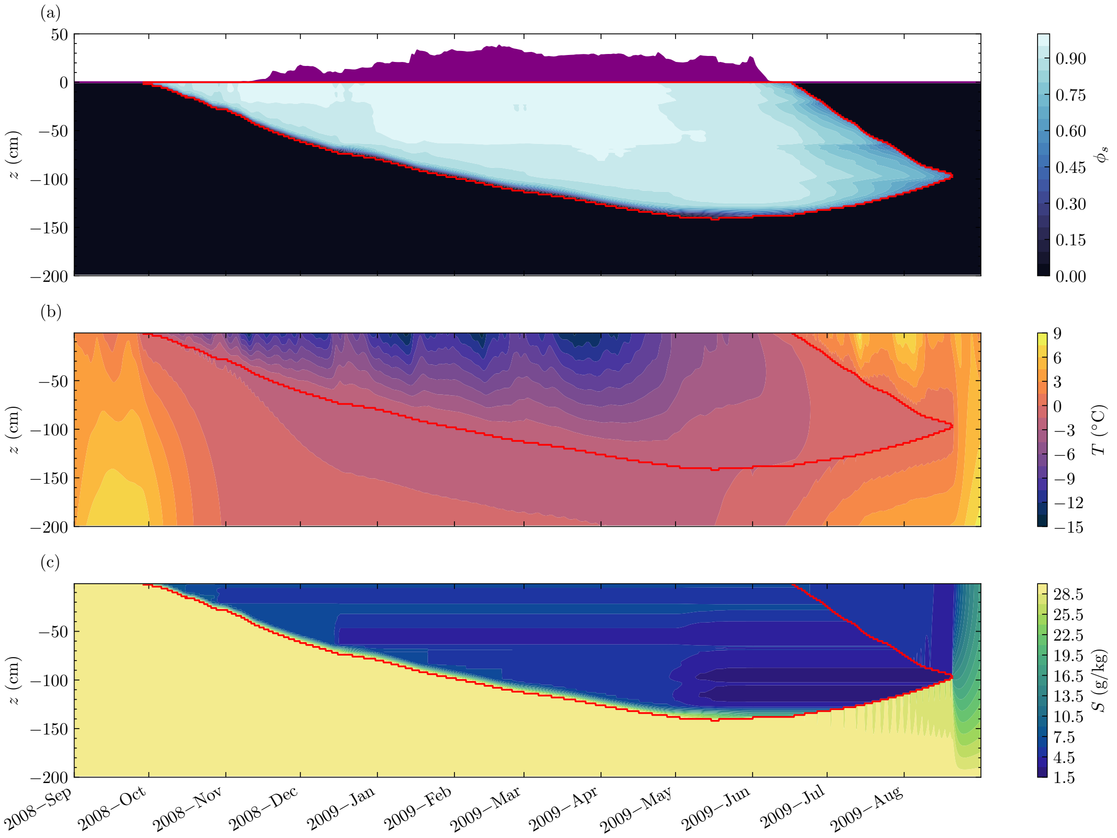

Figure 6.6: Contours of (a) solid fraction, (b) temperature, and (c) bulk salinity for the simulation with $k_{\text{snow}} = 0.42\,\mathrm{W\,m^{-1}\,K^{-1}}$ and other parameters as reported in table 6.1. The ice–ocean interface and top ice surface are plotted as a red lines, and in the upper panel the snow depth from the SnowModel-LG data is shown as the filled purple region atop the ice.

the ice is landfast and therefore not free-floating. Our model does not include any motion or deformation of the solid phase, so ice freezes and melts in place due solely to thermodynamic considerations. As a result, the snow–ice interface is always fixed at $z = 0$ and the ice surface melts downwards from $z = 0$ once the snow cover is lost in summer.

Also, the model neglects accumulation on the ice surface of fresh water generated from the melting snow cover, which can initiate pond formation (Eicken et al. 2002) and percolate downward through sufficiently permeable ice, where it may re-freeze (Polashenski et al. 2017). We have neglected the fresh water flux from snow melt in our model, such that melt ponds in our simulations are formed solely from surface melting of the ice.

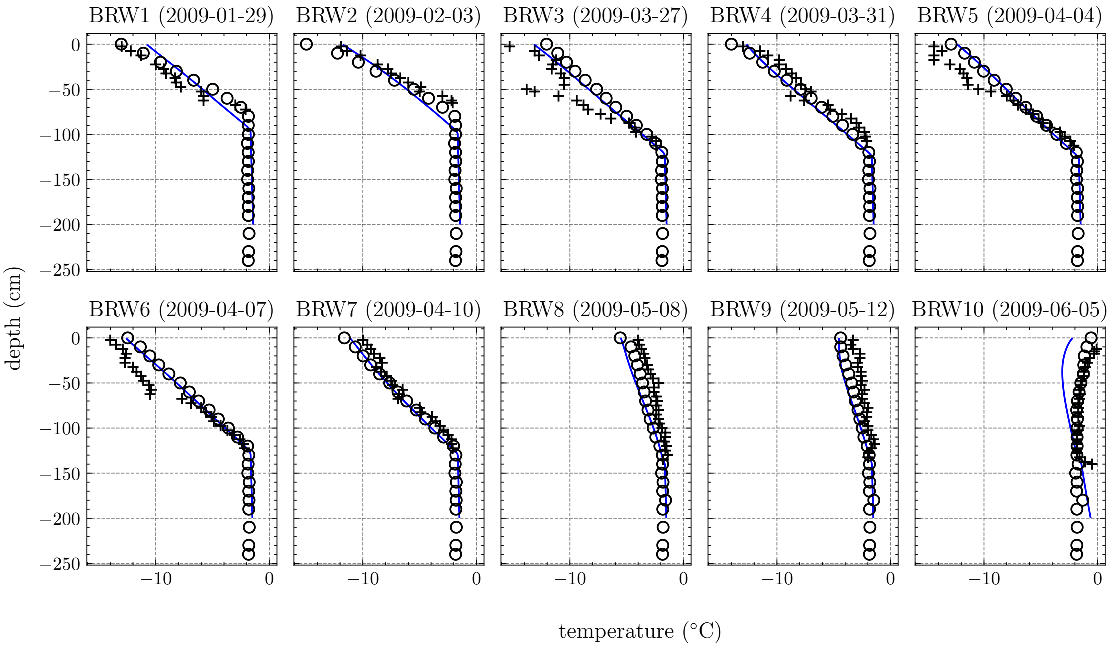

Figure 6.7: Temperature profiles in the ice and ocean for the ten sample periods BRW1–10 of the Barrow field study. Field data are shown from the MBS thermistor string (open circles) and in-situ ice core measurements on extraction (crosses). Simulated temperature profiles (blue line) for $k_{\mathrm{snow}} = 0.42\,\mathrm{W\,m^{-1}\,K^{-1}}$ and the other parameters as reported in table 6.1.

6.4.4 Temperature profiles

Figure 6.7 shows the simulated temperature profiles in the ice and ocean for each sample period at Barrow. From January–May the temperature increases downwards from the ice surface, which is cooled by atmospheric heat fluxes, to the in-situ freezing temperature at the ice–ocean interface. With the onset of the melt season in June, the ice warms and the temperature gradient in the ice reverses. In the melt season, the ice can reach temperatures above the freezing point of seawater while remaining solid, because the desalination of the ice during growth has increased the freezing temperature of the ice.

The simulated temperature profiles are generally in good agreement with the field measurements made during core extraction and via the thermistor string temperature record from the Barrow MBS for each of the ten sample periods BRW1–10 (figure 6.7). The temperature profiles from the ice cores appear to be nosier than the thermistor string measurements, which may indicate a larger sampling error. The simulation underestimates warming in the ice during the onset of the melt season (BRW10). Zhou et al. (2013) noted that there was a significant amount of snow melt between BRW9 and BRW10 and identified the formation of some snow ice in the core extracted during BRW10. One explanation for the underestimate of ice temperature in the simulation in BRW10 could be neglecting the latent heat released during re-freezing of snow melt water percolating through the ice.

The value of eddy diffusivity used in the simulation is sufficient to keep the temperature profile in the ocean relatively uniform, in agreement with the measurements made by the thermistor string for BRW1–9. However, the simulated temperature gradient in the ocean is steeper than the measurements from the MBS at BRW10. This is likely due to the low value of κ_ε used in the simulation (due to computational constraints) which underestimates turbulent heat transport in the ocean when the ocean heat flux increases in the summer. Figure 6.6b suggests that the simulation also likely overestimates temperatures in the melt pond and ocean during the summer, likely for the same reason. Initially, simulated pond temperatures are similar to those observed in melt ponds on Arctic sea ice by Kim et al. (2018), but much higher temperatures are seen in the simulated ponds from July onwards. At this point our model is lacking other important processes such as pond drainage as discussed in §6.4.3.

6.4.5 Bulk salinity profiles

During growth, convective brine rejection acts to desalinate the interior of first-year ice relative to the ocean, leading to the typical C-shaped bulk salinity profiles for sea ice (Malmgren 1927; Notz and Worster 2009) that is also seen in the winter measurements from Barrow in figure 6.8 (Zhou et al. 2013). The simulation correctly reproduces the desalination of the ice interior relative to the ocean during ice growth in periods BRW1–9. This validates our choice of brine-drainage parameterisation (Rees Jones and Worster 2014) and the chosen tuning parameter values. However, there is a larger discrepancy between the simulated and measured ice thickness for periods BRW1 and BRW2 compared to later periods. The fact that our simulations reproduce realistic temperature and bulk salinity profiles suggests that, given a

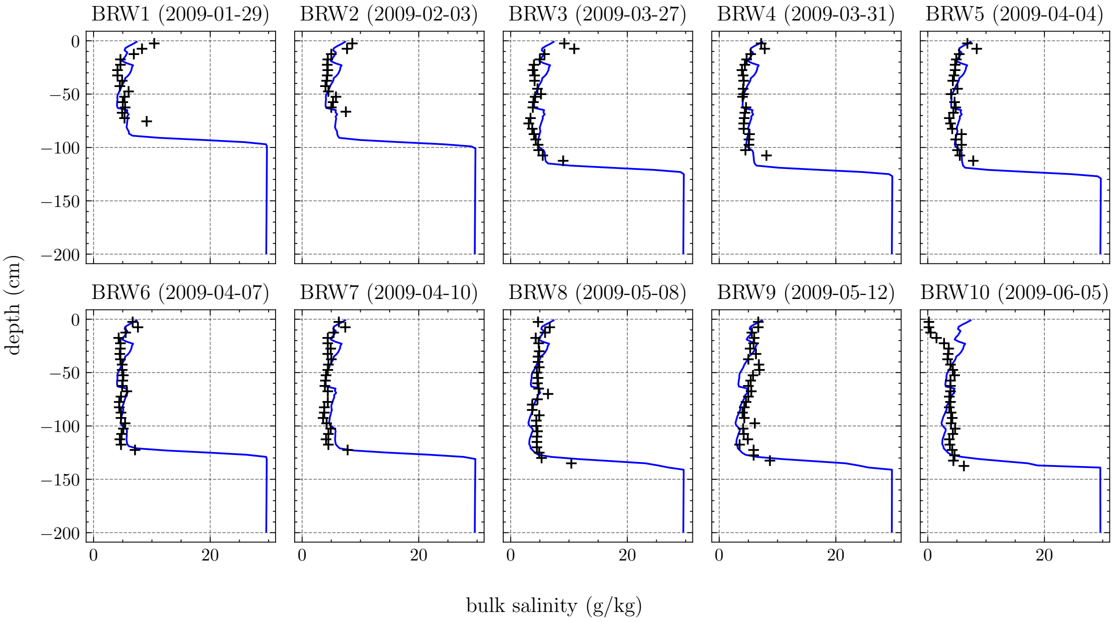

Figure 6.8: Bulk salinity for the ten sample periods BRW1–10 (black crosses) from ice cores and from simulations (blue curves) for $k_{\text{snow}} = 0.42\,\mathrm{W\,m^{-1}\,K^{-1}}$ and the other parameter values as reported in table 6.1.

sufficiently accurate liquidus relation, they are likely able to reproduce realistic porosity profiles under the assumption of local thermodynamic equilibrium.

There is a smooth but rapid vertical transition from porous ice to liquid at the ice–ocean interface. Therefore, simulated bulk salinity profiles will always smoothly transition to the ocean salinity at this interface. Ice core measurements typically underestimate the salinity of porous ice at this interface because brine is easily lost from the very porous ice at the base of the core during extraction, and also because the ice at the base is very fragile (Notz and Worster 2009; Hunke et al. 2011). Therefore, we are likely to see a discrepancy between measured and simulated bulk salinity at the ice base.

The low bulk salinity measurements at the top of the ice in BRW10 are attributed to the percolation of snow melt water downward through the ice, also called flushing (Zhou et al. 2013). Our simulations neglect the flow of fresh water downward through the ice during snow melt, and hence do not reproduce the observed freshening in the upper region of the ice in BRW10. In the absence of this feature, the simulation is likely to overpredict the ice porosity in the upper layers during this period (BRW10).

6.5 Conclusions

In this chapter, we have shown that the transient sea ice model developed in chapters 3–5, when used in conjunction with ERA5 reanalysis data for the atmospheric forcing and snow depths from SnowModel-LG, can accurately predict the heat and salt budgets during the growth of first-year landfast sea ice at Barrow, Alaska. Our simulations accurately predict the temperature and bulk salinity observed in ice cores BRW1–9 (January–May) taken during the 2009 field campaign. This provides confidence in the calculated ice porosity profiles during simulations of the first-year ice at Barrow. This is important because the next chapter uses the simulations developed here to investigate the air content of the ice at Barrow during the 2009 field campaign. The mobility of gas bubbles is found to be highly sensitive to the ice porosity, so it is important that the simulation can accurately predict the porosity of the ice cores in which we will compare simulated and observed bulk gas concentrations. The simulated temperature and bulk salinity profiles agree less well with the ice core measurements taken in June (BRW10), likely due having neglected the downward flux of fresh water at the ice surface from snow melt. We discuss the impact of this phenomenon on the predicted ice porosity in chapter 7, alongside strategies to aid the comparison with bulk gas measurements during this period.

In chapter 8, we adapt the transient three-phase mushy-layer model to investigate the fate of oil droplets (resulting from the weathering of crude oil) in the Arctic sea-ice environment, and their impact on radiative feedbacks in the ice. We use the simulations developed here as a case study to investigate the potential impacts of different concentrations of oil droplets in first-year landfast sea ice. We also find that, with some exceptions, the simulation configuration chosen here is usually capable of generally reproducing the ice thickness record in other years the MBS was deployed at Barrow (see appendix G for details) with errors typically smaller than 20 cm. Therefore, we conclude that our model provides a realistic ice state that we use in chapter 8 to investigate the potential impact of low levels of oil droplet pollution.

As discussed in detail above, the simulated ice thickness is sensitive to the value of the snow thermal conductivity k_{snow}, which is not well constrained. For the parameters investigated, we find that $k_{\text{snow}} = 0.42\,\mathrm{W\,m^{-1}\,K^{-1}}$ can reasonably reproduce the ice thickness record observed at the Barrow MBS during the 2008–2009 growth season for simulations initialised with appropriate ice-free conditions in September 2008 with a maximum overestimate of around 20 cm in January. The optimal value determined for the thermal conductivity of the snow layer is significantly higher than measured values in the literature. However, as noted above, this is a problem common to many one-dimensional numerical models of sea ice growth with a range of proposed explanations in the literature (Sturm and Massom 2017). We also note that our assumption of a uniform snow and ice thickness is an inherent limitation that can severely underpredict the shortwave radiation transmitted to the ice and ocean in the presence of snow drifts or leads (Mallett et al. 2022).

We have approximated the turbulent mixing of heat and salt in the ocean and melt pond using an eddy diffusion parameterisation with $\kappa_\varepsilon = 1 \times 10^{-6}\,\mathrm{m^2\,s^{-1}}$. This value is chosen based on the computational constraints of our explicit numerical method and is likely several orders of magnitude smaller than the true value of κ_ε in the ocean and melt pond. This is not a significant issue during ice growth where heat transport to the ice–ocean interface is constrained by the small ocean heat flux. However, we see significantly higher temperatures than expected in the melt pond and ocean in summer, which is likely due to the heat absorbed through the absorption of shortwave radiation and increased ocean heat flux being less efficiently mixed. This may lead us to underestimate the rate of surface and basal melt, although as noted earlier our model is also missing a mechanism of pond drainage which typically occurs on the timescale of days to weeks as ponds deepen (Eicken et al. 2002; Polashenski et al. 2012).

7

The air content of first-year sea ice

7.1 Introduction

The gas content of sea ice is of interest for several reasons, as discussed in chapter 1. The gas phase in sea ice provides an additional transport pathway for dissolved gases such as CO_2, CH_4, Ar, O_2, and N_2 between the ocean and atmosphere. The gas content of sea ice also strongly affects the bulk density of the ice, which is a key uncertainty for determining ice thickness from satellite measurements of the height of the ice above the waterline (i.e., the freeboard). Ice thickness is estimated from the measured freeboard by assuming that the ice and overlying snow are floating in hydrostatic equilibrium. This calculation requires the bulk density of the ice, which is not usually known and itself depends on the air fraction of the ice.

The air fraction of sea ice can be estimated from measurements of the bulk density using the formulae given in Cox and Weeks (1983). Cox and Weeks (1983) estimate the density of gas-free sea ice at different temperatures and salinities using empirical thermodynamic relationships for the mass fractions of ice, water, dissolved salts, and solid salts. The air fraction is then estimated from the difference between the estimated density of gas-free ice and the measured density. This procedure can also be reversed to estimate the bulk density of sea ice with a known air fraction. However, the air fraction of sea ice is not routinely measured. The air fraction in sea ice cores has been estimated directly from thin sections (e.g., Light et al. 2003) and using more modern techniques such as X-ray tomography (e.g., Crabeck et al. 2016).

In this chapter, we use the three-phase mushy-layer model for sea ice developed in chapters 2 and 3 to estimate the air fraction in sea ice at Barrow, Alaska, during the 2008–2009 season. In §7.2, we describe how the bulk concentration of the three most abundant atmospheric gases in the ice (nitrogen, oxygen, and argon) is estimated from the air content using the solubility of each gas in seawater. In §7.3, we describe some key features of measured profiles of bulk nitrogen, oxygen, and argon concentrations from Barrow. In §7.4, we describe the configuration of our simulations and how we calculate the bulk air budget and estimate the bulk density of the simulated ice. In §7.5, we present the results of the simulations and use the measurements of bulk gas concentrations from Barrow to constrain the dimensionless parameters δ_0 and Da that control the gas dynamics in our model. We also discuss the implications of our results for the bulk density of the ice and compare our own estimates of bulk density to values in the literature. Finally, in §7.6, we summarise the key findings of this chapter.

7.2 The composition of the gas phase

The model developed in chapter 3 treats the gas in sea ice as a single component; however, the gas content of sea ice comprises a mixture of gas species found dissolved in seawater. Partitioning the air in sea ice between different species is important for comparing the simulated gas content with field measurements.

We assume that the bulk gas content of sea ice comprises nitrogen, oxygen, and argon, which together account for over 99% of Earth's atmosphere by volume. We assume that the surface layer of the ocean (before ice formation) is saturated with nitrogen, oxygen, and argon from the atmosphere, which is reasonable for a well-mixed layer of the ocean in contact with the atmosphere. We take the solubility of nitrogen, oxygen, and argon in seawater at a temperature of $-1\,^{\circ}\mathrm{C}$ and salinity of $30\,\mathrm{g\,kg^{-1}}$ to be $\xi_{\mathrm{N_2,SAT}} = 14.75 \times 10^{-6}\,\mathrm{m^3\,kg^{-1}}$, $\xi_{\mathrm{O_2,SAT}} = 8.354 \times 10^{-6}\,\mathrm{m^3\,kg^{-1}}$, and $\xi_{\mathrm{Ar,SAT}} = 0.4058 \times 10^{-6}\,\mathrm{m^3\,kg^{-1}}$, respectively (Weiss 1970). These values are similar to the measured concentrations of nitrogen, oxygen, and argon in the top 50 m of the ocean (Nakayama et al. 2002).

Using the ideal gas law at a temperature of $-1\,^{\circ}\mathrm{C}$ and atmospheric pressure of $1.01 \times 10^{5}\,\mathrm{Pa}$ to convert gas volumes to moles, and then the molar masses of nitrogen, oxygen, and argon of $14.01 \times 10^{-3}\,\mathrm{kg\,mol^{-1}}$, $16.00 \times 10^{-3}\,\mathrm{kg\,mol^{-1}}$, and

$39.95 \times 10^{-3}\,\mathrm{kg\,mol^{-1}}$, respectively, we find that the total mass of air per unit mass of seawater at saturation is $\xi_{\mathrm{SAT}} = 3.111 \times 10^{-5}\,\mathrm{kg\,kg^{-1}}$. We assume that the composition of gases within sea ice, both dissolved and in the free-gas phase, remains the same as the composition at saturation in the ocean. Therefore, the bulk concentrations of nitrogen, oxygen, and argon in the ice in moles per unit volume can be calculated from the dimensionless bulk gas content Γ (introduced in chapter 3) via

$$[\mathrm{N_2}] = \psi_{\mathrm{N_2}} \rho_g \Gamma, \tag{7.2.1}$$

$$[\mathrm{O_2}] = \psi_{\mathrm{O_2}} \rho_g \Gamma, \tag{7.2.2}$$

and

$$[\mathrm{Ar}] = \psi_{\mathrm{Ar}} \rho_g \Gamma, \tag{7.2.3}$$

respectively, where $\rho_g = 1.00\,\mathrm{kg\,m^{-3}}$ is the density of air and $\psi_{\mathrm{N_2}} = 21.167\,\mathrm{mol\,kg^{-1}}$, $\psi_{\mathrm{O_2}} = 11.988\,\mathrm{mol\,kg^{-1}}$, and $\psi_{\mathrm{Ar}} = 0.582\,\mathrm{mol\,kg^{-1}}$ are the moles of nitrogen, oxygen, and argon per unit mass of air at a temperature of $-1\,^{\circ}\mathrm{C}$ and a pressure of $1.01 \times 10^5\,\mathrm{Pa}$, respectively.

7.3 Measurements

Figure 7.1 shows the measured bulk concentration profiles (dissolved and gaseous) of nitrogen (first column), oxygen (second column), and argon (third column) in the first-year landfast sea ice cores extracted during the sampling periods BRW2, BRW4, BRW7, BRW8, and BRW10 of the field study conducted at Barrow, Alaska, in 2009; see chapter 6 for a more detailed description of the field campaign. In the first three columns of figure 7.1, the bulk concentrations of the gases are compared to the in-situ solubility of each gas species (open black circles), which is calculated by multiplying the local liquid fraction by the oceanic solubility (shown as a vertical black line). The liquid fraction values are calculated from the measured temperature and salinity using the formulae of Cox and Weeks (1983). Note that the formulae of Cox and Weeks (1983) are semi-empirical and are not exactly equivalent to the mushy-layer formulae introduced in chapters 2 and 3. Previous modelling of

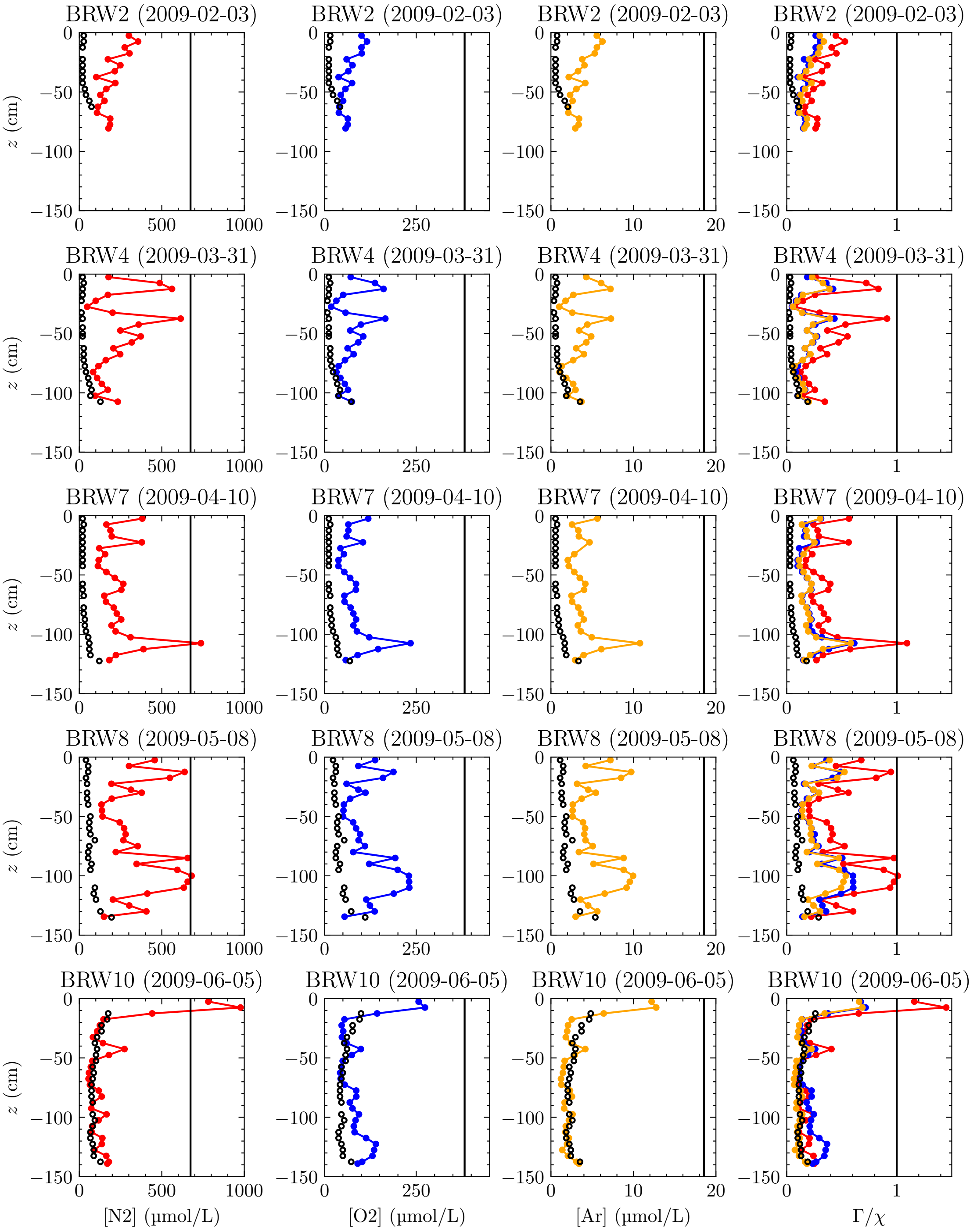

Figure 7.1: Vertical profiles of the bulk concentrations of nitrogen (red, first column), oxygen (blue, second column), and argon (orange, third column) in ice cores taken during sampling periods BRW2, BRW4, BRW7, BRW8, and BRW10 (top to bottom) at Barrow, Alaska in 2009. The open circles indicate the estimated in-situ solubility of each gas species, calculated as the local liquid fraction multiplied by the oceanic solubility value, where the liquid fraction is determined from temperature and salinity measurements. The oceanic solubility values are indicated by the vertical black lines (Weiss 1970). The final column shows estimates of the scaled dimensionless bulk air content Γ/χ calculated from the measurements of nitrogen (red), oxygen (blue), and argon (orange) using equations (7.2.1)–(7.2.3). The oceanic solubility values for all three species collapse to $\Gamma/\chi = 1$ (vertical black line) and the in-situ solubility estimates are the same for all three species (open black circles). The data was kindly provided by Prof. Jean-Louis Tison (see Zhou et al. 2014a; Zhou et al. 2013).

the argon content of sea ice at Barrow (Moreau et al. 2014) included the effect of temperature and salinity variations in sea ice brines on the solubility of argon using the fit of Hamme and Emerson (2004). However, including temperature and salinity effects on the gas solubility is likely to be unnecessary because these are small compared with changes to the in-situ solubility driven by changes in the liquid fraction (Tison et al. 2017; Zhou et al. 2013).

Assuming that the degree of gas–liquid disequilibrium is small, the bulk concentration of gas in excess of the in-situ solubility provides an estimate of the proportion of the gas content residing in bubbles. Except at the base of the cores, the measurements from BRW2–BRW8 (early February to early May) show bulk gas concentrations well in excess of the in-situ solubility for all gas species (figure 7.1, top four rows). Therefore, we conclude that a significant volume of air is trapped in gas bubbles within the ice during this period (Zhou et al. 2013; Zhou et al. 2014a). In contrast, aside from the top 15 cm of the cores, the measurements from BRW10 (early June) show bulk gas concentrations near the in-situ solubility values for all gas species (figure 7.1, bottom row). It has been proposed that the return of gas concentrations to solubility indicates the loss of gas bubbles due to bubble migration as the ice warmed and became more permeable between BRW8 and BRW10 (Zhou et al. 2013). This observation led the authors of Zhou et al. (2013) to propose a porosity threshold of 7.5–10%, above which gas bubbles are able to migrate vertically, motivating later studies to introduce a porosity threshold for bubble transport in models for argon in sea ice (Moreau et al. 2014). In §2.3, we instead related the porosity threshold above which bubbles are able to migrate vertically in sea ice to the ratio of the bubble radius to the pore throat radius, which is characterised by the scaled bubble radius δ_0. In this chapter, we investigate the choice of δ_0 required to reproduce the observed loss of gas bubbles from the ice between BRW8 and BRW10. Regarding the large bulk gas concentrations at the top of the ice in BRW10, Zhou et al. (2013) propose three explanations: (1) air-saturated water from melting snow refreezes at the top of the ice, (2) air intrusion from above as brine drains downward from ice above the freeboard, and (3) the trapping of bubbles migrating upwards from the ice interior due to the formation of impermeable ice layers from the refreezing of snow melt water.

The final column of figure 7.1 shows the normalised dimensionless bulk air content Γ/χ calculated from the measurements of nitrogen (red), oxygen (blue), and argon (orange) using equations (7.2.1)–(7.2.3). Argon is an inert gas, so its concentration in the ice is only affected by variations in solubility, rejection through brine channels, and bubble exsolution and migration. Despite oxygen and nitrogen both being biologically active gases, the shape of the profiles for all three gas species are similar. This similarity suggests, that to a reasonable approximation, physical rather than biological processes control the air content of sea ice. A notable exception is the high concentration of oxygen near the ice base in BRW10 compared to the other gas species. This elevated concentration of oxygen is likely the result of primary production by photosynthetic organisms at the ice base in summer, when light can penetrate the ice (Zhou et al. 2014a).

Across all of these observations, the ratio of the measured bulk nitrogen concentration to the in-situ solubility is consistently around a factor of 2 higher than for oxygen and argon. The BRW10 measurements agree with the calculated in-situ solubility values, so it is unlikely that there is an error in the solubility value used for nitrogen. The measured bulk nitrogen values suggest higher estimates of the bulk air content than those for the other species. There are several possible explanations for this discrepancy. One possibility is that the underlying ocean is super-saturated with nitrogen. Alternatively, it could be that nitrogen exsolves more readily from the liquid phase than oxygen and argon into bubbles in sea ice, which would lead to an elevated proportion of nitrogen in bubbles found in sea ice compared to oceanic values. It is also possible that certain bacteria in sea ice can convert dissolved nitrate NO_3^- in sea ice brines to molecular nitrogen N_2 via denitrification. However, the rates of denitrification in sea ice of around $22.6\,\mathrm{nmol\,N_2\,L^{-1}\,day^{-1}}$ (Rysgaard et al. 2008) are thought to be too low to have a measurable effect on the bulk concentration of nitrogen in sea ice (see § 18.3.2 of Tison et al. 2017, for a discussion).

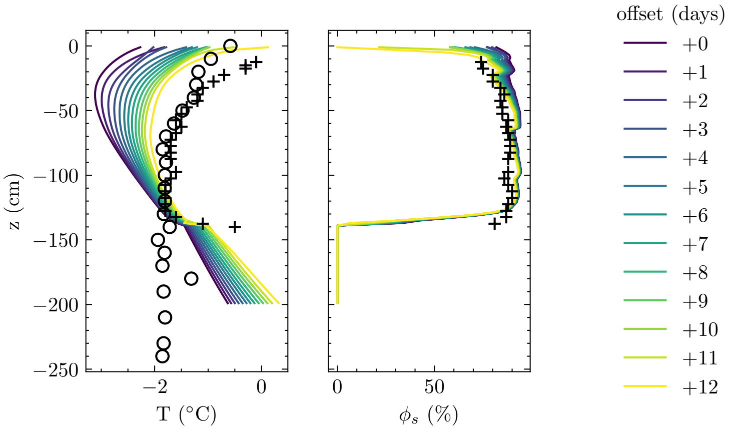

Figure 7.2: Simulated temperature (a) and solid fraction (b) profiles compared with measurements from cores taken during BRW10 (crosses) and thermistor string measurements from the Barrow Mass Balance Site (circles). We show simulation data from the same time as BRW10 and for up to 12 days afterward.

The larger super-saturations of nitrogen in the ice compared with argon or oxygen is not unique to the measurements from Barrow presented here. Similar measurements of bulk concentrations of nitrogen, oxygen, and argon in cores extracted from landfast first-year sea ice in March 2010 from Kapisillit, Greenland (64°26'N, 50°13'W), also show maximum values for the ratio of bulk gas concentrations to in-situ solubility within the ice of about a factor of 2 larger for nitrogen compared with oxygen or argon (Crabeck et al. 2014b). Crabeck et al. (2014b) estimated that the diffusivity of nitrogen in sea ice brines is about twice that of oxygen and argon. This could explain the larger super-saturations of nitrogen in the ice if nitrogen diffuses more rapidly into bubbles within the ice than oxygen or argon, leading to a higher exsolution rate of nitrogen in sea ice. For simplicity, the pore-scale processes controlling the exsolution of dissolved gases into bubbles are neglected in the model results presented in this chapter.

7.4 Methods

7.4.1 Simulation configuration

We use the model described in chapters 3–6 to predict the bulk air content of the ice at Barrow over the 2008–2009 season. From the simulated bulk air content,

Parameter	Symbol	Value
(a)		
reference pore throat radius	R_0	$1.95 \times 10^{-4}\,\mathrm{m}$ (Maus et al. 2021)
pore throat power law exponent	q	0.46 (Maus et al. 2021)
porosity threshold	ϕ_c	0.024 (Maus et al. 2021)
air density	ρ_g	$1\,\mathrm{kg\,m^{-3}}$
gas diffusivity	κ_ξ	$2.49 \times 10^{-5}\,\mathrm{cm^2\,s^{-1}}$ (Crabeck et al. 2014b)†
ocean saturation state	ω_∞	1.0
air solubility in seawater	ξ_{SAT}	$3.11 \times 10^{-5}\,\mathrm{kg\,kg^{-1}}$‡
liquid viscosity	μ_l	$2.78 \times 10^{-3}\,\mathrm{Pa\,s}$
(b)		
buoyancy scale	$\mathcal{B}$	7.26×10^5
expansion coefficient	χ	3.2×10^{-2}
Lewis number for gas diffusion	Le_ξ	50.6

Table 7.1: The parameter values used to simulate air in the sea ice at Barrow, Alaska, in addition to those reported in table 6.1. The dimensionless values (b) are calculated from the dimensional values (a).
†This value for air diffusivity is the value for N_2 in sea ice brines calculated by Crabeck et al. 2014b, which was around a factor of two larger than the value calculated for O_2 or Ar. The value of Le_ξ given in the table is calculated using this value of κ_ξ, but we take $Le_\xi \to \infty$ in the simulations presented in this chapter.
‡Calculated in §7.2 from values for N_2, O_2 and Ar in seawater at a temperature of $-1\,^\circ\mathrm{C}$ and a salinity of $30\,\mathrm{g\,kg^{-1}}$ (Weiss 1970).

we diagnose the bulk concentrations of nitrogen, oxygen and argon as described in §7.2. This allows us to constrain the dimensionless parameters (δ_0 and Da) that reproduce bulk gas concentrations consistent with the measurements from Barrow (February–June 2009) presented in §7.3.

Simulations are initialised and run with the same forcing and physical parameters described in chapter 6, and with a grid resolution of $N_z = 50$. Additionally, we now take the ocean to be saturated with dissolved air so that $\Gamma(z, t = 0) = \chi$. The deep ocean remains saturated throughout the simulation, so that $\Gamma(z = -1, t) = \chi$. This initial configuration is an improvement on the previous simulation of the argon content of the ice at Barrow (Moreau et al. 2014), in which simulations were initialised with an existing ice cover in January 2009 and thus did not capture bubble accumulation and migration within the ice during the initial stages of ice growth. Our simulation uses a similar linear relaxation model for the exsolution of dissolved gas to that used by Moreau et al. (2014), with the exsolution rate quantified by the dimensionless Damköhler number Da. However, Moreau et al.

(2014) used a diffusive parameterisation scheme for brine convection within the ice, whereas we use a convective parameterisation that is known to be more physically representative for the dynamics of dissolved tracers in sea ice (see §3.2.2). Moreau et al. (2014) also did not track the motion of bubbles through the pore space, instead assuming that all argon in the gas phase is removed from the ice to the atmosphere instantaneously when the overlying ice is above a critical porosity threshold. We instead treat the gas phase as a mixture of nitrogen, oxygen, and argon and allow the gas phase to move within the ice according to the microstructural model of bubble motion in sea ice developed in chapter 2. The bubbles in our model can only move vertically when the ice is sufficiently porous, where the threshold is determined by the local porosity and the scaled bubble radius δ_0. Additional parameters required for the simulation of the air content are given in table 7.1. Using the value for the in-situ diffusivity of dissolved gas species through the liquid phase in sea ice we find that the diffusion of dissolved gas is negligible during ice growth compared with brine convection and bubble motion. Hence, the simulations presented here were run without the diffusion of dissolved gas (i.e., $Le_\xi \to \infty$)

At the base of the ice, the solid fraction rapidly transitions to zero (the skeletal layer); as a result, this portion of the ice is much more porous and fragile than the interior. The skeletal layer is difficult to sample because it is delicate and because the interstitial brine is easily lost from the core during extraction (Hunke et al. 2011; Notz 2005). To make a fair comparison between the simulation and ice core measurements, we remove the bottom three grid cells (12 cm) of the simulated ice which we determine from plots of the solid fraction to encompass the skeletal layer. We have chosen to remove three cells since this is the minimum number of cells that need to be removed from the bottom of the ice to ensure that the porosity of the ice does not exceed the values inferred from the temperature and salinity measurements. Note that this approach is somewhat arbitrary, but is one way of dealing with the difficulty in sampling the skeletal layer using ice cores.

Our model is able to well reproduce the observed ice temperature and porosity structure during the sampling periods BRW1–9 (see chapter 6). However, our simulations underpredict warming of the ice observed in BRW10 and, as a result, the simulated ice is less porous than the observations suggest (figure 7.2). This is important because the migration and release of bubbles is highly sensitive to the solid fraction of the ice. Figure 7.2 shows the simulated temperature and solid fraction profiles at BRW10 and up to 12 days later in simulated time (coloured lines) compared with the ice core measurements (crosses) and thermistor string measurements (circles) from BRW10. Figure 7.2 suggests that we can better reproduce the ice state observed at BRW10 by comparing to simulated data from 11 days after the date of BRW10, which we denote BRW10*. Any larger delay and the simulated ice has begun to melt at the surface.

7.4.2 Bulk air budget

We now integrate equation (3.2.41) for the dimensionless bulk air content Γ over the ice thickness to determine the different contributions to the bulk air content of the ice. This calculation will aid with the interpretation of the results of our simulations later in this chapter. Consider a layer of ice in $-h_{\text{ice}} \leq z \leq -h_{\text{pond}}$ atop an ocean saturated with dissolved air (i.e., $\omega = 1$), where h_{pond} is the thickness of any surface melt pond and h_{ice} is the depth of the ice–ocean interface. Here, $h_{\text{pond}} = 0$ for most of the simulation period until a melt pond forms during the melt season. The dimensionless bulk air content Γ is the sum of the dimensionless mass of air dissolved in the interstitial liquid $\phi_l \chi \omega$ and the dimensionless mass of air in bubbles ϕ_g per unit volume of ice. Integrating the conservation equation (3.2.41) (with $Le_{\xi} \to \infty$) for the dimensionless bulk air content over the ice thickness and using the boundary conditions $\omega = 1$ and $\phi_g = 0$ at $z = -h_{\text{ice}}$ yields the following equation for the air budget of sea ice:

$$\frac{\mathrm{d}\widetilde{\Gamma}}{\mathrm{d}t} = F_{\text{base}} - F_{\text{surface}} - F_{\text{bubble}} - F_{\text{convection}}, \tag{7.4.1}$$

where

$$\widetilde{\Gamma} = \int_{-h_{\text{ice}}}^{-h_{\text{pond}}} \Gamma \, \mathrm{d}z, \tag{7.4.2}$$

is the dimensionless integrated bulk air content in the ice. The budget of $\widetilde{\Gamma}$ in the ice is controlled by the following four terms: (1) the incorporation / release of air at the ice–ocean interface during freezing / melting,

$$F_{\text{base}} = \begin{cases} \chi \dfrac{\mathrm{d}h_{\text{ice}}}{\mathrm{d}t}, & \dfrac{\mathrm{d}h_{\text{ice}}}{\mathrm{d}t} \geq 0 \quad \text{(freezing)} \\ \Gamma(z = -h_{\text{ice}}) \dfrac{\mathrm{d}h_{\text{ice}}}{\mathrm{d}t}, & \dfrac{\mathrm{d}h_{\text{ice}}}{\mathrm{d}t} < 0 \quad \text{(melting)} \end{cases}, \tag{7.4.3}$$

(2) the analogous term at the ice–melt-pond interface due to surface melt,

$$F_{\text{surface}} = \Gamma(z = -h_{\text{pond}}) \frac{\mathrm{d}h_{\text{pond}}}{\mathrm{d}t}, \tag{7.4.4}$$

(3) the flux of bubbles from the ice surface to the atmosphere,

$$F_{\text{bubble}} = W_g(z = -h_{\text{pond}}), \quad \text{where} \quad W_g = \mathcal{B}\delta_0^2 d(\delta)\phi_g, \tag{7.4.5}$$

and (4) the loss of air from the ice due to the flux of supersaturated liquid through brine channels in the convecting portion of the ice,

$$F_{\text{convection}} = \chi \frac{\alpha_{\text{RJW14}} Ra_e}{(z_c + h_{\text{ice}})^2} \int_{-h_{\text{ice}}}^{z_c} (\omega - 1)\ \mathrm{d}z. \tag{7.4.6}$$

In the absence of bubble motion (i.e., $\delta_0 \geq 1$) and brine convection, the bulk air content of the ice is equivalent to that of the underlying seawater and $\widetilde{\Gamma} = \chi(h_{ice} - h_{\text{pond}})$. The simplification of the freezing case in equation (7.4.3) is possible because the ice is growing into a well mixed ocean saturated with dissolved air.

Brine convection reduces the bulk air content of the ice compared to the ocean whenever $\omega > 1$. This loss is maximised when $Da \to 0$, meaning that there is no gas exsolution and air behaves as a passive tracer dissolved in the liquid phase. In the limit $Da \to \infty$, $\omega = 1$ during ice growth and $F_{\text{convection}} = 0$. Therefore, a higher efficiency of removal of dissolved gas from the liquid phase by gas exsolution leads to more total gas accumulating in the ice during freezing. An analogous process has previously been suggested to control the accumulation of dissolved silica within growing sea ice (Vancoppenolle et al. 2010), although in that case the silica is removed from the liquid phase by biological processes rather than bubble exsolution.

7.4.3 Estimation of sea ice bulk density

Our simulations neglect both the density difference between the solid and liquid phases (i.e., $\rho_s \approx \rho_l$) and the volume occupied by gas bubbles (i.e., $\phi_s + \phi_l \approx 1$). However, we can still estimate the effect of the simulated gas content on the ice bulk density as follows. For ice below the waterline, we assume that the presence of a volume fraction ϕ_g of gas bubbles must have displaced an equivalent volume fraction of liquid from the pore space. Therefore, we estimate the local bulk density of ice below the waterline using

$$\rho = \begin{cases} \rho_s \phi_s + \rho_l \phi_l' + \rho_g \phi_g, & \text{if} \quad \phi_l' > 0 \\ \rho_s \phi_s + \rho_g (1 - \phi_s), & \text{if} \quad \phi_l' \leq 0 \end{cases}, \quad \text{where} \quad \phi_l' = 1 - \phi_s - \phi_g, \tag{7.4.7}$$

where $\rho_s = 917\,\mathrm{kg\,m^{-3}}$ is the density of pure ice, $\rho_l = 1024\,\mathrm{kg\,m^{-3}}$ is the density of seawater, and $\rho_g = 1\,\mathrm{kg\,m^{-3}}$ is the density of air. The condition on ϕ_l' in equation (7.4.7) ensures that we do not estimate a negative liquid fraction because, under our reduced "tracer" model, the gas fraction is decoupled from the available pore space. Equation (7.4.7) is applicable for ice below the waterline and above the eutectic temperature, where $\phi_l > 0$. The temperature of the ice at Barrow in our simulations is always warmer than the eutectic temperature; however, for completeness, the local bulk density of ice below the eutectic temperature can be estimated via

$$\rho = \rho_s (1 - \phi_g) + \rho_g \phi_g. \tag{7.4.8}$$

The mean bulk density of the ice $\overline{\rho}$, which is needed to calculate the ice thickness from measurements of the freeboard (see equation 1.2.1), can be estimated by taking the mean of equation (7.4.7) over the ice thickness.

For floating sea ice in hydrostatic balance, the freeboard h_f is determined from equation (1.2.1). Our simulations thus far are for landfast ice, which is not necessarily in hydrostatic balance, and do not include a calculation of the freeboard. However, since the ice above the freeboard may be drained of brine, it is of interest to estimate the freeboard of ice in hydrostatic balance and the bulk density of ice above the waterline. We estimate the bulk density of the ice above the waterline by assuming that this ice is completely drained of brine, yielding

$$\rho = \rho_s \phi_s + \rho_g \phi_l, \tag{7.4.9}$$

where ϕ_l is the simulated liquid fraction of the ice when drainage of brine above the freeboard is not accounted for. Using equation (7.4.7) below the waterline and equation (7.4.9) above the waterline, equation (1.2.1) yields a system of equations that together determine the freeboard h_f and mean bulk density of the ice $\overline{\rho}$ for given simulated volume fractions of solid, liquid, and gas, snow depth h_{snow}, and snow density ρ_{snow}. Provided that the freeboard is positive, we determine it numerically as the first position on our computational grid where the buoyancy force on the ice is greater than weight of the ice and overlying snow. The finite grid resolution leads to an overshoot of the freeboard of at most $\Delta z = 4\,\text{cm}$.

Throughout the rest of this chapter, freeboard-density calculations are carried out using $\rho_{\text{snow}} = 355\,\text{kg}\,\text{m}^{-3}$, which is a typical value for snow on sea ice (Sturm and Massom 2017). We also exclude the skeletal layer of the ice from the calculation (i.e., the bottom 12 cm of the ice where the solid fraction rapidly transitions to zero), which may lead to an underestimate of $\overline{\rho}$. The calculations in this section also neglect the feedback of the liquid flow driven by gas exsolution and migration on the transport of heat, salt and gas within the ice.

7.5 Results

7.5.1 Comparison with bulk gas measurements from Barrow

The dependence of the integrated bulk air content on δ_0 and *Da*

Figure 7.3 shows the simulated dimensionless integrated bulk air content $\widetilde{\Gamma}$ for sample periods BRW2, BRW4, BRW7, BRW8, and BRW10 compared with the integrated bulk air content inferred from the measured bulk gas profiles via equations 7.2.1–7.2.3, as discussed in §7.3. Results are shown for dimensionless bubble radii δ_0 between 0.01 and 1, and Damköhler number Da between 0.01 and ∞. We note that the values of $\widetilde{\Gamma}$ inferred from the field observations for each gas species increase

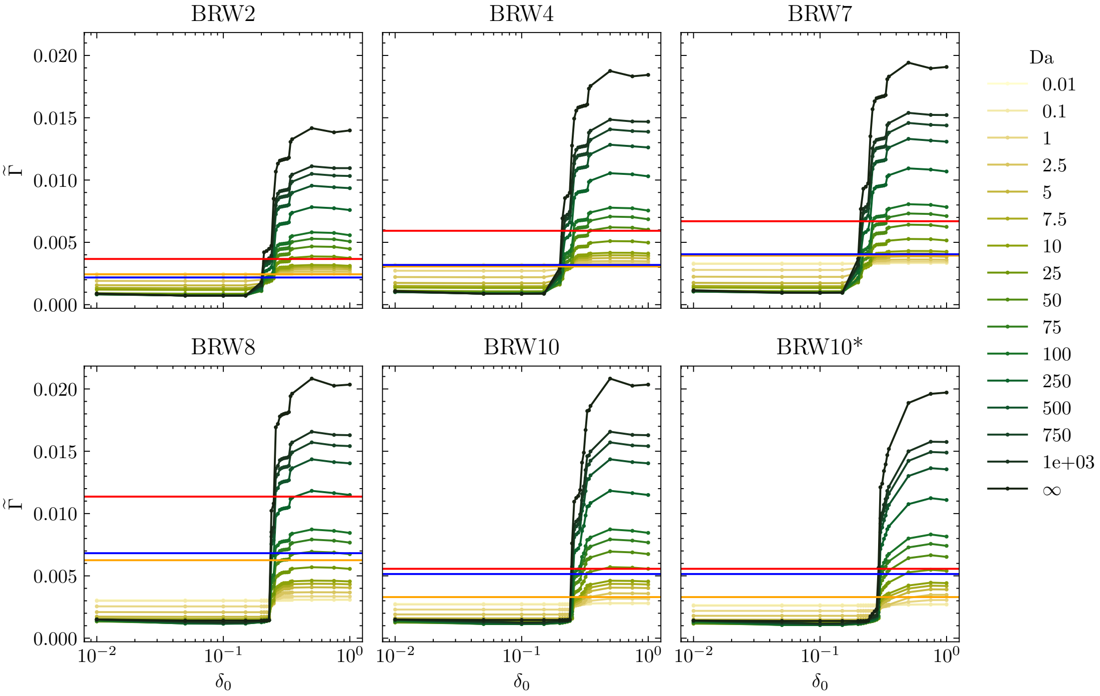

Figure 7.3: Integrated simulated dimensionless bulk air content $\widetilde{\Gamma}$ (excluding the bottom 12 cm of the ice) for sample periods BRW2, BRW4, BRW7, BRW8, and BRW10 versus δ_0 for $0.01 < Da < \infty$ (coloured lines with individual simulations indicated by a filled circle). The integrated dimensionless bulk air content $\widetilde{\Gamma}$ inferred from measured gas profiles (via equations (7.2.1)–(7.2.3)) is shown as horizontal red (nitrogen), blue (oxygen) and orange (argon) lines. The last panel shows simulation data from 11 days after the time of measurement for BRW10, at which point the simulated ice state is more similar to that observed from cores taken during BRW10.

during ice growth, BRW2–8, as gas bubbles accumulate, and then decrease by BRW10 as gas bubbles are lost from the ice. For low $Da = 0.01$, bubble exsolution is negligible and the integrated bulk air content is relatively independent of δ_0. In this low-Da regime, large super-saturations $(\omega - 1)$ are generated during freezing and this highly supersaturated liquid is expelled from the ice through brine channels during convection, leaving the ice depleted of air compared with the underlying ocean (analogous to the desalination of growing sea ice).

For $\delta_0 \gtrapprox 0.4$, exsolved bubbles are largely immobile for the porosities found in the ice, so bubbles accumulate in the ice during ice growth. In this regime, $\widetilde{\Gamma}$ varies little with δ_0 and increases with Da as gas supersaturation generated by freezing is more efficiently converted to gas bubbles within the ice before being expelled through brine channels, with $\widetilde{\Gamma}$ reaching a maximum value of χh_{ice} as $Da \to \infty$. As previously discussed in §7.4, the limit $Da \to \infty$ minimises the loss of gas from the ice via brine convection, with $F_{\text{convection}} = 0$.

For $\delta_0 \lessapprox 0.1$, bubbles are smaller than the pore throat size within the ice and are able to migrate upward and escape to the atmosphere once generated. Therefore, $\widetilde{\Gamma}$ decreases with Da and reaches a minimum determined by the in-situ gas solubility as $Da \to \infty$, for which all gas supersaturation is immediately converted to gas bubbles that escape to the atmosphere.

Neither the small-bubble ($\delta_0 \lessapprox 0.1$) or large-bubble ($\delta_0 \gtrapprox 0.4$) regimes are compatible with both the accumulation of gas in BRW2–8 and the loss of gas to in-situ solubility in BRW10. To fit the data, δ_0 must lie in the narrow range in which bubbles are mostly immobile during ice growth (BRW1–BRW7) but become mobile as the ice warms (BRW10). For this intermediate bubble size regime, consistency with observations further requires that Da must be large enough to allow for the accumulation of gas during ice growth but also small enough to allow some disequilibrium. We note that values of $\widetilde{\Gamma}$ predicted from the measurements of nitrogen are consistently higher than those inferred from oxygen or argon, suggesting that a larger value of Da is required to reproduce the nitrogen measurements compared with the oxygen and argon measurements.

The vertical distribution of gas

Figure 7.4 shows the simulated profiles of normalised bulk air content Γ/χ compared with values inferred from the measurements of bulk argon content. As discussed in §7.3, the measurements of nitrogen, oxygen, and argon show very similar patterns for BRW2–8. Here, we use the vertical distribution of the inert gas argon to further constrain our choice of δ_0. The different values of Da required to fit measurements of argon versus nitrogen are discussed in the following section.

The simulations with $\delta_0 < 0.24$ are incompatible with the observed accumulation of gas in the ice throughout BRW2–8 (figure 7.4) because the bubbles are small enough compared with the pore throat radius to escape the ice before BRW8. The simulations with $\delta_0 \geq 0.3$ are incompatible with the almost complete loss

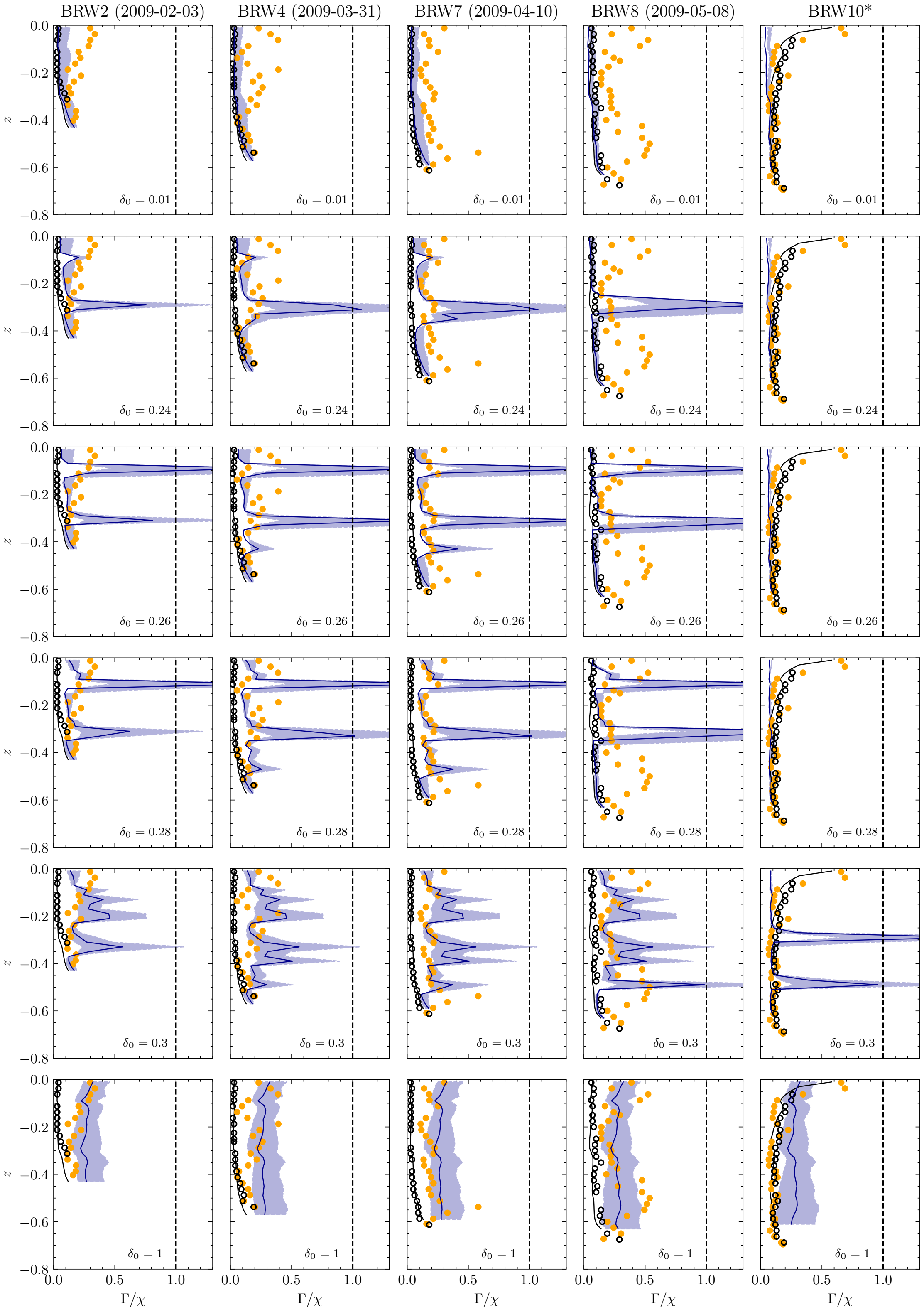

Figure 7.4: Simulated profiles of normalised bulk air content Γ/χ (dark blue line) versus dimensionless depth z in the ice (excluding the bottom 12 cm) with $Da = 25$ and a range of δ_0 values (increasing top to bottom) compared with Γ/χ inferred from measurements of argon using equation (7.2.3) (orange circles). We show data and results for the five sample periods BRW2, BRW4, BRW7, BRW8, and BRW10* (left to right), where the asterisk indicates that the measurements of BRW10 are compared with simulated values from 11 days after the date of BRW10, at which point there is better agreement with the observed solid fraction. The blue shaded region is bounded by simulations for $Da = 2.5$ and $Da = 100$.

of free gas from the ice during BRW10 (figure 7.4) because the bubbles are too large to escape the ice before BRW10*.

The simulations with $\delta_0 = 0.26$ and $\delta_0 = 0.28$ reproduce both the accumulation of gas in the ice during BRW2–8 and the loss of gas during BRW10. However, both are unable to reproduce the trapping of gas bubbles near the ice base observed in BRW8 (and bubbles are trapped at a slightly shallower depth in the ice in BRW7 compared with the observations). The peaks in bulk gas concentration in our model occur where bubbles exsolved in the ice below encounter a low enough porosity that they become trapped by narrower pore throats. Since we have used an identical distribution of bubble sizes and pores, the exact location of these peaks is very sensitive to the bubble size and the porosity profile in the ice. Therefore, slight discrepancies between the porosity profile in the simulated ice and the observations could explain the differences in the locations of peaks in the gas content. A larger uncertainty is the treatment of the gas phase with a single bubble size. We would expect a more realistic distribution of bubble sizes to lead to less localised accumulations of gas in the ice. However, we are still able to capture much of the qualitative distribution of gas in the ice with a single bubble size.

We conclude that $\delta_0 = 0.28$ is a good choice for the scaled bubble radius in our model. This size represents bubbles that are large enough to reproduce the observed accumulation of gas in the ice during growth, but small enough to reproduce the subsequent loss of gas bubbles to the atmosphere as the ice warms.

Estimating δ_0 and *Da*

Figure 7.5 shows the integrated dimensionless bulk air content $\widetilde{\Gamma}$ for $\delta_0 = 0.28$ and selected values of Da in the range $2.5 < Da < 250$. The observed values of $\widetilde{\Gamma}$ inferred from the measurements of nitrogen and oxygen or argon are well reproduced by the simulations with $Da = 100$ and $Da = 2.5$, respectively, in the periods BRW2, BRW4, BRW7, and BRW10 (figures 7.5a and 7.5b). However, a substantially larger value of Da is needed to reproduce the larger $\widetilde{\Gamma}$ values seen in BRW8. For this reason, it is important that future studies are conducted to establish if the gas

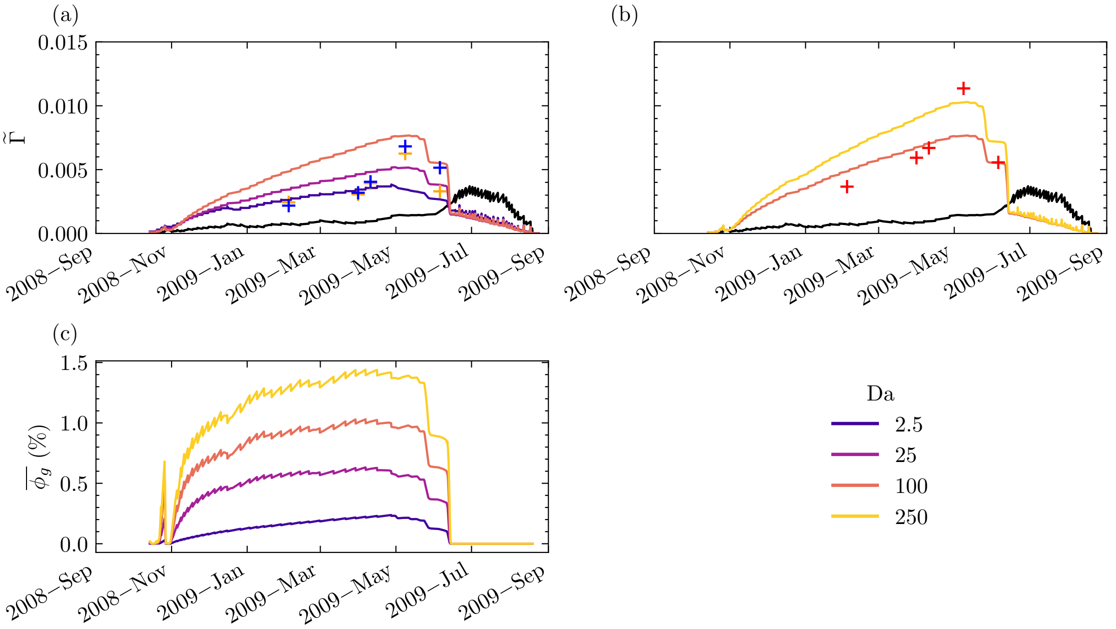

Figure 7.5: The integrated dimensionless bulk air content $\widetilde{\Gamma}$ in the ice versus time (excluding the bottom 12 cm of the ice) for $\delta_0 = 0.28$ and a range of Da values (see legend). Panel (a) compares $\widetilde{\Gamma}$ from the simulations with the values inferred from the measurements of argon (orange crosses) and oxygen (blue crosses), whereas panel (b) shows the values of $\widetilde{\Gamma}$ inferred from the measurements of nitrogen (red crosses). The solid black line indicates the value of $\widetilde{\Gamma}$ determined by integrating the in-situ solubility over the ice thickness. Panel (c) shows the mean gas fraction in the ice ϕ_g versus time (excluding the bottom 12 cm of the ice) for $\delta_0 = 0.28$ and a range of Da values (see legend).

content observed in BRW8 is typical of this time in Arctic sea ice. Zhou et al. (2013) suggested that the substantially higher gas content observed in BRW8 is due to enhanced biological activity in the ice producing hydrophobic compounds which could enhance the rate of gas exsolution. This hypothesis would suggest a biological feedback on the value of Da in the ice. Past simulations of the bulk argon content in the ice at Barrow also found that a larger gas exsolution rate was needed to explain the higher gas content seen in BRW8 (Moreau et al. 2014).

Figure 7.5c shows the mean gas fraction in the ice $\overline{\phi_g}$ for $\delta_0 = 0.28$ and $Da \in \{2.5, 25, 100, 250\}$. We find that the mean gas fraction increases during initial ice growth to a maximum value that is fairly constant during February–May and then decreases in June as the ice warms and bubbles are lost. Overall, the maximum value of $\overline{\phi_g}$ in the ice increases with increasing Da as more gas bubbles are exsolved. Note also the sudden drop in $\overline{\phi_g}$ in late October when transient warming of the ice leads to a release of accumulated gas bubbles.

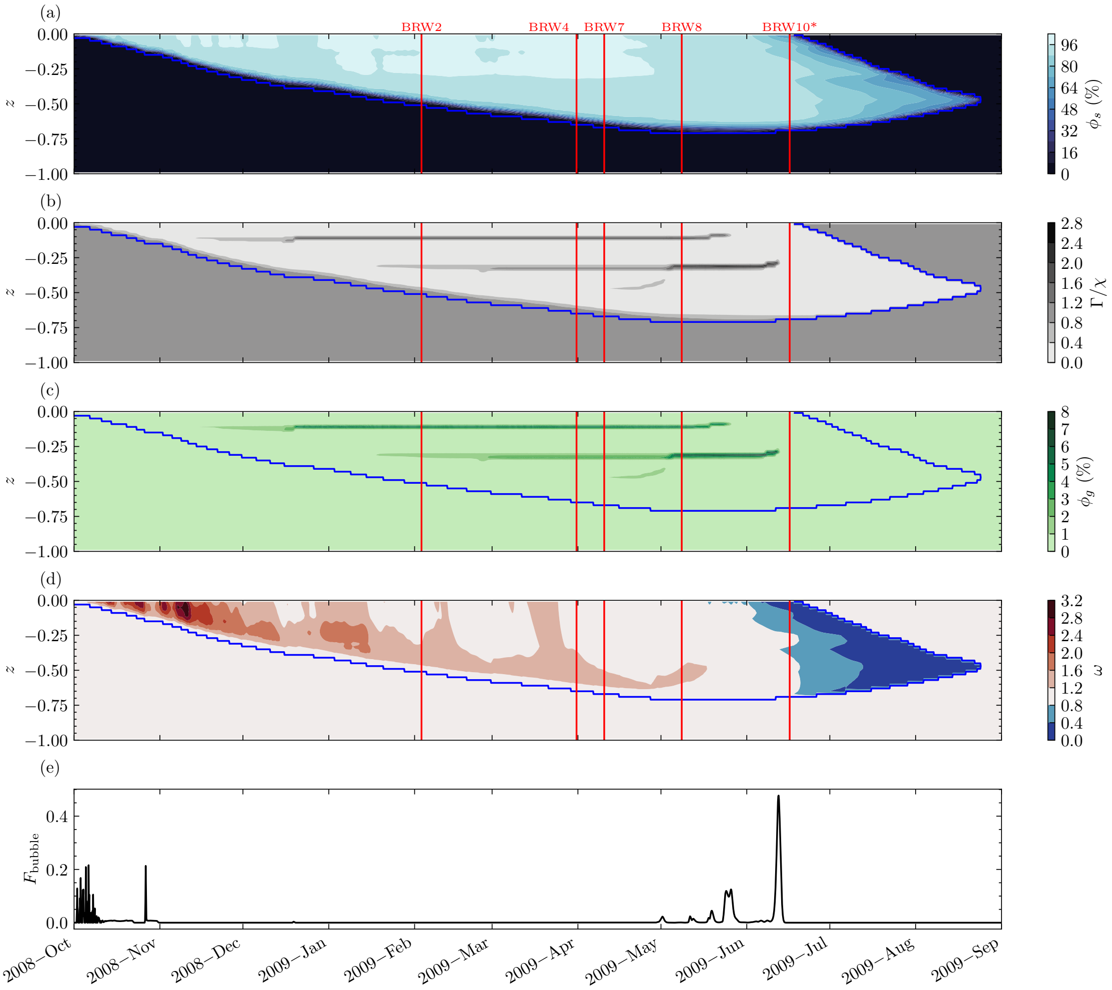

Figure 7.6: Evolution of the simulated (a) solid fraction, (b) normalised bulk gas concentration, (c) gas fraction, and (d) dissolved gas concentration for $Da = 25$ and $\delta_0 = 0.28$. Panel (e) shows the dimensionless flux of gas bubbles from the ice to the atmosphere versus time. In (a–d), the blue curve indicates the ice–ocean and ice–melt-pond interfaces and the red lines indicate the sample periods BRW2, BRW4, BRW7, BRW8, and BRW10*.

Figure 7.6 shows simulated solid fraction, bulk gas concentration, gas fraction, and dissolved gas concentration for $Da = 25$ and $\delta_0 = 0.28$. Gas accumulates in discrete layers below regions of the ice that are impermeable to gas transport. These regions have low porosity, below the threshold for bubble migration, but may still be permeable to liquid flow. Gas bubbles are lost to the atmosphere as the ice above warms and becomes sufficiently porous. The loss of gas bubbles to the atmosphere can be seen in the corresponding peaks in the ice–atmosphere bubble flux shown in figure 7.6e. Potentially, fluxes of gas bubbles from the ice to the atmosphere could be detected using the chamber technique and linked to changes in the thermodynamic state of the ice in the field to provide additional evidence for the porosity threshold for bubble motion in sea ice. The chamber technique has already been used to measure sudden ice–air carbon dioxide fluxes during a rain event (Nomura et al. 2010).

The interstitial liquid in the ice is super-saturated with dissolved gas during ice growth and becomes sub-saturated in the melt season as internal melt dilutes brines which had previously lost gas to the atmosphere via bubbles (figure 7.6d). In our simulation, the melt pond and underlying ocean remain saturated with dissolved gas due to efficient turbulent mixing and exchange with the atmosphere and deep ocean, respectively. It is possible for atmospheric gases to dissolve into sub-saturated brines at the surface of the ice, which would be seen in simulations with $Le_\xi < \infty$. This process was included in the model of Moreau et al. (2014), but was found to be only a small contribution to bulk argon budget because the diffusion of dissolved gas within the ice was relatively slow.

7.5.2 Bulk density

Sea ice bulk density measurements are routinely used to infer the air fraction in the ice using the formulae of Cox and Weeks (1983). However, here, we do the reverse and use the simulated air fraction to estimate the ice bulk density throughout the year. The bulk density of sea ice is a key uncertainty in the procedure used to infer ice thickness from satellite measurements of the freeboard (see chapter 1 for a review). In §7.4.3, we described two different methods to account for the simulated air fraction when estimating the mean bulk density of the ice. The mean bulk density $\overline{\rho}$ is estimated either by assuming that the entire ice thickness is below the waterline (i.e., $h_f = 0$) or by assuming that the ice above the freeboard is fully drained of brine, where the freeboard h_f is itself estimated from equation (1.2.1). In the latter case, we specifically avoid estimating the freeboard or ice density in the presence of a melt pond because this work does not include a hydraulic model for melt water.

Figure 7.7 shows the mean bulk density of the ice versus time in both the former case (panel a) and in the latter case (panel b). In the latter case with

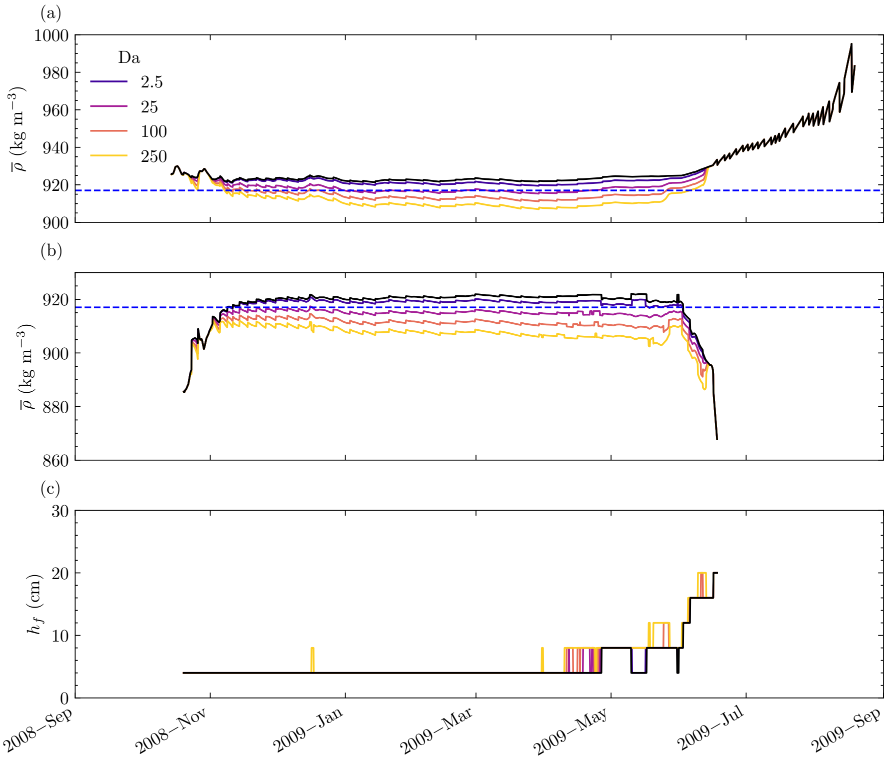

Figure 7.7: Evolution of the mean ice bulk density from simulations for $\delta_0 = 0.28$ and a range of Da values (see legend), as calculated by (a) assuming that all of the ice is below the waterline and (b) calculating the freeboard (see §7.4.3) and then assuming that ice above the waterline is completely drained of brine. The black curves in (a) and (b) show the mean bulk density of gas-free ice (i.e., $\phi_g = 0$). The density of pure ice is indicated by the horizontal dashed blue line. (c) The calculated freeboard corresponding to the ice bulk density in (b).

drainage above sea level, the computed freeboard is shown in panel (c). Note that the freeboard is determined only to the accuracy of the computational grid, $\Delta z = 4\,\mathrm{cm}$, which gives a stepwise appearance. Ice bulk densities are determined from simulations for $\delta_0 = 0.28$ and Da values in the range $2.5 < Da < 250$, which reproduce the range of integrated gas content inferred from measurements of nitrogen, oxygen, and argon during BRW2–10.

The two density estimates are similar during winter and spring (around December to April) because a negligible fraction of the ice is above the freeboard in this period due to rapid loading with snow. Gas-free ice, or ice with a low air fraction due to a low exsolution rate ($Da = 2.5$), has a bulk density slightly above the density of pure ice ($917\,\mathrm{kg\,m^{-3}}$) due to the presence of denser seawater within the ice. Higher values of Da lead to a higher air fraction within the ice, which lowers the bulk density to between 900 kg m^{-3} and 917 kg m^{-3}. The density estimates for the higher values of Da shown in figure 7.7 are consistent with the range of ice bulk densities 900–940 kg m^{-3} reported in the literature for first-year sea ice below the waterline (Timco and Frederking 1996).

There is a significant difference between the two density estimates (figure 7.7a and 7.7b) during initial ice growth (October to November) and at the onset of the melt season (roughly April onwards). During initial ice growth in the absence of snow, the drained ice above the freeboard is a more significant fraction of the ice thickness, leading to an initially lower bulk density of around 885 kg m^{-3} that increases as the ice thickens (figure 7.7b). During the melt season, snow melt causes the freeboard to increase, which leads to a decrease in the bulk density of the ice because ice above the freeboard is drained of dense brine (figure 7.7b). This leads to a decrease in the bulk density of the ice to around 865 kg m^{-3} in June before the formation of a surface melt pond, which is more comparable to the density range reported for sea ice above the waterline of 840–910 kg m^{-3} (Timco and Frederking 1996). Without considering the hydrostatic adjustment of the freeboard, the bulk density of the ice increases during the melt season as gas bubbles are lost from the ice and the ice contains a larger fraction of denser seawater (figure 7.7a).

7.6 Conclusions

In this chapter, we have used the three-phase mushy-layer model for air bubble exsolution and migration in sea ice, developed in chapters 3–6, to simulate the bulk gas content and air fraction of first-year landfast sea ice at Barrow, Alaska, in the 2008–2009 season. Measurements of the bulk concentrations of nitrogen, oxygen, and argon in the ice at Barrow suggest that the ice contains a significant amount of atmospheric gases trapped as bubbles within the ice during its growth. In contrast, the last core measurements taken in June show that gas concentrations have dropped to near the in-situ solubility throughout most of the ice, indicating the loss of gas bubbles to the atmosphere.

Our three-phase model is a novel approach to simulating the entire air content in sea ice, compared with previous approaches for individual gas species that have assumed that bubbles instantaneously transport either gaseous argon (Moreau et al. 2014) or carbon dioxide (Moreau et al. 2015b) to the atmosphere once the ice porosity increases above an imposed threshold. The distribution of gas in the simulated ice is found to be very sensitive to the value of δ_0 and the porosity profile in the ice. Our model can reproduce the accumulation and loss of argon observed in the ice at Barrow with a suitable value of the dimensionless bubble radius $\delta_0 = R_B/R_0 = 0.28$. Through equation (2.3.7), $\delta_0 = 0.28$ corresponds to a critical porosity of 6.3% above which buoyancy driven bubble motion is possible. This porosity threshold is slightly lower than the thresholds of 10% and between 7.5% and 10% for argon transport by bubbles in sea ice identified by Moreau et al. (2014) and Zhou et al. (2013), respectively. Our model does not include the effect of snow melt water percolating downward into the ice from the surface. The percolation and refreezing of snow melt water has been identified as a potential cause of the elevated concentrations of gases seen near the surface of the ice in BRW10 (Zhou et al. 2013).

There are two important novel aspects of the model presented in this chapter compared with previous work (Moreau et al. 2014; Moreau et al. 2015b). Firstly, although we impose a porosity threshold for bubble motion, we have related this threshold to the bubble radius R_B and the pore throat lengthscale R_0 via an idealised model for bubble motion in the pore space of sea ice (see chapter 2). This could allow future work to consider a more realistic distribution of bubble sizes and pore sizes, which may help address the sensitivity of bubble transport in the model to the choice of δ_0. Secondly, we have selected parameters for the model using field observations for the three major gases in air (nitrogen, oxygen, and argon) rather than only argon. By modelling the air content in sea ice as a mixture of atmospheric gases for the first time, we are able to estimate the bulk density of sea ice over a seasonal cycle.

We found that accounting for the total integrated concentration of atmospheric gases observed within the ice requires some disequilibrium between the gas phase and the interstitial liquid in sea ice, as quantified by a Damköhler number of $1 \lessapprox Da \lessapprox 100$. This level of disequilibrium allows some of the oceanic gas content to be trapped in the ice in the gas phase while some is removed by gravity drainage through brine channels. The range of Da values identified in this chapter is consistent with the value $Da \approx 8$ previously identified by Moreau et al. (2014) to best explain the bulk argon content observed in the ice at Barrow. We find that larger exsolution rates are needed to explain the measured nitrogen content of the ice compared with the oxygen and argon content, and also to explain the very high integrated gas content observed in BRW8. It would be valuable for future field studies to measure the evolution of the gas content in sea ice over a seasonal cycle at multiple locations and over multiple seasons to establish if the evolution seen at Barrow in 2008–2009 is typical.

We have used the results of our simulation to estimate the bulk density and freeboard of first-year sea ice over a seasonal cycle. We found the bulk density of the ice to be relatively constant in the winter and spring, and that it decreases with increasing gas exsolution rate. During both the initial growth of the ice and the melt season, the bulk density of the ice is only moderately sensitive to the air fraction generated by gas exsolution and bubble rise, and is instead primarily determined by the adjustment of the freeboard and drainage of the ice above the freeboard. Our results reproduce the pattern for sea ice bulk density observed recently for first-year ice in the Arctic, where the ice density rapidly increased during initial growth from 893 ± 10 to $908 \pm 8\,\mathrm{kg\,m^{-3}}$ in November and then remained relatively constant until the melt season, when it decreased to around $880\,\mathrm{kg\,m^{-3}}$ in July (Salganik et al. 2024). Salganik et al. (2024) suggest that the decrease in ice density during the melt season implies the formation of voids within the ice due to the density change during internal melt (see chapter 1 for more discussion). However, we have found that the observed seasonal variation in the total bulk density of entire first-year ice column can be explained by a combination of air accumulation in winter and freeboard adjustment. Salganik et al. (2024) also found density values below that of pure ice ($917\,\mathrm{kg\,m^{-3}}$) below the waterline in the summer. These low density values remain to be explained but do not have a leading order impact on the total bulk density of the ice column. Our model does not include a description of melt pond drainage, so it would be valuable for future work to consider the bulk density of the ice further into the melt season with a coupled model of hydrostatic balance and melt pond hydraulics. This could also shed light on the role of drainage of the ice above the waterline and melt pond drainage on the budgets of heat, salt, and gas within the ice.

8

The impact of oil droplets in the Arctic on sea-ice melt and the spring under-ice algal bloom

8.1 Introduction

Crude oil enters the ocean via accidental spills, burst pipelines, tanker accidents, shipping and other industrial activities. Oil undergoes a variety of weathering processes in the ocean that result in the formation of small (sub-micron) sized droplets that can be suspended in the water column and travel large distances (see chapter 1 for a review). There has been significant research into the fate of large quantities of oil spilled under sea ice in the Arctic environment with a focus on detection and clean-up operations (see Wilkinson et al. 2017, for a review). However, there has been less focus on the effects of low levels of weathered oil droplets that may be present over large areas of the Arctic Ocean. Recently radiative transfer modelling has shown that the presence of low concentrations of weathered oil droplets in sea ice can significantly reduce the shortwave albedo of the ice at low wavelengths (Redmond Roche and King 2022b). However, this study did not account for the surface scattering layer found on bare sea ice, or the motion of oil droplets within the ice, so the significance of oil pollution on the energy budget of sea ice over a season is still unknown. It has also been suggested that dispersed weathered oil droplets can significantly alter the propagation of photosynthetically active radiation (PAR) in an open ocean environment, which is important for primary production in the ocean (Haule and Freda 2016). However, the impact of oil droplets in sea ice on PAR available to algae at the ice–ocean interface has not been investigated.

In this chapter, we will model the motion of oil droplets in the sea-ice system over a seasonal cycle and assess the potential importance of the oil droplets on the fate of shortwave radiation in the ice. This will be used to predict the enhancement of sea ice melt due to absorption of solar radiation by oil droplets in the ice. We also predict the delay to the spring under-ice algal bloom due to oil droplets in the ice blocking sunlight from reaching the ice–ocean interface. We consider concentrations of oil droplets that are potentially representative of background levels of weathered oil droplets, as opposed to a localised oil spill.

Both weathered oil droplets and gas bubbles can be considered as a dispersed non-wetting phase in the ice, and so oil droplet motion is governed by similar physical processes to gas bubbles. In §8.2, we describe some modifications to the three-phase mushy-layer framework developed in this thesis to describe the ice-water-oil system. We also modify the six-band two-stream (6B2S) radiative transfer model to account for the absorption of shortwave radiation by oil droplets in the ice. In §8.3, we validate our choice of radiative transfer scheme and illustrate the sensitivity of the albedo, transmittance, and absorption fraction of an idealised layer of first-year sea ice to a spatially uniform mass fraction of oil droplets. In §8.4, we present the results of seasonal simulations of the first-year ice at Barrow, Alaska. We illustrate the sensitivity of ice melt and the timing of the spring algal bloom to different mass fractions of oil pollution. We also compare the results found for mobile oil droplets with results for a spatially uniform concentration of oil droplets. Simulations are run using atmospheric forcing for each ice growth season at Barrow from 2000–2001 to 2020–2021, to better understand the significance of oil pollution for first-year sea ice compared with inter-annual variability.

8.2 Model

We make two key modifications to the three-phase mushy-layer model introduced in chapters 3 and 4 to model oil droplets in sea ice, rather than gas bubbles. Gas bubbles in sea ice result from the exsolution of dissolved gases from seawater in the pore space of sea ice during freezing. However, we assume that oil droplets are already present with some initial mass fraction $\mathcal{M}_0$ in Arctic waters and are incorporated into the pore space of the ice during freezing. In §8.2.1, we modify the conservation equation describing the motion of gas bubbles in sea ice to instead describe the motion of oil droplets. In §8.2.2, we modify the calculation of the absorption coefficient used in the shortwave radiation scheme to represent the absorption due to a local mass concentration of oil in the ice/water.

Our phase-averaged three-phase mushy-layer model is formulated in terms of a volume fraction of oil droplets ϕ_{oil}. For consistency with other studies, we define the equivalent mass fraction of oil per unit mass of ice

$$\mathcal{M} = \frac{\rho_{\text{oil}}\phi_{\text{oil}}}{\rho_{\text{ice}}}, \tag{8.2.1}$$

where $\rho_{\text{ice}} = 916\,\text{kg}\,\text{m}^{-3}$. Since the densities of ice, water and oil are all fairly similar, a mass fraction of oil per unit mass of ice of $1\,\text{ng}\,\text{g}^{-1}$ is roughly equivalent to a concentration of 1 part per billion (ppb) by mass of oil in seawater. In this chapter, we investigate a range of plausible mass fractions of oil droplets in seawater of $0 \leq \mathcal{M} \leq 1 \times 10^4\,\text{ng}\,\text{g}^{-1}$ (see chapter 1 for a review). The largest oil mass fraction considered here results in a volume fraction of oil droplets $\phi_{\text{oil}} < 1 \times 10^{-5}$. Therefore, the reduced "tracer" model introduced in chapter 2 is likely to be appropriate, and we approximate $\phi_s + \phi_l \approx 1$ for the thermodynamics and salt dynamics.

As discussed in chapter 1, weathering of oil under oceanic conditions typically produces oil droplets with a log-normal distribution of radii in the micron to sub-micron range (Johansen et al. 2015; Li et al. 2017). Laboratory experiments designed to reproduce the weathering of oil droplets in seawater have found a peak droplet radius in the range 0.05–0.25 µm (Otremba 2007; Redmond Roche 2024). In this chapter, we will utilise Mie calculations performed by Redmond Roche and King (2022b) to determine the mass absorption cross-section (MAC) of oil droplets in ice with a log-normal distribution of droplet radii with a median radius $0.05 \leq R_{\text{med}} \leq 5\,\mu\text{m}$ and geometric standard deviation e. We will take the median oil droplet radius R_{med} as a characteristic scale to determine the motion of oil droplets within the ice and ocean without considering a distribution of droplet radii.

Parameter	**Symbol**	**Value**
density of Romashkino oil	ρ_{oil}	$940\,\text{kg}\,\text{m}^{-3}$
dynamic viscosity of Romashkino oil	μ_{oil}	$3.55 \times 10^{-3}\,\text{Pa}\,\text{s}$
thermal conductivity of snow	k_{snow}	$0.42\,\text{W}\,\text{m}^{-1}\,\text{K}^{-1}$
density of ice	ρ_{ice}	$916\,\text{kg}\,\text{m}^{-3}$
density of ice (shortwave absorption calculation)	ρ'_{ice}	$800\,\text{kg}\,\text{m}^{-3}$

Table 8.1: Parameter values for the transient simulations of oil droplets in sea ice. The remaining required parameter values are given in table 6.1. The oil density (Redmond Roche and King 2022b) and viscosity (Lu et al. 2013) are representative values for Romashkino oil. Two values for the density of ice are given, ρ_{ice} is the density of pure ice used to calculate the mass ratio of oil per unit mass of ice in equation (8.2.1), and ρ'_{ice} is the bulk density of first-year sea ice used to calculate the absorption coefficient, via equation (8.2.9). The latter value differs to remain consistent with Redmond Roche and King (2022b).

8.2.1 Conservation of oil

To model the motion of a dispersed oil phase in the ice and underlying ocean we begin with the dimensionless three-phase “tracer” model for sea-ice introduced in chapter 3. We continue to use equations (3.2.34) and (3.2.36), valid for a two-phase mushy layer, to describe the evolution of the bulk enthalpy and salinity. The temperature, salinity of the liquid phase, solid fraction, and liquid fraction are determined by the enthalpy method using equations (3.3.3) and (3.3.7)-(3.3.9). Convection in the ice and the loss of dissolved salt through brine channels is parameterised using the brine convection parameterisation of Rees Jones and Worster (2014) (see §3.2.2). The turbulence in the underlying ocean and surface melt pond (if present) is parameterised using a constant eddy diffusivity κ_ε where $\phi_l = 1$. We assume no oil dissolves into the liquid phase. Therefore, we no longer need equation (3.2.37) and we set $\mathcal{N} = 0$ going forward.

Oil droplet motion

In chapter 3, we used equation (3.2.11) to determine the volumetric flux of the gas phase due to bubble motion in the ice and ocean. This expression was derived in chapter 2 using an idealised model of bubble motion in the Stokes regime in the pore space of sea ice. We now modify equation (3.2.11) to give the volumetric flux $\boldsymbol{u}_{\text{oil}}$ of oil droplets in the ice and ocean. In contrast to gas bubbles, the oil droplets considered in this chapter are smaller and have a much lower density contrast with seawater and so are significantly less buoyant. Therefore, we hypothesise that liquid motion through brine channels may be able overcome the buoyancy of the droplets and transport oil droplets from the ice to the ocean. We couple the motion of the oil droplets to the liquid motion by setting

$$\boldsymbol{G} = G(\delta)\boldsymbol{I}, \tag{8.2.2}$$

where $G(\delta)$ was introduced in §2.3.2 and $\boldsymbol{I}$ is the identity matrix.[1] We estimate the maximum value of the ratio of the oil droplet radius to the pore throat radius δ_{max} in sea ice using equation (2.3.2) with $1-\phi_s = \phi_c$, where ϕ_c is the critical porosity below which the pore network becomes disconnected. Using the maximum oil droplet radius considered in this chapter, $R_{\text{med}} = 5\,\mu\text{m}$, and parameter values from table 2.1 we find that $\delta_{\text{max}} = 0.143$. Since $\delta_{\text{max}} \ll 1$, we find that $K_1(\delta) \approx 1$ and $G(\delta) \approx 1$. Therefore, for micron sized oil droplets, it is appropriate to neglect the influence of the pore walls by setting $K_1(\delta) = 1$ and $G(\delta) = 1$ in equations (3.2.11) and (8.2.2). Hence, we arrive at the following expression for the dimensionless volumetric flux of oil

$$\boldsymbol{u}_{\text{oil}} = \phi_{\text{oil}} \left[\mathsf{H}(\phi_l - \phi_c) v_{\text{HR}} \boldsymbol{e_z} + \frac{2}{\phi_l} \boldsymbol{u}_l \right], \tag{8.2.3}$$

where H is the unit step function (defined in chapter 3), $\boldsymbol{u}_l$ is the dimensionless Darcy velocity of the liquid phase, and

$$v_{\text{HR}} = 2 \left[\frac{\mu_l + \mu_{\text{oil}}}{2\mu_l + 3\mu_{\text{oil}}} \right] \frac{(\rho_l - \rho_{\text{oil}})\, R_{\text{med}}^2 g h}{3\mu_l \kappa}, \tag{8.2.4}$$

is the dimensionless terminal vertical velocity of a spherical oil droplet of radius R_{med} in an unbounded liquid in the Stokes regime. Here, the density of the oil and liquid phase are ρ_{oil} and ρ_l, respectively, and the dynamic viscosities are μ_{oil} and μ_l, respectively. Equation (8.2.4) is the Hadamard-Rybczynski velocity (Clift et al. 2005) non-dimensionalised by the velocity scale of thermal diffusion κ/h, where h is the depth of the domain, and κ is the thermal diffusivity. Note that we

---

[1] When equation (8.2.2) is substituted into equation (3.2.11) the z component of $\boldsymbol{u}_{\text{oil}}$ is the same as derived in chapter 2 for gas bubbles, but with different material parameters. Extending this to the horizontal components of $\boldsymbol{u}_{\text{oil}}$ is an ad-hoc assumption made to allow lateral liquid motion to transport oil droplets to brine channels in sea ice.

have included the permeability threshold proposed by Maus et al. (2021) in our treatment of buoyant oil motion because the pore network becoming disconnected could prevent the buoyant motion of even very small oil droplets. This permeability threshold is not included in the porosity-permeability relationship used in the RJW14 brine convection scheme, but it is unlikely to significantly change the scheme since there is a negative feedback in the Rayleigh number that inhibits convection as the porosity decreases. The parameter values used in this chapter are either given in table 8.1, or else in table 6.1.

Following chapter 3, but replacing ϕ_g with ϕ_{oil} and equation (3.2.11) with equation (8.2.3), we find the following dimensionless conservation equation for the oil phase

$$\frac{\partial \phi_{\text{oil}}}{\partial t} + v_{\text{HR}} \frac{\partial}{\partial z} \left[\mathsf{H}(\phi_l - \phi_c) \phi_{\text{oil}} \right] + \frac{\partial}{\partial z} \left[w_l \frac{2\phi_{\text{oil}}}{\phi_l} \right] = \frac{1}{Le_\varepsilon} \frac{\partial}{\partial z} \left[\mathsf{H}(\phi_l - 1) \frac{\partial \phi_{\text{oil}}}{\partial z} \right] - \frac{2\mathcal{S}_{\text{RJW14}} \phi_{\text{oil}}}{\phi_l}, \tag{8.2.5}$$

where $Le_\varepsilon = \kappa / \kappa_\varepsilon$ is the Lewis number for eddy diffusion, and w_l and $\mathcal{S}_{\text{RJW14}}$ are the dimensionless convective upwelling velocity and sink term, respectively, calculated using the RJW14 brine convection scheme. In contrast to equation (3.2.38) for free-gas conservation, the above equation includes an advective term due to convection in the ice, a sink term due to the loss of oil droplets from the ice through brine channels, and a diffusive term due to turbulent mixing in the ocean and melt pond. These extra terms result from coupling the motion of oil droplets to the motion of the liquid phase in equation (8.2.3). Note that the scale for the buoyant rise of gas bubbles $\mathcal{B}\delta_0^2$ previously found is replaced here by the scale for the buoyant rise of oil droplets given by the dimensionless Hadamard-Rybczynski velocity v_{HR}.

Boundary conditions

We use boundary conditions for equation (8.2.5)

$$\phi_{\text{oil}}(-1, t) = \frac{\rho_{\text{ice}}}{\rho_{\text{oil}}} \mathcal{M}_0, \tag{8.2.6}$$

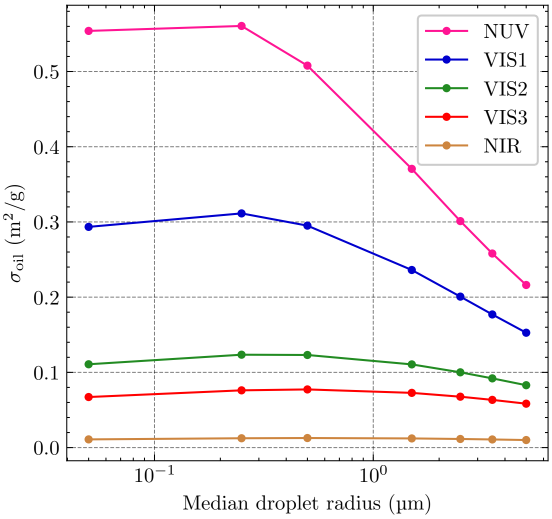

Figure 8.1: The mass absorption cross-section for oil droplets in ice for a log-normal distribution of droplet radii with median radius R_{med} and geometric standard deviation e. The wavelength dependent mass absorption cross-section from Mie calculations (Redmond Roche and King 2022a) is averaged over the spectral bands: NUV (pink), VIS1 (blue), VIS2 (green), VIS3 (red), NIR (brown), which are defined in §4.7. No data is available in the SWIR band.

at the base of the domain where $\mathcal{M}_0$ is the mass fraction of oil droplets in the ocean, and

$$\frac{\partial \phi_{\mathrm{oil}}}{\partial z}(0,\, t) = 0, \tag{8.2.7}$$

which prevents any diffusive oil flux at the ice–air or ice–snow interface at $z = 0$. Additionally, we replace $v_{\mathrm{HR}}(0,\, t)$ with 0 in equation (8.2.5) to prevent oil droplets from rising past the ice–air or ice–snow interface. These boundary conditions cause oil droplets to eventually accumulate at the top of the domain in the absence of brine convection or turbulent mixing. Simulations in this chapter will be initialised with ice-free conditions ($\phi_l = 1$) and a uniform oil fraction

$$\phi_{\mathrm{oil}}(z,\, 0) = \frac{\rho_{\mathrm{ice}}}{\rho_{\mathrm{oil}}}\mathcal{M}_0. \tag{8.2.8}$$

8.2.2 The absorption of shortwave radiation in sea ice by oil droplets

In chapter 4, we introduced the 6B2S model for the propagation of shortwave radiation through snow, ice and seawater. This shortwave radiation scheme is used to calculate the net broadband shortwave irradiance profile $\widetilde{\mathcal{F}}_{\mathrm{net}}$, which determines the radiative source term in equation (3.2.34). The absorption of solar radiation in sea ice contributes significantly to the energy budget of the ice in the melt season. Here, we modify the calculation of the spectral absorption coefficient $k_{2\mathrm{S}}$ for the two-stream model to account for the additional shortwave radiation absorbed by oil droplets.

In general, the absorption coefficient for sea ice can be written as the sum of the ice absorption coefficient and the mass absorption cross-sections weighted by the mass fractions of any impurities present in the ice (Perovich 2017; Lamare et al. 2016). Following Redmond Roche and King (2022b), we calculate the absorption coefficient in each spectral band via

$$k_{2\mathrm{S},\,i} = \frac{k_i + \rho'_{\mathrm{ice}}\mathcal{M}\sigma_{\mathrm{oil},\,i}(R_{\mathrm{med}})}{\overline{\mu}}, \tag{8.2.9}$$

where k_i is the absorption coefficient for pure ice (see table 4.2), $\sigma_{\mathrm{oil},\,i}(R_{\mathrm{med}})$ is the MAC by Romashkino oil in ice, $\rho'_{\mathrm{ice}} = 800\,\mathrm{kg\,m^{-3}}$ is the ice bulk density[2], $\overline{\mu} = 1/2$ is the reciprocal of the mean vertical path extension for isotropic irradiances in each hemisphere (see appendix F), and the index $i = 1, 2, \ldots, 6$ refers to quantities averaged over each of the six spectral bands introduced in chapter 4. Here, the 6B2S radiative transfer scheme (see chapter 4) is used with equation (4.4.6) replaced by equation (8.2.9).

The MAC for droplets of Romashkino oil in ice was computed by Redmond Roche and King (2022b) using Mie calculations for $350 \leq \lambda \leq 800\,\mathrm{nm}$. The available data for $\sigma_{\mathrm{oil}}(R_{\mathrm{med}})$ (Redmond Roche and King 2022a) is averaged over the six spectral bands considered in this thesis and plotted against R_{med} in figure 8.1. The absorption of shortwave radiation by oil is largest at short wavelengths and decreases as the wavelength increases. No data is available for σ_{oil} for $\lambda > 800\,\mathrm{nm}$. However, because the absorption coefficient of ice/water rapidly increases with increasing wavelength, it is reasonable to assume that the effect of oil droplets is negligible at longer wavelengths versus absorption by the ice and water.

---

[2] This value is very low for typical measurements of sea ice bulk density, however it was used in the previous study of the impact of oil droplets on sea ice albedo by Redmond Roche and King (2022b) and so we use it here for consistency.

8.3 Idealised results from the 6B2S model

In this section, we use the 6B2S model to investigate the impact of different levels of oil pollution ($0 \leq \mathcal{M}_0 \leq 10\,000\,\mathrm{ng\,g^{-1}}$) on the optical properties of first-year sea ice. First, we validate that our radiative transfer model can reproduce the decrease in ice albedo with oil mass fraction identified in the literature (Redmond Roche and King 2022b). Then, we present some idealised calculations of the effect of a uniformly distributed mass fraction of oil droplets on the fractions of the incident shortwave radiation reflected, absorbed and transmitted in the ice. We consider the three surface conditions that occur during the seasonal evolution of first-year sea ice: snow-covered ice, bare ice, and ponded ice.

8.3.1 Validation against previous work

We consider a 0.8 m thick layer of first-year sea ice with no SSL and three different mass fractions of oil droplets, $\mathcal{M} = 0\,\mathrm{ng\,g^{-1}}$, $100\,\mathrm{ng\,g^{-1}}$, and $1000\,\mathrm{ng\,g^{-1}}$, distributed uniformly throughout the ice. Figure 8.2 shows excellent agreement between the spectral albedo calculated using our 6B2S model compared with the spectral albedo calculated using the TUV-snow model (Redmond Roche and King 2022b). The spectral albedo of the ice is not particularly sensitive to mass fractions of oil less than around $100\,\mathrm{ng\,g^{-1}}$, however there is a significant reduction of around 20% of the spectral albedo at wavelengths less than 600 nm for $\mathcal{M} = 1000\,\mathrm{ng\,g^{-1}}$. This is explained by the absorption due to oil droplets at these wavelengths becoming significantly larger than that of pure ice for large enough mass fractions of oil. Although a large fraction of the incident shortwave radiation occurs at UV and visible wavelengths, the reduction in the spectral albedo seen in figure 8.2 cannot be applied directly to the energy budget of first-year sea ice. This is because bare sea ice has a surface scattering layer which reflects a significant fraction of the incident radiation before it reaches the ice interior.

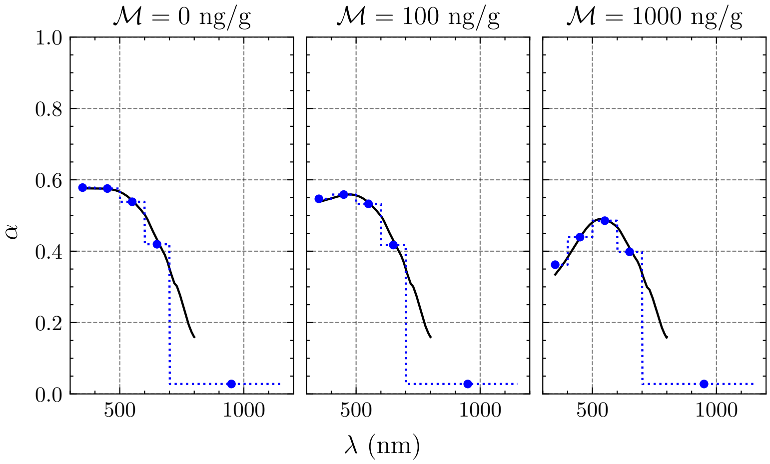

Figure 8.2: The spectral albedo of 0.8 m thick first-year sea ice with no surface scattering layer ($h_{\mathrm{SSL}} = 0$) for three mass fractions of oil pollution ($\mathcal{M} = 0$, 100, $1000\,\mathrm{ng\,g^{-1}}$), where oil is assumed to be uniformly distributed throughout the ice with a median droplet radius of $R_{\mathrm{med}} = 0.05\,\mu\mathrm{m}$. The black curve in each panel shows the spectral albedo computed using the TUV-snow model (Redmond Roche and King 2022b). The blue dotted curve is computed using the 6B2S model described in chapter 4 with equation (8.2.9) and shows the piecewise interpolation of the spectral albedo in the first five wavelength bands. The midpoint of each wavelength band is indicated with a blue filled circle. The optical parameters are the same as described in chapter 4 and the mass absorption cross-section for oil droplets with $R_{\mathrm{med}} = 0.05\,\mu\mathrm{m}$ is calculated in each spectral band using the data provided by Redmond Roche and King (2022a) (see figure 8.1).

8.3.2 The partitioning of solar radiation in sea-ice polluted with oil droplets

We now consider the impact of oil pollution on the fractions of the incident shortwave radiation flux that are reflected, transmitted, and absorbed by first-year sea ice. These fractions are given by the albedo α_i, the transmittance at the ice–ocean interface $\mathcal{T}_i$, and the ice absorption fraction $f_{\mathrm{abs},\,i} = f_{\mathrm{net},\,i}(z = 0) - f_{\mathrm{net},\,i}(z = -h_{\mathrm{ice}})$, respectively, in each spectral band $i = 1, 2, \ldots, 6$. To determine the importance of the extra absorption of shortwave radiation by oil droplets at different stages in the seasonal evolution of first-year sea ice, we consider a 1.5 m thick layer of first-year ice with three different representative surface conditions: snow-covered ice with $h_{\mathrm{snow}} = 20\,\mathrm{cm}$ and $h_{\mathrm{SSL}} = 4\,\mathrm{cm}$; bare ice with $h_{\mathrm{snow}} = 0\,\mathrm{cm}$, and $h_{\mathrm{SSL}} = 4\,\mathrm{cm}$; and ponded ice with $h_{\mathrm{snow}} = 0\,\mathrm{cm}$, $h_{\mathrm{SSL}} = 0\,\mathrm{cm}$ and $h_{\mathrm{melt}} = 20\,\mathrm{cm}$. The spectral albedo, transmittance and absorption fraction for each of these surface conditions are shown in figure 8.3 for ice with a uniformly distributed concentration of oil droplets $0 \leq \mathcal{M}_0 \leq 10\,000\,\mathrm{ng\,g^{-1}}$.

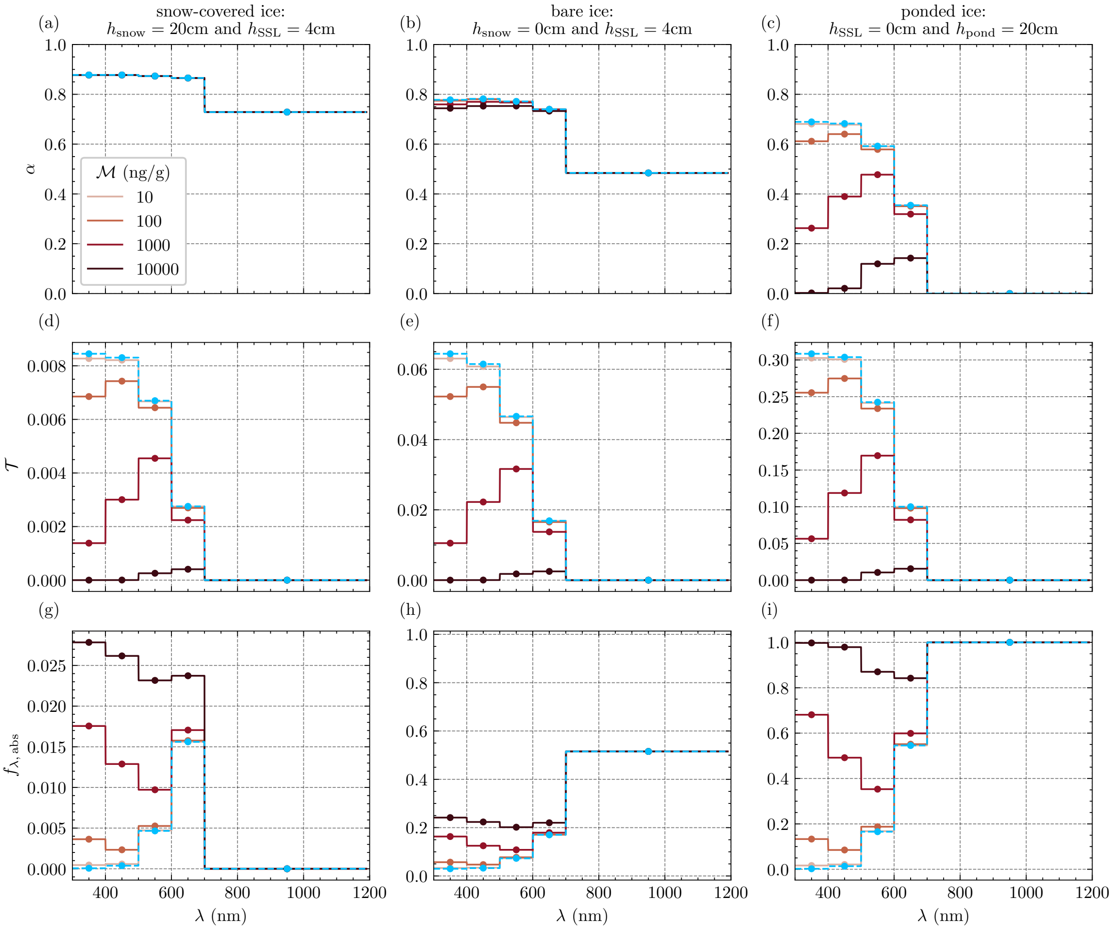

Figure 8.3: The spectral albedo (top row), transmittance (middle row), and absorption fraction (bottom row) of 1.5 m thick first-year sea ice with three different surface conditions: (left column) dry snow with $h_{\text{snow}} = 20\,\text{cm}$ and $h_{\text{SSL}} = 4\,\text{cm}$, (middle column) bare ice with $h_{\text{snow}} = 0\,\text{cm}$ and $h_{\text{SSL}} = 4\,\text{cm}$, and (right column) ponded ice with $h_{\text{pond}} = 20\,\text{cm}$. The piecewise curves are found using the 6B2S model with the midpoints of the wavelength bands indicated by filled circles. The light blue dashed curve in each panel shows the spectral albedo of the ice with no oil pollution. The coloured curves in each panel show the spectral albedo of the ice with increasing mass fractions of oil pollution $10 \leq \mathcal{M} \leq 10\,000\,\text{ng}\,\text{g}^{-1}$. When present, oil droplets are assumed to be uniformly distributed throughout the domain with a median droplet radius of $R_{\text{med}} = 0.05\,\mu\text{m}$. Note that the scale on the y-axes in panels (d), (e), (f), and (g) is different to the other panels.

Snow and the SSL are both highly reflective and so the albedo of snow-covered ice and bare ice is high and not significantly affected by the presence of oil droplets in the interior of the ice (figures 8.3a and 8.3b). However, the albedo of ponded ice is significantly reduced in the UV and visible wavelength bands due to absorption by oil droplets (figure 8.3c). This is comparable to the reduction in the spectral albedo at short wavelengths found by Redmond Roche and King (2022b) for first-year ice with no SSL.

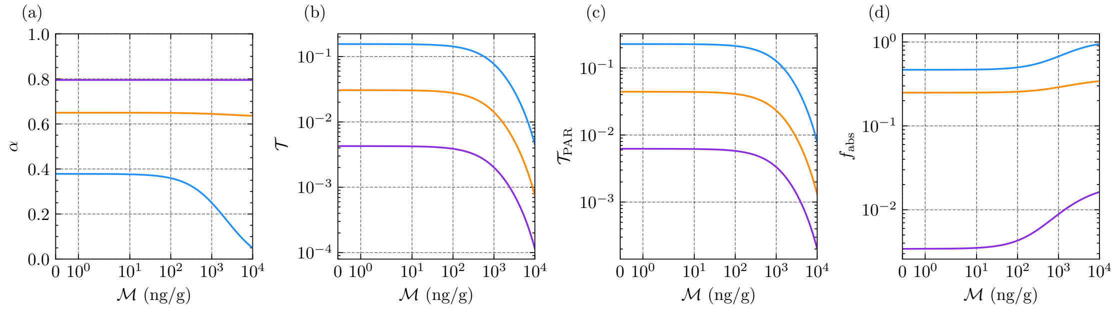

Figure 8.4: The spectrally integrated (a) albedo, (b) transmittance, (c) PAR transmittance, and (d) absorption fraction versus oil mass fraction $\mathcal{M}$ for 1.5 m thick first-year sea ice with three different surface conditions (purple) dry snow with $h_{\text{snow}} = 20\,\text{cm}$ and $h_{\text{SSL}} = 4\,\text{cm}$, (orange) bare ice with $h_{\text{snow}} = 0\,\text{cm}$ and $h_{\text{SSL}} = 4\,\text{cm}$, and (light blue) ponded ice with $h_{\text{pond}} = 20\,\text{cm}$. The curves are calculated using the 6B2S model and integrated over wavelength using a cloudy sky spectrum (see table 4.1) When present, oil droplets are assumed to be uniformly distributed throughout the domain with a median droplet radius of $R_{\text{med}} = 0.05\,\mu\text{m}$. Note that the vertical axis in panel (a) has a linear scale but the vertical axes in panels (b), (c) and (d) have a logarithmic scale.

The transmittance of shortwave radiation at the ice–ocean interface is significantly reduced in the NUV, VIS1, and VIS2 wavelength bands for all three surface conditions for oil mass fractions of $1000\,\text{ng}\,\text{g}^{-1}$ and larger (figures 8.3d, 8.3e, and 8.3f). There is over an order of magnitude reduction in the transmittance in the NUV, VIS1, VIS2, and VIS3 bands for the most extreme $\mathcal{M}_0 = 10\,000\,\text{ng}\,\text{g}^{-1}$ case. Note that there is also an order of magnitude difference between the transmittance of the ice with no oil droplets for each of the three surface conditions since the presence of a snow layer or a SSL dramatically reduces the amount of shortwave radiation that penetrates the ice interior. The reduction in the transmittance of shortwave radiation at the ice base with increasing oil concentration is due to the increased fraction of the radiation absorbed in the ice by oil droplets (see the bottom row of figure 8.3).

The spectrally-integrated albedo $\tilde{\alpha}$, transmittance at the ice–ocean interface $\tilde{\mathcal{T}}$, and the absorption fraction

$$\tilde{f}_{\text{abs}} = \sum_{i=1}^{6} f_{\text{abs},\,i}, \tag{8.3.1}$$

ultimately determine the partitioning of the incoming solar energy in the sea-ice system. The spectral integration is performed using the fraction of the incident broadband shortwave radiation flux in each spectral band under cloudy sky conditions given in table 4.1.

Figure 8.4a shows that the spectrally-integrated albedo is not sensitive to increasing mass fractions of oil droplets for snow-covered or bare ice with a SSL. However, the spectrally-integrated albedo of ponded ice is significantly reduced for oil mass fractions larger than $100\,\mathrm{ng\,g^{-1}}$ and practically drops to zero for $\mathcal{M} = 10\,000\,\mathrm{ng\,g^{-1}}$. Therefore, we find that ponded ice with a high concentration of oil droplets can have a broadband albedo as low as open water. This suggests that the presence of oil droplets in ponded ice may significantly enhance the strength of the ice albedo feedback during the melt season in the Arctic.

The spectrally-integrated transmittance at the ice–ocean interface $\widetilde{\mathcal{T}}$ is shown in figure 8.4b. While the transmittance depends strongly on the surface conditions, the effect of increasing the mass fraction of oil droplets causes a similar reduction in the transmittance for snow-covered ice, bare ice, and ponded ice. The effect of oil droplets on the transmittance becomes noticeable for $\mathcal{M} > 100\,\mathrm{ng\,g^{-1}}$ with $\mathcal{M} = 1000\,\mathrm{ng\,g^{-1}}$, and $\mathcal{M} = 10\,000\,\mathrm{ng\,g^{-1}}$ reducing the transmittance by around a factor of 2, and 10, respectively.

The PAR transmittance $\widetilde{\mathcal{T}}_{\mathrm{PAR}}$ (see figure 8.4c) for oil-free snow-covered ice of around 6×10^{-3} is consistent with the range of values 2×10^{-3}–1.2×10^{-2} reported by Nicolaus et al. (2013) for transects under first-year snow-covered ice at Barrow on 22-03-2010 and 14-05-2010[3]. Nicolaus et al. (2013) also reported values of $\widetilde{\mathcal{T}}_{\mathrm{PAR}}$ in the range 2×10^{-2}–1×10^{-1} under the ice on 11-06-2010. At this time the melt season was well underway and these $\widetilde{\mathcal{T}}_{\mathrm{PAR}}$ are consistent with the values we have calculated for oil-free bare or ponded ice. The PAR transmittance shows a similar reduction with increasing oil mass fraction to the transmittance for all surface conditions. Therefore, ice-algae at the base of oil polluted ice will receive less PAR than ice-algae at the base of unpolluted ice, and so may have to wait until later in the season for larger shortwave radiation fluxes before significant growth can occur.

The spectrally-integrated absorption fraction $\widetilde{f}_{\mathrm{abs}}$ is shown in figure 8.4d and gives the fraction of the incoming solar radiation that is absorbed and heats the ice.

---

[3] Measurements were made along a transect under first-year ice. Essentially all measurements were less than 4×10^{-3}, apart from a small section of the transect where the snow cover was particularly thin.

Snow-covered ice actually shows the largest increase in the absorbed fraction of the incident shortwave radiation as oil mass fraction increases. However, since the overall fraction of the incident radiation absorbed by the ice is so small, and the incoming radiation flux is lower in the winter when the ice has a significant snow cover, the heating effect is likely to be negligible compared with other heat sources. Bare ice shows a fairly modest increase in the spectrally-integrated absorption fraction as the oil mass fraction increases. Ponded ice shows a noticeable increase in the absorption fraction for oil mass fractions larger than $100\,\mathrm{ng\,g^{-1}}$, with nearly 100% of the incident radiation absorbed in the ice and pond for $\mathcal{M} = 10\,000\,\mathrm{ng\,g^{-1}}$. This indicates that ponded ice polluted with oil droplets may experience significantly more heating during the melt season due to the absorption of solar radiation than oil-free ice.

8.4 Case study: the impact of oil pollution on simulated first-year landfast sea ice at Barrow, Alaska

In this section we investigate the effect of background levels of oil pollution in the ocean on simulations of the first-year sea ice at Barrow. We aim to discover if the extra solar energy absorbed by oil droplets, illustrated by the idealised calculations of the previous section, has a significant impact on the ice mass balance of first-year sea ice and the availability of photosynthetically active radiation (PAR) at the ice–ocean interface. Simulations are initialised with ice-free conditions and a spatially uniform mass fraction of oil droplets $\mathcal{M}_0$ in September and the oil mass fraction at $z = -1$ is held fixed at $\mathcal{M}_0$. We consider the oil-free case as a baseline compared with two oil-polluted scenarios: (1) the oil mass fraction remains spatially uniform throughout the domain during ice growth and melt, and (2) the oil mass fraction evolves according to equation (8.2.5) as mobile oil droplets migrate due to their buoyancy and are removed from convecting sea ice via brine channels.

The transient simulations used in this chapter were performed using `seaice3p v1.0.0` with $N_z = 100$ and a very similar configuration to the simulations in chapter 6. Additional parameter values required to simulate oil droplets are given in table 8.1 where the extra absorption of shortwave radiation due to oil droplets is calculated using equation (8.2.9). See appendix H for a brief discussion of the numerical convergence of the simulations in this chapter with increasing N_z.

First, we examine the results of simulations of the 2008–2009 season at Barrow to better understand oil droplet motion and the effect of oil droplets on the shortwave radiation budget in a realistic simulation of first-year sea ice. We then run an ensemble of simulations in each of the simulations from 2000–2001 to 2020–2021 with either uniform oil concentrations or mobile oil droplets and different values of $\mathcal{M}_0$, in order to investigate how the potential impacts of oil pollution in first-year sea ice compare with the interanual variability at Barrow.

8.4.1 Sensitivity to oil droplet radius

Figure 8.5a shows the simulated oil mass fraction $\mathcal{M}$ in first-year sea ice at Barrow, Alaska during the 2008–2009 season for mobile oil droplets with $R_{\text{med}} = 0.05\,\mu\text{m}$ and $\mathcal{M}_0 = 1000\,\text{ng}\,\text{g}^{-1}$. Before any ice forms in September, the ocean is well mixed and the oil concentration is uniform throughout the domain. During ice growth oil droplets are expelled from the ice through brine channels leading to a significant reduction in the oil mass concentration in the ice interior compared with the ocean. This is analogous to the desalination of first-year sea ice by brine convection. Once a surface melt pond forms, turbulence mixes the oil droplets within the pond until the ice completely melts, at which point ocean mixing acts to homogenise the oil concentration back to $\mathcal{M}_0$.

Figures 8.5b and 8.5c show the ice–ocean and ice–melt-pond interfaces for simulations with a uniform concentration of oil droplets and mobile oil droplets, respectively. In the case of a uniform mass fraction of oil droplets, there is only a weak sensitivity to the characteristic droplet radius R_{med} since the MAC of oil droplets in ice decreases slightly as R_{med} increases. This is because oil droplets with larger radii are slightly less efficient absorbers of shortwave radiation in ice (see figure 8.1). Therefore, when R_{med} is larger than $1\,\mu\text{m}$ the rate of surface and basal melt is slightly reduced compared with smaller droplet radii. However,

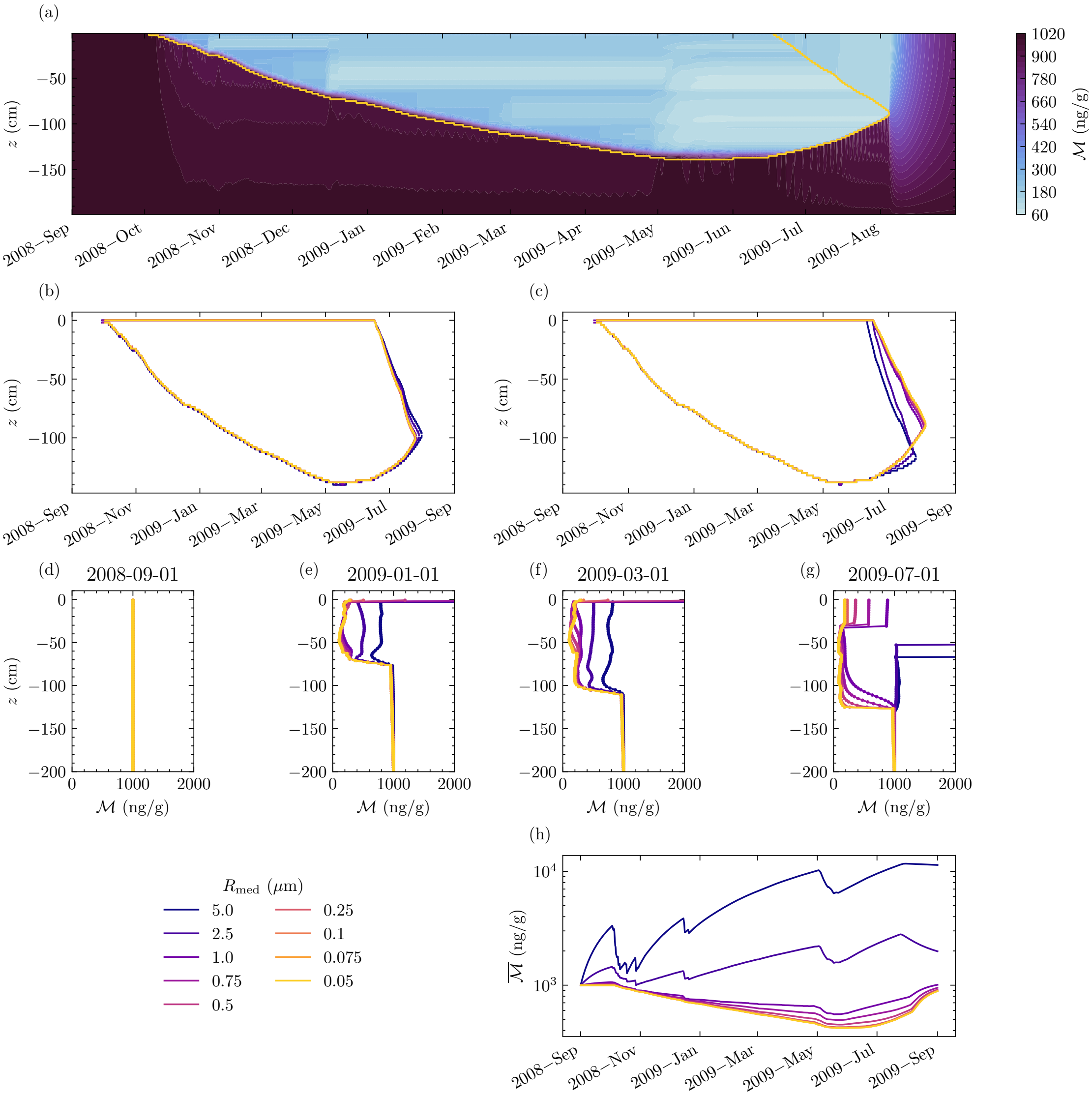

Figure 8.5: The oil mass fraction $\mathcal{M}$ in simulated first-year sea ice for different oil droplet radii R_{med} with $\mathcal{M}_0 = 1000\,\mathrm{ng\,g^{-1}}$. Panel (a) shows the contours of the oil mass fraction $\mathcal{M}$ with the ice–ocean and ice–melt-pond interfaces overlaid in yellow for mobile oil droplets with $R_{\mathrm{med}} = 0.05\,\mu\mathrm{m}$. Panels (b) and (c) show the simulated ice–ocean and ice-meltpond interfaces for simulations with a uniform concentration of oil droplets and mobile oil droplets, respectively for different R_{med} (see legend). Panels (d)-(g) show profiles of the simulated oil mass fraction for mobile oil droplets in September, January, March, and July. The colours of the curves in panels (d)-(g) correspond to the different characteristic oil droplet radii in the legend. Panel (h) shows the mean oil mass fraction in the domain over time for simulations with mobile oil droplets with different values of R_{med} (see the legend).

when oil droplets are mobile (figure 8.5c), surface melt is significantly enhanced for $R_{\text{med}} > 1\,\mu\text{m}$ and basal melt is reduced compared with smaller droplet radii. This is because the rise speed v_{HR} increases with increasing droplet radius, so more oil is able to migrate from the ocean and accumulate at the ice surface without being removed by brine convection. This leads to substantially higher oil concentrations at the ice surface, which overwhelms the reduced MAC, and so the rate of surface melt is significantly enhanced for mobile oil droplets with larger radii.

For small oil droplet radii, the profiles of $\mathcal{M}$ in the ice interior are C-shaped and similar to those for salinity in first-year sea ice (see figures 8.5e and 8.5f). This indicates that buoyant motion of oil droplets is not important for droplet radii less than around $1\,\mu\text{m}$ and the transport is similar to that of a passive tracer. However, as the oil droplet radius increases, more oil is able to migrate and accumulate at the ice surface (uppermost grid cell) without being removed by brine channels.

For $R_{\text{med}} \leq 1\,\mu\text{m}$, there is an overall decrease in the mean oil mass fraction in the domain during ice growth as fluid with a high concentration of oil droplets is expelled from the ice interior by brine convection, and there is not a large buoyancy driven flux from the deep ocean where the concentration of oil droplets is lower (see figure 8.5h). However, for $R_{\text{med}} > 1\,\mu\text{m}$, the mean oil mass fraction in the domain actually increases as more buoyant oil droplets migrate into the domain from the ocean and accumulate in the ice. Sudden drops in the mean oil mass fraction (figure 8.5h) and the bands seen in the contour plot of the oil mass fraction (figure 8.5a) are associated with periods of convection within the ice. This scenario would be less realistic if there is not a continuous source of oil droplets in the ocean. However, for the remainder of this work we will concern ourselves with more realistic sub-micron droplet radii that are typical of weathered oil in the ocean.

Once a pond forms at the ice surface, the oil droplets are mixed by turbulence which produces a uniform oil mass concentration in the pond (see figure 8.5g). The oil concentration in the pond is higher than the ice interior due to the oil that collected at the surface of the ice during growth. The oil concentration in the pond decreases as the pond grows and the oil droplets become more diluted, apart from for large droplet radii where a significant amount of oil is able to migrate into the pond through the ice.

In conclusion, the result of oil motion is to produce a non-uniform distribution of oil in the ice, and this has a larger effect on the ice mass balance (once a surface melt pond has formed) than the decrease in the MAC for oil droplets in ice with increasing R_{med}. For sub-micron oil droplets, there is a significantly lower concentration of oil in the ice and pond compared with the ocean, because the buoyancy of the droplets is not significant compared with turbulent mixing in the ocean and pond, and the brine convection in the ice. For oil droplet radii larger than a micron, the buoyancy of the droplets becomes much more significant compared with turbulent mixing in the ocean and so much more oil is able to accumulate in the ice. Our simulations also use a relatively low value for the eddy diffusivity in the ocean (discussed in chapter 6). For the remainder of this chapter we will compare a uniform concentration of oil droplets to mobile oil droplets with $R_{\mathrm{med}} = 0.5\,\mu\mathrm{m}$.

8.4.2 The impact of oil pollution on the ice mass balance in 2008–2009

Figure 8.6 shows the simulated ice–ocean and ice–melt-pond interfaces with different initial mass fractions of oil droplets $\mathcal{M}_0$, for a uniform droplet distribution and for mobile oil droplets. Note that oil droplets have very little effect on winter growth due to the lack of solar radiation, beyond a very slight lag in the time of the autumn freeze-up. There is not a very significant effect of oil droplets on the evolution of the ice–ocean and ice–melt-pond interfaces for $\mathcal{M}_0 \leq 100\,\mathrm{ng\,g^{-1}}$ in either the uniform or mobile case. However, for $\mathcal{M}_0 = 1000\,\mathrm{ng\,g^{-1}}$, $10\,000\,\mathrm{ng\,g^{-1}}$ the rate of summer surface melt is significantly enhanced compared with the oil-free case, and the ice completely melts significantly earlier in the season compared with $\mathcal{M}_0 = 0\,\mathrm{ng\,g^{-1}}$. For mobile oil droplets, increasing $\mathcal{M}_0$ also significantly enhances the rate of basal melt compared with the oil-free case. However, for a uniform concentration of oil droplets, once the oil concentration reaches $\mathcal{M}_0 = 10\,000\,\mathrm{ng\,g^{-1}}$ most of the available shortwave radiation is absorbed by the oil droplets near the

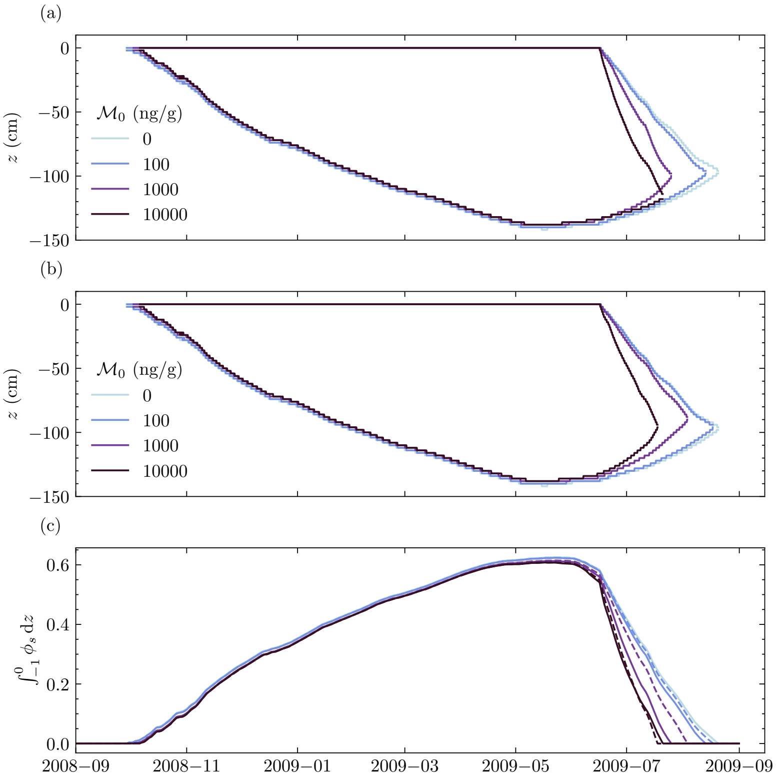

Figure 8.6: Comparison of simulated first-year sea ice at Barrow, Alaska during the 2008–2009 season with different initial mass fractions of oil droplets $\mathcal{M}_0$. Plots of the ice–ocean and ice–melt-pond interfaces for different $\mathcal{M}_0$ (see legend) with (a) a uniform concentration of oil droplets and (b) mobile oil droplets. Panel (c) shows the integrated solid fraction in the domain for the same values of $\mathcal{M}_0$ in panels (a) and (b) for mobile oil droplets (dashed lines) and a uniform concentration of oil droplets (solid lines).

surface of the ice and so while there is significantly more surface melting, the ice–ocean interface evolves very similarly to the oil-free case.

To build understanding of the physical mechanism by which oil droplets increase ice melt, we examine the partitioning of incoming solar radiation for simulations with $\mathcal{M}_0 = 0\,\mathrm{ng\,g^{-1}}$, $100\,\mathrm{ng\,g^{-1}}$, $1000\,\mathrm{ng\,g^{-1}}$, and $10\,000\,\mathrm{ng\,g^{-1}}$ (figure 8.7). At the beginning of the simulations, with ice-free conditions, mobile oil droplets are effectively mixed by eddy diffusion and so are effectively uniformly distributed throughout the domain (see figure 8.5). Increasing $\mathcal{M}_0$ leads to more shortwave radiation being absorbed in the ocean early in the simulation (see figure 8.7d), which delays the formation of ice. Snow covers the ice surface soon after formation, and the incident shortwave radiation flux decreases over winter so no significant amount of solar energy is absorbed by the ice or ocean during winter.

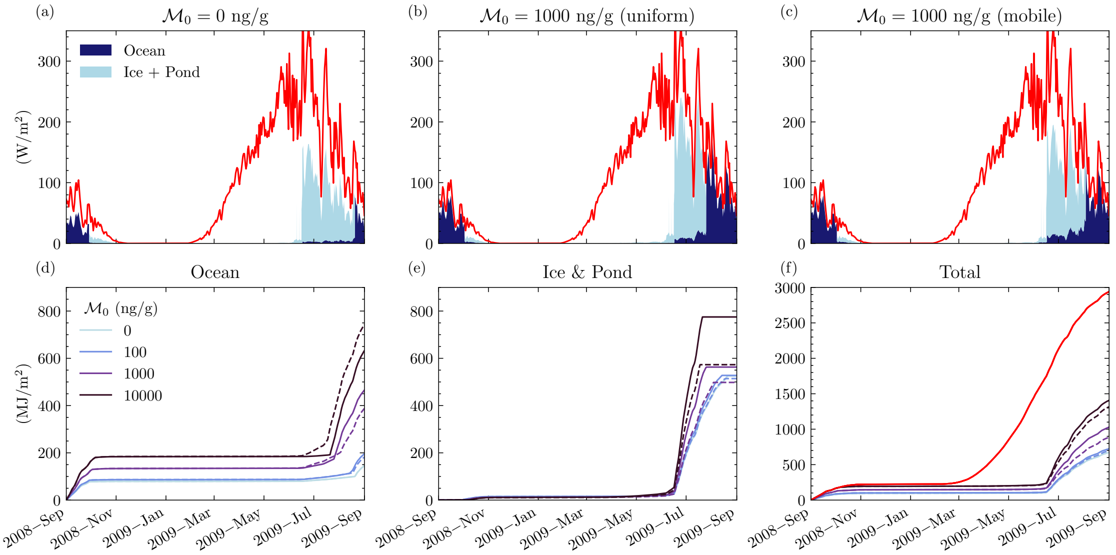

Figure 8.7: The partitioning of incoming solar radiation in simulations of first-year sea ice at Barrow, Alaska in the 2008–2009 season with different initial mass fractions of oil droplets $\mathcal{M}_0$. The top row of plots shows the daily averaged incoming shortwave radiation flux (red) compared with the absorbed shortwave radiation flux in the ocean (dark blue), and the ice and pond (light blue) for (a) no oil pollution, (b) a uniform oil mass fraction of $\mathcal{M}_0 = 1000\,\mathrm{ng\,g^{-1}}$, and (c) mobile oil droplets with $\mathcal{M}_0 = 1000\,\mathrm{ng\,g^{-1}}$. The bottom row of plots shows the integrated energy from shortwave radiation absorbed in (d) the ocean, (e) ice+pond, and (f) the combined total, since the beginning of the simulations on 2008-09-01. Different mass fractions of oil droplets are indicated by the colours in the legend in panel (d) with solid lines corresponding to a uniform concentration of oil droplets and dashed lines corresponding to mobile oil droplets. For comparison, the red line in panel (f) shows the integrated incoming shortwave radiation flux (calculated by integrating the red curve in panel (a) over time).

The presence of oil droplets in the ice interior does not significantly affect the time at which the surface melt pond first forms. Even with a uniform concentration of $\mathcal{M}_0 = 1000\,\mathrm{ng\,g^{-1}}$ the extra solar energy absorbed by bare ice before the formation of a melt pond is not very significant (see figure 8.7b). This is because a large fraction of the incoming shortwave radiation is reflected by the SSL present on the surface of the ice and so cannot be absorbed by oil droplets in the ice interior. Once the surface of the ice begins to melt, the SSL is lost and the fraction of the incident solar radiation that is absorbed greatly increases. This is shown by the large jump in the absorbed shortwave radiation flux seen in the top row of figure 8.7 in June in both the absorption in the ice and pond and the underlying ocean.

In both the uniform and mobile cases, more of the incoming solar energy is absorbed within the ice, pond and ocean as $\mathcal{M}_0$ increases (see figure 8.7f). For comparison, approximately $334\,\mathrm{MJ\,m^{-2}}$ is required to melt a layer of pure $1\,\mathrm{m}$ thick ice at the melting temperature. In the uniform case, most of the extra energy is absorbed in the ice and pond after the SSL melts, because oil droplets near the surface of the ice absorb incoming solar radiation before it reaches the ice base. In the mobile case, there is less oil in the ice interior due to brine convection during ice growth, and so the largest oil concentrations are found in the ocean and at the ice–ocean interface. Figure 8.7d shows that a significant amount of solar energy is absorbed in the ocean for the mobile case. This enhances basal melting in the mobile case and actually leads to earlier melting of the ice for mobile oil droplets when $\mathcal{M}_0 = 10\,000\,\mathrm{ng\,g^{-1}}$ compared with the uniform case even though there is less oil in the domain overall in the mobile case.

Overall, compared with unpolluted ice the rate of summer ice mass loss is significantly higher for ice polluted with a mass concentration of $\mathcal{M}_0 \geq 1000\,\mathrm{ng\,g^{-1}}$ of oil droplets, and either a uniform concentration of oil droplets or mobile oil droplets. At lower oil concentrations the loss of ice mass is faster with a uniform oil concentration than with mobile droplets, but once $\mathcal{M}_0 = 10\,000\,\mathrm{ng\,g^{-1}}$ both cases show similar rates of ice mass loss. This is because enhanced basal melting in the mobile case is offset by increased surface melting in the uniform case.

8.4.3 The impact of oil pollution versus temporal variability at Barrow

To investigate the potential impact of oil pollution on first-year sea ice compared with inter-annual variability, we ran simulations of the first-year sea ice at Barrow for each ice growth season from 2000–2001 to 2020–2021. Each simulation is run for 365 days starting with ice-free conditions on the 1st of September. Aside from the different initial oil mass fractions $\mathcal{M}_0$, the initial configuration of each simulation is the same as in chapter 6.

Surface melt

The time of melt pond formation t_{pond} is determined as the earliest time (after the 1st of January) for which the top cell of the domain becomes entirely liquid, i.e. $\phi_l = 1$. Figure 8.8 shows that increasing the oil mass fraction does not significantly

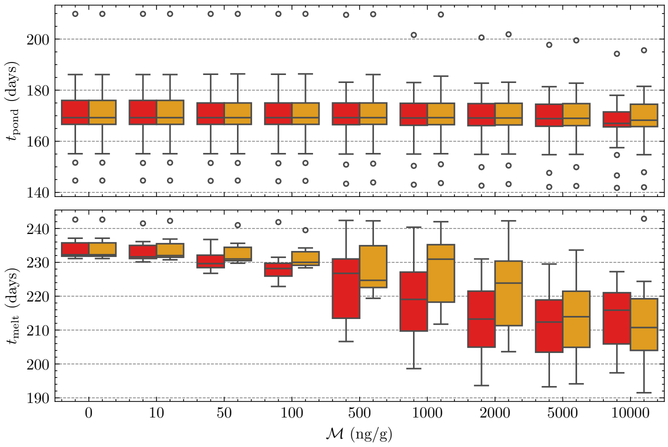

Figure 8.8: Boxplots showing the time (in days since 1st September) at which a melt pond first forms t_{pond} (top) and the time at which the ice completely melts in the summer t_{melt} (bottom) at Barrow, Alaska. Simulations in each season were run with nine different oil mass fractions $0 \leq \mathcal{M}_0 \leq 10\,000\,\mathrm{ng\,g^{-1}}$ with either a uniform distribution of oil droplets (red) or mobile oil droplets (orange). Outliers, defined as more than 1.5 times the interquartile range from the upper or lower quartiles of the ensemble, are shown as unfilled circles.

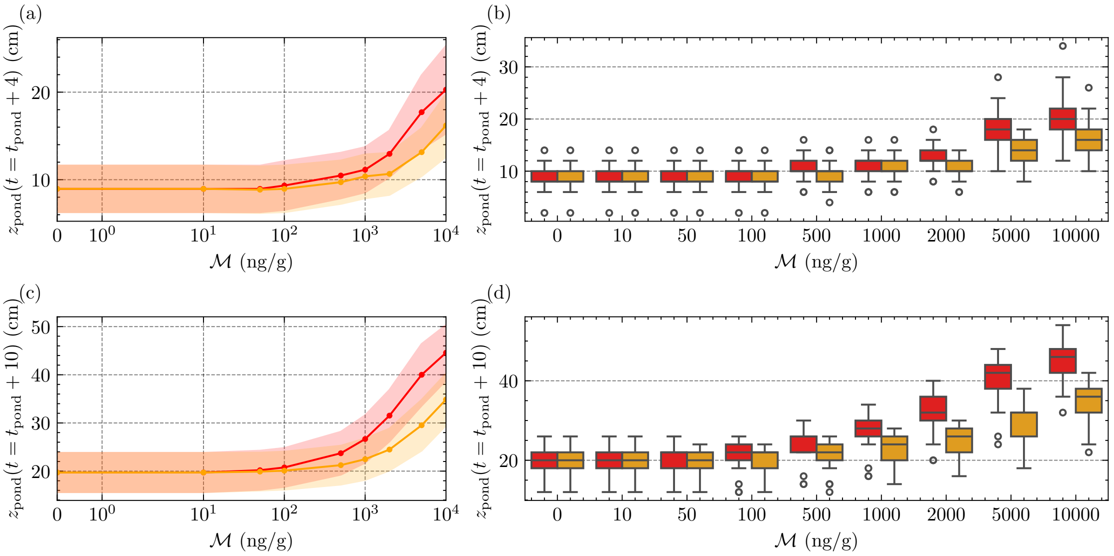

Figure 8.9: Line plots (left column) and boxplots (right column) showing the depth of a surface melt pond z_{pond} at 4 days (top row) and 10 days (bottom row) after it first forms at Barrow, Alaska, as an indicator of surface melting. Simulations were run with nine different oil mass fractions $0 \leq \mathcal{M}_0 \leq 10\,000\,\mathrm{ng\,g^{-1}}$ with either a uniform distribution of oil droplets (red) or mobile oil droplets (orange). For the line plots (left column), the solid line shows the mean of the ensemble (simulated points indicated as filled circles) and the shaded region indicates ±1 standard deviation. For the boxplots (right column), outliers, defined as more than 1.5 times the interquartile range from the upper or lower quartiles of the ensemble, are shown as unfilled circles.

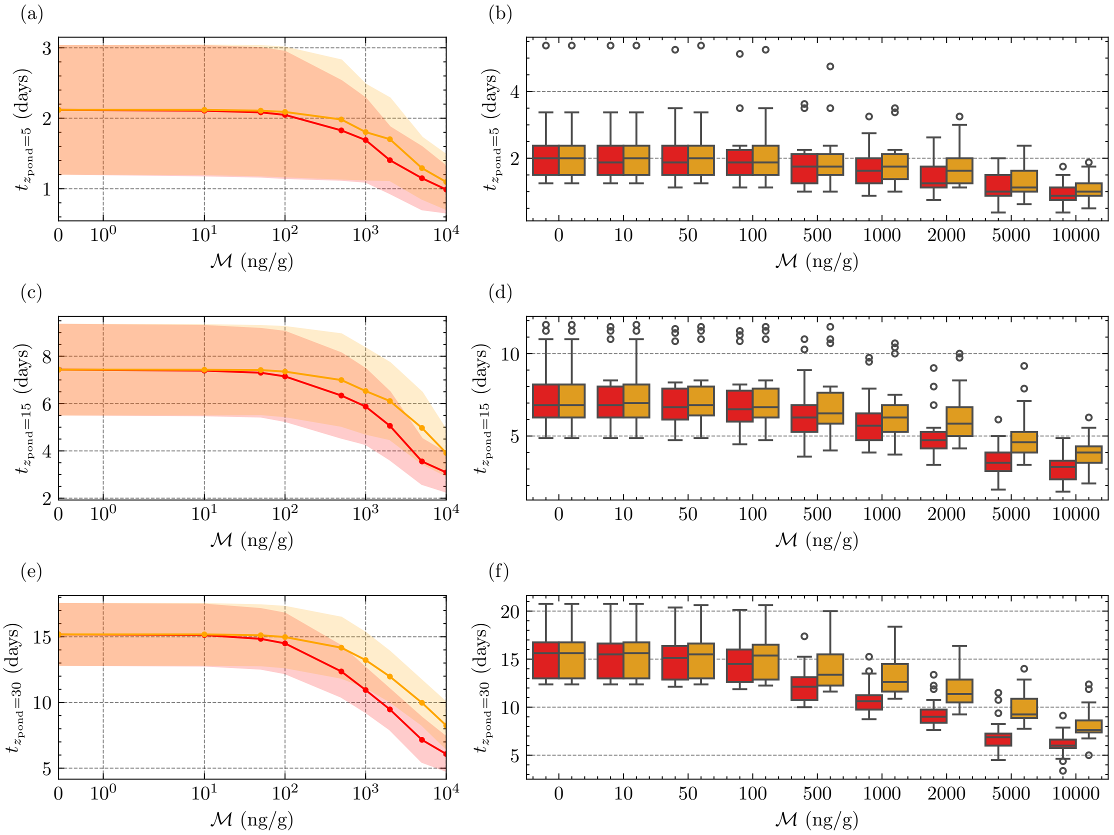

Figure 8.10: Line plots (left column) and boxplots (right column) showing the time after a surface melt pond first forms for it to first exceed a depth of 5 cm (top row), 15 cm (middle row), and 30 cm (bottom row) at Barrow, Alaska. Simulations were run with nine different oil mass fractions $0 \leq \mathcal{M}_0 \leq 10\,000\,\text{ng}\,\text{g}^{-1}$ with either a uniform distribution of oil droplets (red) or mobile oil droplets (orange). For the line plots (left column), the solid line shows the mean of the ensemble (simulated points indicated as filled circles) and the shaded region indicates ±1 standard deviation. For the boxplots (right column), outliers, defined as more than 1.5 times the interquartile range from the upper or lower quartiles of the ensemble, are shown as unfilled circles.

affect the melt pond onset time compared with a natural variability of around 20 days. As previously discussed, the fraction of the incident solar energy absorbed by bare sea is not very significant due to the presence of the SSL. The natural variability in the melt pond onset time is controlled primarily by the date at which sufficient snow has melted to expose the ice surface.

We define the melt time t_{melt} as the time at which the ice completely melts in the summer. Note that in some years the ice does not completely melt in the summer and so t_{melt} is not defined. This is because our model lacks some processes such as melt pond drainage, adjustment of the ice freeboard, and breakup and advection of the ice out to sea that become important later in the melt season.

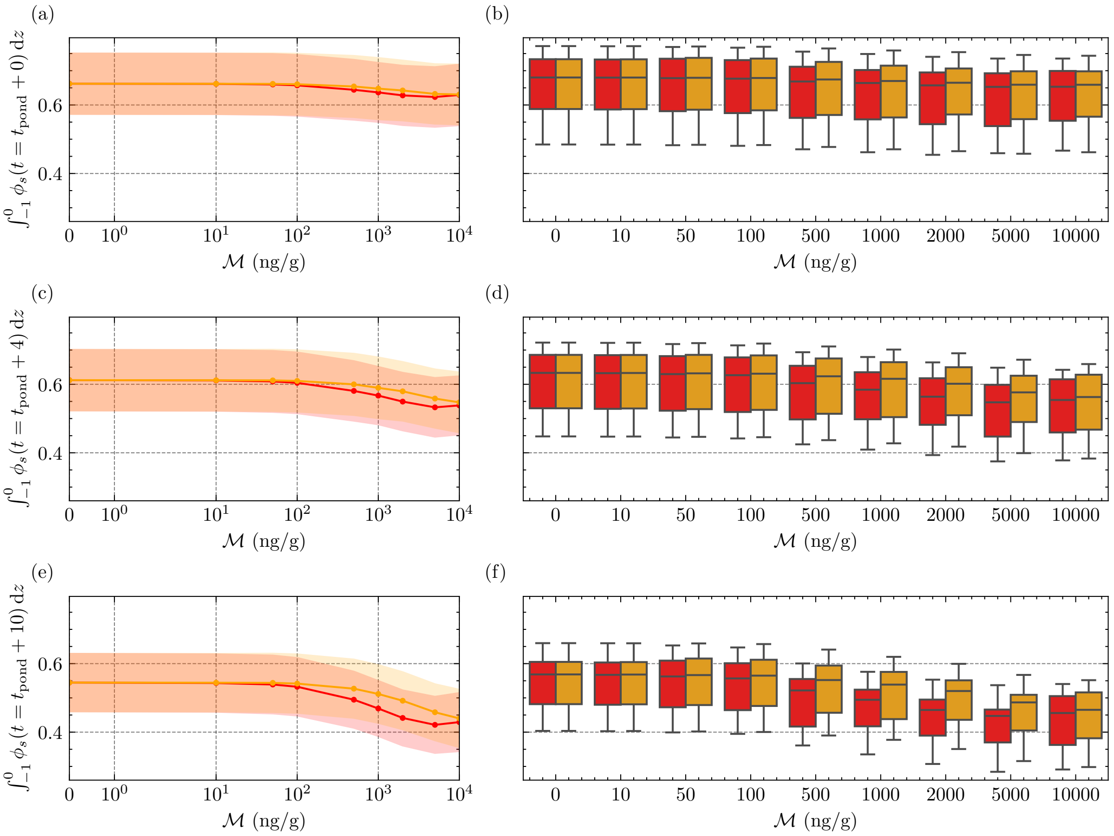

Figure 8.11: Line plots (left column) and boxplots (right column) showing the integrated solid fraction at the time a surface melt pond first forms (top row), 4 days after melt pond formation (middle row), and 10 days after melt pond formation (bottom row) at Barrow, Alaska. Simulations were run with nine different oil mass fractions $0 \leq \mathcal{M}_0 \leq 10\,000\,\mathrm{ng\,g^{-1}}$ with either a uniform distribution of oil droplets (red) or mobile oil droplets (orange). For the line plots (left column), the solid line shows the mean of the ensemble (simulated points indicated as filled circles) and the shaded region indicates ±1 standard deviation. For the boxplots (right column), outliers, defined as more than 1.5 times the interquartile range from the upper or lower quartiles of the ensemble, are shown as unfilled circles.

Despite this figure 8.8 shows that for oil pollution above $100\,\mathrm{ng\,g^{-1}}$ significantly reduces t_{melt} for both the uniform and mobile cases by a maximum of around 20 days. In the uniform case, increasing $\mathcal{M}_0$ from $5000\,\mathrm{ng\,g^{-1}}$ to $10\,000\,\mathrm{ng\,g^{-1}}$ actually seems to increase the melt time slightly. This is likely because in this case more of the incoming solar radiation is absorbed in the pond by oil droplets before reaching the rest of the ice, which contributes to increasing the temperature of the pond instead of melting the ice surface.

The processes that control the formation and evolution of melt ponds on sea ice were reviewed in chapter 1. In particular, melt pond evolution on sea ice can typically be separated into four stages (Eicken et al. 2002). Since our model has no lateral surface topography or snow melt water, the simulated pond is representative of a stage three melt pond deepening due to surface melt of the ice, with no percolation through the ice under the pond.

To investigate the impact of oil on melt pond evolution we define three metrics for pond evolution that can be compared across different seasons. The pond depth t_{lag} days from the time of pond formation $z_{\text{pond}}(t = t_{\text{pond}} + t_{\text{lag}})$ is shown in figure 8.9. The time interval after pond formation for the pond to first reach a depth of z_{target} centimetres is given by $t_{z_{\text{pond}}=z_{\text{target}}} - t_{\text{pond}}$ and is shown in figure 8.10. Finally, we define the integrated solid fraction at t_{lag} days after pond formation as $\int_{-1}^{0} \phi_s(t = t_{\text{pond}} + t_{\text{lag}})\,\mathrm{d}z$, shown in figure 8.11. This is a proxy for the total ice mass in the domain, and so decreasing integrated solid fraction can be due to surface, basal, or internal melting of the ice.

Pond depth both 4 and 10 days after formation begins to noticeably increase with $\mathcal{M}_0$ compared with oil-free ice for $\mathcal{M}_0 > 100\,\mathrm{ng\,g^{-1}}$, both for a uniform concentration of oil droplets and mobile oil droplets. The increase is larger for a uniform concentration of oil droplets than for mobile oil droplets because there is a lower concentration of oil near the surface of the ice in the latter case. The increase in the pond depth after 10 days due to oil droplets becomes comparable to one standard deviation above the ensemble mean for oil-free ice for $\mathcal{M}_0 = 1000\,\mathrm{ng\,g^{-1}}$ in the uniform case and $\mathcal{M}_0 = 2000\,\mathrm{ng\,g^{-1}}$ in the mobile case. The most extreme case of $\mathcal{M}_0 = 10\,000\,\mathrm{ng\,g^{-1}}$ leads to around a doubling of pond depth, as a result of a doubling of the surface melt rate of ponded ice compared with the oil-free case. Similarly the time taken for ponds to reach a depth of 5 cm, 15 cm, and 30 cm decreases with $\mathcal{M}_0$ for $\mathcal{M}_0 > 100\,\mathrm{ng\,g^{-1}}$ for both uniform and mobile oil droplets (figure 8.10). Average pond depths of up to 25 cm were observed on the first-year landfast ice at Barrow in 2009 (Polashenski et al. 2012).

The integrated ice fraction in the domain also decreases once $\mathcal{M}_0 > 100\,\mathrm{ng\,g^{-1}}$, although the decrease is not so large compared with inter-annual variability (see figure 8.11). We also expect that in years with sufficiently warm permeable ice

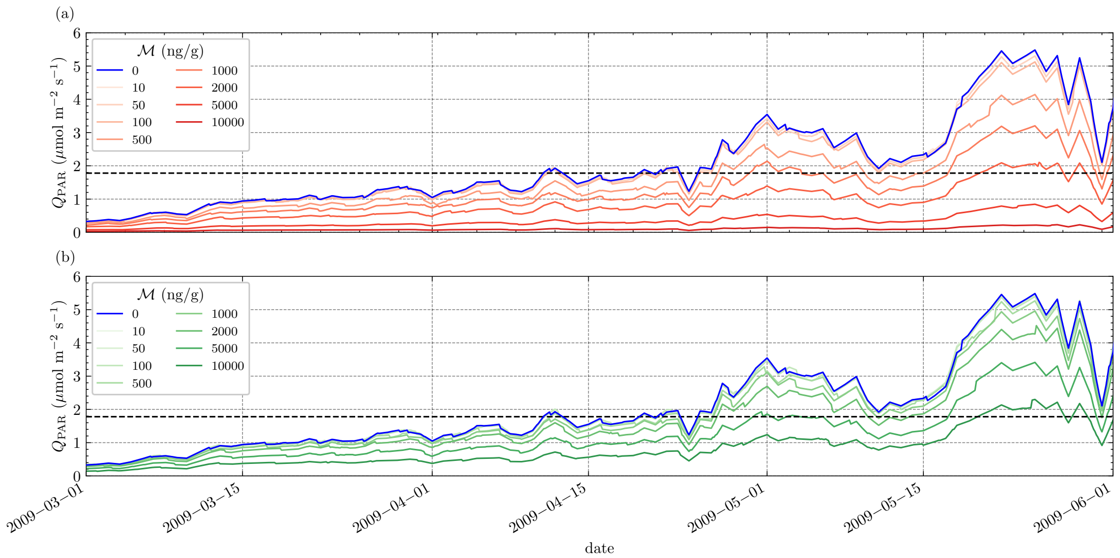

Figure 8.12: The "flat plate" photon flux of photosynthetically active radiation Q_{PAR} at the ice–ocean interface from simulations of first-year sea ice at Barrow, Alaska 2008–2009. The coloured curves correspond to different initial oil mass fractions $\mathcal{M}_0$ with a uniform oil droplet distribution in panel (a) and mobile oil droplets in panel (b). In both panels, the solid blue line shows Q_{PAR} in the oil-free case and the black dashed line shows the algal bloom threshold value $Q_{\mathrm{PAR}} = 1.78\,\mu\mathrm{mol\,m^{-2}\,s^{-1}}$.

under a pond, the meltwater in the pond would be able to percolate through the ice, potentially draining the pond to sea level or fully if the pond base is above sea level. This would reduce the pond depth and increase the albedo of the ice. An even larger increase in albedo would be expected if the pond fully drains exposing bare ice. More ice is lost 10 days from melt pond formation for a uniform oil concentration than for mobile oil droplets, for all $100 \leq \mathcal{M}_0 \leq 5000\,\mathrm{ng\,g^{-1}}$. We note that as $\mathcal{M}_0$ is increased to $10\,000\,\mathrm{ng\,g^{-1}}$, less ice is lost in the uniform case and the overall ice loss is very similar to the mobile case. Based on the results shown in the previous section we hypothesise that this is due to the increased absorption of shortwave radiation at the ice surface, increasing pond temperature without significantly more surface melting, and also preventing radiation reaching the ice base where it could contribute to basal melting.

The spring algal bloom

The absorption of shortwave radiation by oil droplets at low wavelengths within first-year sea ice reduces the amount of photosynthetically active radiation (PAR) at the

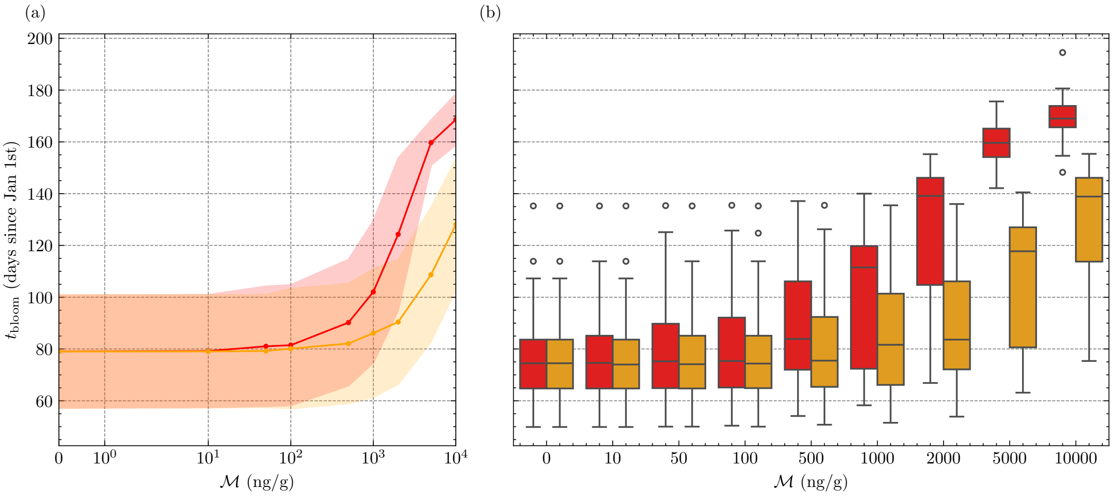

Figure 8.13: Line plots (a) and boxplots (b) showing the spring algal bloom onset time t_{bloom} (in days since the 1st of January) for seasonal simulations of first-year sea ice at Barrow, Alaska. The onset time is determined as the earliest time since the 1st of January for which the photon flux of photosynthetically active radiation Q_{PAR} at the ice–ocean interface exceeds the threshold value $Q_{\mathrm{PAR}} = 1.78\,\mu\mathrm{mol\,m^{-2}\,s^{-1}}$ for at least four subsequent days. Simulations were run with nine different oil mass fractions $0 \leq \mathcal{M}_0 \leq 10\,000\,\mathrm{ng\,g^{-1}}$ with either a uniform distribution of oil droplets (red) or mobile oil droplets (orange). For the line plots (left column), the solid line shows the mean of the ensemble (simulated points indicated as filled circles) and the shaded region indicates ±1 standard deviation. For the boxplots (right column), outliers, defined as more than 1.5 times the interquartile range from the upper or lower quartiles of the ensemble, are shown as unfilled circles.

ice–ocean interface. The onset of the spring algal bloom at the ice–ocean interface is limited by the availability of sufficient PAR for photosynthesis. Therefore, we hypothesise that oil pollution within the ice will delay the onset of the spring algal bloom.

The relevant measure of PAR for sea-ice algae is the "flat-plate" photon flux Q_{PAR} at the ice–ocean interface, which is determined using the 6B2S model via equation (4.7.4) given in chapter 4. Following Stroeve et al. (2024), we define the spring algal bloom onset time t_{bloom} as the earliest time (since the 1st of January) for which Q_{PAR} exceeds $1.78\,\mu\mathrm{mol\,m^{-2}\,s^{-1}}$ for at least four subsequent days. Figure 8.12 shows Q_{PAR} at the ice–ocean interface for simulations of the ice at Barrow (2008–2009) with different oil mass fractions $\mathcal{M}_0$ and either a uniform distribution of oil droplets (panel a) or mobile oil droplets (panel b). The PAR at the ice–ocean interface in oil-polluted ice decreases with increasing $\mathcal{M}_0$. There is a larger reduction in the uniform case than the mobile case. Overall, Q_{PAR} increases from winter to spring as the incoming shortwave radiation flux increases. However, the presence of oil droplets increases the time until Q_{PAR} exceeds the threshold value for an algal bloom (shown as a black line).

Figure 8.13 shows the range of onset times of the spring algal bloom for simulations of first-year sea ice at Barrow from 2000–2001 to 2020–2021, with different oil mass fractions $\mathcal{M}_0$ and either a uniform distribution of oil droplets (red) or mobile oil droplets (orange). For oil-free ice, the interquartile range of the bloom onset time is 65–85 days since the 1st of January. This is consistent with data from the landfast ice at Barrow (compiled by Leu et al. 2015) which shows a sudden increase in the chlorophyll-a concentration[4] beginning from around 70 days since the 1st of January associated with photosynthesis by ice algae. The bloom onset times we have found are also comparable to the range of regionally averaged bloom onset times of 59–86 days and 63–91 days in the Chukchi, and Beaufort Seas (2011–2022), respectively, found by Stroeve et al. (2024) using satellite data. The main source of variability year-to-year is the snow thickness and its impact on the transmission of PAR, since the shortwave radiation flux is very consistent.

Similarly to previous results in this section, the effect of oil pollution on the bloom onset time is not very significant for $\mathcal{M}_0 \leq 100\,\mathrm{ng\,g^{-1}}$. However, a uniform concentration of oil droplets with $\mathcal{M}_0 = 1000\,\mathrm{ng\,g^{-1}}$ delays the median bloom onset time by about a month compared with oil-free ice, from around 75 days to around 110 days since the 1st of January. For mobile oil droplets with $\mathcal{M}_0 = 1000\,\mathrm{ng\,g^{-1}}$ there is a significant but smaller delay in the bloom onset time of around 10 days. These delays are sufficient to shift the bloom onset time to be more comparable to the higher latitudes where the incoming solar radiation flux increases later in the year. For example, Stroeve et al. (2024) found regional averages of 85–97 days since the 1st of January (2011–2022) for the bloom onset time in the central Arctic.

8.5 Discussion & Conclusions

In this chapter, we have used the three-phase transient model for sea ice developed in this thesis to simulate ice growth in an ocean polluted with a low concentration of

---

[4] Chlorophyll-a is a commonly used as an indicator of ice algae biomass.

weathered oil droplets. The oil concentration evolves due to the buoyant motion of the droplets, brine convection during ice growth, and turbulent mixing in the ocean and melt pond. We have modified the shortwave radiative transfer scheme to account for the extra absorption of shortwave radiation by the oil, building on existing radiative transfer modelling of oil droplets in sea ice (Redmond Roche and King 2022b). We have presented the first predictions of the impact of low concentrations of weathered oil droplets on the melting of first-year Arctic sea ice over a season. We have also used the model to predict the transmission of PAR through first-year sea ice polluted with oil droplets. Following existing methodology used to determine the onset time of the spring algal bloom under Arctic sea ice (Stroeve et al. 2024) we found that oil droplet pollution can significantly delay the onset of the bloom.

Our idealised calculations show that a uniform mass fraction of oil droplets above approximately $100\,\mathrm{ng\,g^{-1}}$ reduces the transmittance of solar radiation at the ice–ocean interface for snow-covered, bare, and ponded ice. We also find that the albedo of ponded ice decreases with increasing oil mass fraction above $100\,\mathrm{ng\,g^{-1}}$, due to the increased absorption of radiation by oil in the pond and ice. This is similar to the reduction in first-year ice albedo with increasing oil mass fraction found by Redmond Roche and King (2022b) using a more complex radiative transfer model. However, unlike previous work, we have included a SSL on the surface of bare ice in the model which is important to avoid underestimating the albedo of bare ice and lessens the impact of oil pollution on the albedo of bare ice.

Simulations of the ice at Barrow, Alaska (2008–2009) with a uniform concentration of oil droplets ($\mathcal{M}_0 = 1000\,\mathrm{ng\,g^{-1}}$) show that ice melt is not very sensitive to the median oil droplet radius in the range $0.05 \leq R_{\mathrm{med}} \leq 5\,\mathrm{\mu m}$. This is because the mass absorption cross-section of oil droplets in ice is not very sensitive to R_{med}. However, unlike previous work, we have also simulated the oil concentration within first-year sea ice due to the buoyant motion of mobile oil droplets, their interaction with turbulence in the ocean and melt pond, and their coupling to the convective flow in growing sea ice. We find that the buoyancy of sub-micron sized oil droplets is fairly weak, and hence oil droplets are expelled from the ice through brine channels during ice growth. This results in a lower oil concentration in the domain compared with an imposed uniform concentration of oil droplets. Larger droplet sizes migrate more rapidly so much more oil is able to accumulate in the ice, and this significantly increases surface melt rates.

Laboratory experiments that release a large volume of crude oil under sea ice show that it will migrate to the surface of the ice if it is sufficiently permeable (Asihene et al. 2022; Oggier et al. 2020). However, these results are not directly applicable to the motion of dispersed sub-micron sized oil droplets in brine channels where the oil concentration is lower. Redmond Roche (2024) introduced artificially weathered droplets of oil to the surface of artificial sea ice grown in a laboratory. However, no experiments so far have investigated the motion of dispersed weathered oil droplets released under sea ice. It would be valuable if future experimental work could confirm whether oil droplets are removed from growing sea-ice through brine channels or remain trapped in the ice.

Laboratory experiments have also found that the transition from columnar to granular ice near the ice surface can prevent a connected oil phase migrating to the surface. This is due to the increased tortuosity of the pore space in granular ice (Oggier et al. 2020). This could also plausibly prevent oil droplets from migrating to the surface of the ice, although is not straightforward to assess with the current model for the motion of oil droplets which assumes an idealised pore geometry representative of columnar ice with no tortuosity. It is also plausible that small oil droplets could migrate through any liquid film present within the snowpack. This mechanism would be an interesting avenue for future research, as the presence of oil in the snowpack could cause additional snow melt at the beginning of the melt season. It would also be valuable if future field studies could confirm whether weathered oil droplets are present in melt ponds on Arctic sea ice. We have found ponded ice to be the most susceptible to enhanced melt from oil droplet pollution and this could help constrain the typical mass fractions of oil found in the Arctic.

We have found, that concentrations of oil droplets of $1000\,\mathrm{ng\,g^{-1}}$ and above in Arctic waters are likely to significantly increase the rate of surface and basal melt for ponded first-year sea ice. However, prior to melt pond formation, the effect of oil droplets on the melt of bare ice is relatively inconsequential because the SSL reflects a large amount of the incoming solar radiation. Assuming a uniform distribution of oil droplets throughout the pond, ice and ocean, the mean depth of the pond 10 days after formation (across the 2000–2001 to 2020–2021 seasons) increased from around 20 cm for oil-free ice to around 27 cm, and 44 cm for $\mathcal{M}_0 = 1000\,\mathrm{ng\,g^{-1}}$, and $\mathcal{M}_0 = 10\,000\,\mathrm{ng\,g^{-1}}$ respectively. The effect of oil is less significant in the case of mobile sub-micron sized droplets, because some of the oil is removed from the ice by brine convection. However, the mean melt pond depth 10 days after formation still increased to around 22 cm, and 35 cm for $\mathcal{M}_0 = 1000\,\mathrm{ng\,g^{-1}}$, and $\mathcal{M}_0 = 10\,000\,\mathrm{ng\,g^{-1}}$ respectively. We have also found that the time to melt the entire ice cover in the summer occurs around 10 days earlier for moderate levels of oil pollution due to a strengthening of the ice albedo feedback for ice polluted with oil droplets. We therefore conclude that significant and widespread concentrations of weathered oil droplets in the Arctic Ocean could exacerbate the existing trends towards earlier melt onset and lower minimum sea ice extent (Stroeve et al. 2014).

We have also found that oil droplets in first-year sea ice can significantly delay the onset of the spring algal bloom by absorbing PAR before it can reach the ice–ocean interface. A previous field study at Barrow found that high levels of sediment in the ice could drastically reduce the transmission of PAR to the ice–ocean interface, which completely suppressed the spring algal bloom (Gradinger and Bluhm 2005). This was accompanied by a lack of the typical organisms that feed on the algae under the sediment-laden ice, which supports the idea that the spring algal bloom is an important food source for some Arctic ecosystems. Therefore, we conclude that sufficient concentrations of oil droplets in first-year sea ice may potentially adversely affect primary production in the Arctic Ocean by delaying the onset of the spring algal bloom. Recently, a trend of earlier bloom onset by a few days per decade has been found in the Beaufort Sea (over 1982–2018) driven by thinning snow cover on sea ice (Stroeve et al. 2024). This observed trend could be somewhat offset in the future by increasing levels of oil pollution, depending on the current and future concentration of oil droplets in the Beaufort Sea.

We now discussion some limitations of our approach in this chapter and suggest some avenues for future research. Turbulent mixing of heat, salt and oil in the melt pond and ocean is parameterised using a constant eddy diffusivity. There is no reason to expect the eddy diffusivity to be constant and equal in both the ocean and melt pond, especially as temperature and salinity gradients and shear stresses evolve over time (McPhee 1992; Skyllingstad and Paulson 2007). The value of eddy diffusivity used in this chapter is limited by computational constraints to several orders of magnitude lower than observations in the ocean under sea ice (as discussed in chapter 6). Therefore, we are likely underestimating the heat flux from the ocean to the ice base during the melt season and therefore underestimating the rate of basal ice melt. It is less clear if the model underestimates or overestimates turbulent heat transport in the melt pond, as conditions in the pond are different to the ocean.

The evolution of melt pond depth and coverage on sea ice during the melt season involves a number of processes that are not included in our model. Ponds first form when snow melt water collects in local minima of the ice topography (Eicken et al. 2002), however our model neglects the water produced by snow melt and has a flat ice surface with no horizontal variation. In the model, ponds are initiated and deepen only due to surface melting and we do not allow the ice to move vertically so the ice cannot adjust to be in hydrostatic equilibrium. We do not account for lateral motion of melt water and drainage of ponds through the ice which can change pond depths and coverage in the field (Eicken et al. 2002; Polashenski et al. 2012; Polashenski et al. 2017). The flushing of melt water in ponds downward through the ice also changes ice salinity and porosity (Notz and Worster 2009; Polashenski et al. 2017), and could potentially transport oil droplets from the pond back into the ice. Overall, our simple treatment of surface melt and pond formation could be less accurate once pond drainage occurs, typically 1–2 weeks after pond formation (Polashenski et al. 2012). However, our results still demonstrate the potentially important increase in melt rates due to oil droplets in the melt season.

We have focussed on the landfast ice at Barrow as a simple case which requires atmospheric conditions from a single location and where there is not significant mechanical deformation of the ice (Druckenmiller et al. 2009). The methodology developed in this thesis could be easily extended to other locations with first-year landfast ice in the Arctic Ocean. However, the simulation of drifting ice in the Arctic Ocean would require utilising atmospheric data along the Lagrangian trajectory of the ice. We would also need to account for deformation of the ice in regions where this is significant. Ice melt at Barrow is typically accompanied by the breakup of the fast ice which can be advected out to sea (Mahoney et al. 2007), whereas the ice in our model is assumed to remain at a fixed location and melt in place.

There are also some complexities we have avoided by assuming that the ice and snow cover are horizontally uniform. We have shown that our radiative transfer model is able to accurately predict the transmittance of PAR at the ice–ocean interface through snow and first-year ice. However, snow cover on sea ice is typically very uneven as the wind redistributes the snow and creates drifts (Sturm and Massom 2017). Leads or macroscopic cracks can also be present in the sea ice cover. Therefore, sufficient light could still reach the ice base and initiate a bloom at locations where the snow cover is particularly thin, or through leads. This could be investigated by using a distribution of snow depths and ice thicknesses (see the supplementary material in Stroeve et al. 2024), although in this chapter we have found that the predicted times for the onset of the spring algal bloom at Barrow are fairly consistent with observations (Gradinger and Bluhm 2005; Lee et al. 2008; Leu et al. 2015).

Previous investigation of the impact of oil droplets on sea ice albedo considered two different crude oil types: petrobaltic oil, a light fairly transparent oil; and Romashkino oil, a heavy and dark oil (Redmond Roche and King 2022b). These oils roughly encompass the range of optical properties for most crude oils with petrobaltic oil being least absorbing and Romashkino oil being most absorbing of solar radiation. Indeed, the authors of Redmond Roche and King (2022b) found that droplets of Romashkino oil caused a much larger reduction in sea ice albedo than petrobaltic oil. The results of this chapter have been obtained using the density, viscosity, and mass absorption cross-section for Romashkino crude oil. The viscosity of different crude oils can vary by several orders of magnitude (Liu et al. 2023), but this does not have a significant effect on the magnitude of the rise velocity used in the model. The density of all but the lightest crude oils is between $870\,\mathrm{kg\,m^{-3}}$ and $1000\,\mathrm{kg\,m^{-3}}$ (see Liu et al. 2023, for example), which is less than the density of seawater and is not a significant variation compared with the effect of oil droplet radius on the rise velocity. Our results should hence be thought of as an upper bound on the impact of oil droplets, because different crude oils could be less significant absorbers of solar radiation. However, it is important to consider Romashkino oil as a plausible worst-case scenario for spilled oil in the Arctic since it is commonly found in marine engines (De Carolis et al. 2014).

9

Conclusions

Sea ice is an important component of the Earth's climate system and a vital part of polar ecosystems (see chapter 1). Sea ice is a reactive porous medium comprising of ice crystals and saline brine, often modelled using two-phase mushy-layer theory (Worster 2000; Feltham et al. 2006; Hunke et al. 2011). However, gas bubbles have been observed in sea ice that can provide an additional transport pathway for biogeochemical cycles in the Arctic, and strongly effect the bulk density of sea ice, impacting estimates of sea-ice thickness from satellite measurements (see §1.2 for a review). Meanwhile, oil droplets within sea ice strongly absorb solar radiation, enhancing melt and reducing the light available to ice-algae for photosynthesis (see §1.3 for a review). In this thesis we have developed a general framework for a three-phase mushy-layer model of sea ice, including solid ice crystals, liquid brine, and a third phase that could represent either a gaseous phase arising from the exsolution of dissolved gases from the interstitial liquid, or a second immiscible liquid phase such as oil.

We derived a set of conservation equations for a three-phase mushy layer in chapter 2 including a new expression for the vertical transport of dispersed gas bubbles in the mushy layer as a function of the bubble radius and the local porosity, informed by empirical relationships for the pore geometry (Maus et al. 2021). The implications of the model for gas exsolution and migration have been explored during the steady directional solidification of saltwater (chapter 2) and in a one-dimensional transient model for sea-ice evolution (chapters 3–5). We validated the performance of the transient sea ice model against the observed thickness, temperature and salinity of landfast ice at Barrow, Alaska (chapter 6) and studied the corresponding seasonal evolution of the gas content in the ice (chapter 7), as well as the potential impact of oil pollution (chapter 8). In the remainder of this chapter we will summarise the key results of this thesis (§9.1), and then discuss the potential wider implications and directions for future work (§9.2).

9.1 Summary of key results & their implications

9.1.1 Three-phase mushy-layer model

In chapter 2, we derived a novel formulation for a three-phase mushy layer that applies to the exsolution and migration of gas bubbles in sea ice. Previous modelling of argon (Moreau et al. 2014), oxygen (Moreau et al. 2015a), and carbon (Moreau et al. 2015b) concentrations in sea ice used a simplified model of bubble transport where bubbles were immediately lost to the atmosphere when the overlying ice exceeded a critical porosity threshold of 10% (Moreau et al. 2014). A key result of this thesis is the model we have derived for the motion of gas bubbles in the sea ice pore space. Using results for the Stokes flow around rising spherical bubbles/droplets in cylindrical liquid filled pores, we calculated the gas flux in terms of the gas fraction and porosity-dependent properties of the pore geometry (§2.3). As the local porosity of the ice increases, the pore throat radius decreases, and any bubbles larger than the pore throat radius are rendered immobile. This determines a critical porosity threshold, in terms of the bubble radius, above which gas bubbles can migrate vertically in the ice. This provides a physical mechanism for the ad-hoc porosity threshold introduced by Moreau et al. (2014).

Another key result from chapter 2, is the reduced “tracer” model for gas bubbles, which requires three conditions to be satisfied: (1) the gas volume fraction is small compared with the local porosity, (2) the gas is nearly incompressible, and (3) the solid and liquid phases within the mushy layer are of equal density. Under this approximation, the displacement of liquid in the pore space by gas exsolution and migration is small and can be neglected, and the conservation equations reduce to those applicable to a two-phase mushy layer with extra reactive tracer equations for the dissolved gas concentration and free-phase gas fraction. In chapter 2, we showed that the reduced model is a good approximation to the full equations for steady solidification of saltwater saturated with air. The reduced model is much more computationally tractable, whereas we struggled to find a numerical scheme that could handle the transient case of the full three-phase mushy-layer equations without numerical instabilities.

9.1.2 Transient sea-ice model

In chapters 3–5, we developed a one-dimensional transient model for sea ice evolution using the reduced model for a three-phase mushy layer derived in chapter 2. The model is forced using atmospheric data from the ERA5 reanalysis for the air temperature, humidity, shortwave and longwave radiation fluxes, and wind speed. We do not model the snowpack explicitly. Instead we have used snow depth data from SnowModel-LG as an additional forcing with a tuned thermal conductivity of the snowpack. The model includes parameterisations for brine convection, heat transfer through the snow layer, turbulent mixing in the underlying ocean and surface melt pond, and shortwave radiative transfer in the ice. The model does not include the adjustment of the freeboard position of the ice or the hydraulics controlling the drainage of melt ponds laterally and downward through sufficiently permeable ice (see chapter 8 for a more detailed discussion of these limitations). However, in chapter 7, we showed that the freeboard position for the simulated ice can be estimated post-hoc by assuming hydrostatic balance. A simplified two-stream radiative transfer model (see chapter 4) was calibrated to reproduce reflection and transmission of shortwave radiation through snow, ice, and water, and with sufficient spectral resolution to include the absorption of shortwave radiation by oil droplets.

The conservation equations are solved numerically using the enthalpy method with a finite volume scheme (see chapter 5). These numerical methods are implemented by the Python package `seaice3p v1.0.0` we have written for this thesis. The choice of Python for the implementation of the model was motivated by ease of use and the availability of high quality existing libraries for scientific computing. However, The explicit numerical scheme used in this thesis is sufficient but not well suited to large values of the eddy diffusivity and the RJW14 brine convection scheme, requiring small time steps. The implications of this limitation on the eddy diffusivity for the simulations in this thesis are discussed in chapter 6).

The treatment of heat and salt transport was validated against observations of the thickness, temperature and salinity of first-year landfast sea ice at Barrow, Alaska in the 2008–2009 season (chapter 6). The key uncertainties for the modelled ice thickness were the thermal conductivity assigned to the snow layer, which was tuned to to best matched the observed ice growth, and the ocean heat flux prescribed at the bottom of the domain. We prescribed a monthly averaged ocean heat flux representative of measurements throughout the Arctic Ocean (Krishfield and Perovich 2005). While there is significant variability in the ocean heat flux depending on local oceanographic conditions and also variability year to year, this approach allowed us to capture the essential seasonal cycle of the ocean heat flux and the resulting basal melt of the ice in the melt season.

The reduced "tracer" model for gas/oil developed in this thesis does not modify the heat, salt, and fluid transport equations for a two-phase mushy layer. Therefore, the reduced model can be added to existing mushy sea ice models without significant changes to the existing numerical scheme. This provides a straightforward way to test some of the conclusions of this thesis in other validated sea ice models.

9.1.3 The gas content of first-year sea ice

This thesis represents a new approach to modelling the air content of sea ice over a seasonal cycle using a three-phase mushy-layer model, as opposed to previous studies that modelled the concentrations of individual gases in sea ice using an ad-hoc porosity threshold for bubble migration (Moreau et al. 2014; Moreau et al. 2015a; Moreau et al. 2015b). Chapter 7 used the transient three-phase sea ice model to simulate the evolution of the gas content of the ice at Barrow, Alaska in the 2008–2009 season, assuming that the exsolved air consists of fixed ratios of nitrogen, oxygen, and argon (see §7.2). We compared the predicted profiles of nitrogen, oxygen, and argon with measurements from ice cores (Zhou et al. 2013; Zhou et al. 2014a). Two key observed behaviours are that, (1) atmospheric gases accumulate well above their in-situ solubility during ice growth, suggesting gas bubbles remained trapped in the ice during winter, and (2) warming ice in May/June saw gas content of the ice decreased to the in-situ solubility, suggesting that gas bubbles were able to escape the ice.

There are two key dimensionless parameters in the model that control the gas content of the ice: the Damköhler number (Da) and the dimensionless bubble radius ($\delta_0 = R_B/R_0$). The Damköhler number is the ratio of the time scale for gas exsolution to the time scale for conductive heat transfer in the ice, which roughly corresponds to the time scale for ice growth. The dimensionless bubble radius is the ratio of the bubble radius R_B to the characteristic pore throat size R_0 in sea ice. From comparison to field measurements, we found that bubbles must be large enough to be trapped and accumulate in the relatively cold impermeable ice during growth, but small enough to escape the ice as the ice warms in May/June. This leads to an estimate $\delta_0 \approx 0.3$ that is consistent with previously suggested porosity thresholds for bubble migration in the ice at Barrow (Zhou et al. 2013; Moreau et al. 2014). Due to the threshold behaviour of the model, the simulated gas profiles are very sensitive to the value of δ_0 and the porosity of the simulated ice. It remains an open question to what extent the seasonal evolution of the gas content of the ice in the Arctic as a whole is similar to the observations at Barrow in 2009. Therefore, it is unclear how well our model can generalise to other locations with this value of δ_0.

While δ_0 is responsible for the distribution of gas bubbles in the ice and the timing of their escape when the ice warms, Da controls the total integrated gas content of the ice. Brine convection removes liquid that is supersaturated with gas from the ice, which is replaced with water from the underlying ocean. In the absence of any gas exsolution, this would lead to a decrease in the bulk gas concentration within the ice, which is analogous to the desalination of first-year sea ice (Notz and Worster 2009; Thomas et al. 2020). However, the exsolution of gas bubbles allows this gas to remain in the ice instead of being removed by brine convection. In the limit $Da \to \infty$ all supersaturation would be instantly relieved by gas exsolution. However the results of chapter 7 show that the observed gas concentrations within sea ice are too low to be consistent with this limit. Therefore, $1 \lessapprox Da \lessapprox 100$ is required to allow some accumulation of gas bubbles in the ice during growth, but not too much gas. This aspect of our model is similar to the previous results of Moreau et al. (2014) that also used a linear relaxation model for gas exsolution with a tune-able parameter to control the exsolution rate. By comparison with the same measurements of argon concentrations in the ice at Barrow, Moreau et al. (2014) identified an exsolution rate for their model corresponding to $Da \approx 8$.

Using the values of δ_0 and Da estimated from the comparison with the observations of bulk gas concentrations at Barrow, we predicted the accompanying seasonal evolution of the mean gas fraction within the ice. We find that the mean gas fraction increases to a maximum value of around 1% quickly during initial ice growth and then remains relatively stable until spring. However, once the ice warms, and gas bubbles escape to the atmosphere, the mean gas fraction within the ice drops to zero before the ice thins by melting. This would correspond to a bulk density that decreases as the gas fraction increases in winter, and then increases in the melt season as the accumulated gas escapes the ice. This prediction is consistent with observed ice bulk density measurements from the growth season, but not during the melt season. To investigate this discrepancy further we estimated the freeboard position for the ice if it were in hydrostatic balance, and re-calculated the ice bulk density assuming all the liquid brine in the ice above the freeboard had drained and been replaced with air. This estimate was consistent with the observed seasonal evolution of the bulk density of free floating pack ice in the Arctic observed by Salganik et al. (2024).

9.1.4 The impact of dispersed weathered oil droplets on first-year sea ice

In chapter 8, we adapted the transient three-phase mushy-layer model for sea ice to model the motion of oil droplets within the ice, and account for their impact on the absorption of shortwave radiation (Redmond Roche and King 2022b). In contrast to previous studies (Redmond Roche and King 2022b), we also included the impact on the transmission of shortwave radiation of the surface scattering layer (SSL) and melt pond formation along with the motion of oil droplets within the ice. This allowed us to investigate the impact of low concentrations of weathered oil droplets on the ice, that may become more prevalent as the Arctic Ocean becomes more accessible to shipping and oil extraction (see chapter 1). We found that oil pollution within the ice did not have a significant effect on the absorption of solar radiation and ice melt prior to the formation of a melt pond, due to the highly reflective SSL covering the surface of the ice. However, for oil concentrations above around $1000\,\mathrm{ng\,g^{-1}}$ we found an increase to simulated melt rates at Barrow after pond formation, that was significant compared with interannual variability, leading to the ice melting around 10 days earlier. We also found that the presence of oil droplets in the ice can significantly reduce the photosynthetically active radiation reaching algae at the base of the ice, which could potentially delay the onset of the spring algal bloom by around a week or two. This could have knock-on effects for the Arctic ecosystem in areas polluted with weathered oil droplets and may potentially offset observed trends toward earlier spring blooms due to the thinning of snow cover in the Beaufort Sea (Stroeve et al. 2024).

The concentrations of oil droplets considered in this thesis were motivated by previous studies (Haule and Freda 2016; Redmond Roche and King 2022b; Redmond Roche 2024) and estimations of oil concentrations resulting from oil spills (see chapter 1 for a review). However, it would be valuable to gather measurements of the concentration of oil droplets in the ocean, ice and melt ponds in the Arctic to assess the validity of the concentrations considered in this thesis. Several recent studies have investigated the fate of oil released under sea ice under laboratory conditions (Oggier et al. 2020; Dilliplaine et al. 2021; Asihene et al. 2022), and also doped artificial sea ice with weathered oil droplets (Redmond Roche 2024). However, it would be valuable to take quantitative measurements of the distribution of oil droplets within sea ice that has been grown from water containing weathered oil droplets. This could be done using the imaging methods developed by Desmond et al. (2021). It would answer the question of whether dispersed weathered oil droplets are likely to be removed from the ice by brine convection or remain trapped in the pore space, which would have implications for their radiative effect.

9.2 Directions for future work

We have used the transient three-phase mushy-layer model to estimate the gas content of the landfast ice at Barrow, Alaska, its impact on the bulk density of the ice (chapter 7), and the potential impact of dispersed weathered oil droplets on the absorption of solar radiation in the ice (chapter 8). However, future work should focus on how the results of this case study at Barrow can be generalised to first-year ice throughout the Arctic across multiple seasons. The computational model we have developed (`seaice3p v1.0.0`) can in principle be forced with atmospheric data (from ERA5 reanalysis or similar), snow depth data (SnowModel-LG or similar), and ocean heat fluxes for any location in the Arctic. However, to extend a spatial analysis beyond landfast ice would require additional modelling for the motion and deformation of free-floating pack ice with forcing applied along a Lagrangian trajectory.

In this thesis, we have built understanding using a simplified model for the motion of identically sized gas bubbles moving through cylindrical pores (chapter 2). However, in reality the gas bubbles in sea ice have a distribution of sizes and are distributed amongst a complex network of pores (Light et al. 2003; Crabeck et al. 2016). Future work could extend the framework developed here to include a distribution of bubble sizes and pore sizes, perhaps informed by new work on the motion of bubbles in the sea ice pore space and the processes controlling their size distribution. We have also neglected the tortuosity of the pore space in our model which could prevent otherwise mobile buoyant bubbles from migrating vertically in the ice. This could be more important for the granular ice texture found near the surface of the ice which has a more tortuous pore space than the columnar ice texture that dominates the interior of the ice and consists of longer vertically aligned pores (Oggier and Eicken 2022). There is also the possibility of gas bubbles being trapped in completely closed inclusions in the ice, where the solubility may be controlled by local pressure conditions in the inclusion (Crabeck et al. 2019), which we have not considered thus far.

We have used the computationally convenient reduced model for the transient simulations in this thesis, however the underlying approximations of this model break down when the gas or oil fraction approaches the local porosity. We found it challenging to develop a numerical scheme that can handle the full three-phase mushy-layer equations without numerical instabilities in scenarios where $\phi_g \to 1-\phi_s$. However, future work in this direction could develop a more general transient model capable of exploring the displacement of liquid from the pore space by gas exsolution and migration, or the infiltration of air into the ice and snow above the freeboard. This could help investigate the feasibility of the proposed mechanism to generate gas bubbles and density reductions in warming sea ice suggested by Salganik et al. (2024) (discussed in §1.2), although we have found that this is not necessary to explain the observed reduction of bulk density in the summer (see chapter 7).

The methods developed in this thesis could be coupled to existing numerical models for the growth of sea-ice algae and extended to include other species (see Vancoppenolle and Tedesco 2017, for example). This could be used to investigate the biological feedbacks between gas transport and sea-ice algae. It could also provide a more in depth study of the impact of dispersed oil droplets on the growth of sea-ice algae, as opposed to the PAR threshold for an algal bloom used by Stroeve et al. (2024) and adopted in this thesis.

The Arctic Ocean has been recognised as an important source of methane to the atmosphere as a result of methane bubbles degassing from the sediments under shallow waters on the continental shelves (Kort et al. 2012). These methane bubbles rise through the water column (Chernykh et al. 2023) and can become trapped in the sea ice (He et al. 2013; Zhou et al. 2014b). Therefore the motion of methane bubbles in sea ice is an important consideration for future fluxes of methane from the Arctic Ocean to the atmosphere, and could be investigated using the framework developed in this thesis. As well as degassing from oceanic sediments, global warming is promoting the release of methane from permafrost in the Arctic which is another example of a porous medium in which the dynamics of freezing/melting and gas bubble transport are important (Rößger et al. 2022).

There are many other geophysical systems that exhibit important phenomena due to the dynamics of gas bubbles in a reactive porous medium that could be investigated using similar approaches to this thesis. Peat bogs are an example of a chemically reactive porous medium comprised of solid organic matter, liquid water, and gas bubbles that are important for the global carbon cycle (Beaulne et al. 2021). The dynamics of gas bubbles are important for quantifying the flux of greenhouse gases between the peat and the atmosphere (Strack et al. 2005). The multicomponent mineral melt found in magma chambers can be thought of as a three-phase mushy layer that contains volatiles such as dissolved water and carbon dioxide (Huppert and Worster 2012), and the exsolution of these gaseous volatiles can be important for the dynamics of volcanic eruptions (Huppert and Woods 2002; Girona et al. 2015; Parmigiani et al. 2016; Liao 2022). I hope that the results and methods developed in this thesis can be used to further investigate the truly complex, fascinating, and beautiful *multiphase* nature of sea ice and other natural systems.

Appendices

A

Enthalpy in a three-phase mushy layer

We consider the bulk enthalpy per unit volume H of a mixture of solid, liquid and gaseous phases in thermal equilibrium at temperature T. Assuming that each phase is an ideal mixture yields an expression for the enthalpy of each phase. The solid-phase enthalpy is given by

$$H_s = \rho_s \left(\mathcal{W}_s h_{\mathrm{H_2O(s)}} + S_s h_{\mathrm{NaCl\cdot 2\,H_2O(s)}} \right), \tag{A.0.1}$$

where $h_{\mathrm{H_2O(s)}}$ is the specific enthalpy of ice, $h_{\mathrm{NaCl\cdot 2\,H_2O(s)}}$ is the specific enthalpy of hydrohalite, and we assume no dissolved gas is incorporated into the solid phase. The liquid-phase enthalpy is given by

$$H_l = \rho_l \left(\mathcal{W}_l h_{\mathrm{H_2O(l)}} + S_l h_{\mathrm{NaCl(aq)}} + \xi_l h_{\mathrm{air\ (aq)}} \right), \tag{A.0.2}$$

where $h_{\mathrm{H_2O(l)}}$ is the specific enthalpy of liquid water, $h_{\mathrm{NaCl(aq)}}$ is the specific enthalpy of dissolved salt, and $h_{\mathrm{air\ (aq)}}$ is the specific enthalpy of dissolved air. The gas-phase enthalpy is given by

$$H_g = \rho_g h_{\mathrm{air\ (g)}}, \tag{A.0.3}$$

where $h_{\mathrm{air\ (g)}}$ is the specific enthalpy of air. Conservation of bulk enthalpy yields

$$\frac{\partial H}{\partial t} + \boldsymbol{\nabla} \cdot (H_l \boldsymbol{u}_l) + \boldsymbol{\nabla} \cdot (H_g \boldsymbol{u}_g) = \boldsymbol{\nabla} \cdot \left(\bar{k} \boldsymbol{\nabla} T \right), \tag{A.0.4}$$

where $H = \phi_s H_s + \phi_l H_l + \phi_g H_g$ and we neglect the transport of energy by molecular diffusion of dissolved salt and air within the liquid phase.

We neglect the impact of pressure changes on the enthalpy of the system, assuming these changes are small compared with atmospheric pressure, so that

$$\mathrm{d}h = c_p \mathrm{d}T, \tag{A.0.5}$$

where c_p is the specific heat capacity of the material at constant pressure, and h is the specific enthalpy of the material. Using equation (A.0.5), we expand equation (A.0.4) using the conservation equations (2.2.5), (2.2.7), (2.2.8), and (2.2.9) with $\kappa_S = \kappa_\xi = 0$ to obtain

$$\begin{aligned}\overline{\rho c_p}\frac{\partial T}{\partial t} + \left(\rho_l c_{p,l}\boldsymbol{u}_l + \rho_g c_{p,g}\boldsymbol{u}_g\right)\cdot\boldsymbol{\nabla}T &= \boldsymbol{\nabla}\cdot\left(\bar{k}\boldsymbol{\nabla}T\right) + L\frac{\partial}{\partial t}\left(\rho_s\phi_s\mathcal{W}_s\right)\\ &+ \Delta h^{\text{diss}}_{\text{salt}}\frac{\partial}{\partial t}\left(\rho_s\phi_s S_s\right)\\ &+ \Delta h^{\text{diss}}_{\text{air}} N,\end{aligned}$$

Here, the specific heat capacity of each phase is related to the specific heat capacity of each component by

$$c_{p,s} = \mathcal{W}_s c_{p,\mathrm{H_2O(s)}} + S_s c_{p,\mathrm{NaCl\cdot 2\,H_2O(s)}}, \tag{A.0.6}$$

$$c_{p,l} = \mathcal{W}_l c_{p,\mathrm{H_2O(l)}} + S_l c_{p,\mathrm{NaCl(aq)}} + \xi_l c_{p,\mathrm{air\ (aq)}}, \tag{A.0.7}$$

$$c_{p,g} = c_{p,\mathrm{air\ (g)}}. \tag{A.0.8}$$

We assume that the heat capacity of each component can be treated as constant over the temperature range considered. The specific latent heat of fusion for water $L = h_{\mathrm{H_2O(l)}} - h_{\mathrm{H_2O(s)}}$ is the heat released during freezing per unit mass. Similarly, there is an enthalpy change per unit mass of $\Delta h^{\text{diss}}_{\text{salt}} = h_{\mathrm{NaCl(aq)}} - h_{\mathrm{NaCl\cdot 2\,H_2O(s)}}$ associated with the precipitation of hydrohalite,

$$\mathrm{NaCl_{(aq)}} + 2\,\mathrm{H_2O_{(l)}} \longrightarrow \mathrm{NaCl\cdot 2\,H_2O_{(s)}}, \tag{A.0.9}$$

and of $\Delta h^{\text{diss}}_{air} = h_{\mathrm{air\ (aq)}} - h_{\mathrm{air\ (g)}}$ associated with air exsolution. The enthalpy changes during phase change are again approximated as constant over the considered temperature range.

Finally we make the approximation that salt and air form only a small part of the system by mass, taking S_l, ξ_l, $S_s \approx 0$. This allows us to neglect the temperature changes associated with hydrohalite precipitation and air exsolution and approximate $\mathcal{W}_s$, $\mathcal{W}_l \approx 1$. We then recover equation (2.2.13), where the specific heat capacities of the solid and liquid phases are those of ice and water, respectively.

B

Volume change upon the exsolution of a saturated solution

Consider a volume V' of liquid comprising a mass $M_{\mathcal{W}}$ of water and a M_g of dissolved air. This solution then has density

$$\rho_l' = \frac{M_{\mathcal{W}} + M_g}{V'},$$

and contains a mass fraction of water

$$\mathcal{W}_l = \frac{M_{\mathcal{W}}}{M_{\mathcal{W}} + M_g}.$$

If this solution is saturated with dissolved air, then we additionally have

$$\xi_l^{\mathrm{sat}} = \frac{M_g}{M_{\mathcal{W}} + M_g}.$$

Consider exsolving all of this dissolved gas into a free gas phase of density ρ_g, leaving pure water of density ρ_l. The new total volume of the system is

$$V = \frac{M_{\mathcal{W}}}{\rho_l} + \frac{M_g}{\rho_g}.$$

Under the approximations $\rho_l' \approx \rho_l$ (Watanabe and Iizuka 1985) and $\rho_l \gg \rho_g$, the relative volume change is

$$\frac{V - V'}{V'} = \frac{\rho_l \xi_l^{\mathrm{sat}}}{\rho_g} = \chi.$$

C

Numerical method for the steady-state three-phase mushy-layer boundary value problem

We have developed the software package `mush3p v1.0.1`, written in Python `v3.12.3`, to numerically solve the equations for a three-phase mushy layer undergoing steady directional solidification, as set out in §2.4. Our code uses the scientific computing packages `Numpy v1.26.4` (Harris et al. 2020) and `Scipy v1.14.0` (Virtanen et al. 2020).

We solve the boundary value problem within the mushy layer using a 4th order collocation algorithm implemented by `scipy.integrate.solve_bvp`. We transform the free-boundary problem to a fixed domain $-1 \leq \eta \leq 0$ by introducing the scaled coordinate $\eta = -z/z_L$. The free parameters for the solution Φ and z_L are promoted to variables to be found by the numerical solver. We write the problem in the form

$$\frac{\mathrm{d}\boldsymbol{y}}{\mathrm{d}\eta} = \boldsymbol{f}(\eta, \boldsymbol{y}), \tag{C.0.1}$$

where for the full three-phase mushy layer

$$\boldsymbol{y}(\eta) = \begin{bmatrix} \theta \\ \theta' \\ \omega \\ p_H \\ z_L \\ \Phi \end{bmatrix}, \quad \boldsymbol{f}(\eta, \boldsymbol{y}) = \begin{bmatrix} \theta' \\ -\dfrac{z_L \theta'}{1-\phi_g}\left[1 - \Phi - \dfrac{1}{z_L}\dfrac{\mathrm{d}\phi_g}{\mathrm{d}z} + St\dfrac{\mathcal{C}(1-\Phi)}{(\mathcal{C}-\theta)^2}\right] \\ \dfrac{Da\mathcal{N}(\mathcal{C}-\theta)z_L}{\mathcal{C}(1-\Phi)} - \dfrac{\theta'\omega}{\mathcal{C}-\theta} \\ \dfrac{\Phi - \phi_g}{\Pi(\phi_l)} \\ 0 \\ 0 \end{bmatrix}, \tag{$C.0.2a, b$}$$

using the scaled coordinate η and rearranging equations (2.4.5), (2.4.3), and (2.4.6) using equations (2.4.12) and (2.4.18). Here, θ' denotes the first derivative of θ with respect to η and ϕ_g, ϕ_l, and $\Pi(\phi_l)$ are calculated from equations (2.4.19), (2.4.18), (2.4.12), and (2.4.7). The boundary conditions are given by

$$\boldsymbol{b}(\boldsymbol{y}(-1), \boldsymbol{y}(0)) = \begin{bmatrix} \theta(-1) \\ \theta(0) + 1 \\ \omega(-1) - \omega_\infty \\ p_H(0) \\ \theta'(-1) - z_L(-1)\theta_\infty[1 - \Phi(-1)] \\ \Phi(0) - \left(1 + \dfrac{\psi_0}{\chi\omega_\infty}\right)^{-1} \end{bmatrix} = \boldsymbol{0}, \tag{C.0.3}$$

where ψ_0 is the dimensionless gas density evaluated at the top boundary $\eta = 0$ from equation (2.4.11). The initial guess for each solution component is taken to be a linear function of η that satisfies the relevant boundary conditions.

For the reduced model (§2.4.7), neglecting $\phi_g \ll 1$ and $\Phi \ll 1$ in equation (C.0.2) yields the simplified system of ordinary differential equations (ODEs)

$$\frac{\mathrm{d}\boldsymbol{y}_R}{\mathrm{d}\eta} = \boldsymbol{f}_R(\eta, \boldsymbol{y}_R), \quad \boldsymbol{y}_R(\eta) = \begin{bmatrix} \theta \\ \theta' \\ \omega \\ z_L \end{bmatrix}, \quad \boldsymbol{f}_R(\eta, \boldsymbol{y}_R) = \begin{bmatrix} \theta' \\ -z_L\theta'\left[1 + St\dfrac{\mathcal{C}}{(\mathcal{C} - \theta)^2}\right] \\ \dfrac{Da\mathcal{N}(\mathcal{C} - \theta)z_L}{\mathcal{C}} - \dfrac{\theta'\omega}{\mathcal{C} - \theta} \\ 0 \end{bmatrix}, \tag{C.0.4a, b}$$

where $\phi_l = 1 - \phi_s$, ϕ_s is given by equation (2.4.25), ϕ_g is given by equation (2.4.26), and the variables p_H and Φ are removed from the ODE system. The associated boundary conditions, under the approximation $\Phi \ll 1$, are

$$\boldsymbol{b}_R(\boldsymbol{y}(-1), \boldsymbol{y}(0)) = \begin{bmatrix} \theta(-1) \\ \theta(0) + 1 \\ \omega(-1) - \omega_\infty \\ \theta'(-1) - z_L(-1)\theta_\infty \end{bmatrix} = \boldsymbol{0}. \tag{C.0.5}$$

D

The dependence of the maximum supersaturation in a steady three-phase mushy layer on the Damköhler number

Here, we derive a scaling for the maximum supersaturation achieved in the mushy layer in the reduced model, when $Da \gg 1$. We assume that $\omega(z)$ reaches a local maximum at z_m, where

$$\frac{\mathrm{d}\omega}{\mathrm{d}z} = 0,$$

and $z_L < z_m < 0$. Therefore, at $z = z_m$ conservation of dissolved gas for the reduced model (2.4.27) becomes

$$\omega \frac{\mathrm{d}\phi_l}{\mathrm{d}z} = -Da\phi_l(\omega - 1), \tag{D.0.1}$$

which represents the balance of increasing supersaturation due to the rejection of dissolved gas during freezing, and reduction of supersaturation by gas exsolution. Upon rearrangement equation (D.0.1) yields

$$\omega - 1 = \frac{-\frac{\mathrm{d}\phi_l}{\mathrm{d}z}}{\frac{\mathrm{d}\phi_l}{\mathrm{d}z} + Da\phi_l}.$$

For $Da \gg 1$, we find

$$\max_{z_L < z < 0} \left[\omega(z) - 1\right] \sim -\frac{1}{Da}\frac{1}{\phi_l}\frac{\mathrm{d}\phi_l}{\mathrm{d}z} = O\left(\frac{1}{Da}\right), \tag{D.0.2}$$

where the final equality exploits the fact that, in the reduced model, ϕ_l is independent of the gas dynamics and so does not depend on Da.

E

Eddy diffusion

In completely liquid regions (i.e., $\phi_l = 1$), the conservation equations for dissolved salt, dissolved gas, and energy (introduced in chapter 2) take the form of generic advection-diffusion-reaction equations

$$\frac{\partial q}{\partial t} + \boldsymbol{\nabla} \cdot (q \boldsymbol{u}_l) = \boldsymbol{\nabla} \cdot (\kappa_q \boldsymbol{\nabla} q) + \mathcal{Q}, \tag{E.0.1}$$

where κ_q is the molecular diffusivity of a quantity q in the liquid and $\mathcal{Q}$ are source terms that do not depend on turbulent fluctuations. When q is the energy, salinity, or dissolved gas concentration, the appropriate diffusivity is $\overline{k}/(\rho_l c_{p,l})$, κ_S, or κ_ξ, respectively.

We decompose $q = \overline{q} + q'$ and $\boldsymbol{u}_l = \overline{\boldsymbol{u}_l} + \boldsymbol{u}_l'$ into a mean component (denoted with an overbar) and a fluctuating component (denoted with a dash). Hence, performing standard Reynolds averaging (see chapter 11 of Vallis 2017) on equation (E.0.1) yields

$$\frac{\partial \overline{q}}{\partial t} + \boldsymbol{\nabla} \cdot (\overline{q}\, \overline{\boldsymbol{u}_l}) = \boldsymbol{\nabla} \cdot \left(\kappa_q \boldsymbol{\nabla} \overline{q} - \overline{\boldsymbol{u}_l' q'} \right) + \overline{\mathcal{Q}}. \tag{E.0.2}$$

Finally, we utilise the standard closure (see chapter 13 of Vallis 2017)

$$\overline{q' \boldsymbol{u}_l'} = -\kappa_\varepsilon \boldsymbol{\nabla} \overline{q}, \tag{E.0.3}$$

where κ_ε is the eddy diffusivity to obtain an equation for the evolution of the mean quantities. Substituting equation (E.0.3) into equation (E.0.2) yields the enhanced diffusivities given by equations (3.2.7)–(3.2.9)) in chapter 3.

F

Derivation of the two-stream approximation

Here we derive the two-stream approximation, given by (4.4.4) and (4.4.3), from the radiative transfer equation (4.3.1) largely following Stamnes et al. (2017). If the phase function and radiance field are independent of the azimuthal direction (4.3.1) can be written as

$$\mu \frac{\mathrm{d}I}{\mathrm{d}\tau} = -I + \frac{\omega_0}{2} \int_{-1}^{1} \mathscr{P}(\mu,\, \mu') I(\tau,\, \mu', \lambda)\, \mathrm{d}\mu', \tag{F.0.1}$$

where $\mu = \cos(\vartheta)$. Integrating (F.0.1) over the upper and lower hemispheres yields

$$\frac{\mathrm{d}F_\lambda^+}{\mathrm{d}\tau} = -2\pi I^+ + 2\pi \frac{\omega_0}{2} \int_{-1}^{0} \int_{-1}^{1} \mathscr{P}(\mu,\, \mu') I(\tau,\, \mu',\, \lambda)\, \mathrm{d}\mu' \mathrm{d}\mu, \tag{F.0.2}$$

and

$$\frac{\mathrm{d}F_\lambda^-}{\mathrm{d}\tau} = -2\pi I^- + 2\pi \frac{\omega_0}{2} \int_{0}^{1} \int_{-1}^{1} \mathscr{P}(\mu,\, \mu') I(\tau,\, \mu',\, \lambda)\, \mathrm{d}\mu' \mathrm{d}\mu, \tag{F.0.3}$$

respectively, where I^+ and I^- are the radiances averaged over the upper and lower hemispheres respectively. So far (F.0.2) and (F.0.3) are exact, however we now approximate the radiance in the scattering integral term with the hemispherical averages, which yields

$$\frac{\mathrm{d}F_\lambda^+}{\mathrm{d}\tau} = -\frac{F_\lambda^+}{\overline{\mu}^+} + \omega_0 \left[(1-b) \frac{F_\lambda^+}{\overline{\mu}^+} + b \frac{F_\lambda^-}{\overline{\mu}^-} \right], \tag{F.0.4}$$

and

$$\frac{\mathrm{d}F_\lambda^-}{\mathrm{d}\tau} = -\frac{F_\lambda^-}{\overline{\mu}^-} + \omega_0 \left[(1-b) \frac{F_\lambda^-}{\overline{\mu}^-} + b \frac{F_\lambda^+}{\overline{\mu}^+} \right], \tag{F.0.5}$$

where $\overline{\mu}^\pm = F_\lambda^\pm / 2\pi I^\pm$, and b is the backscatter ratio for the phase function. The backscatter ratio can be expressed using double integrals of the phase function (see e.g. Stamnes et al. 2017) as

$$b \equiv \frac{1}{2} \int_{-1}^{0} \int_{0}^{1} \mathscr{P}(\mu,\, \mu')\, \mathrm{d}\mu' \mathrm{d}\mu = \frac{1}{2} \int_{0}^{1} \int_{-1}^{0} \mathscr{P}(\mu,\, \mu')\, \mathrm{d}\mu' \mathrm{d}\mu, \tag{F.0.6}$$

$$1 - b \equiv \frac{1}{2}\int_{-1}^{0}\int_{-1}^{0} \mathscr{P}(\mu,\, \mu')\,\mathrm{d}\mu'\mathrm{d}\mu = \frac{1}{2}\int_{0}^{1}\int_{0}^{1} \mathscr{P}(\mu,\, \mu')\,\mathrm{d}\mu'\mathrm{d}\mu, \tag{F.0.7}$$

or as a single integral

$$b \equiv \frac{1}{2}\int_{0}^{1} \mathscr{P}(-\mu,\, 1)\,\mathrm{d}\mu. \tag{F.0.8}$$

Finally, if we assume the radiance field is isotropic in both hemispheres then $\overline{\mu}^{\pm} = \mp 1/2$. Substituting this into (F.0.4) and (F.0.5), and using equations (4.3.2) and (4.3.3), yields the two-stream equations given in chapter 4 with $\overline{\mu} = 1/2$.

The Henyey-Greenstein phase function (Henyey and Greenstein 1941) given by

$$\mathscr{P}_{\mathrm{HG}}(\vartheta,\, \vartheta') = \frac{1 - g^2}{(1 + g^2 - 2g\cos(\vartheta - \vartheta'))^{3/2}}, \tag{F.0.9}$$

where g is the asymmetry parameter, is often used to model scattering in media where scattering is strongly forward peaked, such as sea ice. In this case (F.0.8) yields

$$b_{\mathrm{HG}}(g) = \frac{1-g}{2g}\left(\frac{1+g}{\sqrt{1+g^2}} - 1\right). \tag{F.0.10}$$

The value of $g = 0.98$ used by Redmond Roche and King (2022b) gives $b_{\mathrm{HG}} = 0.00423$.

G

Simulated ice thickness at Barrow, Alaska 2006-2015

In chapter 6, we identified $k_{\text{snow}} = 0.42\,\text{W}\,\text{m}^{-1}\,\text{K}^{-1}$ best reproduced the observed ice thickness at Barrow, Alaska from January-June 2009. In this appendix we present the simulated ice thickness at Barrow, Alaska in 2006-2015 (excluding 2013 when no field data was collected) using the same parameter values used in chapter 6. Figure G.1 shows the snow depth data from the SnowModel-LG dataset (Liston et al. 2021), that is used to force the simulations, compared with the snow depth measurements from the Barrow mass balance site (Eicken 2012). Note that up to three different instruments were deployed each year at the MBS to measure snow depth. While periods identified as bad data in the metadata have been removed, slippage of the instruments or just heterogeneity in the snowpack can lead to discrepancies between the measurements. Figure G.2 shows the simulated ice thickness compared with ice thickness data from the Barrow mass balance site (MBS).

Despite parameter values being chosen based only on the 2008–2009 season at Barrow our model does a reasonable job of reproducing the observed ice thickness at Barrow in other years, with some year-to-year variability. Apart from 2008–2009, particularly good agreement is seen in 2005–2006, 2011–2012, and 2013–2014, which are seasons in which the snow depth data used is in better agreement with the observed snow depth at the MBS. In contrast, the simulation severely overestimates the ice thickness in 2014–2015, which can be attributed to the fact that there was hardly any snow in the SnowModel-LG dataset compared with the observed snow depth at the MBS. While modelled snow depth attempts to accurately recreate

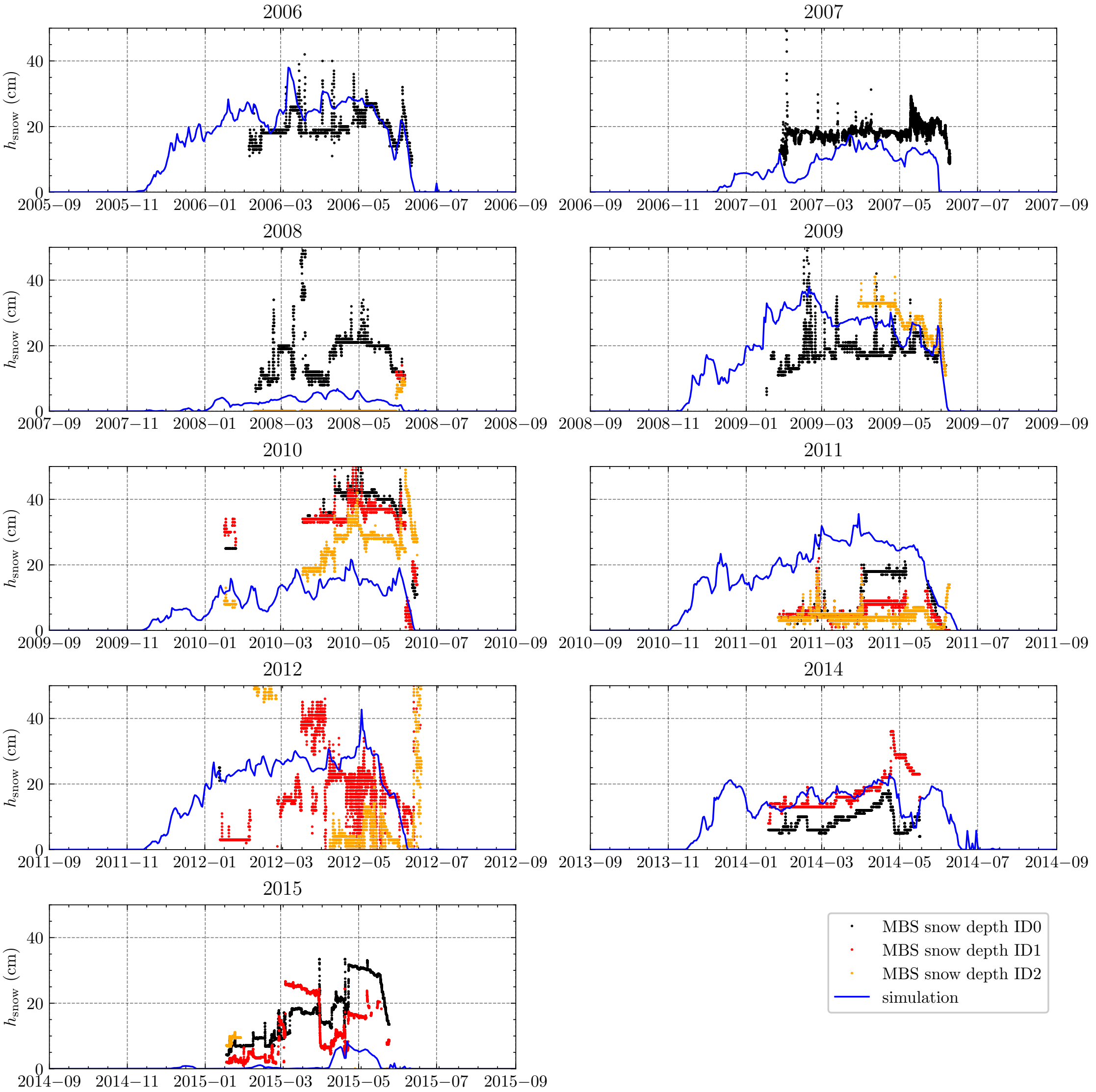

Figure G.1: Snow depth data from the SnowModel-LG dataset (blue line) extracted at the location of the Barrow mass balance site, which is used as forcing data for the simulations in figure G.2. Snow depth measurements from the Barrow mass balance site (coloured circles) from up to three different acoustic instruments deployed at the site (SIZONET; Eicken 2012). There was no data available for 2013.

the average over a model grid cell, it can be difficult to capture the heterogeneity of the snowpack at a single point.

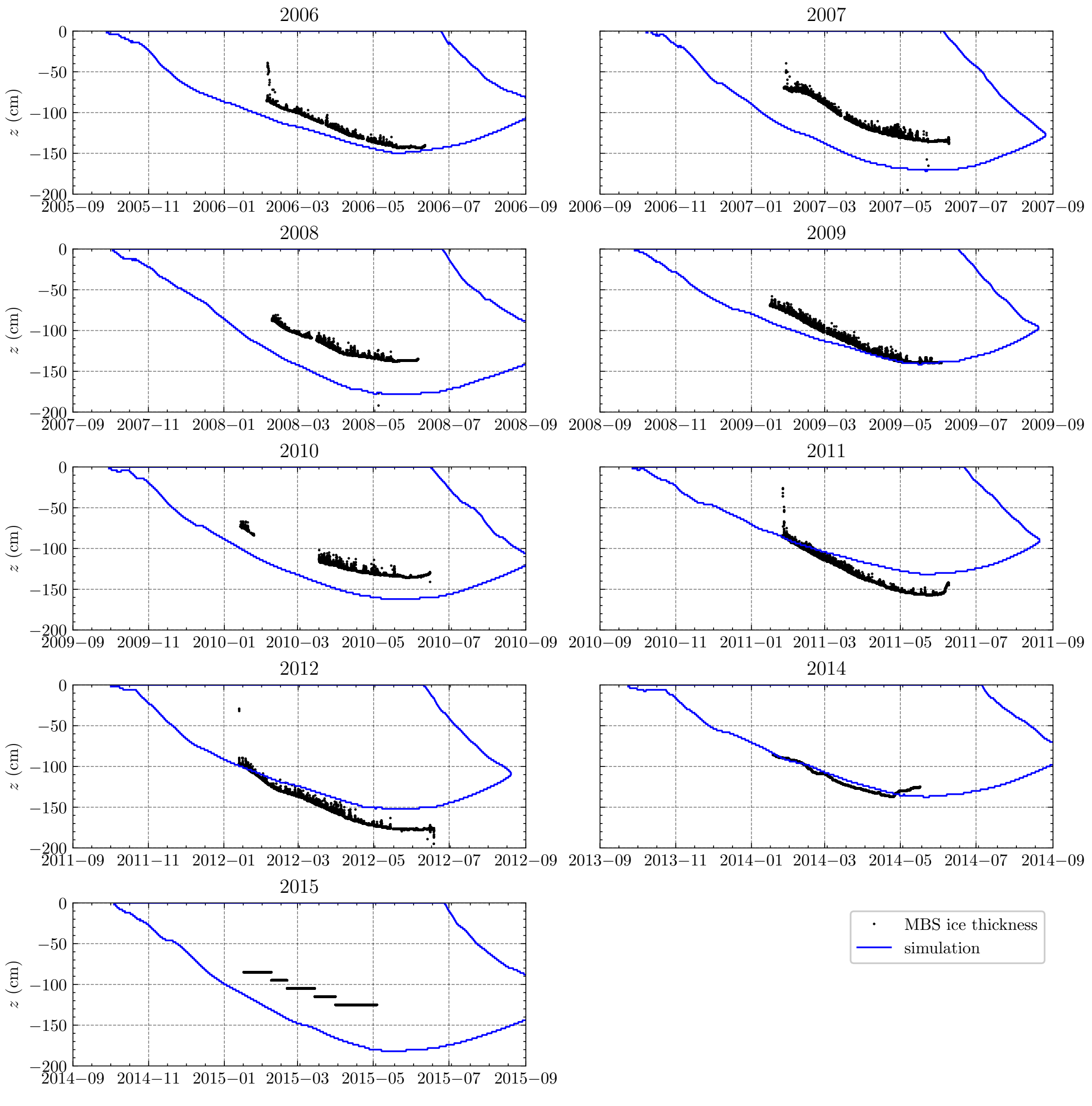

Figure G.2: Simulated ice thickness at Barrow, Alaska in 2006-2015 with $k_{\text{snow}} = 0.25\,\mathrm{W\,m^{-1}\,K^{-1}}$, and the remaining parameters given in table 6.1 (blue curves). Also shown for comparison is ice thickness data from the Barrow mass balance site plotted as black dots (SIZONET; Eicken 2012). There was no data available for 2013. In 2015 the underwater altimeter used to measure ice thickness failed very soon after deployment. Therefore, in 2015, the ice thickness is determined instead using the thermistor string with ±5 cm accuracy. This method cannot be used accurately once the ice base begins to melt.

H

Convergence of transient simulations of sea ice with oil droplets

The simulations of transient sea ice evolution with differing mass fractions of oil droplets in chapter 8 were run using `seaice3p v1.0.0` with a vertical resolution of $N_z = 100$. Computational constraints rendered simulations at much higher resolutions impractical. In this appendix, we show how key metrics from a simulation of the first-year ice at Barrow, Alaska (2008–2009) with are affected by varying the vertical resolution in the range $20 \leq N_z \leq 175$. The remaining parameter values, initialisation and forcing for the simulations are identical to the simulations in §8.4.

Figure H.1 shows that our choice of $N_z = 100$ is sufficient to resolve the ice-ocean and ice-melt-pond interfaces to an accuracy of 2 cm relative to the highest resolution simulation we have run ($N_z = 175$). Figure H.2 shows the variation of six metrics defined in chapter 8 versus N_z. Both the algal bloom onset time and integrated solid fraction have clearly converged by $N_z = 100$. However, the algal bloom onset time in the case of uniform oil concentration with $\mathcal{M}_0 = 1000\,\mathrm{ng\,g^{-1}}$ shows oscillations between two values which can occur if the transmitted PAR flux at the ice base crosses the threshold value several times in a short time period. The

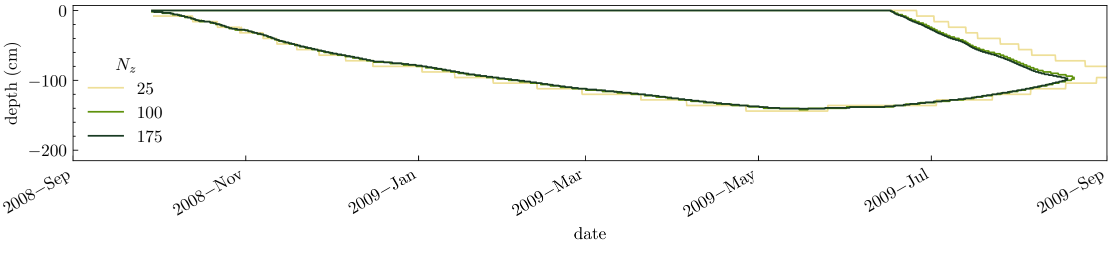

Figure H.1: The position of the ice-ocean and ice-melt-pond interfaces over time for simulations of the first-year ice at Barrow, Alaska (2008–2009) with $\mathcal{M}_0 = 1000\,\mathrm{ng\,g^{-1}}$ at three different vertical resolutions N_z.

maximum ice depth also shows good convergence with oscillations only the size of one grid cell as N_z increases. The remaining three metrics shown in figure H.2 for the melt pond onset time, depth after 10 days and 30 cm growth time show less convincing convergence at these grid resolutions. This likely indicates the need for higher grid resolution for convergence of the turbulent heat transport by the eddy diffusion parameterisation used in the melt pond. However, at the resolution used in this thesis ($N_z = 100$), the error in these metrics is likely less than around one day for the melt pond onset time and 30 cm growth time, and less than around 5 cm for the melt pond depth after 10 days.

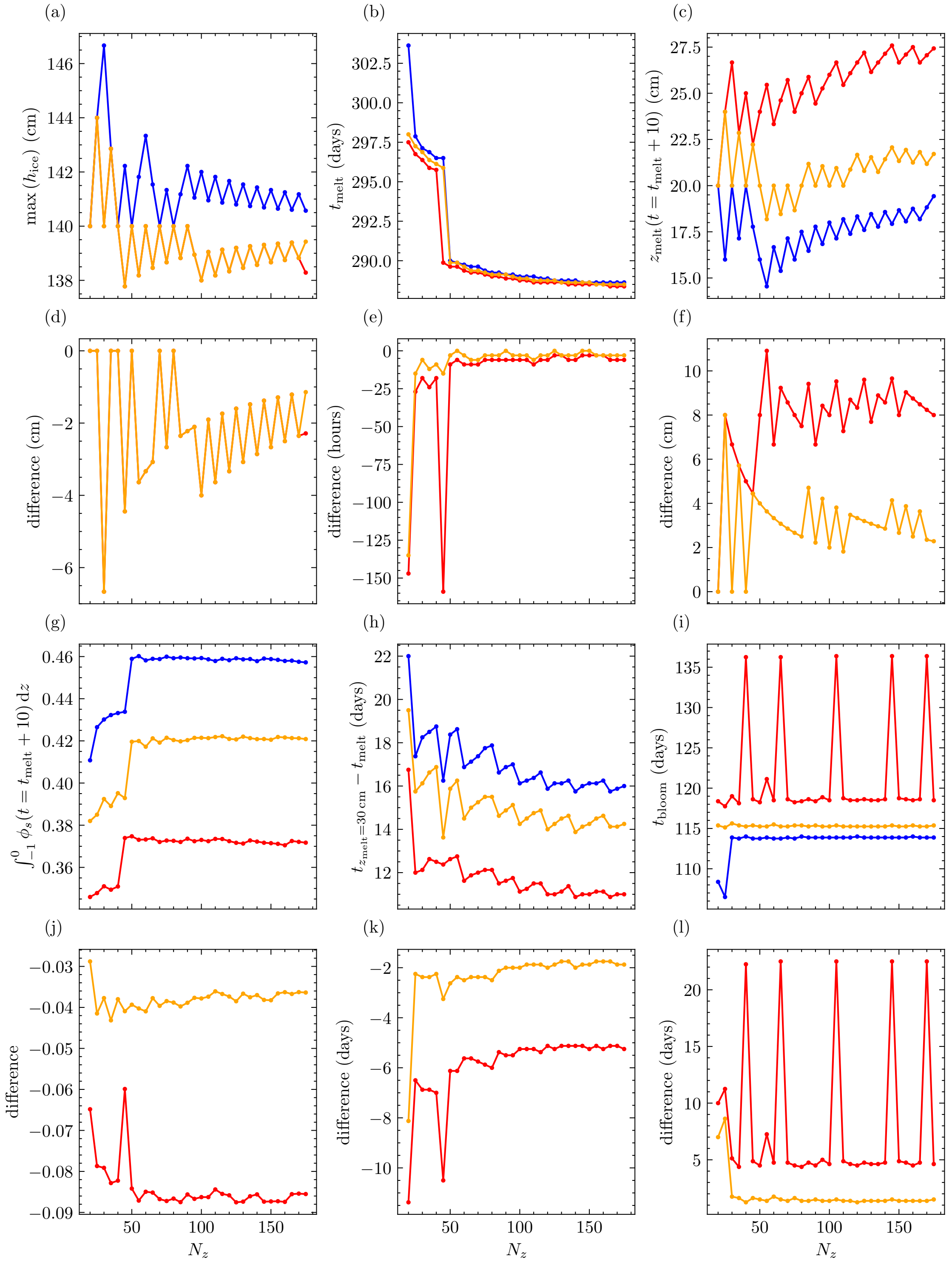

Figure H.2: Plots showing the variation of six metrics from a simulation of the first-year ice at Barrow, Alaska (2008–2009) versus N_z. (a) the maximum ice depth, (b) melt pond onset time, (c) melt pond depth 10 days after onset, (g) integrated solid fraction 10 days after the onset of a melt pond, (h) time taken for a melt pond to first reach a depth of 30 cm, and (i) the algal bloom onset time. Three different simulation configurations are considered: oil-free $\mathcal{M}_0 = 0\,\mathrm{ng\,g^{-1}}$ (blue), uniform oil concentration $\mathcal{M}_0 = 1000\,\mathrm{ng\,g^{-1}}$ (red), and mobile oil droplets with $\mathcal{M}_0 = 1000\,\mathrm{ng\,g^{-1}}$ (orange). Panels (d), (e), (f), (j), (k), and (l) show the difference between each metric in the panel above, between the uniform concentration and oil-free simulation (red) and the mobile droplet and oil-free simulation (orange).

Bibliography

Aagaard, K., L. Coachman, and E. Carmack (1981). “On the Halocline of the Arctic Ocean”. In: *Deep Sea Research Part A. Oceanographic Research Papers* 28.6, pp. 529–545. DOI: `10.1016/0198-0149(81)90115-1`.

Abernathey, R. P., I. Cerovecki, P. R. Holland, E. Newsom, M. Mazloff, and L. D. Talley (2016). “Water-Mass Transformation by Sea Ice in the Upper Branch of the Southern Ocean Overturning”. In: *Nature Geoscience* 9.8, pp. 596–601. DOI: `10.1038/ngeo2749`.

Al Quddus, N., W. A. Moussa, and S. Bhattacharjee (2008). “Motion of a Spherical Particle in a Cylindrical Channel Using Arbitrary Lagrangian–Eulerian Method”. In: *Journal of Colloid and Interface Science* 317.2, pp. 620–630. DOI: `10.1016/j.jcis.2007.09.060`.

Albert, M. R. and W. R. Mcgilvary (1992). “Thermal Effects Due to Air Flow and Vapor Transport in Dry Snow”. In: *Journal of Glaciology* 38.129, pp. 273–281. DOI: `10.3189/S0022143000003683`.

Alexandrov, V., S. Sandven, J. Wahlin, and O. M. Johannessen (2010). “The Relation between Sea Ice Thickness and Freeboard in the Arctic”. In: *The Cryosphere* 4.3, pp. 373–380. DOI: `10.5194/tc-4-373-2010`.

Amiri, F. and S. Butler (2024). “Pore-Scale Mushy Layer Modelling”. In: *Journal of Fluid Mechanics* 983, A30. DOI: `10.1017/jfm.2024.150`.

Anderson, D., P. Guba, and A. Wells (2022). “Mushy-Layer Convection”. In: *Physics Today* 75.2, pp. 34–39. DOI: `10.1063/PT.3.4940`.

Anderson, D. M. and P. Guba (2020). “Convective Phenomena in Mushy Layers”. In: *Annual Review of Fluid Mechanics* 52.1, pp. 93–119. DOI: `10.1146/annurev-fluid-010719-060332`.

Andreas, E. L., P. S. Guest, P. O. G. Persson, C. W. Fairall, T. W. Horst, R. E. Moritz, and S. R. Semmer (2002). “Near-surface Water Vapor over Polar Sea Ice Is Always near Ice Saturation”. In: *Journal of Geophysical Research: Oceans* 107.C10. DOI: `10.1029/2000JC000411`.

Andreas, E. L., P. O. G. Persson, A. A. Grachev, R. E. Jordan, T. W. Horst, P. S. Guest, and C. W. Fairall (2010). “Parameterizing Turbulent Exchange over Sea Ice in Winter”. In: *Journal of Hydrometeorology* 11.1, pp. 87–104. DOI: `10.1175/2009JHM1102.1`.

Arrigo, K. R. (2014). “Sea Ice Ecosystems”. In: *Annual Review of Marine Science* 6.1, pp. 439–467. DOI: `10.1146/annurev-marine-010213-135103`.

Arrigo, K. R. (2017). “Sea Ice as a Habitat for Primary Producers”. In: *Sea Ice.* John Wiley & Sons, Ltd. Chap. 14, pp. 352–369. DOI: `10.1002/9781118778371.ch14`.

Arrigo, K. R. et al. (2012). “Massive Phytoplankton Blooms Under Arctic Sea Ice”. In: *Science* 336.6087, pp. 1408–1408. DOI: `10.1126/science.1215065`.

Asihene, E. et al. (2022). “Toward the Detection of Oil Spills in Newly Formed Sea Ice Using C-Band Multipolarization Radar”. In: *IEEE Transactions on Geoscience and Remote Sensing* 60, pp. 1–15. DOI: `10.1109/TGRS.2021.3123908`.

Assur, A. (1960). *Composition of Sea Ice and Its Tensile Strength.* Tech. rep. 44. U.S. Army Snow, Ice, and Permafrost Research Establishment (SIPRE), p. 49.

Backhaus, J. (1997). “Formation and Export of Water Masses Produced in Arctic Shelf Polynyas — Process Studies of Oceanic Convection”. In: *ICES Journal of Marine Science* 54.3, pp. 366–382. DOI: `10.1006/jmsc.1997.0230`.

Bakke, T., J. Klungsøyr, and S. Sanni (2013). “Environmental Impacts of Produced Water and Drilling Waste Discharges from the Norwegian Offshore Petroleum

Industry”. In: *Marine Environmental Research* 92, pp. 154–169. DOI: `10.1016/j.marenvres.2013.09.012`.

Barrie, L. A., J. W. Bottenheim, R. C. Schnell, P. J. Crutzen, and R. A. Rasmussen (1988). “Ozone Destruction and Photochemical Reactions at Polar Sunrise in the Lower Arctic Atmosphere”. In: *Nature* 334.6178, pp. 138–141. DOI: `10.1038/334138a0`.

Beaulne, J., M. Garneau, G. Magnan, and É. Boucher (2021). “Peat Deposits Store More Carbon than Trees in Forested Peatlands of the Boreal Biome”. In: *Scientific Reports* 11.1, p. 2657. DOI: `10.1038/s41598-021-82004-x`.

Ben Othman, H., F. R. Pick, A. Sakka Hlaili, and C. Leboulanger (2023). “Effects of Polycyclic Aromatic Hydrocarbons on Marine and Freshwater Microalgae – A Review”. In: *Journal of Hazardous Materials* 441, p. 129869. DOI: `10.1016/j.jhazmat.2022.129869`.

Berenshtein, I., C. B. Paris, N. Perlin, M. M. Alloy, S. B. Joye, and S. Murawski (2020). “Invisible Oil beyond the *Deepwater Horizon* Satellite Footprint”. In: *Science Advances* 6.7, eaaw8863. DOI: `10.1126/sciadv.aaw8863`.

Blunt, M. J. (2017). *Multiphase Flow in Permeable Media: A Pore-Scale Perspective.* Cambridge: Cambridge University Press. DOI: `10.1017/9781316145098`.

Borhan, A. and J. Pallinti (1995). “Buoyancy-Driven Motion of Viscous Drops through Cylindrical Capillaries at Small Reynolds Numbers”. In: *Industrial & Engineering Chemistry Research* 34.8, pp. 2750–2761. DOI: `10.1021/ie00047a026`.

Bretherton, F. P. (1961). “The Motion of Long Bubbles in Tubes”. In: *Journal of Fluid Mechanics* 10.02, p. 166. DOI: `10.1017/S0022112061000160`.

Briegleb, B. and B. Light (2007). *A Delta-Eddington Mutiple Scattering Parameterization for Solar Radiation in the Sea Ice Component of the Community Climate System Model.* Tech. rep. UCAR/NCAR, 5209 KB. DOI: `10.5065/D6B27S71`.

C3S (2018). *ERA5 Hourly Data on Single Levels from 1940 to Present.* DOI: `10.24381/CDS.ADBB2D47`.

Calleja, H. and T. Pering (2023). “Crystals and Inclined Conduits: Analogue Experiments for Slug-Driven Volcanism”. In: *Volcanica* 6.1, pp. 147–160. DOI: `10.30909/vol.06.01.147160`.

Castellani, G., M. Losch, B. A. Lange, and H. Flores (2017). “Modeling Arctic Sea-ice Algae: Physical Drivers of Spatial Distribution and Algae Phenology”. In: *Journal of Geophysical Research: Oceans* 122.9, pp. 7466–7487. DOI: `10.1002/2017JC012828`.

Chandrasekhar, S. (2016). *Radiative Transfer.* Dover Books on Physics. New York: Dover Publications.

Chen, L., G. Yan, T. Wang, H. Ren, J. Calbó, J. Zhao, and R. McKenzie (2012). “Estimation of Surface Shortwave Radiation Components under All Sky Conditions: Modeling and Sensitivity Analysis”. In: *Remote Sensing of Environment* 123, pp. 457–469. DOI: `10.1016/j.rse.2012.04.006`.

Chernykh, D., N. Shakhova, V. Yusupov, E. Gershelis, B. Morgunov, and I. Semiletov (2023). “First Calibrated Methane Bubble Wintertime Observations in the Siberian Arctic Seas: Selected Results from the Fast Ice”. In: *Geosciences* 13.8, p. 228. DOI: `10.3390/geosciences13080228`.

Chiareli, A. O. P. and M. G. Worster (1995). “Flow Focusing Instability in a Solidifying Mushy Layer”. In: *Journal of Fluid Mechanics* 297, pp. 293–305. DOI: `10.1017/S0022112095003107`.

Clift, R., J. R. Grace, and M. E. Weber (2005). *Bubbles, Drops, and Particles.* Courier Corporation.

Comiso, J. C., W. N. Meier, and R. Gersten (2017). “Variability and Trends in the A Rctic S Ea Ice Cover: Results from Different Techniques”. In: *Journal of Geophysical Research: Oceans* 122.8, pp. 6883–6900. DOI: `10.1002/2017JC012768`.

Cox, G. F. N. and W. F. Weeks (1983). “Equations for Determining the Gas and Brine Volumes in Sea-Ice Samples”. In: *Journal of Glaciology* 29.102, pp. 306–316.

Crabeck, O., B. Delille, D. Thomas, N.-X. Geilfus, S. Rysgaard, and J.-L. Tison (2014a). “CO2 and CH4 in Sea Ice from a Subarctic Fjord under Influence of Riverine Input”. In: *Biogeosciences* 11.23, pp. 6525–6538. DOI: `10.5194/bg-11-6525-2014`.

Crabeck, O., R. J. Galley, L. Mercury, B. Delille, J.-L. Tison, and S. Rysgaard (2019). “Evidence of Freezing Pressure in Sea Ice Discrete Brine Inclusions and Its Impact on Aqueous-Gaseous Equilibrium”. In: *Journal of Geophysical Research: Oceans* 124.3, pp. 1660–1678. DOI: `10.1029/2018JC014597`.

Crabeck, O., B. Delille, S. Rysgaard, D. N. Thomas, N.-X. Geilfus, B. Else, and J.-L. Tison (2014b). “First “in Situ” Determination of Gas Transport Coefficients (DO2, DAr, and DN2) from Bulk Gas Concentration Measurements (O2, N2 , Ar) in Natural Sea Ice”. In: *Journal of Geophysical Research: Oceans* 119.10, pp. 6655–6668. DOI: `10.1002/2014JC009849`.

Crabeck, O., R. Galley, B. Delille, B. Else, N.-X. Geilfus, M. Lemes, M. Des Roches, P. Francus, J.-L. Tison, and S. Rysgaard (2016). “Imaging Air Volume Fraction in Sea Ice Using Non-Destructive X-ray Tomography”. In: *The Cryosphere* 10.3, pp. 1125–1145. DOI: `10.5194/tc-10-1125-2016`.

Custard, K. D., A. R. W. Raso, P. B. Shepson, R. M. Staebler, and K. A. Pratt (2017). “Production and Release of Molecular Bromine and Chlorine from the Arctic Coastal Snowpack”. In: *ACS Earth and Space Chemistry* 1.3, pp. 142–151. DOI: `10.1021/acsearthspacechem.7b00014`.

Dang, C., C. S. Zender, and M. G. Flanner (2019). “Intercomparison and Improvement of Two-Stream Shortwave Radiative Transfer Schemes in Earth System Models for a Unified Treatment of Cryospheric Surfaces”. In: *The Cryosphere* 13.9, pp. 2325–2343. DOI: `10.5194/tc-13-2325-2019`.

De Carolis, G., M. Adamo, and G. Pasquariello (2014). “On the Estimation of Thickness of Marine Oil Slicks From Sun-Glittered, Near-Infrared MERIS and MODIS Imagery: The Lebanon Oil Spill Case Study”. In: *IEEE Transactions on Geoscience and Remote Sensing* 52.1, pp. 559–573. DOI: `10.1109/TGRS.2013.2242476`.

Desmond, D. S., D. Saltymakova, T. D. Neusitzer, N. Firoozy, D. Isleifson, D. G. Barber, and G. A. Stern (2019). “Oil Behavior in Sea Ice: Changes in Chemical Composition and Resultant Effect on Sea Ice Dielectrics”. In: *Marine Pollution Bulletin* 142, pp. 216–233. DOI: `10.1016/j.marpolbul.2019.03.021`.

Desmond, D. S. et al. (2021). “Investigation into the Geometry and Distribution of Oil Inclusions in Sea Ice Using Non-Destructive X-ray Microtomography and Its Implications for Remote Sensing and Mitigation Potential”. In: *Marine Pollution Bulletin* 173, p. 112996. DOI: `10.1016/j.marpolbul.2021.112996`.

Dilliplaine, K., M. Oggier, R. E. Collins, H. Eicken, R. Gradinger, and B. A. Bluhm (2021). “Crude Oil Exposure Reduces Ice Algal Growth in a Sea-Ice Mesocosm Experiment”. In: *Polar Biology* 44.3, pp. 525–537. DOI: `10.1007/s00300-021-02818-3`.

Dormand, J. and P. Prince (1980). “A Family of Embedded Runge-Kutta Formulae”. In: *Journal of Computational and Applied Mathematics* 6.1, pp. 19–26. DOI: `10.1016/0771-050X(80)90013-3`.

Druckenmiller, M. L., H. Eicken, M. A. Johnson, D. J. Pringle, and C. C. Williams (2009). “Toward an Integrated Coastal Sea-Ice Observatory: System Components and a Case Study at Barrow, Alaska”. In: *Cold Regions Science and Technology* 56.2-3, pp. 61–72. DOI: `10.1016/j.coldregions.2008.12.003`.

Ebert, E. E. and J. A. Curry (1993). “An Intermediate One-Dimensional Thermodynamic Sea Ice Model for Investigating Ice-Atmosphere Interactions”. In: *Journal of Geophysical Research: Oceans* 98.C6, pp. 10085–10109. DOI: `10.1029/93JC00656`.

Ehn, J. K., C. J. Mundy, and D. G. Barber (2008). “Bio-optical and Structural Properties Inferred from Irradiance Measurements within the Bottommost Layers in an Arctic Landfast Sea Ice Cover”. In: *Journal of Geophysical Research: Oceans* 113.C3, 2007JC004194. DOI: `10.1029/2007JC004194`.

Eicken, H., C. Bock, R. Wittig, H. Miller, and H.-O. Poertner (2000). “Magnetic Resonance Imaging of Sea-Ice Pore Fluids: Methods and Thermal Evolution of Pore Microstructure”. In: *Cold Regions Science and Technology* 31.3, pp. 207–225. DOI: `10.1016/S0165-232X(00)00016-1`.

Eicken, H. (2012). *Automated Ice Mass Balance Site (SIZONET)*. DOI: `10.5065/D6MW2F2H`.

Eicken, H., H. R. Krouse, D. Kadko, and D. K. Perovich (2002). “Tracer Studies of Pathways and Rates of Meltwater Transport through Arctic Summer Sea Ice”. In: *Journal of Geophysical Research: Oceans* 107.C10. DOI: `10.1029/2000JC000583`.

Eide, L. and S. Martin (1975). “The Formation of Brine Drainage Features in Young Sea Ice”. In: *Journal of Glaciology* 14.70, pp. 137–154. DOI: `10.3189/S0022143000013460`.

Feltham, D. L., N. Untersteiner, J. S. Wettlaufer, and M. G. Worster (2006). “Sea Ice Is a Mushy Layer”. In: *Geophysical Research Letters* 33.14. DOI: `10.1029/2006GL026290`.

Fingas, M. and B. Hollebone (2003). “Review of Behaviour of Oil in Freezing Environments”. In: *Marine Pollution Bulletin* 47.9-12, pp. 333–340. DOI: `10.1016/S0025-326X(03)00210-8`.

Flocco, D., D. L. Feltham, E. Bailey, and D. Schroeder (2015). “The Refreezing of Melt Ponds on A Rctic Sea Ice”. In: *Journal of Geophysical Research: Oceans* 120.2, pp. 647–659. DOI: `10.1002/2014JC010140`.

Fons, S., N. Kurtz, and M. Bagnardi (2023). “A Decade-plus of Antarctic Sea Ice Thickness and Volume Estimates from CryoSat-2 Using a Physical Model and Waveform Fitting”. In: *The Cryosphere* 17.6, pp. 2487–2508. DOI: `10.5194/tc-17-2487-2023`.

Fransso, A., M. Chierici, K. Abrahamsson, M. Andersson, A. Granfors, K. Gårdfeldt, A. Torstensson, and A. Wulff (2015). “Co2-System Development in Young Sea Ice and CO2 Gas Exchange at the Ice/Air Interface Mediated by Brine and Frost Flowers in Kongsfjorden, Spitsbergen”. In: *Annals of Glaciology* 56.69, pp. 245–257. DOI: `10.3189/2015AoG69A563`.

Frantz, C. M., B. Light, S. M. Farley, S. Carpenter, R. Lieblappen, Z. Courville, M. V. Orellana, and K. Junge (2019). “Physical and Optical Characteristics of Heavily Melted “Rotten” Arctic Sea Ice”. In: *The Cryosphere* 13.3, pp. 775–793. DOI: `10.5194/tc-13-775-2019`.

Fukami, H., K. Kojima, and H. Aburakawa (1985). "The Extinction and Absorption of Solar Radiation Within a Snow Cover". In: *Annals of Glaciology* 6, pp. 118–122. DOI: `10.3189/1985AoG6-1-118-122`.

Gautier, D. L. et al. (2009). "Assessment of Undiscovered Oil and Gas in the Arctic". In: *Science* 324.5931, pp. 1175–1179. DOI: `10.1126/science.1169467`.

Girona, T., F. Costa, and G. Schubert (2015). "Degassing during Quiescence as a Trigger of Magma Ascent and Volcanic Eruptions". In: *Scientific Reports* 5.1, p. 18212. DOI: `10.1038/srep18212`.

Gleitz, M., M. R. V.D. Loeff, D. N. Thomas, G. S. Dieckmann, and F. J. Millero (1995). "Comparison of Summer and Winter Inorganic Carbon, Oxygen and Nutrient Concentrations in Antarctic Sea Ice Brine". In: *Marine Chemistry* 51.2, pp. 81–91. DOI: `10.1016/0304-4203(95)00053-T`.

Golden, K. M., S. F. Ackley, and V. I. Lytle (1998). "The Percolation Phase Transition in Sea Ice". In: *Science* 282.5397, pp. 2238–2241. DOI: `10.1126/science.282.5397.2238`.

Gong, Y., X. Zhao, Z. Cai, S. O'Reilly, X. Hao, and D. Zhao (2014). "A Review of Oil, Dispersed Oil and Sediment Interactions in the Aquatic Environment: Influence on the Fate, Transport and Remediation of Oil Spills". In: *Marine Pollution Bulletin* 79.1-2, pp. 16–33. DOI: `10.1016/j.marpolbul.2013.12.024`.

Gradinger, R. (2009). "Sea-Ice Algae: Major Contributors to Primary Production and Algal Biomass in the Chukchi and Beaufort Seas during May/June 2002". In: *Deep Sea Research Part II: Topical Studies in Oceanography* 56.17, pp. 1201–1212. DOI: `10.1016/j.dsr2.2008.10.016`.

Gradinger, R. R. and B. A. Bluhm (2005). *Susceptibility of Sea Ice Biota to Disturbances in the Shallow Beaufort Sea: Phase 1: Biological Coupling of Sea Ice with the Pelagic and Benthic Realms.* Tech. rep. Coastal Marine Institute, School of Fisheries and Ocean Sciences, University of Alaska Fairbanks.

Grenfell, T. C. (1979). "The Effects of Ice Thickness on the Exchange of Solar Radiation Over the Polar Oceans". In: *Journal of Glaciology* 22.87, pp. 305–320. DOI: `10.3189/S0022143000014295`.

Grenfell, T. C. (1983). "A Theoretical Model of the Optical Properties of Sea Ice in the Visible and near Infrared". In: *Journal of Geophysical Research: Oceans* 88.C14, pp. 9723–9735. DOI: `10.1029/JC088iC14p09723`.

Grenfell, T. C. (1991). "A Radiative Transfer Model for Sea Ice with Vertical Structure Variations". In: *Journal of Geophysical Research: Oceans* 96.C9, pp. 16991–17001. DOI: `10.1029/91JC01595`.

Grenfell, T. C. and D. Hedrick (1983). "Scattering of Visible and near Infrared Radiation by NaCl Ice and Glacier Ice". In: *Cold Regions Science and Technology* 8.2, pp. 119–127. DOI: `10.1016/0165-232X(83)90003-4`.

Grenfell, T. C., B. Light, and M. Sturm (2002). "Spatial Distribution and Radiative Effects of Soot in the Snow and Sea Ice during the SHEBA Experiment". In: *Journal of Geophysical Research: Oceans* 107.C10. DOI: `10.1029/2000JC000414`.

Grenfell, T. C. and G. A. Maykut (1977). "The Optical Properties of Ice and Snow in the Arctic Basin". In: *Journal of Glaciology* 18.80, pp. 445–463. DOI: `10.3189/S0022143000021122`.

Grenfell, T. C. and D. K. Perovich (1984). "Spectral Albedos of Sea Ice and Incident Solar Irradiance in the Southern Beaufort Sea". In: *Journal of Geophysical Research: Oceans* 89.C3, pp. 3573–3580. DOI: `10.1029/JC089iC03p03573`.

Grenfell, T. C. and D. K. Perovich (2004). “Seasonal and Spatial Evolution of Albedo in a Snow-ice-land-ocean Environment”. In: *Journal of Geophysical Research: Oceans* 109.C1, 2003JC001866. DOI: `10.1029/2003JC001866`.

Grenfell, T. C. and D. K. Perovich (2008). “Incident Spectral Irradiance in the Arctic Basin during the Summer and Fall”. In: *Journal of Geophysical Research: Atmospheres* 113.D12, 2007JD009418. DOI: `10.1029/2007JD009418`.

Griewank, P. J. and D. Notz (2013). “Insights into Brine Dynamics and Sea Ice Desalination from a 1-D Model Study of Gravity Drainage: Gravity Drainage”. In: *Journal of Geophysical Research: Oceans* 118.7, pp. 3370–3386. DOI: `10.1002/jgrc.20247`.

Haas, C. (2017). “Sea Ice Thickness Distribution”. In: *Sea Ice*. Ed. by D. N. Thomas. 1st ed. Wiley, pp. 42–64. DOI: `10.1002/9781118778371.ch2`.

Haberman, W. L. and R. M. Sayre (1958). *Motion of Rigid and Fluid Spheres in Stationary and Moving Liquids inside Cylindrical Tubes.* Tech. rep. 1143. U.S. Navy Dept.

Hamme, R. C. and S. R. Emerson (2004). “The Solubility of Neon, Nitrogen and Argon in Distilled Water and Seawater”. In: *Deep Sea Research Part I: Oceanographic Research Papers* 51.11, pp. 1517–1528. DOI: `10.1016/j.dsr.2004.06.009`.

Harris, C. R. et al. (2020). “Array Programming with NumPy”. In: *Nature* 585.7825, pp. 357–362. DOI: `10.1038/s41586-020-2649-2`.

Hartholt, G. P., A. C. Hoffmann, L. P. B. M. Janssen, H. W. Hoogstraten, and J. H. Moes (1994). “Finite Element Calculations of Flow Past a Spherical Bubble Rising on the Axis of a Cylindrical Tube”. In: *ZAMP Zeitschrift fur angewandte Mathematik und Physik* 45.5, pp. 733–745. DOI: `10.1007/BF00942750`.

Haule, K. and W. Freda (2016). “The Effect of Dispersed Petrobaltic Oil Droplet Size on Photosynthetically Active Radiation in Marine Environment”. In: *Environmental Science and Pollution Research* 23.7, pp. 6506–6516. DOI: `10.1007/s11356-015-5886-4`.

He, X., L. Sun, Z. Xie, W. Huang, N. Long, Z. Li, and G. Xing (2013). “Sea Ice in the Arctic Ocean: Role of Shielding and Consumption of Methane”. In: *Atmospheric Environment* 67, pp. 8–13. DOI: `10.1016/j.atmosenv.2012.10.029`.

Henyey, L. G. and J. L. Greenstein (1941). “Diffuse Radiation in the Galaxy.” In: *The Astrophysical Journal* 93, pp. 70–83. DOI: `10.1086/144246`.

Herman, G. F. (1986). “Arctic Stratus Clouds”. In: *The Geophysics of Sea Ice*. Ed. by N. Untersteiner. Boston, MA: Springer US, pp. 465–488. DOI: `10.1007/978-1-4899-5352-0_7`.

Higdon, J. J. L. and G. P. Muldowney (1995). “Resistance Functions for Spherical Particles, Droplets and Bubbles in Cylindrical Tubes”. In: *Journal of Fluid Mechanics* 298, pp. 193–210. DOI: `10.1017/S0022112095003272`.

Hitchen, J. (2017). “Understanding the Growth and Convective Instability of Mushy Layers, with Application to Young Sea Ice”. http://purl.org/dc/dcmitype/Text. University of Oxford.

Hitchen, J. R. and A. J. Wells (2025). “Structure of Mushy Layers Grown from Perfectly and Imperfectly Conducting Boundaries. Part 1. Diffusive Solidification”. In: *Journal of Fluid Mechanics* 1002, A25. DOI: `10.1017/jfm.2024.808`.

Hobbs, P. V. (1974). *Ice Physics.* Oxford: Clarendon Press.

Holland, M. M. and C. M. Bitz (2003). “Polar Amplification of Climate Change in Coupled Models”. In: *Climate Dynamics* 21.3-4, pp. 221–232. DOI: `10.1007/s00382-003-0332-6`.

Holland, M. M., C. M. Bitz, and B. Tremblay (2006). “Future Abrupt Reductions in the Summer Arctic Sea Ice”. In: *Geophysical Research Letters* 33.23, 2006GL028024. DOI: `10.1029/2006GL028024`.

Honda, M. and N. Suzuki (2020). “Toxicities of Polycyclic Aromatic Hydrocarbons for Aquatic Animals”. In: *International Journal of Environmental Research and Public Health* 17.4, p. 1363. DOI: `10.3390/ijerph17041363`.

Hoyer, S. and J. Hamman (2017). “Xarray: N-D Labeled Arrays and Datasets in Python”. In: *Journal of Open Research Software* 5.1, p. 10. DOI: `10.5334/jors.148`.

Hudson, S. R. (2011). “Estimating the Global Radiative Impact of the Sea Ice–Albedo Feedback in the Arctic”. In: *Journal of Geophysical Research* 116.D16, p. D16102. DOI: `10.1029/2011JD015804`.

Hunke, E. C., D. Notz, A. K. Turner, and M. Vancoppenolle (2011). “The Multiphase Physics of Sea Ice: A Review for Model Developers”. In: *The Cryosphere* 5.4, pp. 989–1009. DOI: `10.5194/tc-5-989-2011`.

Huntington, H. P. and S. E. Moore (2008). “Assessing the Impacts of Climate Change on Arctic Marine Mammals”. In: *Ecological Applications* 18.sp2, S1–S2. DOI: `10.1890/06-0282.1`.

Huppert, H. E. and M. G. Worster (2012). “Flows Involving Phase Change”. In: *Handbook of Environmental Fluid Dynamics*. Ed. by H. J. S. Fernando. Boca Raton, FL: CRC Press, Taylor & Francis Group.

Huppert, H. E. and A. W. Woods (2002). “The Role of Volatiles in Magma Chamber Dynamics”. In: *Nature* 420.6915, pp. 493–495. DOI: `10.1038/nature01211`.

Huppert, H. E. and M. G. Worster (1985). “Dynamic Solidification of a Binary Melt”. In: *Nature* 314.6013, pp. 703–707. DOI: `10.1038/314703a0`.

Jeffery, N., E. C. Hunke, and S. M. Elliott (2011). “Modeling the Transport of Passive Tracers in Sea Ice”. In: *Journal of Geophysical Research: Oceans* 116.C7, 2010JC006527. DOI: `10.1029/2010JC006527`.

Jeffries, M. O., R. A. Shaw, K. Morris, A. L. Veazey, and H. R. Krouse (1994). “Crystal Structure, Stable Isotopes (Δ^{18} O), and Development of Sea Ice in the Ross, Amundsen, and Bellingshausen Seas, Antarctica”. In: *Journal of Geophysical Research: Oceans* 99.C1, pp. 985–995. DOI: `10.1029/93JC02057`.

Johannessen, O. M. and M. W. Miles (2011). “Critical Vulnerabilities of Marine and Sea Ice–Based Ecosystems in the High Arctic”. In: *Regional Environmental Change* 11.S1, pp. 239–248. DOI: `10.1007/s10113-010-0186-5`.

Johansen, Ø., M. Reed, and N. R. Bodsberg (2015). “Natural Dispersion Revisited”. In: *Marine Pollution Bulletin* 93.1, pp. 20–26. DOI: `10.1016/j.marpolbul.2015.02.026`.

Jones, A. E., P. S. Anderson, E. W. Wolff, J. Turner, A. M. Rankin, and S. R. Colwell (2006). “A Role for Newly Forming Sea Ice in Springtime Polar Tropospheric Ozone Loss? Observational Evidence from Halley Station, Antarctica”. In: *Journal of Geophysical Research: Atmospheres* 111.D8. DOI: `10.1029/2005JD006566`.

Jones, N. D., A. Moure, and X. Fu (2024). “Pattern Formation of Freezing Infiltration in Porous Media”. In: *Physical Review Fluids* 9.12, p. 123802. DOI: `10.1103/PhysRevFluids.9.123802`.

Joseph, J. H., W. J. Wiscombe, and J. A. Weinman (1976). “The Delta-Eddington Approximation for Radiative Flux Transfer”. In: *Journal of the Atmospheric Sciences* 33.12, pp. 2452–2459. DOI: `10.1175/1520-0469(1976)033<2452:TDEAFR>2.0.CO;2`.

Jutila, A., S. Hendricks, R. Ricker, L. Von Albedyll, T. Krumpen, and C. Haas (2022). “Retrieval and Parameterisation of Sea-Ice Bulk Density from Airborne Multi-Sensor Measurements”. In: *The Cryosphere* 16.1, pp. 259–275. DOI: `10.5194/tc-16-259-2022`.

Kaartokallio, H. (2004). “Food Web Components, and Physical and Chemical Properties of Baltic Sea Ice”. In: *Marine Ecology Progress Series* 273, pp. 49–63. DOI: `10.3354/meps273049`.

Kaartokallio, H. (2001). “Evidence for Active Microbial Nitrogen Transformations in Sea Ice (Gulf of Bothnia, Baltic Sea) in Midwinter”. In: *Polar Biology* 24.1, pp. 21–28. DOI: `10.1007/s003000000169`.

Kaleschke, L. et al. (2004). “Frost Flowers on Sea Ice as a Source of Sea Salt and Their Influence on Tropospheric Halogen Chemistry”. In: *Geophysical Research Letters* 31.16, 2004GL020655. DOI: `10.1029/2004GL020655`.

Katz, R. F. and M. G. Worster (2008). “Simulation of Directional Solidification, Thermochemical Convection, and Chimney Formation in a Hele-Shaw Cell”. In: *Journal of Computational Physics* 227.23, pp. 9823–9840. DOI: `10.1016/j.jcp.2008.06.039`.

Keller, T. and J. Suckale (2019). “A Continuum Model of Multi-Phase Reactive Transport in Igneous Systems”. In: *Geophysical Journal International* 219.1, pp. 185–222. DOI: `10.1093/gji/ggz287`.

Khozanah, D. Yogaswara, and I. Wulandari (2021). “Oil and Grease (OG) Content in Seawater and Sediment of The Jakarta Bay and Its Surrounding”. In: *IOP Conference Series: Earth and Environmental Science* 789.1, p. 012015. DOI: `10.1088/1755-1315/789/1/012015`.

Kierzenka, J. and L. F. Shampine (2001). “A BVP Solver Based on Residual Control and the Maltab PSE”. In: *ACM Transactions on Mathematical Software* 27.3, pp. 299–316. DOI: `10.1145/502800.502801`.

Kikkas, K. and E. Romashkina (2018). “Potential Opportunities for the Arctic Transport Space”. In: *IOP Conference Series: Earth and Environmental Science* 180, p. 012016. DOI: `10.1088/1755-1315/180/1/012016`.

Kim, J.-H., W. Moon, A. J. Wells, J. P. Wilkinson, T. Langton, B. Hwang, M. A. Granskog, and D. W. Rees Jones (2018). “Salinity Control of Thermal Evolution of Late Summer Melt Ponds on Arctic Sea Ice”. In: *Geophysical Research Letters* 45.16, pp. 8304–8313. DOI: `10.1029/2018GL078077`.

Kort, E. A. et al. (2012). “Atmospheric Observations of Arctic Ocean Methane Emissions up to 82° North”. In: *Nature Geoscience* 5.5, pp. 318–321. DOI: `10.1038/ngeo1452`.

Kotovitch, M., S. Moreau, J. Zhou, M. Vancoppenolle, G. S. Dieckmann, K.-U. Evers, F. Van der Linden, D. N. Thomas, J.-L. Tison, and B. Delille (2016). “Air-Ice Carbon Pathways Inferred from a Sea Ice Tank Experiment”. In: *Elementa: Science of the Anthropocene* 4. Ed. by J. W. Deming and S. F. Ackley, p. 000112. DOI: `10.12952/journal.elementa.000112`.

Krishfield, R. A. and D. K. Perovich (2005). “Spatial and Temporal Variability of Oceanic Heat Flux to the Arctic Ice Pack”. In: *Journal of Geophysical Research: Oceans* 110.C7, 2004JC002293. DOI: `10.1029/2004JC002293`.

Kwok, R. (2010). “Satellite Remote Sensing of Sea-Ice Thickness and Kinematics: A Review”. In: *Journal of Glaciology* 56.200, pp. 1129–1140. DOI: `10.3189/002214311796406167`.

Kwok, R., G. Spreen, and S. Pang (2013). “Arctic Sea Ice Circulation and Drift Speed: Decadal Trends and Ocean Currents”. In: *Journal of Geophysical Research: Oceans* 118.5, pp. 2408–2425. DOI: `10.1002/jgrc.20191`.

Lacis, A. A., D. J. Wuebbles, and J. A. Logan (1990). “Radiative Forcing of Climate by Changes in the Vertical Distribution of Ozone”. In: *Journal of Geophysical Research: Atmospheres* 95.D7, pp. 9971–9981. DOI: `10.1029/JD095iD07p09971`.

Laidler, G. J., J. D. Ford, W. A. Gough, T. Ikummaq, A. S. Gagnon, S. Kowal, K. Qrunnut, and C. Irngaut (2009). “Travelling and Hunting in a Changing Arctic: Assessing Inuit Vulnerability to Sea Ice Change in Igloolik, Nunavut”. In: *Climatic Change* 94.3-4, pp. 363–397. DOI: `10.1007/s10584-008-9512-z`.

Lamare, M. L., J. Lee-Taylor, and M. D. King (2016). “The Impact of Atmospheric Mineral Aerosol Deposition on the Albedo of Snow & Sea Ice: Are Snow and Sea Ice Optical Properties More Important than Mineral Aerosol Optical Properties?” In: *Atmospheric Chemistry and Physics* 16.2, pp. 843–860. DOI: `10.5194/acp-16-843-2016`.

Lannuzel, D. et al. (2020). “The Future of Arctic Sea-Ice Biogeochemistry and Ice-Associated Ecosystems”. In: *Nature Climate Change* 10.11, pp. 983–992. DOI: `10.1038/s41558-020-00940-4`.

Lavoie, D., K. Denman, and C. Michel (2005). “Modeling Ice Algal Growth and Decline in a Seasonally Ice-covered Region of the Arctic (Resolute Passage, Canadian Archipelago)”. In: *Journal of Geophysical Research: Oceans* 110.C11, 2005JC002922. DOI: `10.1029/2005JC002922`.

Le Bars, M. and M. G. Worster (2006). “Interfacial Conditions between a Pure Fluid and a Porous Medium: Implications for Binary Alloy Solidification”. In: *Journal of Fluid Mechanics* 550.-1, p. 149. DOI: `10.1017/s0022112005007998`.

Lebrun, M., M. Vancoppenolle, G. Madec, M. Babin, G. Becu, A. Lourenço, D. Nomura, F. Vivier, and B. Delille (2023). “Light Under Arctic Sea Ice in Observations and Earth System Models”. In: *Journal of Geophysical Research: Oceans* 128.3, e2021JC018161. DOI: `10.1029/2021JC018161`.

Lecomte, O., T. Fichefet, M. Vancoppenolle, F. Domine, F. Massonnet, P. Mathiot, S. Morin, and P. Barriat (2013). “On the Formulation of Snow Thermal Conductivity in Large-Scale Sea Ice Models”. In: *Journal of Advances in Modeling Earth Systems* 5.3, pp. 542–557. DOI: `10.1002/jame.20039`.

Lee, S. H., T. E. Whitledge, and S.-H. Kang (2008). “Spring Time Production of Bottom Ice Algae in the Landfast Sea Ice Zone at Barrow, Alaska”. In: *Journal of Experimental Marine Biology and Ecology* 367.2, pp. 204–212. DOI: `10.1016/j.jembe.2008.09.018`.

Lee-Taylor, J. and S. Madronich (2002). “Calculation of Actinic Fluxes with a Coupled Atmosphere–Snow Radiative Transfer Model”. In: *Journal of Geophysical Research: Atmospheres* 107.D24. DOI: `10.1029/2002JD002084`.

Leppäranta, M. (1993). “A Review of Analytical Models of Sea-ice Growth”. In: *Atmosphere-Ocean* 31.1, pp. 123–138. DOI: `10.1080/07055900.1993.9649465`.

Leu, E., C. Mundy, P. Assmy, K. Campbell, T. Gabrielsen, M. Gosselin, T. Juul-Pedersen, and R. Gradinger (2015). “Arctic Spring Awakening – Steering

Principles behind the Phenology of Vernal Ice Algal Blooms". In: *Progress in Oceanography* 139, pp. 151–170. DOI: `10.1016/j.pocean.2015.07.012`.

LeVeque, R. J. (2002). *Finite Volume Methods for Hyperbolic Problems.* Cambridge Texts in Applied Mathematics. Cambridge: Cambridge University Press. DOI: `10.1017/CBO9780511791253`.

Li, Z., M. Spaulding, D. French McCay, D. Crowley, and J. R. Payne (2017). "Development of a Unified Oil Droplet Size Distribution Model with Application to Surface Breaking Waves and Subsea Blowout Releases Considering Dispersant Effects". In: *Marine Pollution Bulletin* 114.1, pp. 247–257. DOI: `10.1016/j.marpolbul.2016.09.008`.

Liao, Y. (2022). "The Roles of Heat and Gas in a Mushy Magma Chamber". In: *Journal of Geophysical Research: Solid Earth* 127.7, e2022JB024357. DOI: `10.1029/2022JB024357`.

Light, B., G. A. Maykut, and T. C. Grenfell (2003). "Effects of Temperature on the Microstructure of First-Year Arctic Sea Ice". In: *Journal of Geophysical Research: Oceans* 108.C2. DOI: `10.1029/2001JC000887`.

Light, B., G. A. Maykut, and T. C. Grenfell (2004). "A Temperature-dependent, Structural-optical Model of First-year Sea Ice". In: *Journal of Geophysical Research: Oceans* 109.C6, 2003JC002164. DOI: `10.1029/2003JC002164`.

Light, B., T. C. Grenfell, and D. K. Perovich (2008). "Transmission and Absorption of Solar Radiation by Arctic Sea Ice during the Melt Season". In: *Journal of Geophysical Research: Oceans* 113.C3. DOI: `10.1029/2006JC003977`.

Light, B. et al. (2022). "Arctic Sea Ice Albedo: Spectral Composition, Spatial Heterogeneity, and Temporal Evolution Observed during the MOSAiC Drift". In: *Elementa: Science of the Anthropocene* 10.1, p. 000103. DOI: `10.1525/elementa.2021.000103`.

Liston, G., J. Stroeve, and P. Itkin (2021). *Lagrangian Snow Distributions for Sea-Ice Applications, Version 1.* DOI: `10.5067/27A0P5M6LZBI`.

Liu, Y., J. Zeng, S. Liu, and H. Long (2023). "Physical Properties Variation of Crude Oil under Natural Laboratory and Its Geological Implications: Dongying Sag, Eastern China". In: *Frontiers in Earth Science* 11, p. 1169318. DOI: `10.3389/feart.2023.1169318`.

Loose, B. and P. Schlosser (2011). "Sea Ice and Its Effect on CO_2 Flux between the Atmosphere and the Southern Ocean Interior". In: *Journal of Geophysical Research: Oceans* 116.C11, 2010JC006509. DOI: `10.1029/2010JC006509`.

Lu, J. W. and F. Chen (1994). "Instability-Mode Competition Due to Change of Partition Coefficient of Binary Alloy Unidirectionally Solidified from Below". In: *Journal of Crystal Growth* 140.1-2, pp. 182–190. DOI: `10.1016/0022-0248(94)90512-6`.

Lu, L., Z. Liu, H. Liu, and Y. Yan (2013). "Study on Technical Measures of Romashkino Oil Field after Entering Ultra-High Water Cut Stage". In: *Engineering* 05.07, pp. 622–628. DOI: `10.4236/eng.2013.57074`.

Macfarlane, A. R., H. Löwe, L. Gimenes, D. N. Wagner, R. Dadic, R. Ottersberg, S. Hämmerle, and M. Schneebeli (2023). "Temporospatial Variability of Snow's Thermal Conductivity on Arctic Sea Ice". In: *The Cryosphere* 17.12, pp. 5417–5434. DOI: `10.5194/tc-17-5417-2023`.

Madec, G. et al. (2024). *NEMO Ocean Engine Reference Manual.* Version v5.0. DOI: `10.5281/zenodo.14515373`.

Mahabadi, N., X. Zheng, T. S. Yun, L. Paassen, and J. Jang (2018). “Gas Bubble Migration and Trapping in Porous Media: Pore-scale Simulation”. In: *Journal of Geophysical Research. Solid earth* 123.2, pp. 1060–1071. DOI: `10.1002/2017JB015331`.

Mahmoud, M. R., M. Roushdi, and M. Aboelkhear (2024). “Potential Benefits of Climate Change on Navigation in the Northern Sea Route by 2050”. In: *Scientific Reports* 14.1, p. 2771. DOI: `10.1038/s41598-024-53308-5`.

Mahoney, A., H. Eicken, and L. Shapiro (2007). “How Fast Is Landfast Sea Ice? A Study of the Attachment and Detachment of Nearshore Ice at Barrow, Alaska”. In: *Cold Regions Science and Technology* 47.3, pp. 233–255. DOI: `10.1016/j.coldregions.2006.09.005`.

Mallett, R. D. C. et al. (2022). “Sub-Kilometre Scale Distribution of Snow Depth on Arctic Sea Ice from Soviet Drifting Stations”. In: *Journal of Glaciology*, pp. 1–13. DOI: `10.1017/jog.2022.18`.

Malmgren, F. (1927). *On the Properties of Sea-Ice.* (Repr. from: The Norwegian North Polar Expedition with the "Maud" 1918-1925, Scientific Results). Grieg.

Malone, T. F. (1951). *Compendium of Meteorology.* Boston: American Meteorological Society.

Marion, G. M., M. V. Mironenko, and M. W. Roberts (2010). “FREZCHEM: A Geochemical Model for Cold Aqueous Solutions”. In: *Computers & Geosciences* 36.1, pp. 10–15. DOI: `10.1016/j.cageo.2009.06.004`.

Marks, A. A. and M. D. King (2013a). “The Effects of Additional Black Carbon on the Albedo of Arctic Sea Ice: Variation with Sea Ice Type and Snow Cover”. In: *The Cryosphere* 7.4, pp. 1193–1204. DOI: `10.5194/tc-7-1193-2013`.

Marks, A. A. and M. D. King (2013b). “The Effects of Additional Black Carbon on the Albedo of Arctic Sea Ice: Variation with Sea Ice Type and Snow Cover”. In: *The Cryosphere* 7.4, pp. 1193–1204. DOI: `10.5194/tc-7-1193-2013`.

Martin, S. (1979). “A Field Study of Brine Drainage and Oil Entrainment in First-Year Sea Ice”. In: *Journal of Glaciology* 22.88, pp. 473–502. DOI: `10.3189/S0022143000014477`.

Maslanik, J., J. Stroeve, C. Fowler, and W. Emery (2011). “Distribution and Trends in Arctic Sea Ice Age through Spring 2011”. In: *Geophysical Research Letters* 38.13, p. L13502. DOI: `10.1029/2011GL047735`.

Maus, S., M. Schneebeli, and A. Wiegmann (2021). “An X-ray Micro-Tomographic Study of the Pore Space, Permeability and Percolation Threshold of Young Sea Ice”. In: *Cryosphere* 15.8, pp. 4047–4072. DOI: `10.5194/tc-15-4047-2021`.

May, R. M., K. H. Goebbert, J. E. Thielen, J. R. Leeman, M. D. Camron, Z. Bruick, E. C. Bruning, R. P. Manser, S. C. Arms, and P. T. Marsh (2022). “MetPy: A Meteorological Python Library for Data Analysis and Visualization”. In: *Bulletin of the American Meteorological Society* 103.10, E2273–E2284. DOI: `10.1175/BAMS-D-21-0125.1`.

Maykut, G. A. and M. G. McPhee (1995). “Solar Heating of the Arctic Mixed Layer”. In: *Journal of Geophysical Research: Oceans* 100.C12, pp. 24691–24703. DOI: `10.1029/95JC02554`.

Maykut, G. A. and N. Untersteiner (1971). “Some Results from a Time-Dependent Thermodynamic Model of Sea Ice”. In: *Journal of Geophysical Research* 76.6, pp. 1550–1575. DOI: `10.1029/JC076i006p01550`.

McPhee, M. G. (1992). “Turbulent Heat Flux in the Upper Ocean under Sea Ice”. In: *Journal of Geophysical Research: Oceans* 97.C4, pp. 5365–5379. DOI: `10.1029/92JC00239`.

Meyer, C. R. and I. J. Hewitt (2017). “A Continuum Model for Meltwater Flow through Compacting Snow”. In: *The Cryosphere* 11.6, pp. 2799–2813. DOI: `10.5194/tc-11-2799-2017`.

Miller, L. A., T. N. Papakyriakou, R. E. Collins, J. W. Deming, J. K. Ehn, R. W. Macdonald, A. Mucci, O. Owens, M. Raudsepp, and N. Sutherland (2011). “Carbon Dynamics in Sea Ice: A Winter Flux Time Series”. In: *Journal of Geophysical Research: Oceans* 116.C2. DOI: `10.1029/2009JC006058`.

Millero, F. J., R. Feistel, D. G. Wright, and T. J. McDougall (2008). “The Composition of Standard Seawater and the Definition of the Reference-Composition Salinity Scale”. In: *Deep Sea Research Part I: Oceanographic Research Papers* 55.1, pp. 50–72. DOI: `10.1016/j.dsr.2007.10.001`.

Moreau, S., H. Kaartokallio, M. Vancoppenolle, J. Zhou, M. Kotovitch, G. S. Dieckmann, D. Thomas, J.-L. Tison, and B. Delille (2015a). “Assessing the O2 Budget under Sea Ice: An Experimental and Modelling Approach”. In: *Elementa: Science of the Anthropocene* 3. Ed. by J. W. Deming and L. A. Miller, p. 000080. DOI: `10.12952/journal.elementa.000080`.

Moreau, S., M. Vancoppenolle, B. Delille, J.-L. Tison, J. Zhou, M. Kotovitch, D. Thomas, N.-X. Geilfus, and H. Goosse (2015b). “Drivers of Inorganic Carbon Dynamics in First-Year Sea Ice: A Model Study”. In: *Journal of Geophysical Research: Oceans* 120.1, pp. 471–495. DOI: `10.1002/2014JC010388`.

Moreau, S., M. Vancoppenolle, J. Zhou, J.-L. Tison, B. Delille, and H. Goosse (2014). “Modelling Argon Dynamics in First-Year Sea Ice”. In: *Ocean Modelling* 73, pp. 1–18. DOI: `10.1016/j.ocemod.2013.10.004`.

Morel, A. and R. C. Smith (1974). “Relation between Total Quanta and Total Energy for Aquatic Photosynthesis”. In: *Limnology and Oceanography* 19.4, pp. 591–600. DOI: `10.4319/lo.1974.19.4.0591`.

Müller, M., M. Knol-Kauffman, J. Jeuring, and C. Palerme (2023). “Arctic Shipping Trends during Hazardous Weather and Sea-Ice Conditions and the Polar Code’s Effectiveness”. In: *npj Ocean Sustainability* 2.1, p. 12. DOI: `10.1038/s44183-023-00021-x`.

Mullins, W. W. and R. F. Sekerka (1964). “Stability of a Planar Interface During Solidification of a Dilute Binary Alloy”. In: *Journal of Applied Physics* 35.2, pp. 444–451. DOI: `10.1063/1.1713333`.

Mundy, C. J. et al. (2009). “Contribution of Under-ice Primary Production to an Ice-edge Upwelling Phytoplankton Bloom in the Canadian Beaufort Sea”. In: *Geophysical Research Letters* 36.17, 2009GL038837. DOI: `10.1029/2009GL038837`.

Mundy, C., M. Gosselin, Y. Gratton, K. Brown, V. Galindo, K. Campbell, M. Levasseur, D. Barber, T. Papakyriakou, and S. Bélanger (2014). “Role of Environmental Factors on Phytoplankton Bloom Initiation under Landfast Sea Ice in Resolute Passage, Canada”. In: *Marine Ecology Progress Series* 497, pp. 39–49. DOI: `10.3354/meps10587`.

Nakayama, N., S. Watanabe, and S. Tsunogai (2002). “Nitrogen, Oxygen and Argon Dissolved in the Northern North Pacific in Early Summer”. In: *Journal of Oceanography* 58, pp. 775–785.

Nicolaus, M., C. Petrich, S. R. Hudson, and M. A. Granskog (2013). “Variability of Light Transmission through Arctic Land-Fast Sea Ice during Spring”. In: *The Cryosphere* 7.3, pp. 977–986. DOI: `10.5194/tc-7-977-2013`.

Nomura, D., H. Eicken, R. Gradinger, and K. Shirasawa (2010). “Rapid Physically Driven Inversion of the Air–Sea Ice CO2 Flux in the Seasonal Landfast Ice off Barrow, Alaska after Onset of Surface Melt”. In: *Continental Shelf Research* 30.19, pp. 1998–2004. DOI: `10.1016/j.csr.2010.09.014`.

Nomura, D., M. A. Granskog, A. Fransson, M. Chierici, A. Silyakova, K. I. Ohshima, L. Cohen, B. Delille, S. R. Hudson, and G. S. Dieckmann (2018). “CO_2 Flux over Young and Snow-Covered Arctic Pack Ice in Winter and Spring”. In: *Biogeosciences* 15.11, pp. 3331–3343. DOI: `10.5194/bg-15-3331-2018`.

NORCOR (1975). *The Interaction of Crude Oil with Arctic Sea Ice.* Tech. rep. 27. NORCOR Engineering and Research Limited.

Notz, D. (2005). “Thermodynamic and Fluid-Dynamical Processes in Sea Ice”. PhD thesis. University of Cambridge.

Notz, D. and M. G. Worster (2008). “In Situ Measurements of the Evolution of Young Sea Ice”. In: *Journal of Geophysical Research: Oceans* 113.C3, 2007JC004333. DOI: `10.1029/2007JC004333`.

Notz, D. and M. G. Worster (2009). “Desalination Processes of Sea Ice Revisited”. In: *Journal of Geophysical Research: Oceans* 114.C05006. DOI: `10.1029/2008JC004885`.

Oggier, M. and H. Eicken (2022). “Seasonal Evolution of Granular and Columnar Sea Ice Pore Microstructure and Pore Network Connectivity”. In: *Journal of Glaciology*, pp. 1–16. DOI: `10.1017/jog.2022.1`.

Oggier, M., H. Eicken, J. Wilkinson, C. Petrich, and M. O’Sadnick (2020). “Crude Oil Migration in Sea-Ice: Laboratory Studies of Constraints on Oil Mobilization and Seasonal Evolution”. In: *Cold Regions Science and Technology* 174, p. 102924. DOI: `10.1016/j.coldregions.2019.102924`.

Olbricht, W. L. (1996). “Pore-Scale Prototypes of Multiphase Flow in Porous Media”. In: *Annual Review of Fluid Mechanics* 28.Volume 28, 1996, pp. 187–213. DOI: `10.1146/annurev.fl.28.010196.001155`.

Otremba, Z. (2007). “Oil Droplets as Light Absorbents in Seawater”. In: *Optics Express* 15.14, p. 8592. DOI: `10.1364/OE.15.008592`.

Overland, J. E. (1985). “Atmospheric Boundary Layer Structure and Drag Coefficients over Sea Ice”. In: *Journal of Geophysical Research: Oceans* 90.C5, pp. 9029–9049. DOI: `10.1029/JC090iC05p09029`.

Parkinson, J. (2019). “Nonlinear Convection in Sea Ice and Other Mushy Layers”. PhD thesis. University of Oxford.

Parmigiani, A., S. Faroughi, C. Huber, O. Bachmann, and Y. Su (2016). “Bubble Accumulation and Its Role in the Evolution of Magma Reservoirs in the Upper Crust”. In: *Nature* 532.7600, pp. 492–495. DOI: `10.1038/nature17401`.

Peppin, S. S. L., P. Aussillous, H. E. Huppert, and M. G. Worster (2007). “Steady-State Mushy Layers: Experiments and Theory”. In: *Journal of Fluid Mechanics* 570, pp. 69–77. DOI: `10.1017/S0022112006003028`.

Perovich, D. K., T. C. Grenfell, B. Light, and P. V. Hobbs (2002). “Seasonal Evolution of the Albedo of Multiyear Arctic Sea Ice”. In: *Journal of Geophysical Research: Oceans* 107.C10. DOI: `10.1029/2000JC000438`.

Perovich, D. (2011). “The Changing Arctic Sea Ice Cover”. In: *Oceanography* 24.3, pp. 162–173. DOI: `10.5670/oceanog.2011.68`.

Perovich, D. K. (1990). “Theoretical Estimates of Light Reflection and Transmission by Spatially Complex and Temporally Varying Sea Ice Covers”. In: *Journal of Geophysical Research: Oceans* 95.C6, pp. 9557–9567. DOI: `10.1029/JC095iC06p09557`.

Perovich, D. K. (2005). “On the Aggregate-scale Partitioning of Solar Radiation in Arctic Sea Ice during the Surface Heat Budget of the Arctic Ocean (SHEBA) Field Experiment”. In: *Journal of Geophysical Research: Oceans* 110.C3, 2004JC002512. DOI: `10.1029/2004JC002512`.

Perovich, D. K. (2017). “Sea Ice and Sunlight”. In: *Sea Ice*. John Wiley & Sons, Ltd. Chap. 4, pp. 110–137. DOI: `10.1002/9781118778371.ch4`.

Perovich, D. K. and T. C. Grenfell (1982). “A Theoretical Model of Radiative Transfer in Young Sea Ice”. In: *Journal of Glaciology* 28.99, pp. 341–356. DOI: `10.3189/S0022143000011680`.

Perovich, D. K., G. A. Maykut, and T. C. Grenfell (1986). “Optical Properties Of Ice And Snow In The Polar Oceans. I: Observations”. In: *1986 Technical Symposium Southeast*. Ed. by M. A. Blizard. Orlando, p. 232. DOI: `10.1117/12.964238`.

Perovich, D. K. and C. Polashenski (2012). “Albedo Evolution of Seasonal Arctic Sea Ice”. In: *Geophysical Research Letters* 39.8, 2012GL051432. DOI: `10.1029/2012GL051432`.

Perovich, D. K., J. A. Richter-Menge, K. F. Jones, and B. Light (2008). “Sunlight, Water, and Ice: Extreme Arctic Sea Ice Melt during the Summer of 2007”. In: *Geophysical Research Letters* 35.11, 2008GL034007. DOI: `10.1029/2008GL034007`.

Peterson, A. K. (2018). “Observations of Brine Plumes below Melting Arctic Sea Ice”. In: *Ocean Science* 14.1, pp. 127–138. DOI: `10.5194/os-14-127-2018`.

Petrich, C. and H. Eicken (2017). “Overview of Sea Ice Growth and Properties”. In: *Sea Ice*. John Wiley & Sons, Ltd. Chap. 1, pp. 1–41. DOI: `10.1002/9781118778371.ch1`.

Polashenski, C., K. M. Golden, D. K. Perovich, E. Skyllingstad, A. Arnsten, C. Stwertka, and N. Wright (2017). “Percolation Blockage: A Process That Enables Melt Pond Formation on First Year A Rctic Sea Ice”. In: *Journal of Geophysical Research: Oceans* 122.1, pp. 413–440. DOI: `10.1002/2016JC011994`.

Polashenski, C., D. Perovich, and Z. Courville (2012). “The Mechanisms of Sea Ice Melt Pond Formation and Evolution”. In: *Journal of Geophysical Research: Oceans* 117.C1, 2011JC007231. DOI: `10.1029/2011JC007231`.

Powers, D., K. O’Neill, and S. C. Colbeck (1985). “Theory of Natural Convection in Snow”. In: *Journal of Geophysical Research: Atmospheres* 90.D6, pp. 10641–10649. DOI: `10.1029/JD090iD06p10641`.

Provost, C., N. Sennéchael, J. Miguet, P. Itkin, A. Rösel, Z. Koenig, N. Villacieros-Robineau, and M. A. Granskog (2017). “Observations of Flooding and Snow-ice Formation in a Thinner A Rctic Sea-ice Regime during the N-ICE 2015 Campaign: Influence of Basal Ice Melt and Storms”. In: *Journal of Geophysical Research: Oceans* 122.9, pp. 7115–7134. DOI: `10.1002/2016JC012011`.

Pustogvar, A. and A. Kulyakhtin (2016). “Sea Ice Density Measurements. Methods and Uncertainties”. In: *Cold Regions Science and Technology* 131, pp. 46–52. DOI: `10.1016/j.coldregions.2016.09.001`.

Reagan, J. R. et al. (2023). *World Ocean Atlas 2023*. DOI: `10.25921/VA26-HV25`.

Redmond Roche, B. H. and M. D. King (2024). “Calculations of Arctic Ice-Ocean Interface Photosynthetically Active Radiation (PAR) Transmittance Values”. In: *Earth and Space Science* 11.2, e2023EA002948. DOI: `10.1029/2023EA002948`.

Redmond Roche, B. and M. King (2022a). *Quantifying the Effects of Background Concentrations of Crude Oil Pollution on Sea Ice Albedo.* DOI: `10.5281/ZENODO.12707591`.

Redmond Roche, B. H. (2024). "Quantifying the Effects of Background Concentrations of Crude Oil Pollution on Polar Sea Ice and Assessing How Sea Ice and Snow Affect PAR Transmittance at the Ice-Ocean Interface". PhD thesis. Royal Holloway, University of London.

Redmond Roche, B. H. and M. D. King (2022b). "Quantifying the Effects of Background Concentrations of Crude Oil Pollution on Sea Ice Albedo". In: *The Cryosphere* 16.10, pp. 3949–3970. DOI: `10.5194/tc-16-3949-2022`.

Rees Jones, D. (2014). "The Convective Desalination of Sea Ice". PhD thesis. Apollo - University of Cambridge Repository. DOI: `10.17863/CAM.16136`.

Rees Jones, D. W. and M. G. Worster (2013a). "A Simple Dynamical Model for Gravity Drainage of Brine from Growing Sea Ice". In: *Geophysical Research Letters* 40.2, pp. 307–311. DOI: `10.1029/2012GL054301`.

Rees Jones, D. W. and M. G. Worster (2013b). "Fluxes through Steady Chimneys in a Mushy Layer during Binary Alloy Solidification". In: *Journal of Fluid Mechanics* 714, pp. 127–151. DOI: `10.1017/jfm.2012.462`.

Rees Jones, D. W. and M. G. Worster (2014). "A Physically Based Parameterization of Gravity Drainage for Sea-ice Modeling". In: *Journal of Geophysical Research: Oceans* 119.9, pp. 5599–5621. DOI: `10.1002/2013JC009296`.

Rogers, R. R. and M. K. Yau (1996). *A Short Course in Cloud Physics.* Third edition. International Series in Natural Philosophy Volume 113. Burlington, Massachusetts: Butterworth-Heinemann.

Rogowska, J. and J. Namieśnik (2010). "Environmental Implications of Oil Spills from Shipping Accidents". In: *Reviews of Environmental Contamination and Toxicology Volume 206.* Ed. by D. M. Whitacre. Vol. 206. New York, NY: Springer New York, pp. 95–114. DOI: `10.1007/978-1-4419-6260-7_5`.

Rößger, N., T. Sachs, C. Wille, J. Boike, and L. Kutzbach (2022). "Seasonal Increase of Methane Emissions Linked to Warming in Siberian Tundra". In: *Nature Climate Change* 12.11, pp. 1031–1036. DOI: `10.1038/s41558-022-01512-4`.

Rudels, B. and D. Quadfasel (1991). "Convection and Deep Water Formation in the Arctic Ocean-Greenland Sea System". In: *Journal of Marine Systems* 2.3-4, pp. 435–450. DOI: `10.1016/0924-7963(91)90045-V`.

Rysgaard, S., J. Bendtsen, B. Delille, G. S. Dieckmann, R. N. Glud, H. Kennedy, J. Mortensen, S. Papadimitriou, D. N. Thomas, and J.-L. Tison (2011). "Sea Ice Contribution to the Air–Sea CO2 Exchange in the Arctic and Southern Oceans". In: *Tellus B: Chemical and Physical Meteorology* 63.5, pp. 823–830. DOI: `10.1111/j.1600-0889.2011.00571.x`.

Rysgaard, S., R. N. Glud, M. K. Sejr, M. E. Blicher, and H. J. Stahl (2008). "Denitrification Activity and Oxygen Dynamics in Arctic Sea Ice". In: *Polar Biology* 31.5, pp. 527–537. DOI: `10.1007/s00300-007-0384-x`.

Rysgaard, S. and R. N. Glud (2004). "Anaerobic N_2 Production in Arctic Sea Ice". In: *Limnology and Oceanography* 49.1, pp. 86–94. DOI: `10.4319/lo.2004.49.1.0086`.

Sakshaug, E. (2004). "Primary and Secondary Production in the Arctic Seas". In: *The Organic Carbon Cycle in the Arctic Ocean.* Ed. by R. Stein and R. W. MacDonald. Berlin, Heidelberg: Springer Berlin Heidelberg, pp. 57–81. DOI: `10.1007/978-3-642-18912-8_3`.

Salganik, E., O. Crabeck, N. Fuchs, N. Hutter, P. Anhaus, and J. C. Landy (2024). “Impacts of Air Fraction Increase on Arctic Sea-Ice Thickness Retrieval during Melt Season”. In: *EGUsphere*, pp. 1–30. DOI: `10.5194/egusphere-2024-2398`.

Schulze, T. P. and M. G. Worster (2005). “A Time-Dependent Formulation of the Mushy-Zone Free-Boundary Problem”. In: *Journal of Fluid Mechanics* 541, pp. 193–202. DOI: `10.1017/S0022112005006221`.

Serreze, M. C. and J. Stroeve (2015). “Arctic Sea Ice Trends, Variability and Implications for Seasonal Ice Forecasting”. In: *Philosophical Transactions of the Royal Society A: Mathematical, Physical and Engineering Sciences* 373.2045, p. 20140159. DOI: `10.1098/rsta.2014.0159`.

Shiu, W. Y., M. Bobra, A. M. Bobra, A. Maijanen, L. Suntio, and D. Mackay (1990). “The Water Solubility of Crude Oils and Petroleum Products”. In: *Oil and Chemical Pollution* 7.1, pp. 57–84. DOI: `10.1016/S0269-8579(05)80034-6`.

Skarke, A., C. Ruppel, M. Kodis, D. Brothers, and E. Lobecker (2014). “Widespread Methane Leakage from the Sea Floor on the Northern US Atlantic Margin”. In: *Nature Geoscience* 7.9, pp. 657–661. DOI: `10.1038/ngeo2232`.

Skyllingstad, E. D. and C. A. Paulson (2007). “A Numerical Study of Melt Ponds”. In: *Journal of Geophysical Research: Oceans* 112.C8, 2006JC003729. DOI: `10.1029/2006JC003729`.

Smith, M. M., B. Light, A. R. Macfarlane, D. K. Perovich, M. M. Holland, and M. D. Shupe (2022). “Sensitivity of the Arctic Sea Ice Cover to the Summer Surface Scattering Layer”. In: *Geophysical Research Letters* 49.9, e2022GL098349. DOI: `10.1029/2022GL098349`.

Sørensen, L., A. G. Melbye, and A. M. Booth (2014). “Oil Droplet Interaction with Suspended Sediment in the Seawater Column: Influence of Physical Parameters and Chemical Dispersants”. In: *Marine Pollution Bulletin* 78.1-2, pp. 146–152. DOI: `10.1016/j.marpolbul.2013.10.049`.

Spreen, G. and S. Kern (2017). “Methods of Satellite Remote Sensing of Sea Ice”. In: *Sea Ice*. Ed. by D. N. Thomas. 1st ed. Wiley, pp. 239–260. DOI: `10.1002/9781118778371.ch9`.

Spreen, G., R. Kwok, and D. Menemenlis (2011). “Trends in Arctic Sea Ice Drift and Role of Wind Forcing: 1992-2009: TRENDS IN ARCTIC SEA ICE DRIFT AND WIND”. In: *Geophysical Research Letters* 38.19, p. L19501. DOI: `10.1029/2011GL048970`.

Stamnes, K., G. E. Thomas, and J. J. Stamnes (2017). *Radiative Transfer in the Atmosphere and Ocean*. 2nd ed. Cambridge University Press. DOI: `10.1017/9781316148549`.

Stefan, J. (1891). “Ueber Die Theorie Der Eisbildung, Insbesondere Über Die Eisbildung Im Polarmeere”. In: *Annalen der Physik* 278.2, pp. 269–286. DOI: `10.1002/andp.18912780206`.

Strack, M., E. Kellner, and J. M. Waddington (2005). “Dynamics of Biogenic Gas Bubbles in Peat and Their Effects on Peatland Biogeochemistry”. In: *Global Biogeochemical Cycles* 19.1, 2004GB002330. DOI: `10.1029/2004GB002330`.

Stroeve, J. C., T. Markus, L. Boisvert, J. Miller, and A. Barrett (2014). “Changes in Arctic Melt Season and Implications for Sea Ice Loss”. In: *Geophysical Research Letters* 41.4, pp. 1216–1225. DOI: `10.1002/2013GL058951`.

Stroeve, J. C. et al. (2024). “Mapping Potential Timing of Ice Algal Blooms From Satellite”. In: *Geophysical Research Letters* 51.8, e2023GL106486. DOI: `10.1029/2023GL106486`.

Stroeve, J., M. Vancoppenolle, G. Veyssiere, M. Lebrun, G. Castellani, M. Babin, M. Karcher, J. Landy, G. E. Liston, and J. Wilkinson (2021). "A Multi-Sensor and Modeling Approach for Mapping Light Under Sea Ice During the Ice-Growth Season". In: *Frontiers in Marine Science* 7, pp. 591–600. DOI: `10.3389/fmars.2020.592337`.

Sturm, M., J. Holmgren, M. König, and K. Morris (1997). "The Thermal Conductivity of Seasonal Snow". In: *Journal of Glaciology* 43.143, pp. 26–41. DOI: `10.3189/S0022143000002781`.

Sturm, M. and R. A. Massom (2017). "Snow in the Sea Ice System: Friend or Foe?" In: *Sea Ice*. Ed. by D. N. Thomas. 1st ed. Wiley, pp. 65–109. DOI: `10.1002/9781118778371.ch3`.

Sturm, M., D. K. Perovich, and J. Holmgren (2002). "Thermal Conductivity and Heat Transfer through the Snow on the Ice of the Beaufort Sea". In: *Journal of Geophysical Research: Oceans* 107.C10. DOI: `10.1029/2000JC000409`.

Suckale, J., T. Keller, K. V. Cashman, and P.-O. Persson (2016). "Flow-to-fracture Transition in a Volcanic Mush Plug May Govern Normal Eruptions at Stromboli". In: *Geophysical Research Letters* 43.23. DOI: `10.1002/2016GL071501`.

Svensson, U. and A. Omstedt (1994). "Simulation of Supercooling and Size Distribution in Frazil Ice Dynamics". In: *Cold Regions Science and Technology* 22.3, pp. 221–233. DOI: `10.1016/0165-232X(94)90001-9`.

Takahashi, T. et al. (2009). "Climatological Mean and Decadal Change in Surface Ocean pCO2, and Net Sea–Air CO2 Flux over the Global Oceans". In: *Deep Sea Research Part II: Topical Studies in Oceanography*. Surface Ocean CO2 Variability and Vulnerabilities 56.8, pp. 554–577. DOI: `10.1016/j.dsr2.2008.12.009`.

Taylor, P. D. and D. L. Feltham (2004). "A Model of Melt Pond Evolution on Sea Ice". In: *Journal of Geophysical Research: Oceans* 109.C12, 2004JC002361. DOI: `10.1029/2004JC002361`.

Thomas, M., M. Vancoppenolle, J. L. France, W. T. Sturges, D. C. E. Bakker, J. Kaiser, and R. Von Glasow (2020). "Tracer Measurements in Growing Sea Ice Support Convective Gravity Drainage Parameterizations". In: *Journal of Geophysical Research: Oceans* 125.2, e2019JC015791. DOI: `10.1029/2019JC015791`.

Thorndike, A. S. and R. Colony (1982). "Sea Ice Motion in Response to Geostrophic Winds". In: *Journal of Geophysical Research: Oceans* 87.C8, pp. 5845–5852. DOI: `10.1029/JC087iC08p05845`.

Thorpe, S. A. (1982). "On the Clouds of Bubbles Formed by Breaking Wind-Waves in Deep Water, and Their Role in Air-Sea Gas Transfer". In: *Philosophical Transactions of the Royal Society of London. Series A, Mathematical and Physical Sciences* 304.1483, pp. 155–210. DOI: `10.1098/rsta.1982.0011`.

Timco, G. and R. Frederking (1996). "A Review of Sea Ice Density". In: *Cold Regions Science and Technology* 24.1, pp. 1–6. DOI: `10.1016/0165-232X(95)00007-X`.

Tison, J.-L., B. Delille, and S. Papadimitriou (2017). "Gases in Sea Ice". In: *Sea Ice*. John Wiley & Sons, Ltd. Chap. 18, pp. 433–471. DOI: `10.1002/9781118778371.ch18`.

Tsurikov, V. L. (1979). "The Formation and Composition of the Gas Content of Sea Ice". In: *Journal of Glaciology* 22.86, pp. 67–81. DOI: `10.3189/S0022143000014064`.

Turner, A., E. Hunke, and C. Bitz (2013). "Two Modes of Sea-Ice Gravity Drainage: A Parameterization for Large-Scale Modeling". In: *Journal of Geophysical Research: Oceans* 118.5, pp. 2279–2294. DOI: `10.1002/jgrc.20171`.

Untersteiner, N. and F. I. Badgley (1965). "The Roughness Parameters of Sea Ice". In: *Journal of Geophysical Research* 70.18, pp. 4573–4577. DOI: `10.1029/JZ070i018p04573`.

Vallis, G. K. (2017). *Atmospheric and Oceanic Fluid Dynamics: Fundamentals and Large-Scale Circulation.* 2nd ed. Cambridge: Cambridge University Press. DOI: `10.1017/9781107588417`.

Vancoppenolle, M., G. Madec, M. Thomas, and T. McDougall (2019). "Thermodynamics of Sea Ice Phase Composition Revisited". In: *Journal of Geophysical Research: Oceans* 124.1, pp. 615–634. DOI: `10.1029/2018JC014611`.

Vancoppenolle, M., C. M. Bitz, and T. Fichefet (2007). "Summer Landfast Sea Ice Desalination at Point Barrow, Alaska: Modeling and Observations". In: *Journal of Geophysical Research: Oceans* 112.C4. DOI: `10.1029/2006JC003493`.

Vancoppenolle, M., H. Goosse, A. de Montety, T. Fichefet, B. Tremblay, and J.-L. Tison (2010). "Modeling Brine and Nutrient Dynamics in Antarctic Sea Ice: The Case of Dissolved Silica". In: *Journal of Geophysical Research: Oceans* 115.C2. DOI: `10.1029/2009JC005369`.

Vancoppenolle, M. and L. Tedesco (2017). "Numerical Models of Sea Ice Biogeochemistry". In: *Sea Ice.* John Wiley & Sons, Ltd. Chap. 20, pp. 492–515. DOI: `10.1002/9781118778371.ch20`.

Vérin, G., F. Domine, M. Babin, G. Picard, and L. Arnaud (2022). "Metamorphism of Snow on Arctic Sea Ice during the Melt Season: Impact on Spectral Albedo and Radiative Fluxes through Snow". In: *The Cryosphere* 16.9, pp. 3431–3449. DOI: `10.5194/tc-16-3431-2022`.

Virtanen, P. et al. (2020). "SciPy 1.0: Fundamental Algorithms for Scientific Computing in Python". In: *Nature Methods* 17.3, pp. 261–272. DOI: `10.1038/s41592-019-0686-2`.

Wang, F., M. Pućko, and G. Stern (2017). "Transport and Transformation of Contaminants in Sea Ice". In: *Sea Ice.* Ed. by D. N. Thomas. 1st ed. Wiley, pp. 472–491. DOI: `10.1002/9781118778371.ch19`.

Wang, S. and K. A. Pratt (2017). "Molecular Halogens Above the Arctic Snowpack: Emissions, Diurnal Variations, and Recycling Mechanisms: Arctic Molecular Halogens". In: *Journal of Geophysical Research: Atmospheres* 122.21, pp. 11, 991–12, 007. DOI: `10.1002/2017JD027175`.

Warren, S. G. and R. E. Brandt (2008). "Optical Constants of Ice from the Ultraviolet to the Microwave: A Revised Compilation". In: *Journal of Geophysical Research: Atmospheres* 113.D14, 2007JD009744. DOI: `10.1029/2007JD009744`.

Watanabe, H. and K. Iizuka (1985). "The Influence of Dissolved Gases on the Density of Water". In: *Metrologia* 21.1, pp. 19–26. DOI: `10.1088/0026-1394/21/1/005`.

Watts, J., T. G. Bell, K. Anderson, B. J. Butterworth, S. Miller, B. Else, and J. Shutler (2022). "Impact of Sea Ice on Air-Sea CO2 Exchange – A Critical Review of Polar Eddy Covariance Studies". In: *Progress in Oceanography* 201, p. 102741. DOI: `10.1016/j.pocean.2022.102741`.

Weiss, R. (1970). "The Solubility of Nitrogen, Oxygen and Argon in Water and Seawater". In: *Deep Sea Research and Oceanographic Abstracts* 17.4, pp. 721–735. DOI: `10.1016/0011-7471(70)90037-9`.

Weiss, R. (1974). "Carbon Dioxide in Water and Seawater: The Solubility of a Non-Ideal Gas". In: *Marine Chemistry* 2.3, pp. 203–215. DOI: `10.1016/0304-4203(74)90015-2`.

Wells, A. J., J. R. Hitchen, and J. R. G. Parkinson (2019). "Mushy-Layer Growth and Convection, with Application to Sea Ice". In: *Philosophical Transactions of the Royal Society A: Mathematical, Physical and Engineering Sciences* 377.2146, p. 20180165. DOI: `10.1098/rsta.2018.0165`.

Wilkinson, J., C. Beegle-Krause, K.-U. Evers, N. Hughes, A. Lewis, M. Reed, and P. Wadhams (2017). "Oil Spill Response Capabilities and Technologies for Ice-Covered Arctic Marine Waters: A Review of Recent Developments and Established Practices". In: *Ambio* 46.S3, pp. 423–441. DOI: `10.1007/s13280-017-0958-y`.

Windom, H. L. (2019). "Elemental Composition of Suspended Particles across the Southeastern Continental Shelf off the Coast of North Florida and South Georgia: Provenance, Transport, Fate and Implications to Mid-Outer Shelf Water Column Processes." In: *Continental Shelf Research* 178, pp. 27–40. DOI: `10.1016/j.csr.2019.03.005`.

Worster, M. G. (2000). "Solidification of Fluids". In: *Perspectives in Fluid Dynamics: A Collective Introduction to Current Research.* Cambridge: University Press, pp. 393–446.

Worster, M. G. (1986). "Solidification of an Alloy from a Cooled Boundary". In: *Journal of Fluid Mechanics* 167.-1, p. 481. DOI: `10.1017/s0022112086002938`.

Worster, M. G. (1992). "Instabilities of the Liquid and Mushy Regions during Solidification of Alloys". In: *Journal of Fluid Mechanics* 237, pp. 649–669. DOI: `10.1017/S0022112092003562`.

Worster, M. G. (1997). "Convection in Mushy Layers". In: *Annual Review of Fluid Mechanics* 29.1, pp. 91–122. DOI: `10.1146/annurev.fluid.29.1.91`.

Worster, M. G. and D. W. Rees Jones (2015). "Sea-Ice Thermodynamics and Brine Drainage". In: *Philosophical Transactions of the Royal Society A: Mathematical, Physical and Engineering Sciences* 373.2045, p. 20140166. DOI: `10.1098/rsta.2014.0166`.

Xie, J., R. P. Raj, L. Bertino, A. Samuelsen, and T. Wakamatsu (2019). "Evaluation of Arctic Ocean Surface Salinities from the Soil Moisture and Ocean Salinity (SMOS) Mission against a Regional Reanalysis and in Situ Data". In: *Ocean Science* 15.5, pp. 1191–1206. DOI: `10.5194/os-15-1191-2019`.

Zhong, W., S. T. Cole, J. Zhang, R. Lei, and M. Steele (2022). "Increasing Winter Ocean-to-Ice Heat Flux in the Beaufort Gyre Region, Arctic Ocean Over 2006–2018". In: *Geophysical Research Letters* 49.2, e2021GL096216. DOI: `10.1029/2021GL096216`.

Zhou, J., B. Delille, F. Brabant, and J.-L. Tison (2014a). "Insights into Oxygen Transport and Net Community Production in Sea Ice from Oxygen, Nitrogen and Argon Concentrations". In: *Biogeosciences* 11.18, pp. 5007–5020. DOI: `10.5194/bg-11-5007-2014`.

Zhou, J., J.-L. Tison, G. Carnat, N.-X. Geilfus, and B. Delille (2014b). "Physical Controls on the Storage of Methane in Landfast Sea Ice". In: *The Cryosphere* 8.3, pp. 1019–1029. DOI: `10.5194/tc-8-1019-2014`.

Zhou, J., B. Delille, H. Eicken, M. Vancoppenolle, F. Brabant, G. Carnat, N.-X. Geilfus, T. Papakyriakou, B. Heinesch, and J.-L. Tison (2013). "Physical and Biogeochemical Properties in Landfast Sea Ice (Barrow, Alaska): Insights on Brine and Gas Dynamics across Seasons". In: *Journal of Geophysical Research: Oceans* 118.6, pp. 3172–3189. DOI: `10.1002/jgrc.20232`.